UNIVERSITÀ DEGLI STUDI DI NAPOLI FEDERICO II
POLO DELLE SCIENZE E DELLE TECNOLOGIE
DOTTORATO DI RICERCA IN RISCHIO SISMICO
XXI CICLO

PERFORMANCE-BASED APPROACH IN SEISMIC DESIGN OF EMBEDDED RETAINING WALLS

TESI PER IL CONSEGUIMENTO DEL TITOLO

CIRO VISONE

NAPOLI, NOVEMBRE 2008

RELATORE

PROF. FILIPPO SANTUCCI DE MAGISTRIS

COORDINATORE DEL DOTTORATO

PROF. PAOLO GASPARINI

UNIVERSITÀ DEGLI STUDI DI NAPOLI FEDERICO II

PERFORMANCE-BASED APPROACH IN SEISMIC DESIGN OF EMBEDDED RETAINING WALLS

CIRO VISONE

A dissertation submitted for the
Degree of Doctor of Philosophy
at University of Napoli Federico II, Italy
Napoli, November 2008

To my wife

ABSTRACT

The increasing use of the underground spaces and the last seismic events in the urban areas have driven many researchers of different countries to deepen the knowledge on the dynamic behaviour of the structure embedded in the subsoil.

This thesis attempts to give some contributes on the application of the performance based approach for the seismic design of the embedded retaining walls.

After an overview on the earth pressure theories proposed by different authors, the static and seismic design methods commonly adopted in the current practice and based on pseudostatic approaches are recalled.

Several limitations on these procedures can be recognized: the difficulties on the definition of the seismic coefficient; the calculation of the expected earthquake-induced displacements around the construction. Moreover, in the framework of the Performance-Based Design, these methods do not able to describe the response of the retaining systems to a given earthquake. The seismic displacements of the flexible walls are evaluated by means of Newmark sliding block procedures, that were developed for rigid structures, and the yield sequence of the different structural components can not be predicted. Then, the application of the hierarchical resistance criteria in the dimensioning of the various parts can not be applied.

In this thesis, different level of analysis are highlighted in relation to the importance of the structure and to the design phase.

An innovative procedure that can be included in the framework of the "pushover analyses" is also proposed for the seismic design of the embedded retaining walls.

Finally, the results obtained by the application of the different methods for the ideal case study of cantilever diaphragms embedded in dry loose and dense sand are presented. The material properties used in the analyses are referred to the Fraction E (BS 100/170) of the Leighton Buzzard sand, for which a series of triaxial and torsional tests on reconstituted samples was conducted.

INDEX

LIST OF FIGURES

LIST OF TABLES

1 INTRODUCTION.

In the last decades, for the shortage of shallow spaces and for the difficulties connected to the tyre transportation, it is attended to an increasing utilization of the urban subsoils for the realization of transport infrastructures and many others civil engineering constructions. Underground lines have been realized and are in construction in many important Italian cities, such as Milano, Roma, Napoli, Torino. The train crossings of the High Velocity Train lines (TAV) are also under construction in the cities of Bologna, Firenze, etc.. All of the Italian cities are interested to the realization of subway parking and underpasses. The major part of these constructions have required or will require deep excavations and tunnels that are often placed close to existing buildings. In many cases, the structures pass near to the historical centres of the cities, where poor safety conditions for the existing constructions can be recognized.

The availability of commercial codes, advanced constitutive models to describe the soil behaviour when subjected to stress paths similar to those induced by the excavations, and the spread of suitable laboratory ed in situ techniques have allowed more reliable the evaluation of the safety conditions and the prediction of the behaviour of these types of structures during both the construction and the serviceability phases. Furthermore, the monitoring of full scale constructions has permitted to evaluate the reliability degree of simplified design methods, such as those based on the limit equilibrium, and to develop empirical methods to predict the effects of excavations on the adjacent structures. Finally, the introduction of the limit states design methods by using the partial factor of safety (EN1997-1), allows evaluating the safety of the constructions for which can not be defined a single global factor of safety.

These progresses concern particularly the earth retaining structures in absence of seismic loadings. The evaluation of the safety conditions of these structures in seismic areas has not reached the same improvements. In these cases, the complex dynamic soil-structure interaction render the simplified methods very difficult and unrealistic. The examinations can be performed by means of the pseudostatic approaches based on the limit equilibrium only for simple cases, such as cantilever or single-anchor retaining walls, and adopting conventional seismic coefficients that suffer to some limitations for the fact that they were defined for structures over the ground. The recent European codes (EN 1998-5) have tackled in a marginal manner the check of safety conditions of embedded structures suggesting for the flexible retaining walls the use of seismic coefficients equal to the ratio between the expected maximum acceleration in the site of interest and the gravity acceleration.

In this context, it becomes clear the necessity to improve the knowledge on the seismic behaviour of the embedded retaining walls, especially to develop innovative seismic design methods able to give good predictions in the practical applications.

On these basis, a research line (Linea 6 "Metodi Innovativi per il progetto delle opere geotecniche e la valutazione della stabilità dei pendii") of the Consortium of the University Network of Seismic Engineering Laboratories (ReLUIS, www.reluis.it) was devoted to develop and validate innovative design methods for the earth retaining structures and tunnels placed in seismic areas.

The main activities of the ReLUIS research line are based on:

- physical modelling, by performing centrifuge tests on simplified scheme models;

- reference numerical modelling, by carrying out a series of indications on how to conduct reliable dynamic analyses by using commercial codes;
- dynamic analyses on calibrated numerical models to highlight the main aspects of the seismic soil-structure interaction;
- simplified analyses, that should be validated on the basis of the results of the physical modelling and of the advanced dynamic analyses.

The centrifuge physical modelling will be executed at the Schofield Centre of University of Cambridge on prototypes of cantilever and propped diaphragms embedded in uniform sandy layers. The dynamic Cambridge Centrifuge was equipped with a seismic actuator (SAM – Stored Angular Momentum) constituted by two rotating eccentric masses that move with a constant angular velocity (Madabhushi et al., 1998). The SAM actuator stores energy in a pair of spinning flywheels driving a reciprocating rod. This energy can be released to a model by means of a fast-acting hydraulic clutch. This actuator imparts an approximately sinusoidal input motion to the model, with control over amplitude (± 2.5mm), frequency (< 500Hz) and duration being available.

The layouts of the models with the geometries and the equipments of the programmed centrifuge tests are plotted in Figure 1-1.

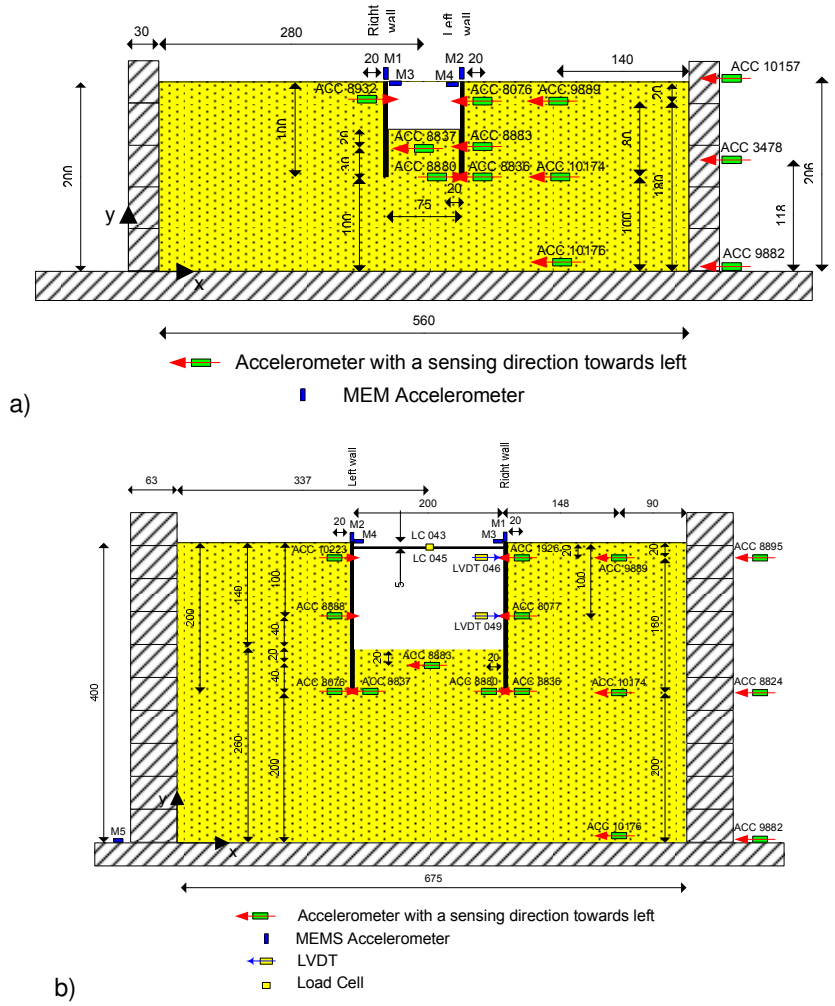

Figure 1-1. *Geometry and equipments of the dynamic centrifuge tests in ReLUIS experimental program: a) cantilever diaphragms; b) propped diaphragms.*

The models will be prepared air-pluviating dry sand into the box till to reach the level of the wall base. After the positioning of sensors and diaphragms, the sand will be also deposited to create the desired geometry.

The tests on the cantilever walls will be conducted to an acceleration of 80g. At the prototype scale, the centrifuge models will simulate a 4 meters high excavation retained by a vertical wall of 8m embedded in dry sandy layers with a thick of 16m. The prototypes of the propped diaphragms are constituted by a retained height of 5.60m with a depth of embedment of 2.40m into the sand. The thickness of the soil layer is the same of cantilever prototypes. The tests will be performed to an acceleration of 40g.

The material adopted for the centrifuge tests at the Schofield Centre is the Fraction E of the Leighton Buzzard Sand for which an advanced characterization of the mechanical behaviour can not be found in the literature.

At the same time, to increase the knowledge about the dynamic behaviour of the soil-retaining wall system in case of earthquake, the Structural and Geotechnical Dynamic Laboratory StreGa of University of Molise is hired on the Structural Health Monitoring (SHM) of a cantilever sheet pile walls placed near to the "Casa dello Studente" building in Campobasso seat (Italy).

The retaining system is constituted by two piles rows connected by means of a concrete beam. The piles have a diameter of 800mm and are arranged to have the centres at the vertexes of equilateral triangles. Two of these piles have been instrumented with embedded piezoelectric accelerometers.

Figure 1-2 and Figure 1-3 show plan views of the retaining wall and of the monitored piles.

Three sensor modules have been placed in each pile. The positions have been chosen in order to be as far as possible from the computed locations of the center of rotation in both the building and operational phases. Additional two sensors have been placed on top of each pile, into a box over the top beams which connects all piles. A sketch of the piles instrumentation and some structural details are shown in Figure 1-4.

The dimensions of sensor modules are not negligible and cause some changes in the piles geometry. To avoid singularities in the overall behaviour of the structure, specific computations and additional reinforcements have been provided in order to guarantee for the instrumented piles similar stiffness and strength characteristics of the adjacent ones.

In this context of the research interests devoted to the study of the dynamic behaviour of embedded retaining walls by the scientific community, the present thesis finds its main role.

The activities developed during this work have both an experimental and a numerical character.

The first part was dedicated to the validation of the commercial FE code PLAXIS v.8.2 (Brinkgreve, 2002) for the development of dynamic soil-structure interaction analyses The program was chosen because it is largely adopted both from practitioners and academics. However, the obtained results have a general character and can be extended to other FE codes.

At the same time, some laboratory apparatuses of the Laboratory of Soil Dynamics (DYNALAB) of the Hydraulic, Geotechnical and Environmental Engineering Department (D.I.G.A. – Dipartimento di Ingegneria Idraulica, Geotecnica ed Ambientale) at University of Napoli Federico II were calibrated to investigate the mechanical behaviour of the Fraction E of Leighton Buzzard Sand that will be used in the centrifuge tests.

Figure 1-2. *Plan view of the monitored piles of "Casa dello Studente" (CB – Italy).*

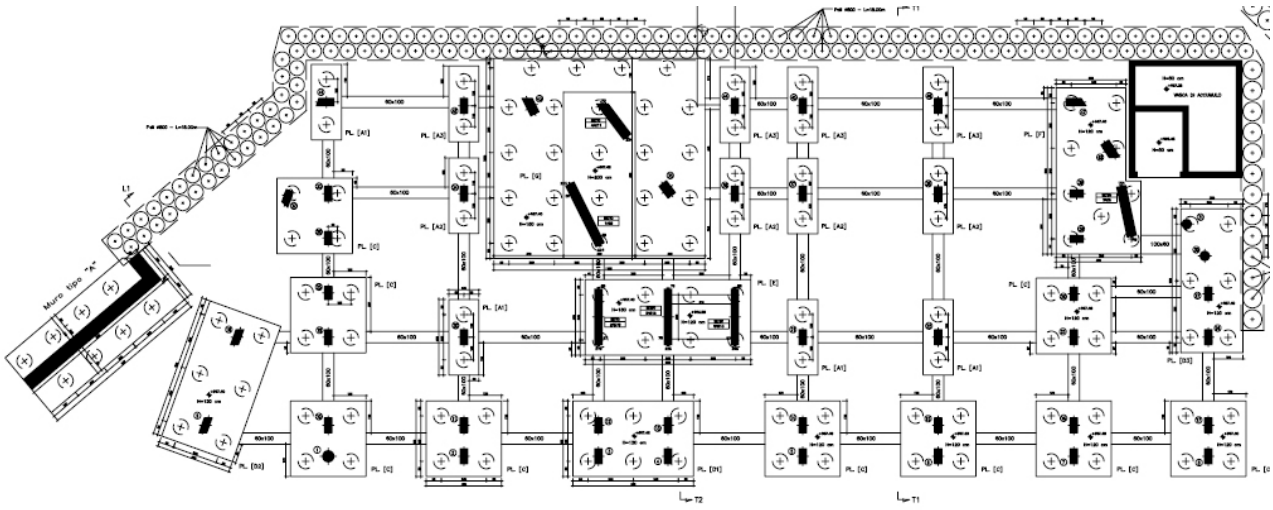

Figure 1-3. *Plan view of "Casa dello Studente" building foundations and monitored sheet pile wall.*

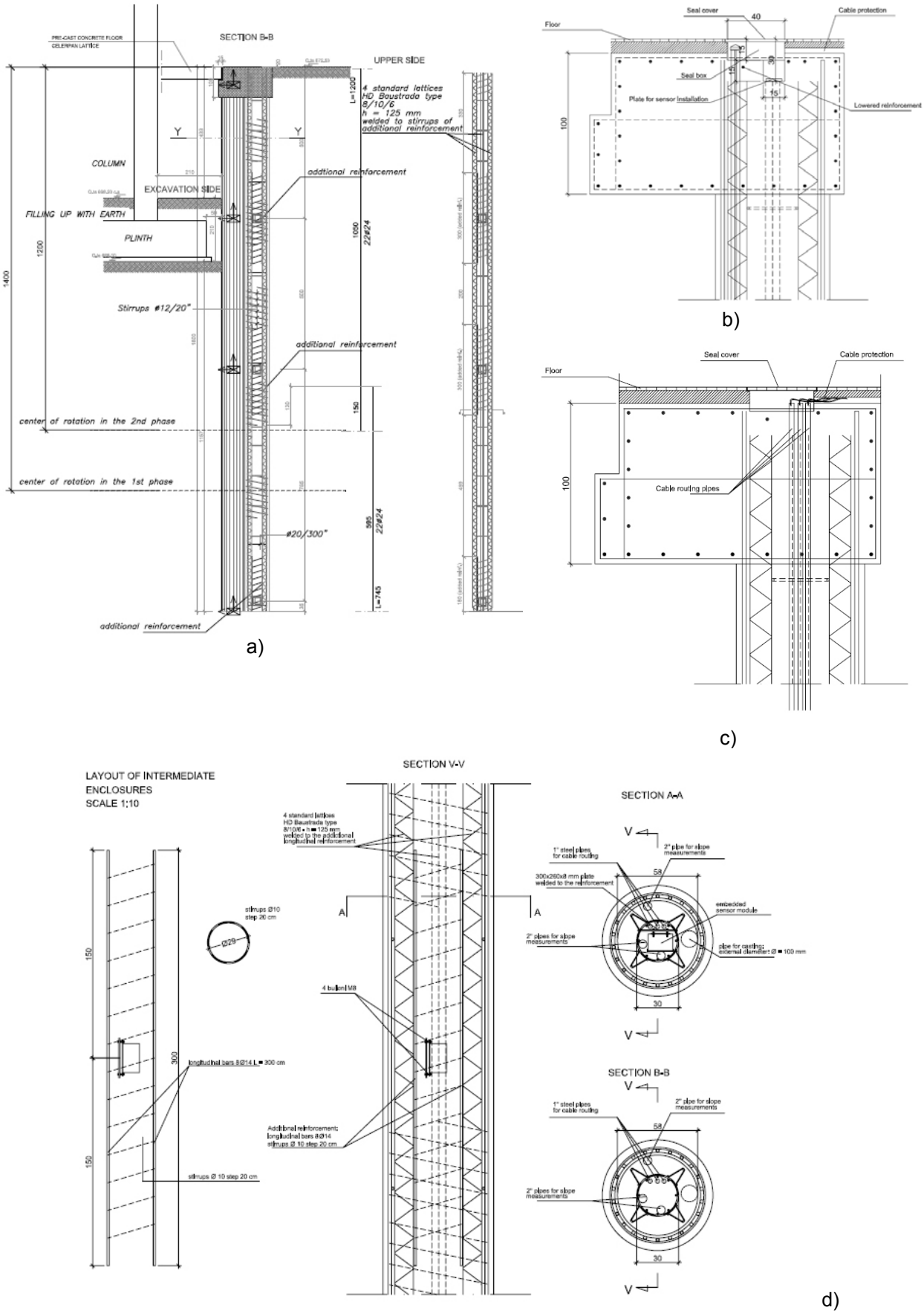

Figure 1-4. *Sketch of piles instrumentation: a) vertical position of the sensors; b) and c) details of piles head and sensor housing; d) layout of intermediate enclosures.*

An experimental campaign was then developed on the LB sand by means of triaxial compressions and extensions, resonant column and torsional shear tests. The results are presented in the Annex A of this thesis.

The calibration of the Dynamic Module of PLAXIS code was carried out by simulating numerically the one-dimensional shear waves vertical propagation into ideal visco-elastic layers. The main aspects of the research are described in the Annex B. The performed parametric study have been allowed recognizing the various sources of damping existing in dynamic time-domain analyses and correctly defining the numerical parameters to assume in the numerical calculations. In particular, the use of the Rayleigh damping formulation to model the soil viscous damping was extended to account for the numerical damping introduced in the analyses by the time integration scheme. Interesting indications and suggestions were also given on how to reduce the spurious effects of the reflected waves on the lateral boundaries of the discrete models and to rightly simulate the free field conditions.

Before to deal the seismic behaviour of the embedded retaining walls, an extensive bibliographic study on the earth pressure theories, both in static and seismic conditions, on the typologies of retaining walls and on the static design methods of them was done. A brief review of the literature on these topics can be found in the Chapters 2, 3 and 4.

The Chapter 5 was entirely devoted to the application of the Performance-Based Design (PBD) philosophy to the embedded retaining walls. Three types of analysis, depending on the accuracy degree required by the structure to design, were presented. Simplified analyses can be simply conducted by adopting the limit equilibrium methods and modelling the seismic actions on the walls as pseudostatic forces. For cantilever RC diaphragms embedded in cohesionless materials, two charts for the preliminary design of the needed depth of embedment and for the prediction of the maximum bending moment were shown. The earthquake-induced displacements can be roughly estimated by means of empirical formulas proposed in the literature or, having defined an appropriate seismic input motion, recurring to Newmark type analyses. A more advanced design method can be performed by using a FE model of the problem in which the seismic performances of the retaining system, in terms of displacements or forces in structural elements, are described by capacity curves. The methodology can be included in the framework of the "pushover analyses" and was proposed for the first time in Visone & Santucci de Magistris (2007). Dynamic analyses represent the most accurate instrument to predict the seismic behaviour of the geotechnical systems but they require an adequate subsoil characterization and advanced knowledge in numerical modelling and earthquake engineering.

Finally, the performance based design presented here was applied to the seismic design of cantilever RC diaphragm walls embedded in dry loose and dense sandy layers. The geometry of the free walls centrifuge models and the LB sand properties were assumed. The analyses, performed following the different level of accuracy provided by the PBD, have the main scope to supply preliminary predictions on the seismic response of the centrifuge models. The results of the study were presented in the Chapter 6.

At the end, the reached objectives and the future developments of the research were summarized in the last Chapter 7.

2 GENERALITIES OF RETAINING WALLS.

Retaining walls can be defined as structures which retain ground, comprising soil, rock or backfill and water. The material is retained at a slope steeper than it would eventually adopt if no structure was present. Retaining structures include all types of walls and support systems in which structural elements have forces imposed by the retained material.

They are used throughout seismically active areas and frequently represent key elements of ports and harbors, transportation systems, lifelines, and other constructed facilities. Earthquakes have caused permanent deformation of retaining structures in many historical earthquakes. In some cases, these deformations were negligibly small; in others they caused significant damage. In some cases, retaining structures have collapsed during earthquakes, with disastrous physical and economic consequences.

In this chapter, the generalities of the retaining structures, with a particular attention to the embedded walls, are recalled.

2.1 TYPES OF RETAINING WALLS.

The problem of retaining soil is one of the oldest in geotechnical engineering; some of the earliest and most fundamental principles of soil mechanics were developed to allow rational design of retaining walls. Many different approaches to soil retention have been developed and used successfully. In recent years, the development of metallic, polymer and geotextile reinforcement leds to the development of many innovative types of mechanically stabilized earth retention systems.

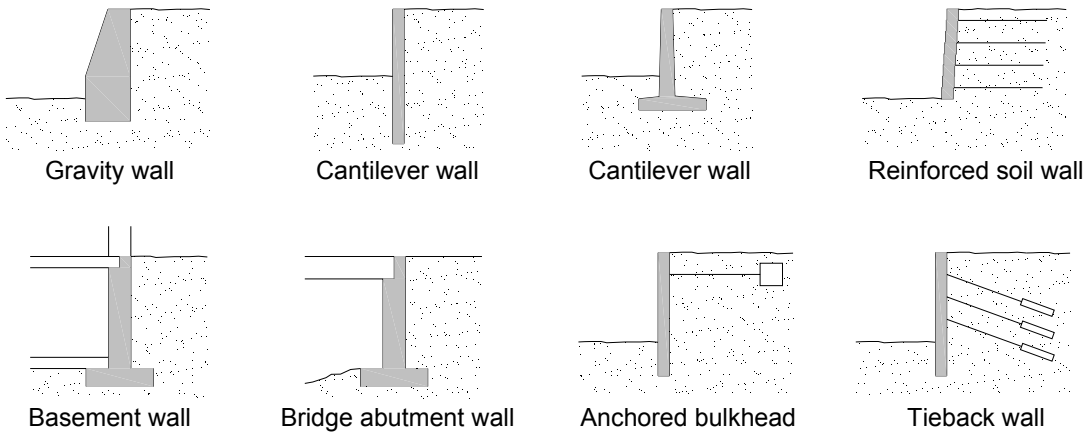

Figure 2-1. *Common types of earth retaining structures.*

Retaining walls are often classified in terms of their relative mass, flexibility and anchorage conditions (see Figure 2-1). Gravity walls are the oldest and simplest type of retaining wall. Gravity walls are thick and stiff enough so that they do not bend; their movement develops essentially as rigid-body translation and/or rotation. Certain types of composite wall system, such as crib walls and mechanically stabilized walls, are thick enough so that they bend very little and consequently are often designed as gravity walls (including appropriate consideration of internal stability). Cantilever walls, which bend as well as translate and rotate, rely on their flexural strength to resist to the lateral earth

pressures. The actual distribution of lateral earth pressure on a cantilever wall is influenced by the relative stiffness and deformation of both the wall and the soil. Braced walls are constrained against certain types of movement by the presence of external bracing elements. In the cases of basement walls and bridge abutment walls, lateral movements of the tops of the walls may be restrained by the structures they support. Tieback walls and anchored bulkheads are restrained against lateral movement by anchors embedded in the soil behind the walls. The provision of lateral support at different locations along a braced wall may keep bending moments so low that relatively flexible structural sections can be used.

2.2 TYPES OF RETAINING WALL FAILURES.

To design retaining walls, it is necessary to define failure and to know how walls can fail. Under static conditions, retaining walls are subjected to the body forces related to the mass of the wall, to the soil pressures and to the external forces such as those transmitted by braces. A properly designed retaining wall will achieve equilibrium of these forces without introducing shear stresses that approach the shear strength of the soil or the failure of the wall material. During an earthquake, however, inertial forces and changes in soil strength may violate equilibrium and cause permanent deformation of the wall. Failure, whether by sliding, tilting and bending, or some other mechanism, occurs when these permanent deformations become excessive. The question of what level of deformation is excessive depends on many factors and is best addressed on a site specific basis.

Gravity walls usually fail by rigid body mechanisms such as sliding and/or overturning or by gross instability. Sliding occurs when horizontal force equilibrium is not maintained (i.e., when the lateral pressures on the back of the wall produce a thrust that exceeds the available sliding resistance on the base of the wall). Overturning failures occur when moment equilibrium is not satisfied; bearing failures at the base of the wall are often involved. Gravity walls may also be damaged by gross instability of the soils behind and beneath them. Such failures may be treated as slope stability failures that encompass the wall. Composite wall systems, such as crib walls, bin walls and mechanically stabilized walls, can fail in the same ways or by a number of internal mechanisms that might involve shearing, pullout or tensile failure of various wall elements.

Cantilever walls are subject to the same failure mechanisms. Soil pressures and bending moments in cantilever walls depend on the geometry, stiffness and strength of the wall-soil system. If the bending moments required for equilibrium exceed the flexural strength of the wall, flexural failure may occur. The structural ductility of the wall itself may influence the level of deformation produced by flexural failure.

Braced walls usually fail by gross instability, tilting, flexural failure and/or failure of bracing elements. Tilting of braced walls typically involves rotation about the point at which the brace acts on the wall, often the top of the wall as in the cases of basement and bridge abutment walls. Anchored walls with inadequate penetration may tilting by kicking out at their toes. As in the case of cantilever walls, anchored walls may fail in flexure, although the point of failure (maximum bending moment) is likely to be different. Failure of bracing elements can include anchor pullout, tie-rod failure or bridge buckling.

Backfill settlements can also impose additional axial and transverse loading on bracing elements such as tierods and tiebacks.

2.3 ULTIMATE LIMIT STATES FOR RETAINING WALLS.

A limit state is a set of performance criteria (e.g. vibration levels, deflection, strength), or stability criteria (buckling, twisting, collapse) that must be met when the structure is subject to loads.
In accordance with the most recent construction codes, the design of a structure must satisfy the following requirements:

- safety towards the ultimate limit states: capability to avoid collapse, loss of equilibrium and heavy instability, total or partial, which might endanger the safety of the people or involve loss of goods or to cause heavy environmental and social damages or make the structure out of order;
- safety towards the serviceability limit states: capability to guarantee the expected performances for serviceability conditions;
- robustness towards the exceptional actions: capability to avoid damages out of proportion respect to the causes as fires, explosions, impacts.

For all types of retaining structures, the following limit states should be considered:

- loss of overall stability;
- failure of a structural element such as a wall, anchorage, wale or strut or failure of the connection between such elements;
- combined failure in ground and in structural element;
- failure by hydraulic heave and piping;
- movement of the retaining structure which may cause collapse or affect the appearance or efficient use of the structure or nearby structures or services which rely on it;
- unacceptable leakage through or beneath the wall;
- unacceptable transport of soil particles through or beneath the wall
- unacceptable change in groundwater regime.

In addition, the following limit states should be considered for gravity walls and for composite retaining structures:

- bearing resistance failure of the soil below the base;
- failure by sliding at the base;
- failure by toppling;

and for embedded walls:

- failure by rotation or translation of the wall or parts thereof;
- failure by lack of vertical equilibrium.

When they are relevant, combinations of the above mentioned limit states should be taken into account.
Examples of limit modes for the most commonly used retaining structures are plotted in the next figures (EN1997-1).

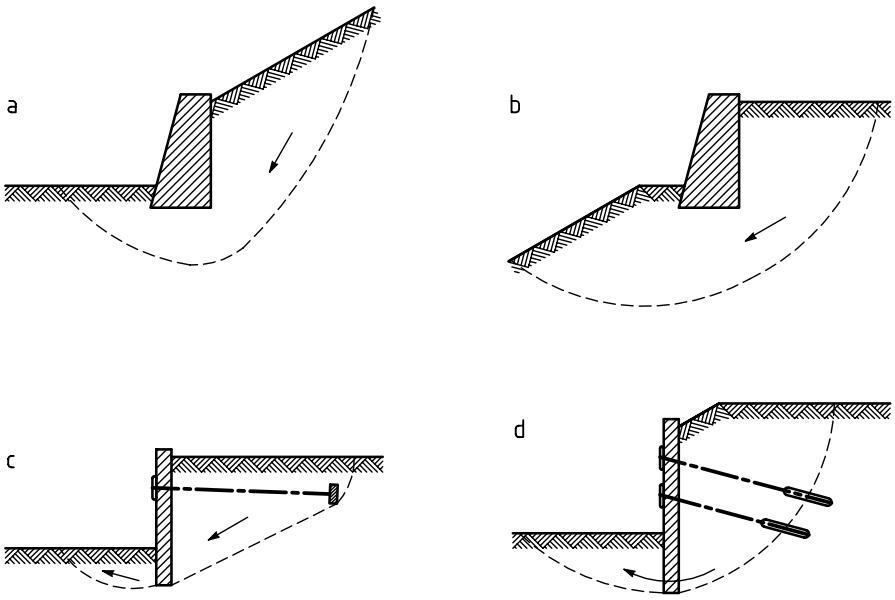

Figure 2-2. *Examples of limit modes for overall stability of retaining structures.*

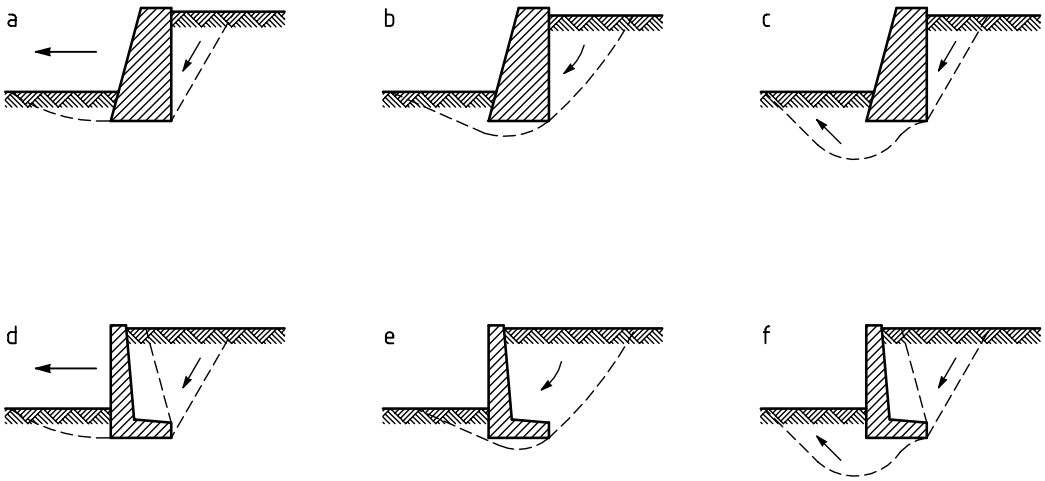

Figure 2-3. *Examples of limit modes for foundation failures of gravity walls.*

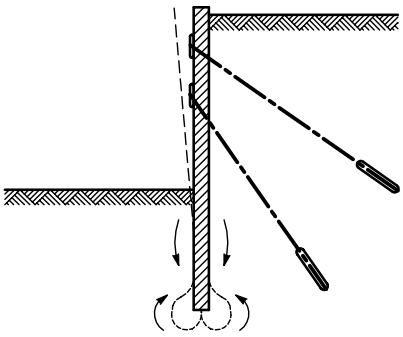

Figure 2-4. *Examples of limit modes for vertical failure of embedded walls.*

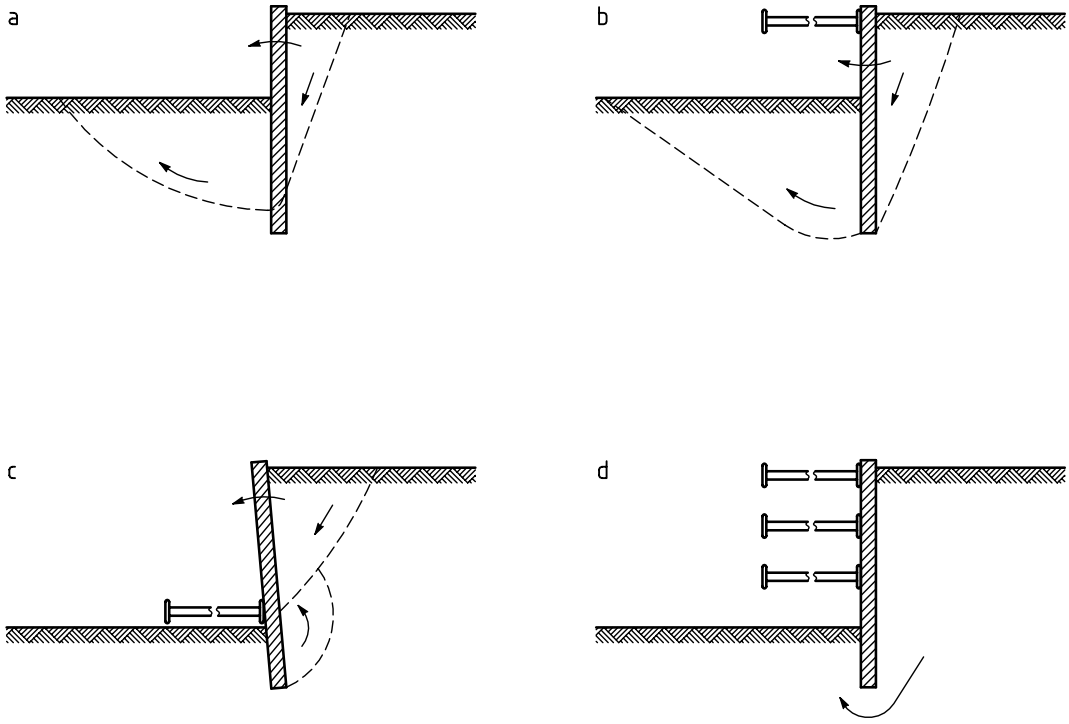

Figure 2-5. *Examples of limit modes for rotational failures of embedded walls.*

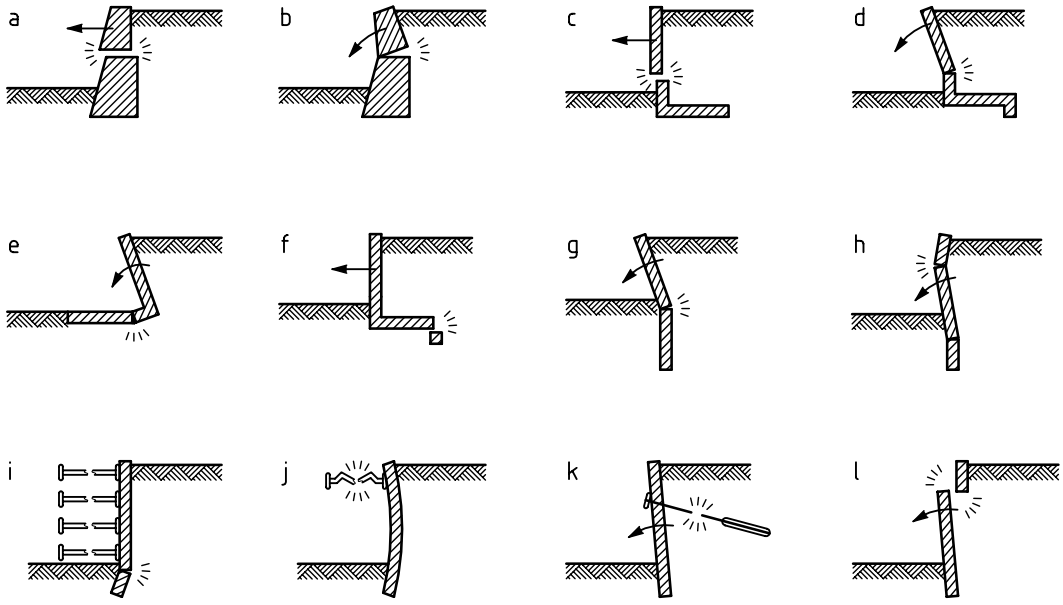

Figure 2-6. *Examples of limit modes for structural failure of retaining structures.*

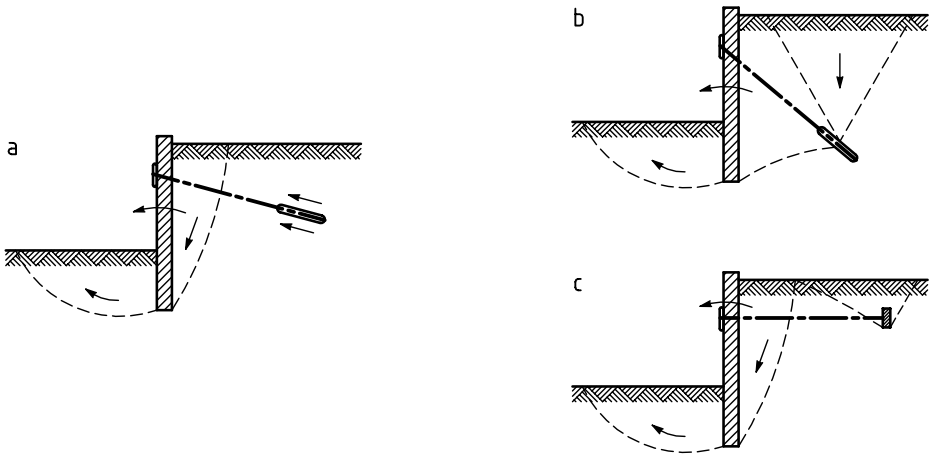

Figure 2-7. *Examples of limit modes for failure by pullout of anchors.*

2.4 EMBEDDED WALLS: TYPES AND USES.

The preliminary design of a retaining structure is complicated to the various available typologies and to the design constraints. The problem derive from the necessity to sustain a backfill or loads transmitted from adjacent constructions. The structure geometry, the limitations imposed from the nature of the soil and the ground water table conditions, the available construction methodologies and the local experiences play a fundamental role for the choice of the more appropriate type of retaining system.
Here, only the embedded retaining walls are considered. The main technologies employed for the realization of them are recalled.
The first classification of the embedded walls is done on the basis of their constraints scheme. Thus, the walls can be distinguished as:

- cantilever walls, used to sustain backfills lower than 5-6 m;
- embedded walls with a single constraint, for backfills till to 10 m;
- embedded walls with various constraint levels, to retain heights higher than 10 m.

The embedded walls can be realized with wood, steel and reinforced concrete piles driven into the ground (*sheet piles walls*, without removing the soil) or with the cast of RC piles or diaphragm into previously formed holes (*bulkheads*, with the removal of the soil). The execution modes influence the mechanical behaviour of the soil interacting with the wall.

2.4.1 Sheet pile walls.

The sheet piles walls are flexible earth retaining structures mainly used in the marine engineering and for provisional constructions. They can be employed in unfavourable soils conditions (for example, in soft clays) because they do not require foundations. The poor mechanical soil properties permit to drive the piles directly from the ground surface. The constructive technique is suitable for the presence of water, where other types of retaining systems can not be utilized. As mentioned before, the piles can be constituted by:

- wood, typically used for provisional structures with low heights of excavation. For definitive retaining systems, protection treatments of the wood are needed

- steel, the most adopted material in the excavations of marine engineering for its advantages in the variety of transversal sections and the consequent large range of flexural strength, the economy, the stability during the driving, the possibility to combine various profiles to increase the flexural stiffness, the retrieval and the reuse of the piles for provisional constructions, the lightness, the possibility to lengthen the elements by welding or bolting. Some typical transversal sections are plotted in Figure 2-8;
- reinforced concrete, used for permanent structures with a large variety of transversal sections. The most common type is a plate with male-female joints. Sometimes concrete injections are utilized to waterproof the wall. In order to reduce the cracking in the tensile zones and the corrosion of steel reinforcements, the prestressed reinforced concrete is considered. Usually the high weight of every element and the large volume of displaced soil during the installation make these type of element less competitive than the steel piles.

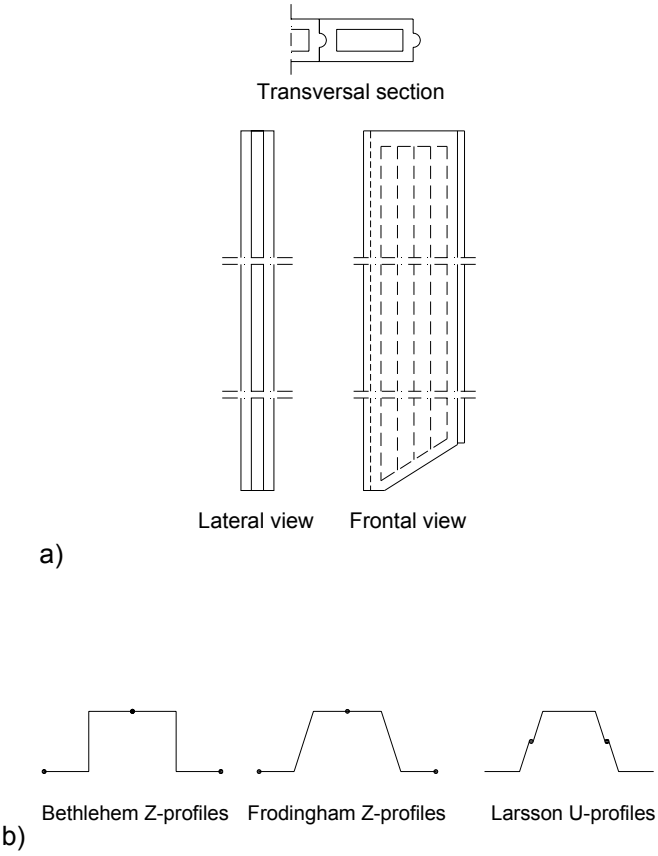

Figure 2-8. *Elements for sheet piles walls: a) reinforced concrete; b) steel.*

2.4.1.1 Cantilever sheet piles walls.

The stability of this type of structures is due to an adequate depth of embedment into the soil under the excavation surface. To contrast the backfill thrust, the wall behaves as a cantilever beam fixed into the soil. The erosion in front of the wall may represent a problem, since the stability depends mainly to the passive resistance of the soil that develops in this zone. The cantilever sheet walls are economic for low retained heights due to the maximum bending moment, and then the required flexural strength,

increases with the cube of the excavation height. The lateral displacements due to the structural deflection are significant. Free sheet walls are more suitable for provisional constructions.

2.4.1.2 Anchored sheet piles walls.

The anchored sheet walls entrust their stability to the embedded portion and the anchors placed near to the top of the wall. Marine engineering is the more widespread field of application of the anchored sheet walls but, in the last years, they have found other employments (bridge abutment, basement walls, etc.). This type of structure may be used for heights of excavation till to 20m, in relation to the soil conditions. The anchors acts reducing the lateral displacements, the bending moments and the embedded depth requires for the equilibrium respect to the correspondent cantilever sheet walls. To contain the lateral movements of higher heights of excavation, more than one anchors levels can be adopted.

There are two methods to install the wall and the backfill. In the first, the excavation precedes the driving of the piles and the backfill is completely replaced. In the second, the elements is driven into the ground before than the excavation is done and, then, the backfill is constituted from in-situ soil and reported soil. The two methods give different earth pressure conditions on the wall.

Generally, it is assumed that the backfill is realized before than the wall and the displacements of the anchors are sufficient to mobilize active earth pressure behind the wall over the excavation level. British Standards (BS6349) suggest that, when the backfill is formed after the wall installation, the design should be conducted assuming intermediate values of earth pressures comprised to the active and at rest pressures.

2.4.1.3 Types of anchors for sheet piles walls.

Most of the problems encountered in the practical experiences of excavation sustained by anchored sheet piles walls are due to design or construction errors of the anchors. The main types of anchors are reported in Figure 2-9.

A single anchor is constituted by a steel bar connected to a contrast element, anchor foundation, that can be realized with a concrete block or a beam. Rather than the block, the foundation may be carried out with piles or with reinforced concrete plates. The anchors foundation should be placed at a sufficient distance from the wall, in order to avoid the superposition of passive zone of the foundation and the active zone behind the wall.

The anchor with the stand piles is recommended to Tschebotarioff (1973) for sheet walls in soft soils that may not be removed with dredging. The anchors with stand piles can be employed when the capacity of other anchors can not guarantee adequate safety conditions. The anchor with tensile micropiles (raking anchor) is often constituted by a steel pile with H-shape section inclined to 45° and linked to horizontal steel beams.

The injected bulb anchor consists of a element subject to tension that connects the walls to a fixed part obtained with concrete injections in stiff soils or rocks. This type of anchor requires favourable soil conditions near to the wall that can not verify in alluvial deposits.

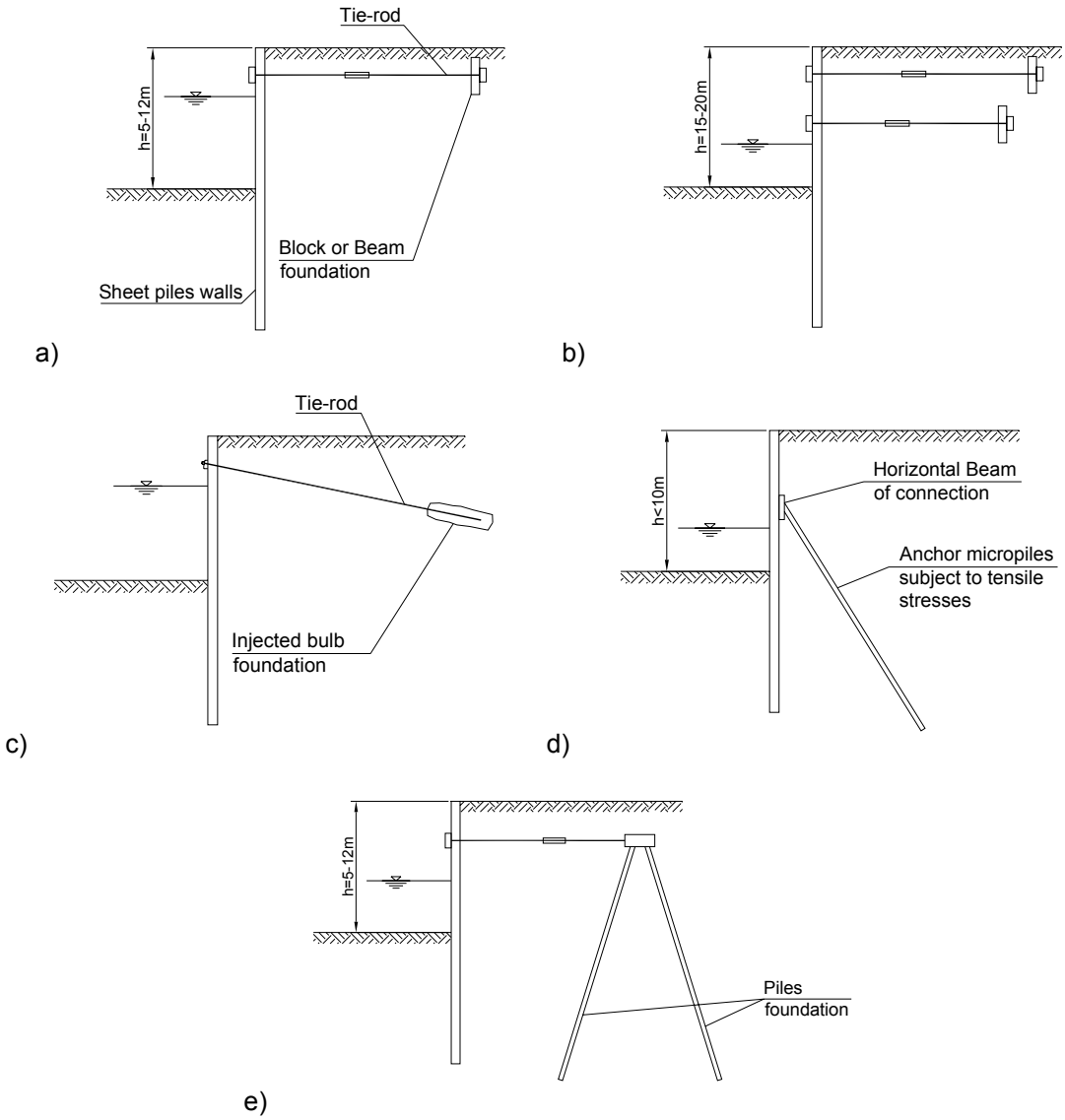

Figure 2-9. *Examples of anchored sheet walls: a) quay wall with a single level of anchors; b) sheet walls with multiple anchors levels; c) injected bulb anchor; d) raking anchor; e) anchor with stand piles.*

2.4.2 Bulkheads.

The diaphragm and drilled piles bulkheads are mainly used as retaining structures and structural elements for deeper basement walls of buildings, road subways, underground railway stations, shallow tunnels, underground parking, subterranean industrial plants, quay walls, wharfs and port structures.

The main aspects that have contributed to the diffusion of this type of structures are:

- the commercial availability of bentonite-mud;
- the experiences collected in urban areas, that suggest their use in complex soil conditions too;
- the solution of some practical problems as the improvement of the excavation techniques and the development of yard plants for the making of the concrete.

The adoption of the diaphragm and drilled piles bulkheads is very convenient when the wall has provisional and definitive character.

The cost of the structure is affected from the depth of embedment required to the stability and hydraulic conditions above the dredge level, the presence of rock blocks and other constructions, the necessity of anchors, props and struts, and from some yard factors as the availability of the services, the time and the space constraints.
The constructive sequence of a continuous concrete diaphragm using modern techniques and equipments is plotted in Figure 2-10.

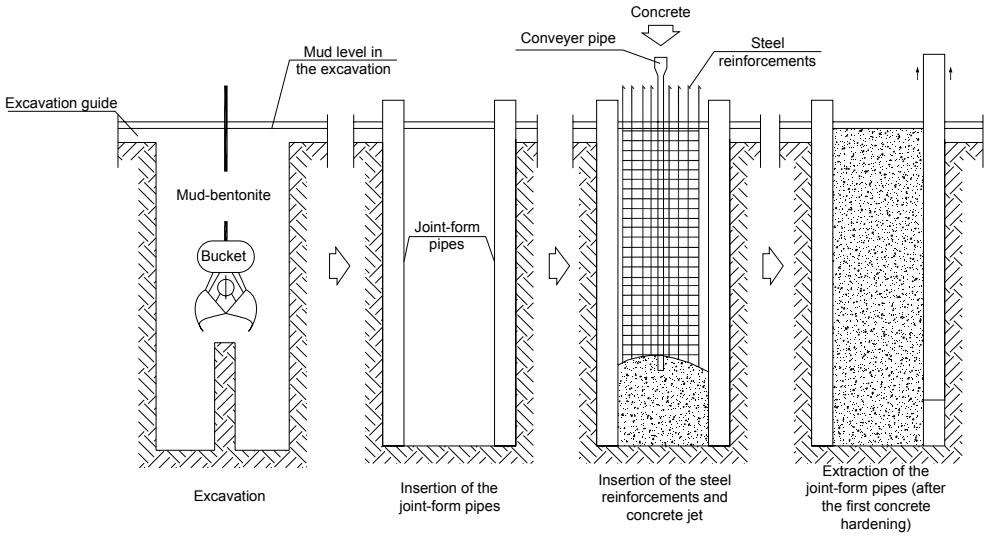

a) Constructive sequence of the primary series panels

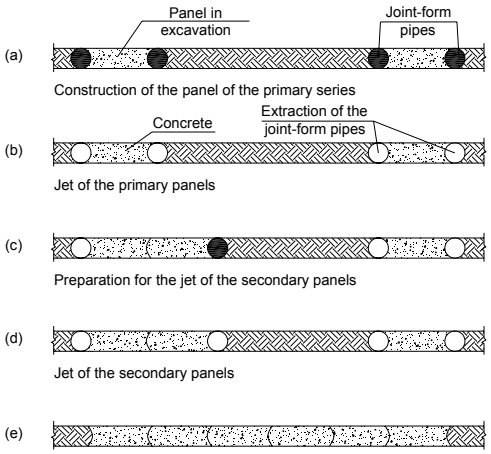

b) Constructive sequence of the primary, secondary and closure panels.

Figure 2-10. *Realization of a reinforced concrete diaphragm (Leiper, 1984).*

At the end of the excavation and before the concrete jet, the extremity of each panel is defined from a steel joint-form pipe or from the previously realized panel. The excavation is carried out by using a bucket and sustained by bentonite-mud. After the positioning of the joint-form pipe and the steel

reinforcements into the trench, the concrete jet is performed by using a conveyer pipe from the bottom of the hole. The joint-form pipes allows having a good level of joint between the panels.
The diaphragms can be realized with prefabricated reinforced concrete panels. Their main disadvantage is the high weight of each panel.
The reinforced concrete sheet piles may be adopted in every type of subsoil condition. The piles can be placed side by side, tangent and secant, in relation to the distance between the piles (larger, equal or lower than the pile diameter, respectively), according to the required support and the waterproofing of the excavation. The top of the piles is often connected by a reinforced concrete beam to distribute the loads.

2.4.3 Walls with many anchor levels and props.

Relatively flexible retaining walls might be designed by adopting anchor levels or multiple props at small distances. This kind of construction is adopted:

- for provisional excavations;
- to retain relatively resistant soil (fractured rock) for very deep excavation;
- to guarantee a partial sustaining to the jet grouted excavations
- to minimize the losses of soil in critical areas near to deeper excavations.

The anchors can be used for every type of the face covering. In some cases, they are placed to a small relative distance to form retaining structure in reinforced soils.

3 EARTH PRESSURE THEORY.

The seismic behaviour of retaining walls depends on the total lateral earth pressures that develop during earthquake shaking. These total pressures include both the static gravitational pressures that exist before an earthquake occurs, and transient dynamic pressures induced by the earthquake. Since the response of a wall is influenced by both, a review of static and dynamic earth pressures is presented.

In the literature different notation was used for the definition of the problem geometry and the strength parameters of the backfill. In order to avoid confusion on the symbols, in this chapter are signed:

γ – unit weight of the soil

ϕ - friction angle of the soil

c – cohesion of the soil

Ψ – dilation angle of the soil

ε – inclination angle of the backfill respect to horizontal

β - inclination angle of the wall internal face respect to vertical

δ – soil-wall friction angle

Ψ_W – dilative component of the soil-wall friction angle

α – angle of the planar failure surface respect to horizontal

θ – inclination angle of the seismic coefficient k with the vertical.

Figure 1-1 illustrates the assumed symbology. The subscript E indicates the seismic conditions, both for active and passive earth pressure states. In the following, the static loading system is denoted without the subscript.

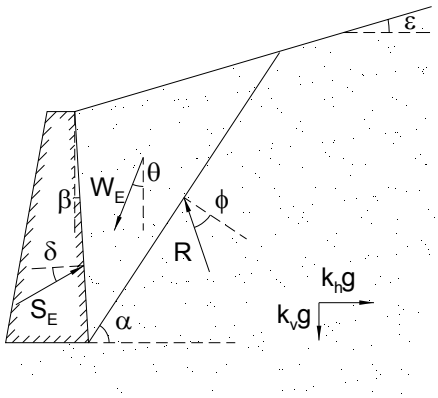

Figure 3-1. *Utilized symbols for the geometry of the problem.*

3.1 STATIC PRESSURES ON RETAINING WALLS.

Static earth pressures on retaining structures are strongly influenced by wall and soil movements. *Active earth pressures* develop as a retaining wall moves away from the soil behind it, including extensional lateral strain in the soil. When the wall movement is sufficient to mobilize the strength of the soil behind the wall, minimum active earth pressures act on the wall. Because very little wall movement is required to develop minimum active earth pressures (for the usual case of cohesionless

backfill materials), free-standing retaining walls are usually designed on the basis of minimum active earth pressures. Where lateral wall movements are restrained, such as in the cases of tieback walls, anchored bulkheads, basement walls, and bridge abutments, static earth pressures may be greater than minimum active. *Passive earth pressures* develop as a retaining wall moves toward the soil, thereby producing compressive lateral strain in the soil. When the strength of the soil is fully mobilized, maximum passive earth pressures act on the wall. The stability of many free-standing retaining walls depends on the balance between active pressures acting predominantly on one side of the wall and passive pressures acting on the other.

Even under static conditions, prediction of actual retaining walls forces and deformations is a complicated soil-structure interaction problem. Deformations are rarely considered explicitly in design – the typical approach is to estimate the forces acting on a wall and then to design the wall to resist those forces with a factor of safety high enough to produce acceptably small deformations. A number of simplified approaches are available to evaluate static loads on retaining walls. The most commonly used are described in the following sections.

3.1.1 Rankine theory.

Rankine (1857) developed the simplest procedure for computing minimum active and maximum passive earth pressures. By making assumptions about the stress conditions and strength envelope of the soil behind a retaining wall (the backfill soil), Rankine was able to render the lateral earth pressure problem determinate and directly compute the static pressures acting on retaining walls.

For minimum active conditions, Rankine expressed the pressure at a point on the back of a retaining wall as:

$$p_A = K_A \cdot \sigma'_V - 2c\sqrt{K_A} \qquad (3\text{-}1)$$

where K_A is the coefficient of minimum active earth pressure, σ'_V is the vertical effective stress at the point of interest, and c is the cohesive strength of the soil. When the principal stress planes are vertical and horizontal (as in the case of a smooth vertical wall retaining a horizontal backfill), the coefficient of minimum active earth pressure is given by:

$$K_A = \frac{1-\sin\phi}{1+\sin\phi} = \tan^2\left(45 - \frac{\phi}{2}\right) \qquad (3\text{-}2)$$

For the case of a cohesionless backfill inclined at an angle ε with the horizontal, infinite slope solutions can be used (Terzaghi, 1943; Taylor, 1948) to compute K_A as:

$$K_A = \cos\varepsilon \frac{\cos\varepsilon - \sqrt{\cos^2\varepsilon - \cos^2\phi}}{\cos\varepsilon + \sqrt{\cos^2\varepsilon - \cos^2\phi}} \qquad (3\text{-}3)$$

for $\varepsilon \le \phi$. The pressure distribution on the back of the wall, as indicated by equation (3-1), depends on the relative magnitudes of the frictional and cohesive components of the backfill soil strength. Although the presence of the cohesion indicates that tensile stresses will develop between the upper portion of the wall and the backfill, tensile stresses do not actually develop in the field. The creep, stress relaxation, and low permeability characteristics of cohesive soils render them undesirable as backfill

material for retaining structures, and their use for this purpose is generally avoided whenever possible. For dry homogeneous cohesionless backfill, Rankine theory predicts a triangular active pressure distribution oriented parallel to the backfill surface. The active earth pressure resultant, or *active thrust* S_A, acts at a point located H/3 above the base of a wall of height H, with magnitude:

$$S_A = \frac{1}{2} K_A \gamma H^2 \qquad (3\text{-}4)$$

Under maximum passive conditions, Rankine theory predicts wall pressures given by:

$$p_P = K_P \cdot \sigma'_V + 2c\sqrt{K_P} \qquad (3\text{-}5)$$

where K_P is the coefficient of maximum passive earth pressure. For smooth, vertical walls retaining horizontal backfills:

$$K_P = \frac{1+\sin\phi}{1-\sin\phi} = \tan^2\left(45 + \frac{\phi}{2}\right) \qquad (3\text{-}6)$$

and:

$$K_P = \cos\varepsilon \frac{\cos\varepsilon + \sqrt{\cos^2\varepsilon - \cos^2\phi}}{\cos\varepsilon - \sqrt{\cos^2\varepsilon - \cos^2\phi}} \qquad (3\text{-}7)$$

for backfills inclined at ε to the horizontal. For a dry homogeneous backfill, Rankine theory predicts a triangular passive pressure distribution oriented parallel to the backfill surface.
The passive earth pressure resultant, or passive thrust S_P, acts at a point located H/3 above the base of a wall of height H, with magnitude:

$$S_P = \frac{1}{2} K_P \gamma H^2 \qquad (3\text{-}8)$$

In Figure 3-2 are plotted the graphical representations of the equations (3-2) and (3-6).

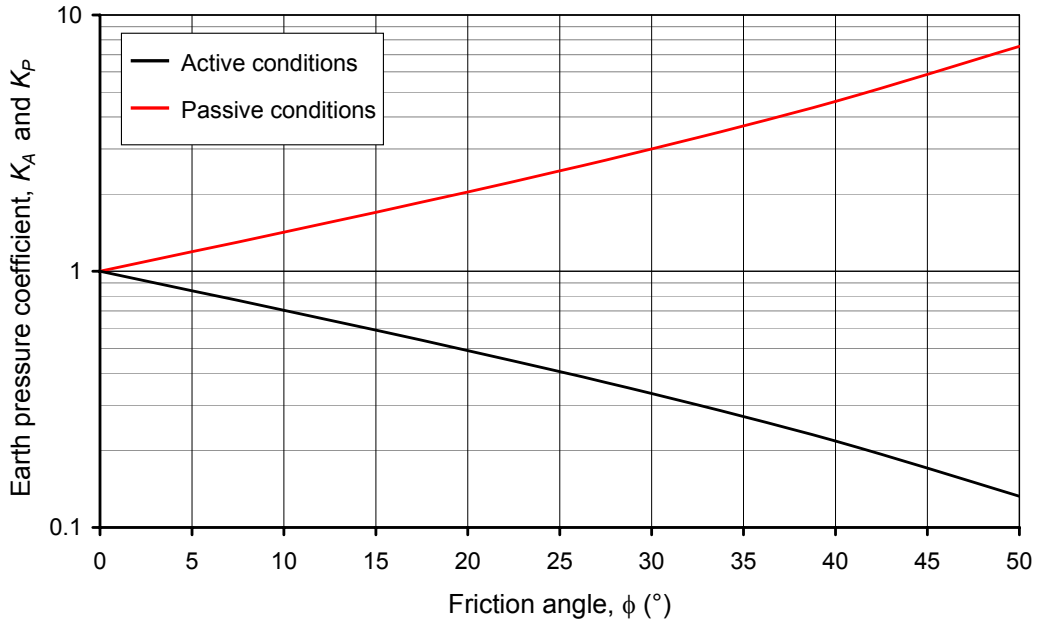

Figure 3-2. *Rankine active and passive earth pressure coefficients for a horizontal backfill.*

The presence of water in the backfill behind a retaining wall influences the effective stresses and hence the lateral earth pressure that acts on the wall. For wall design the hydrostatic pressure due to the water must be added to the lateral earth pressure. Because the total lateral thrust on a wall retaining a saturated backfill is considerably greater than that on a wall retaining dry backfill, the provision of backfill drainage is an important part of retaining wall design.

3.1.2 Coulomb theory.

Coulomb (1776) was the first to study the problem of lateral earth pressures on retaining structures. By assuming that the force acting on the back of a retaining wall resulted from the weight of a wedge of soil above a planar failure surface, Coulomb used force equilibrium to determine the magnitude of the soil thrust acting on the wall for both minimum active and maximum passive conditions. Since the problem is indeterminate, a number of potential failure surfaces must be analyzed to identify the critical failure surface (i.e., the surface that produces the greatest active thrust or the smallest passive thrust).

Under minimum active earth pressure conditions, the active thrust on a wall with the geometry shown in Figure 1-1 is obtained from the force equilibrium. For the critical failure surface, the active thrust on a wall retaining a cohesionless soil can be expressed as:

$$S_A = \frac{1}{2} K_A \gamma H^2 \qquad (3\text{-}9)$$

where

$$K_A = \frac{\cos^2(\phi - \beta)}{\cos^2\beta\cos(\delta + \beta)\left[1 + \sqrt{\frac{\sin(\delta + \phi)\sin(\phi - \varepsilon)}{\cos(\delta + \beta)\cos(\varepsilon - \beta)}}\right]^2} \qquad (3\text{-}10)$$

δ is the angle of interface friction between the wall and the soil, while ε and β are shown in Figure 1-1. The critical failure surface is inclined at an angle:

$$\alpha_A = \phi + \arctan\left[\frac{\tan(\phi - \varepsilon) + C_1}{C_2}\right] \qquad (3\text{-}11)$$

to the horizontal where

$$C_1 = \sqrt{\tan(\phi - \varepsilon)\left[\tan(\phi - \varepsilon) + \cot(\phi - \beta)\right]\left[1 + \tan(\delta + \beta)\cot(\phi - \beta)\right]}$$
$$C_2 = 1 + \left\{\tan(\delta + \beta)\left[\tan(\phi - \varepsilon) + \cot(\phi - \beta)\right]\right\}$$

Coulomb theory does not explicitly predict the distribution of active pressure, but it can be shown to be triangular for linear backfill surfaces with no surface loads. In such cases, S_A acts at a point located H/3 above the base of a wall of height H.

For maximum passive conditions in cohesionless backfills, Coulomb theory predicts a passive thrust:

$$S_P = \frac{1}{2} K_P \gamma H^2 \qquad (3\text{-}12)$$

where:

$$K_P = \frac{\cos^2(\phi+\beta)}{\cos^2\beta\cos(\delta-\beta)\left[1+\sqrt{\frac{\sin(\delta+\phi)\sin(\phi-\varepsilon)}{\cos(\delta-\beta)\cos(\varepsilon-\beta)}}\right]^2} \qquad (3\text{-}13)$$

The critical failure surface for maximum passive earth pressure conditions is inclined to the horizontal at :

$$\alpha_P = -\phi + \arctan\left[\frac{\tan(\phi+\varepsilon)+C_3}{C_4}\right] \qquad (3\text{-}14)$$

where:

$$C_3 = \sqrt{\tan(\phi+\varepsilon)\left[\tan(\phi+\varepsilon)+\cot(\phi+\beta)\right]\left[1+\tan(\delta-\beta)\cot(\phi+\beta)\right]}$$
$$C_4 = 1+\left\{\tan(\delta-\beta)\left[\tan(\phi+\varepsilon)+\cot(\phi+\beta)\right]\right\}$$

It should be noted that the Coulomb theory gives the entire earth pressure coefficient. If the normal component to the wall is the objective of the analysis, the calculated values of the coefficients should be multiplied for cosδ.

In Figure 3-3. ***Coulomb active and passive earth pressure coefficients for a horizontal backfill sustained by a vertical wall.***Figure 3-3 are plotted the values of the earth pressures coefficients calculated with the Coulomb theory for a vertical wall (β=0) that retains a horizontal backfill (ε=0) for different soil-wall friction angles δ. For δ=0, the results are the same given by the Rankine theory.

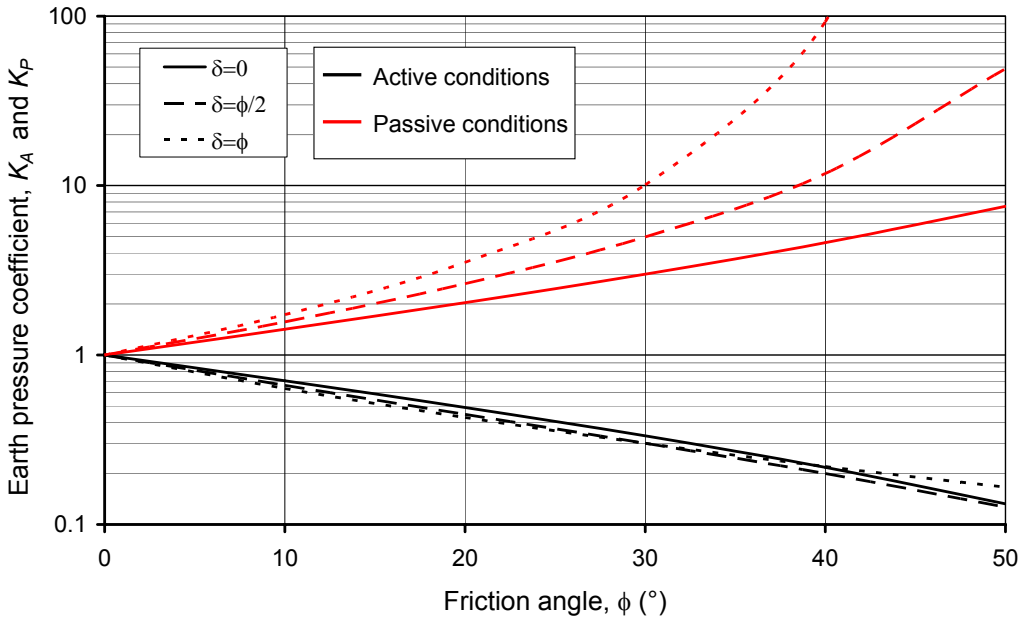

Figure 3-3. *Coulomb active and passive earth pressure coefficients for a horizontal backfill sustained by a vertical wall.*

The variations of the planar failure surface with δ in active and passive conditions are shown in Figure 3-4.

In contrast to the Rankine approach, Coulomb theory can be used to predict soil thrust on walls with irregular backfill slopes, concentrated loads on the backfill surface, and seepage forces. By

considering the soil above a potential failure plane as a free body and including forces due to concentrated loads, boundary water pressures, and so on, the magnitude of the resultant thrust (S_A or S_P) can easily computed.

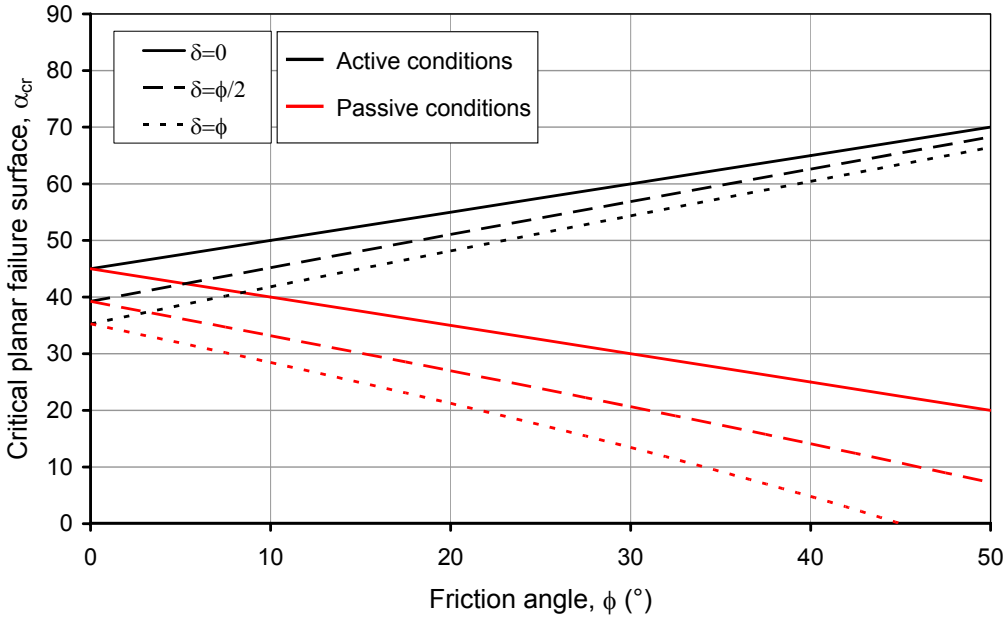

Figure 3-4. *Critical planar failure surface for a horizontal backfill sustained by a vertical wall.*

3.1.3 Logarithmic spiral method.

Although the major principal stress axis may be nearly perpendicular to the backfill surface at some distance behind a rough wall (δ>0), the presence of shear stresses on the wall-soil interface can shift its position near the back of the wall. If the inclination of the principal stress axes varies within the backfill, the inclination of the failure surface must also vary. In other words, the failure surface must be curved. A logarithmic spiral function has been used to describe such curved failure surfaces for active and passive earth pressure conditions.

For active earth pressure conditions, the critical failure surface consists of a curved portion near the back of the wall and a linear portion that extends up to the ground surface (Figure 3-5a). The active earth pressure distribution is triangular for walls retaining planar, cohesionless backfills. Thus the active soil thrust can be expressed in the same form as equation (3-4), where the log spiral coefficients of minimum active earth pressure for various wall and backfill inclinations are given in Table 3-1 (Caquot & Kerisel, 1948). The active earth pressure coefficients given by the log spiral approach are generally considered to be slightly more accurate than those given by Rankine or Coulomb theory, but the difference is so small that the more convenient Coulomb approach is usually used.

The effect of wall friction on the shape of the critical failure surface is more noticeable for passive earth pressure conditions. The passive failure surface also has curved and linear portions, but the curved portion is much more pronounced than for active conditions (Figure 3-5b). For planar cohesionless backfills, the passive earth pressure distribution is triangular, so the passive thrust can be expressed in the form of equation (3-8), where the log spiral coefficients of maximum passive earth pressure for various wall and backfill inclinations are given in Table 3-2Table 3-1 (Caquot &

Kerisel, 1948). The passive earth pressure coefficients given by the log spiral method are considerably more accurate than those given by Rankine or Coulomb theory; the Rankine and Coulomb coefficients tend to underpredict and overpredict the maximum passive earth pressure, respectively. Rankine theory greatly underpredicts actual passive earth pressures and is rarely used for that purpose. Coulomb theory overpredicts passive pressures (an unconservative error) by about 11% for $\delta=\phi/2$ and 100% for $\delta=\phi$. For that reason, Coulomb theory is rarely used to evaluate passive earth pressures when $\delta>\phi/2$.

Figure 3-6 shows the earth pressure coefficients evaluated with the logarithmic spiral method for a horizontal backfill sustained by a vertical wall.

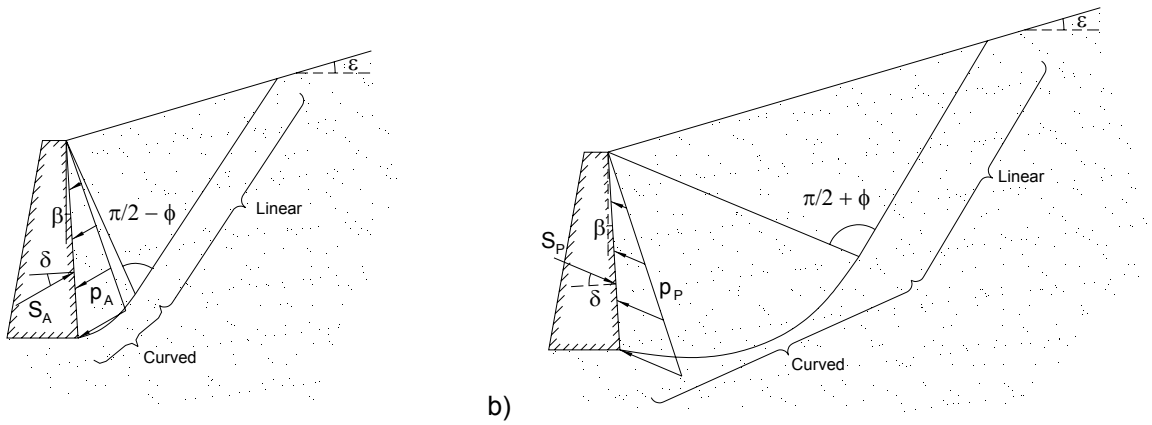

Figure 3-5. *Logarithmic spiral representation of the critical failure surface for: a) minimum active pressure conditions; b) maximum passive pressure conditions.*

ε	β	ϕ	20°		25°		30°		35°		40°		45°	
		δ	0°	20°	0°	25°	0°	30°	0°	35°	0°	40°	0°	45°
-15°	-10°	K_A	0.37	0.31	0.30	0.26	0.24	0.21	0.19	0.17	0.14	0.14	0.11	0.11
	0°		0.42	0.37	0.35	0.31	0.29	0.26	0.24	0.23	0.19	0.19	0.16	0.17
	10°		0.45	0.41	0.39	0.36	0.34	0.31	0.29	0.27	0.24	0.25	0.21	0.23
0°	-10°		0.42	0.37	0.34	0.30	0.27	0.24	0.21	0.19	0.16	0.15	0.12	0.12
	0°		0.49	0.44	0.41	0.37	0.33	0.30	0.27	0.26	0.22	0.22	0.17	0.19
	10°		0.55	0.50	0.47	0.43	0.40	0.38	0.34	0.33	0.28	0.30	0.24	0.26
15°	-10°		0.55	0.50	0.41	0.37	0.32	0.29	0.23	0.22	0.17	0.17	0.13	0.14
	0°		0.65	0.61	0.51	0.48	0.41	0.37	0.32	0.32	0.25	0.25	0.20	0.21
	10°		0.75	0.72	0.60	0.58	0.49	0.46	0.41	0.42	0.34	0.35	0.28	0.31

Table 3-1. *Values of the active earth pressure coefficient for log-spiral failure surface (after Caquot & Kerisel, 1948).*

ε	β	ϕ	20°		25°		30°		35°		40°		45°	
		δ	0°	20°	0°	25°	0°	30°	0°	35°	0°	40°	0°	45°
-15°	-10°	K_A	1.32	1.95	1.66	2.90	2.05	4.39	2.52	6.97	3.09	11.8	3.95	22.7
	0°		1.09	1.62	1.33	2.31	1.56	3.35	1.82	5.04	2.09	7.99	2.48	14.3
	10°		0.87	1.29	1.03	1.79	1.17	2.50	1.30	3.58	1.33	5.09	1.54	8.86
0°	-10°		2.33	3.45	2.96	5.17	3.82	8.17	5.00	13.8	6.68	25.5	9.20	52.9
	0°		2.04	3.01	2.46	4.29	3.00	6.42	3.69	10.2	4.59	17.5	5.83	33.5
	10°		1.74	2.57	1.89	3.50	2.33	4.98	2.70	7.47	3.14	12.0	3.69	21.2
15°	-10°		3.36	4.95	4.56	7.95	6.30	13.5	8.98	24.8	12.2	50.4	20.0	115
	0°		2.99	4.42	3.86	6.72	5.04	10.8	6.72	18.6	10.4	39.6	12.8	73.6
	10°		2.63	3.88	3.23	5.62	3.97	8.51	4.98	13.8	6.37	24.3	8.20	46.9

Table 3-2. *Values of the passive earth pressure coefficient for log-spiral failure surface (after Caquot & Kerisel, 1948).*

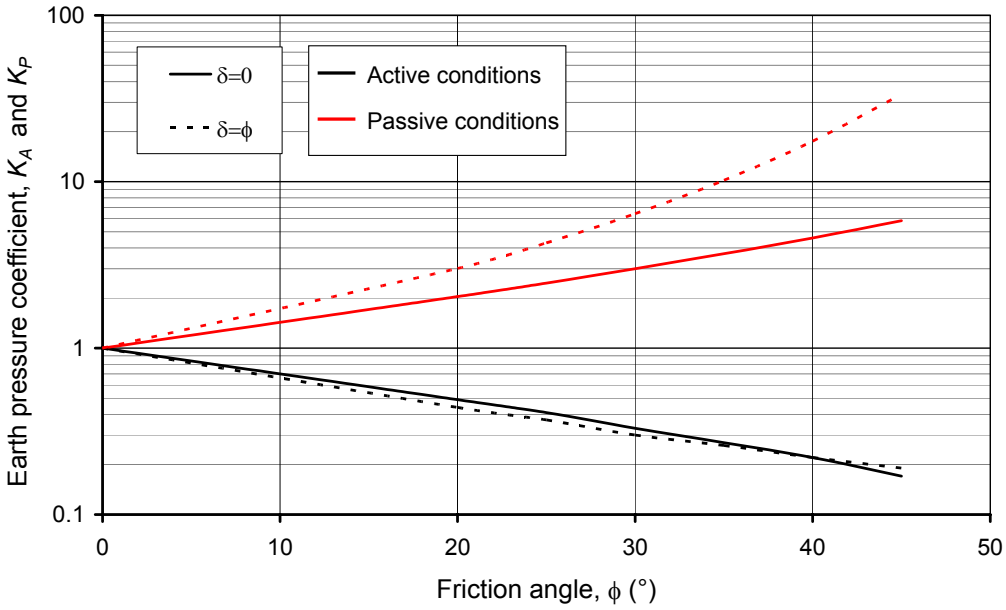

Figure 3-6. *Active and passive earth pressure coefficients for a horizontal backfill sustained by a vertical wall (after Caquot & Kerisel, 1948).*

3.1.4 Slip line method.

Sokolovskii (1965) introduced a theory termed the "Slip-Line Field Theory". In this analysis, it is assumed that failure occurs at constant volumes of soil along slip lines that meet the Mohr-Coulomb failure criterion. This method has the advantage of providing a statistically admissible stress state that satisfy the following equations of the plane equilibrium involving the normal, σ, and shear, τ, stresses and using a system of rectangular coordinates x, y with x-axis oriented in the vertical direction:

$$\begin{aligned} \frac{\partial \sigma_x}{\partial x} + \frac{\partial \tau_{yx}}{\partial y} &= \gamma \\ \frac{\partial \tau_{xy}}{\partial x} + \frac{\partial \sigma_y}{\partial y} &= 0 \end{aligned} \qquad (3\text{-}15)$$

The Mohr-Coulomb criteria states that at yield the following formula must apply everywhere in the soil mass:

$$\left(\sigma_x - \sigma_y\right)^2 + 4\tau_{xy}^2 = \left(\sigma_x + \sigma_y\right)^2 \sin^2 \phi \qquad (3\text{-}16)$$

The solution of these equations is called Kotter's equation and gives the orientation of the slip lines together with the stresses on the failure surface.

Sokolovoskii accomplished the solution for the active and the passive lateral earth pressure through the use of the finite difference method for a horizontal backfill. The results are resumed in the Table 3-3 and Table 3-4, while, in Figure 3-7 are plotted the values related to a vertical wall.

It is useful to remember that the K_A and K_P values are the entire earth pressure coefficients. To have the normal components to the wall, the values should be multiplied for cosδ.

β	ϕ	10°			20°			30°			40°		
	δ	0°	5°	10°	0°	10°	20°	0°	15°	30°	0°	20°	40°
-30°		0.72	0.68	0.68	0.60	0.57	0.57	0.50	0.47	0.50	0.42	0.40	0.46
-20°		0.73	0.70	0.70	0.58	0.54	0.54	0.46	0.43	0.45	0.35	0.34	0.38
-10°		0.72	0.70	0.68	0.54	0.50	0.50	0.40	0.37	0.38	0.29	0.27	0.29
0°	K_A	0.70	0.67	0.65	0.49	0.45	0.44	0.33	0.30	0.31	0.22	0.20	0.22
10°		0.65	0.61	0.59	0.42	0.38	0.37	0.26	0.24	0.24	0.16	0.14	0.15
20°		0.58	0.54	0.52	0.35	0.31	0.30	0.20	0.18	0.17	0.11	0.09	0.10
30°		0.49	0.45	0.44	0.27	0.24	0.23	0.13	0.12	0.11	0.06	0.05	0.05

Table 3-3. *Values of the active earth pressure coefficient calculated by Sokolovskii (1965) with the slip line method.*

β	ϕ	10°			20°			30°			40°		
	δ	0°	5°	10°	0°	10°	20°	0°	15°	30°	0°	20°	40°
-30°		1.04	1.11	1.16	1.26	1.49	1.73	1.49	2.08	2.80	1.86	3.17	5.42
-20°		1.18	1.29	1.35	1.51	1.83	2.13	1.90	2.79	3.80	2.50	4.70	8.23
-10°		1.31	1.43	1.52	1.77	2.19	2.57	2.39	3.62	5.03	3.37	6.77	12.3
0°	K_P	1.42	1.56	1.66	2.04	2.55	3.04	3.00	4.62	6.55	4.60	9.69	18.2
10°		1.49	1.65	1.76	2.30	2.93	3.53	3.65	5.82	8.42	6.16	13.9	26.6
20°		1.53	1.70	1.83	2.53	3.31	4.03	4.42	7.38	10.7	8.34	19.5	39.0
30°		1.52	1.71	1.85	2.76	3.67	4.51	5.28	9.07	13.5	11.3	28.4	56.7

Table 3-4. *Values of the passive earth pressure coefficient calculated by Sokolovskii (1965) with the slip line method.*

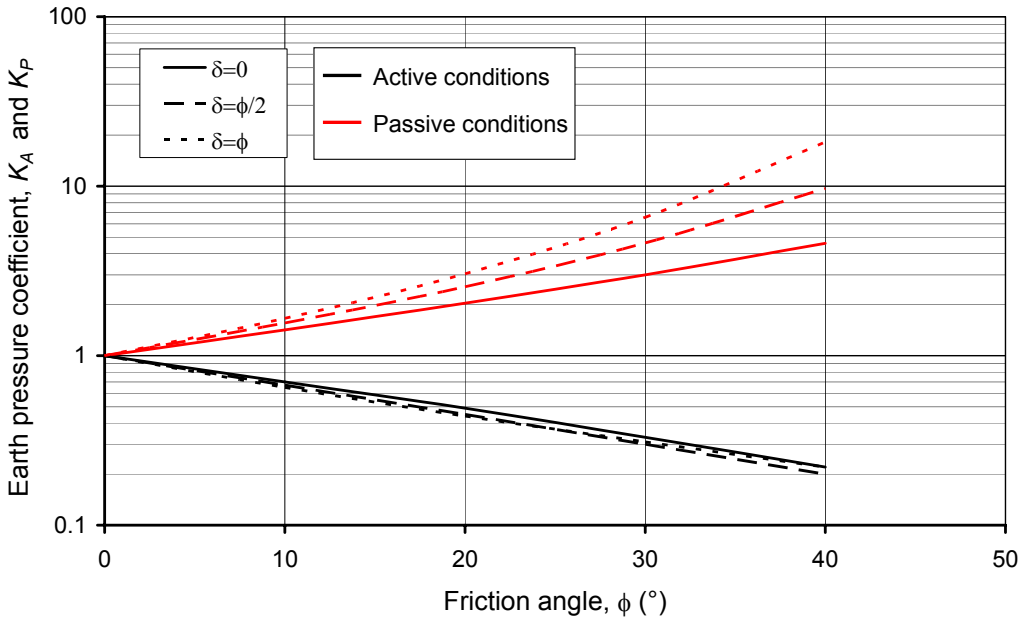

Figure 3-7. *Active and passive earth pressure coefficients for a horizontal backfill sustained by a vertical wall using slip line method (Sokolovskii, 1965).*

3.1.5 Limit analysis methods.

Limit analysis is considered to be an efficient method for computing the collapse load in a direct manner. This approach is, therefore, of intense practical interest to practicing engineers. There have been an enormous number of applications in metal structures. Applications of limit analysis to reinforced concrete structures are more recent and are given in a book by Chen (1982). Applications to typical stability problems in soil mechanics have been the most highly developed aspect of limit analysis. Earth pressure evaluation is one of most widespread employment available in the scientific literature. Here, the solutions obtained with the application of the upper and lower bound theorems of limit analysis are reported.

3.1.5.1 Upper Bound solution.

Chen & Liu (1990) have assumed translational horizontal wall movements and the log-sandwich failure mechanism reported by Chen (1975) to calculate active and passive lateral earth pressures by the upper-bound limit analysis method taking into account the soil-wall interface friction.

Failure mechanisms as generalized from James and Bransby (1970) are adopted for both the passive and the active cases. They are shown in Figure 3-8. The failure surfaces are assumed to follow the stress characteristics which are also the velocity characteristics for a perfectly plastic material. The mechanism consists of three zones. The first zone, Zone I, is the Rankine zone. The stress condition in this zone is not influenced by the characteristics of the soil-wall interface. The second zone, Zone II, is the mixed zone, which is subjected to the influence of the interface characteristics. According to Hettiaratchi and Reece (1975), this zone should be of triangular shape if the angle of wall friction, δ, is uniformly distributed along the interface as generally assumed. The third zone, Zone III, which is a transition zone, is formed by a logarithmic spiral of angle ϕ and the two adjacent boundaries. This kind of combination was reported by Chen and Rosenfarb (1973) to give the best upper bound in the several mechanisms investigated.

Since the upper bound method of limit analysis is based on energy equilibrium rather than on force-equilibrium as employed in the limit equilibrium method, the particular benefit of adopting logarithmic spiral surface with a frictional angle of ϕ is no longer relevant to the upper bound technique. Furthermore, James and Bransby (1970) found that the actual observed failure surfaces follow closely the velocity characteristics and in the Rankine zone $\theta_1 = \pi/2 + \psi$ for the passive pressure case, where the angle of dilation ψ is much smaller than ϕ. This mechanism has been adopted by Habibagahi and Ghahramani (1977) who solved the earth pressure problems by the limit equilibrium technique based on a so-called *zero extension line theory*. Much experimental evidence, such as that discussed by Scott (1963), also shows that the actual failure takes place on planes with smaller angles than those predicted by the Mohr-Coulomb criterion which gives the stress characteristics with $\theta_1 = \pi/2 \pm \phi$.

A possible explanation for the difference in the stress characteristics and the velocity characteristics for most soils is that the introduction of the friction in real soils causes the velocity characteristics, which are originally consistent with the stress characteristics for a perfectly plastic material. Consequently, $\theta_1 = \pi/2 + \xi$ with an equivalent friction angle ξ being smaller than ϕ and no less than ψ. Hence it is justified to adopt a logarithmic spiral with a ξ, with $\psi \leq \xi \leq \phi$, if the solution can be improved.

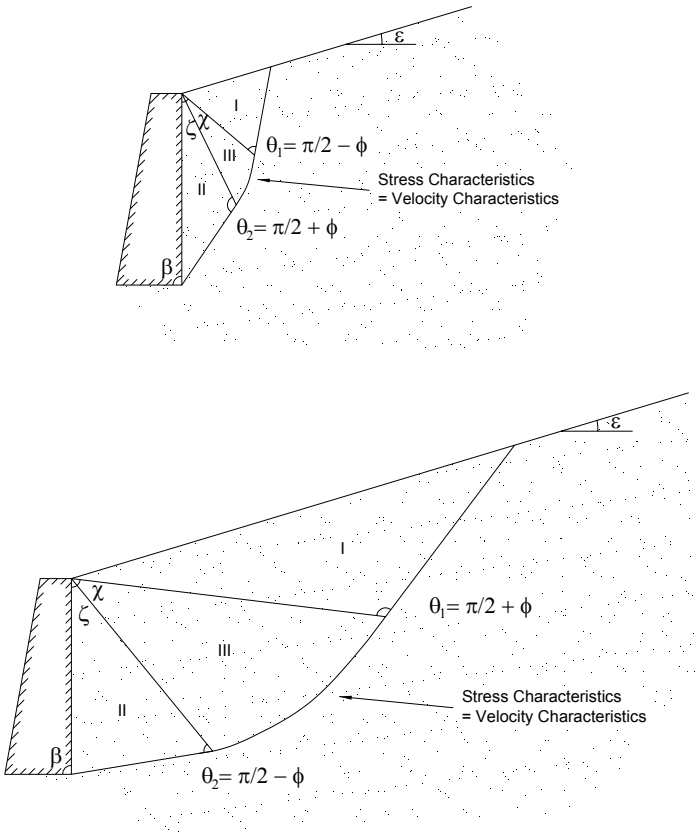

Figure 3-8. *Log-sandwich failure mechanisms for lateral earth pressure limit analysis (modified after Chen & Rosenfarb, 1973)*

However, it should be noted that when $\xi \leq \phi$ the solution is only an equilibrium solution and not necessarily an upper bound. For the upper bound theorem of limit analysis to be applicable, the material must be perfectly plastic so that $\xi = \phi$ in the Rankine zone. It can be shown that the active pressure coefficient K_A-values are not altered and K_P-values are somewhat lowered by the use of ξ-spiral rather than ϕ-spiral, especially when the values of the angle of repose of the wall, β, the backfill slope angle, ε, and the friction angle, ϕ, are high. This tends to indicate that the conventionally adopted ϕ-spiral failure surface is not necessarily the best mechanism that gives the close-to-exact solution for a given problem. One possible explanation for the fact that the use of ξ-spiral results in essentially no improvement for K_A-values but some improvement for K_P-values is that the prefailure volume flow, which is believed to have certain effects on the stress characteristics, is negligible in the active case but of considerable amount in the passive case. To account for this fact, ξ-spiral may be adopted for analysis in the passive case.

The chosen mechanisms of failure as shown in Figure 3-8 have the flexibility of being able to be reduced to a simple Coulomb planar failure mechanism when $\chi = 0$, or a logarithmic Rankine mechanism when $\varsigma = 0$ or a logarithmic spiral mechanism when $\varsigma = 0$ and $\chi = \beta + \varepsilon$. For the special case of $\phi = 0$, the failure mechanism becomes a circular arc, which seems to agree with actual observation of sliding in undrained cohesive soil masses.

Applying the upper-bound technique for the ξ-spiral failure mechanism, Chen & Liu (1990) obtained the following relationships for the coefficients of the active K_A and the passive K_P earth pressure:

$$K_A = \frac{\cos(\varsigma+\xi)\sin(\beta-\psi_w)}{\left[\sin^2\beta\cos\xi\left[\begin{array}{l}\sin(\beta-\delta)\cos(\varsigma-\phi-\psi_w+\xi)+\\+\cos\delta(\tan\delta-\tan\psi_w)\cos(\beta-\varsigma+\phi-\xi)\cos\psi_w\end{array}\right]\right]}\cdot$$
$$\cdot\left[\begin{array}{l}\sin\varsigma\cos(\beta-\varsigma+\phi-\xi)+\dfrac{\cos(\varsigma+\xi)}{\cos\xi\left(a^2+1\right)}\left(\begin{array}{l}\cos(\beta-\varsigma+\phi-\xi)\cdot\left[e^{-a\chi}(-a\cos\chi+\sin\chi)+a\right]+\\+\sin(\beta-\varsigma+\phi-\xi)\left[e^{-a\chi}(-a\sin\chi-\cos\chi+1)\right]\end{array}\right)+\\+\dfrac{\cos(\varsigma+\xi)\sin(\beta+\varepsilon+\varsigma-\chi)\cos(\beta-\varsigma-\chi+\phi-\xi)e^{-a\chi}}{\cos(\beta+\varepsilon-\varsigma-\chi-\xi)}\end{array}\right] \qquad (3\text{-}17)$$

$$K_P = \frac{\cos(\varsigma-\xi)\sin(\beta+\psi_w)}{\left[\sin^2\beta\cos\xi\left[\begin{array}{l}\sin(\beta+\delta)\cos(\varsigma+\phi+\psi_w-\xi)+\\-\cos\delta(\tan\delta-\tan\psi_w)\cos(\beta-\varsigma-\phi+\xi)\cos\psi_w\end{array}\right]\right]}\cdot$$
$$\cdot\left[\begin{array}{l}\sin\varsigma\cos(\beta-\varsigma-\phi+\xi)+\dfrac{\cos(\varsigma-\xi)}{\cos\xi\left(a^2+1\right)}\left(\begin{array}{l}\cos(\beta-\varsigma-\phi+\xi)\cdot\left[e^{a\chi}(a\cos\chi+\sin\chi)-a\right]+\\+\sin(\beta-\varsigma-\phi+\xi)\left[e^{a\chi}(a\sin\chi-\cos\chi)+1\right]\end{array}\right)+\\+\dfrac{\cos(\varsigma-\xi)\sin(\beta+\varepsilon-\varsigma-\chi)\cos(\beta-\varsigma-\chi-\phi+\xi)e^{a\chi}}{\cos(\beta+\varepsilon-\varsigma-\chi+\xi)}\end{array}\right] \qquad (3\text{-}18)$$

where $a = 2\tan\xi + \tan(2\phi - \xi)$ and ψ_w is the dilating components of the soil-wall friction angle δ.

For a problem with assigned geometrical configuration, β and ε, and material strength parameters, ϕ, δ and ψ_w, the practical application of these formulas can be done by varying the two angles ς, χ and determining the maximum value of K_A and the minimum value of K_P.

The results reported by Chen & Liu (1990) for different values of β, ϕ and δ are given in Table 3-5 and Table 3-6. As for the Coulomb theory, the normal components of the earth pressures can be determined by multiplying the values for cosδ. In Figure 3-9 are depicted the trends of K_A and K_P for a vertical wall that retains a horizontal backfill.

β	ϕ	20°			30°			40°			50°		
	δ	0°	10°	20°	0°	15°	30°	0°	20°	40°	0°	25°	50°
-30°	K_A	0.77	0.74	0.76	0.62	0.61	0.67	0.49	0.50	0.62	0.38	0.42	0.65
-15°		0.60	0.56	0.56	0.45	0.42	0.44	0.33	0.32	0.36	0.23	0.23	0.31
0°		0.49	0.45	0.43	0.33	0.30	0.30	0.22	0.20	0.21	0.13	0.13	0.15
15°		0.41	0.37	0.34	0.24	0.21	0.21	0.13	0.12	0.12	0.06	0.06	0.06
30°		0.34	0.29	0.27	0.17	0.14	0.13	0.07	0.05	0.05	0.01	0.01	0.01

Table 3-5. *Values of the active earth pressure coefficient given by the upper-bound method for log-sandwich failure mechanisms (Chen & Liu, 1990).*

β	ϕ	20°			30°			40°			50°		
	δ	0°	10°	20°	0°	15°	30°	0°	20°	40°	0°	25°	50°
-30°	K_P	1.74	2.00	2.29	2.15	2.82	3.77	2.71	4.23	7.45	3.48	7.39	20.18
-15°		1.78	2.16	2.56	2.38	3.42	4.57	3.26	6.08	11.67	4.63	13.12	41.27
0°		2.04	2.58	3.17	3.00	4.71	7.10	4.60	10.09	20.91	7.55	28.68	98.06
15°		2.61	3.45	4.39	4.35	7.42	11.79	7.80	19.67	43.09	15.98	75.20	267.69
30°		3.79	5.27	6.96	7.38	13.67	22.70	16.15	45.47	103.16	43.72	234.22	848.58

Table 3-6. *Values of the passive earth pressure coefficient given by the upper-bound method for log-sandwich failure mechanisms (Chen & Liu, 1990).*

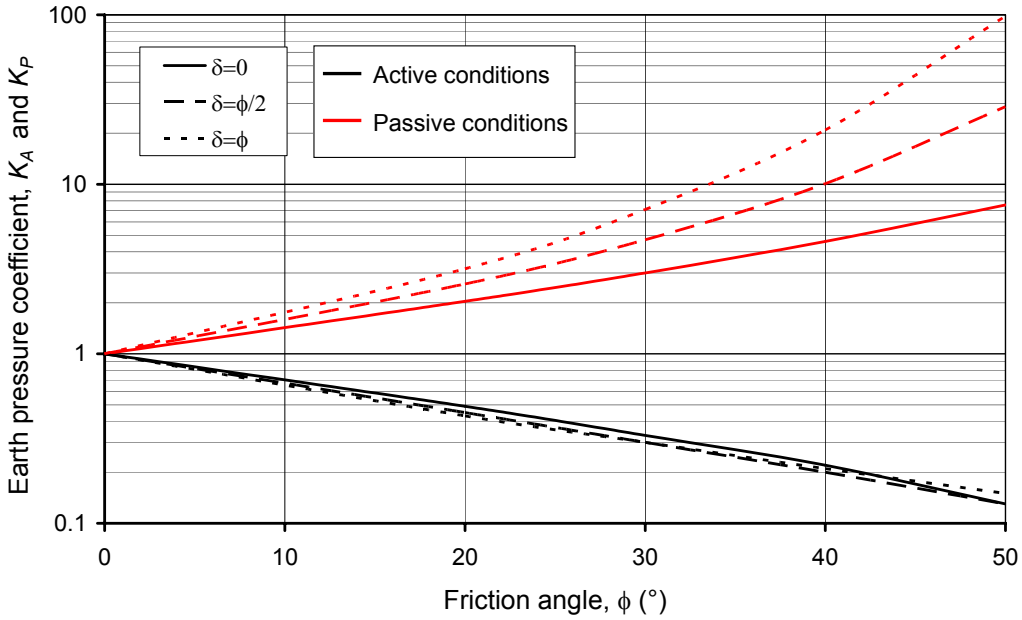

Figure 3-9. *Active and passive earth pressure coefficients for a horizontal backfill sustained by a vertical wall (Chen & Liu, 1990).*

3.1.5.2 Lower Bound solution.

The lower-bound method of limit analysis is different from the upper-bound method in that the equilibrium and yield condition instead of the work equation and failure mechanism are considered. Lancellotta (2002) has used this approach to obtain an analytical solution for the passive earth pressure acting on a rough retaining wall. Considering a fan of stress discontinuities that divides two regions, one placed near to the wall in which the stress state is affected from the soil-wall friction and the other one with the half space stress conditions, and determining the shift between the two extreme Mohr circles of the stress states in the two regions, the author has deduced the following closed form for the passive earth pressure coefficient K_P:

$$K_P = \left[\frac{\cos\delta}{1-\sin\phi}\left(\cos\delta + \sqrt{\sin^2\phi - \sin^2\delta}\right)\right] e^{2\theta\tan\phi} \qquad (3\text{-}19)$$

where:

$$2\theta = \sin^{-1}\left(\frac{\sin\delta}{\sin\phi}\right) + \delta \qquad (3\text{-}20)$$

For completeness, in the paper is reported the expression of active earth pressure coefficient, too:

$$K_A = \left[\frac{\cos\delta}{1+\sin\phi}\left(\cos\delta - \sqrt{\sin^2\phi - \sin^2\delta}\right)\right] e^{-2\theta\tan\phi} \qquad (3\text{-}21)$$

where:

$$2\theta = \sin^{-1}\left(\frac{\sin\delta}{\sin\phi}\right) - \delta \qquad (3\text{-}22)$$

Equations (3-19) and (3-21) can be expressed as a single equation:

$$K_{P,A} = \left[\frac{\cos\delta}{1 \mp \sin\phi}\left(\cos\delta \pm \sqrt{\sin^2\phi - \sin^2\delta}\right)\right] e^{\pm 2\theta \tan\phi} \qquad (3\text{-}23)$$

with:

$$2\theta = \sin^{-1}\left(\frac{\sin\delta}{\sin\phi}\right) \pm \delta \qquad (3\text{-}24)$$

Unlike the previous theories, the values given by the equation (3-23) represent the normal components to the vertical wall of the earth pressure coefficients. The total earth pressure coefficients can be obtained dividing for cosδ the results of the relationships.

Figure 3-10 shows the values of K_A and K_P for a horizontal backfill retained by a vertical wall evaluated with the equations (3-19) and (3-21).

The main advantages of this solution are the closed form of the equations, respect to the tabled values given by the upper-bound method, and the conservative estimation of the exact solution of the soil passive resistance in plane conditions. This fact has a great relevance in engineering practice.

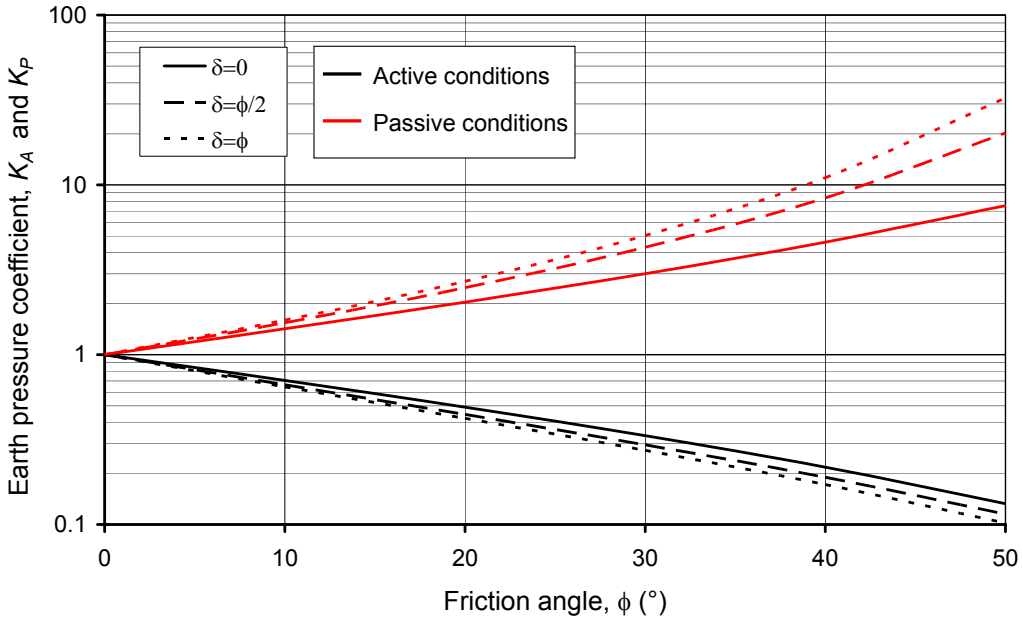

Figure 3-10. *Active and passive earth pressure coefficients for a horizontal backfill sustained by a vertical wall (Lancellotta, 2002).*

3.1.6 Comparisons between the different static methods.

As can be noted from the graphical representations of the results obtained from the application of the different theories, the active earth pressures coefficients is not strongly affected by the soil wall friction angle δ, while, small variations of δ produce large differences on K_P values calculated with the various methods.

From Figure 3-11 to Figure 3-14 the comparisons between the normal components to the wall of the active and passive earth pressure coefficients evaluated with the different methods for a horizontal

backfill (ε=0) retained by smooth (δ=0) and rough (δ=ϕ) vertical walls are plotted. Note that the earth pressure coefficients was estimated till to a soil friction angle ϕ=40°, for the slip line method, and ϕ=45°, for the logarithmic spiral method.

In active and passive conditions, for a smooth wall, the computed K_{An} and K_{Pn} values are practically the same.

For a rough wall, in the active conditions, the differences becomes relatively much larger. Rankine and Coulomb methods give the upper and lower threshold trends, while the other methods carry out very similar solutions.

The passive earth pressure coefficients are more sensible to the soil wall friction. If the slip line method can be interpreted as the most accurate determination close to the exact solution, the upper bound limit analysis provides K_P values very similar to those expected while the lower bound approach gives conservative and easy-to-calculate passive coefficients.

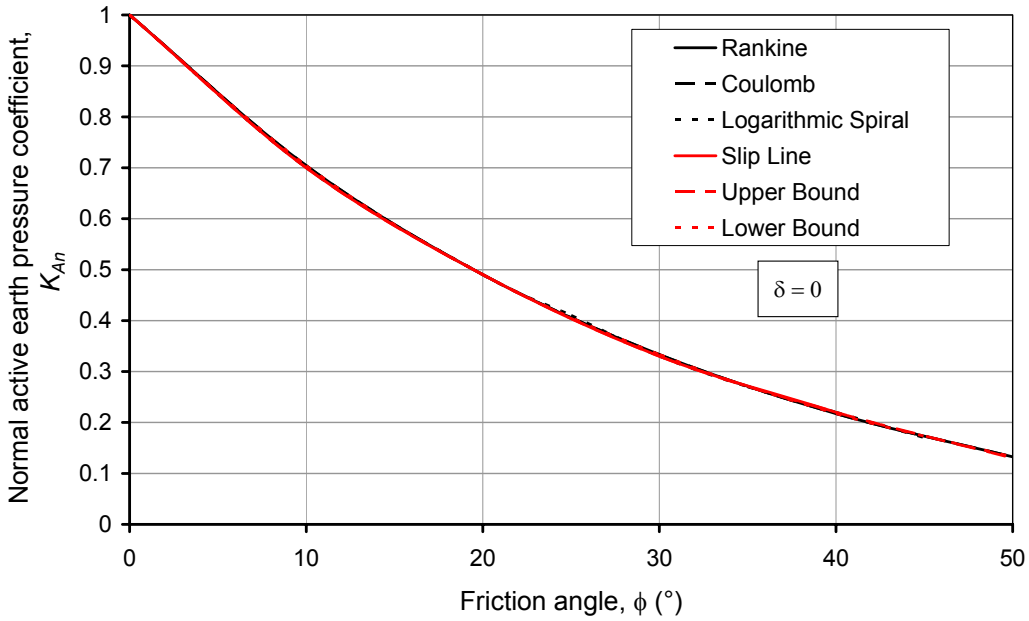

Figure 3-11. *Comparisons between the normal components of the active earth pressure coefficient given by the various methods for a horizontal backfill sustained by a smooth vertical wall (δ=0).*

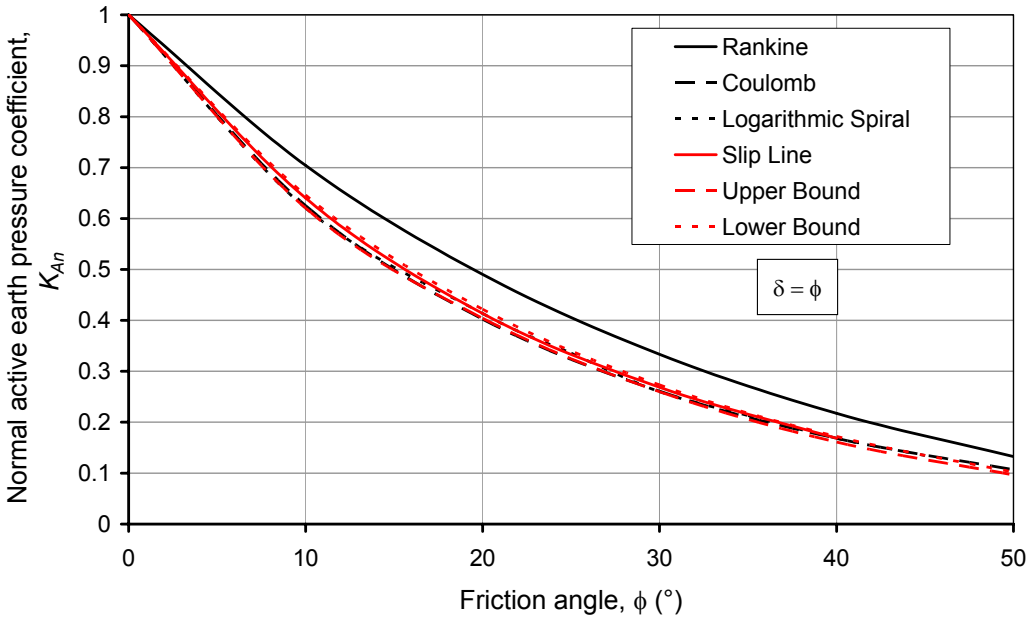

Figure 3-12. *Comparisons between the normal components of the active earth pressure coefficient given by the various methods for a horizontal backfill sustained by a rough vertical wall (δ=ϕ).*

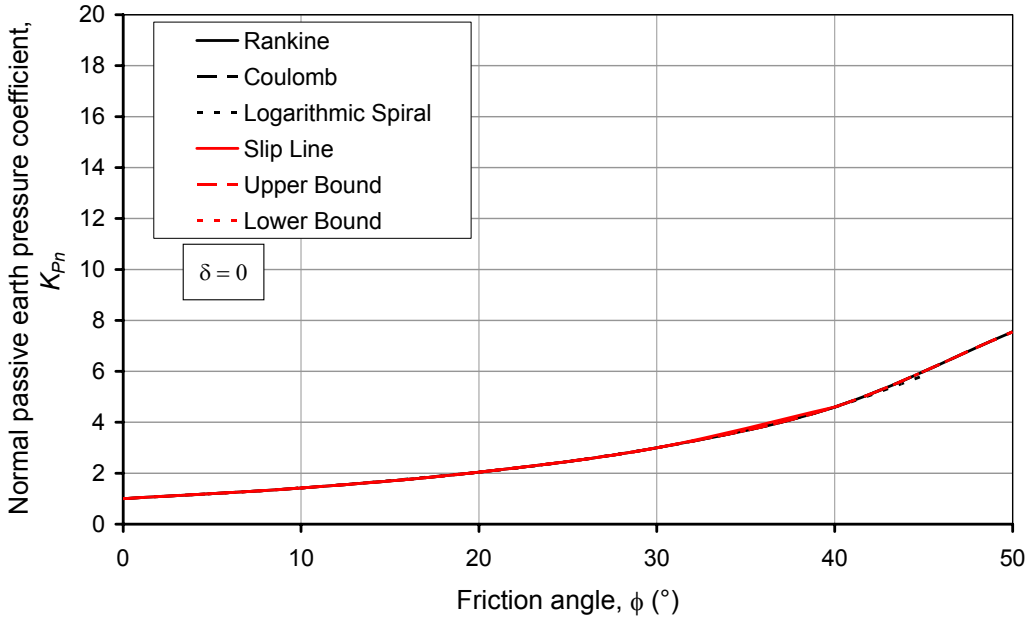

Figure 3-13. *Comparisons between the normal components of the passive earth pressure coefficient given by the various methods for a horizontal backfill sustained by a smooth vertical wall (δ=0).*

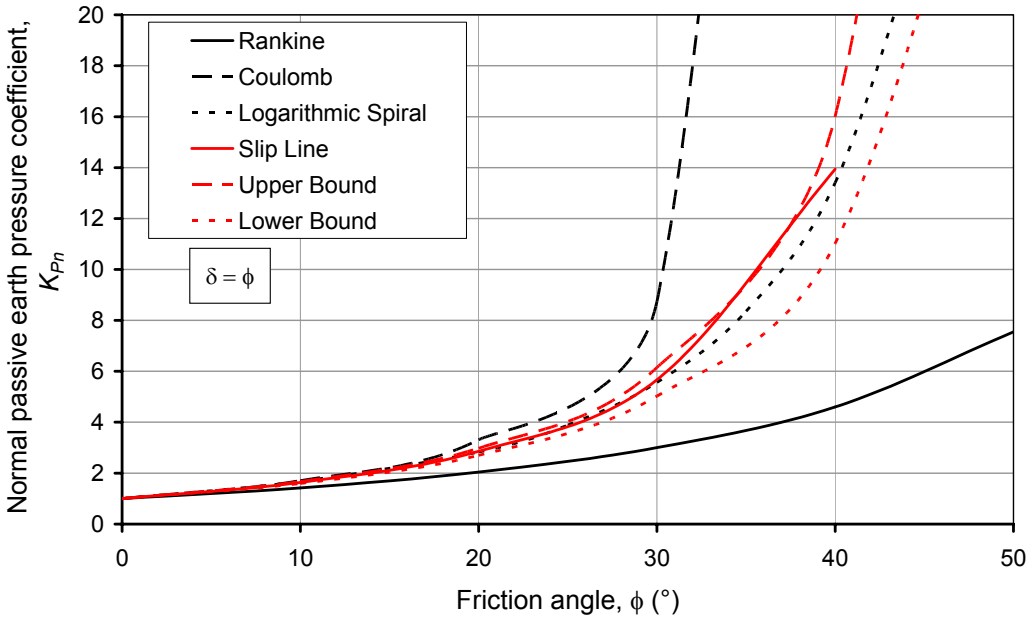

Figure 3-14. *Comparisons between the normal components of the passive earth pressure coefficient given by the various methods for a horizontal backfill sustained by a rough vertical wall (δ=ϕ).*

3.2 SEISMIC PRESSURES ON RETAINING WALLS.

A common approach to the seismic design of retaining walls involves estimating the loads imposed on the wall during earthquake shaking and then ensuring that the wall can resist those loads. Because the actual loading on retaining walls during the earthquakes is extremely complicated, seismic pressures on retaining walls are usually estimated using simplified methods.

Retaining walls that can move sufficiently to develop minimum active and/or maximum passive earth pressures are referred to as yielding walls. The dynamic pressures acting on yielding walls are usually estimated by pseudostatic procedures in which the effects of an earthquake are represented by constant horizontal and/or vertical accelerations.

Some retaining structures, such as massive gravity walls founded on rock or basement walls braced at both top and bottom, do not move sufficiently to mobilize shear strength of the backfill soil. As a result, the limiting conditions of minimum active or maximum passive earth pressures can not be developed. This type of walls are denoted as nonyielding walls.

An earthquake has two possible effects on a soil-wall system. One is to increase the driving force. The other is to decrease the shearing resistance of the soil. The reduction in the shearing resistance of a soil during an earthquake appears only when the magnitude of the earthquake exceeds a certain limit and the ground conditions are favourable for such a reduction. The evaluation of such a reduction requires considerable knowledge in earthquake engineering and soil dynamics.

Research conducted by Okamoto (1956) indicated that when the average ground acceleration is larger than 0.3g, there is a considerable reduction in strength for most soils. However, he claimed that in many cases, the ground acceleration is less than 0.3g and the mechanical properties of mostly of the soils do not change significantly in these cases. Here, only the increase in driving forces is to be considered. The shear strength of the soil is assumed unaffected by the influence of the seismic loading.

In the quasi-static analysis of seismic lateral earth pressures, a constant seismic coefficient, k, is assumed for the entire soil mass involved. A seismic force, which is equal to k times the weight of a soil mass, is assumed to act at the center of gravity of the sliding soil mass. The seismic force is assumed to act in a direction at an angle θ from the vertical as shown in Figure 1-1.

In the following, the main theories developed for the study of the earth pressure on yielding walls in seismic conditions with a pseudostatic approach and on nonyielding walls are presented.

3.2.1 Mononobe-Okabe theory.

Okabe (1926) and Mononobe & Matsuo (1929) developed the basis of a pseudostatic analysis of seismic earth pressures on retaining structures that has become popularly known as the Mononobe-Okabe (M-O) method. The M-O method is a direct extension of the static Coulomb theory to pseudostatic conditions. In a M-O analysis, pseudostatic accelerations are applied to a Coulomb active (or passive) wedge. The pseudostatic soil thrust is then obtained from the force equilibrium of the wedge.

In addition to those under static conditions, the forces acting on an active wedge in a dry cohesionless backfill wedge are constituted by horizontal and vertical pseudostatic forces whose magnitudes are

related to the mass of the wedge by the pseudostatic accelerations $a_h = k_h g$ and $a_v = k_v g$. The total active thrust can be expressed in a form similar to that developed for static conditions, that is:

$$S_{AE} = \frac{1}{2} K_{AE} \gamma H^2 (1 - k_v) \qquad (3\text{-}25)$$

where the dynamic active earth pressure coefficient, K_{AE}, is given by:

$$K_{AE} = \frac{\cos^2(\phi - \beta - \theta)}{\cos\theta \cos^2\beta \cos(\delta + \beta + \theta)\left[1 + \sqrt{\frac{\sin(\delta + \phi)\sin(\phi - \varepsilon - \theta)}{\cos(\delta + \beta + \theta)\cos(\varepsilon - \beta)}}\right]^2} \qquad (3\text{-}26)$$

where $\phi - \varepsilon \geq \theta$, and $\theta = \tan^{-1}[k_h/(1-k_v)]$. The critical failure surface, which is flatter than the critical failure surface for static conditions, is inclined (Zarrabi-Kashani, 1979) at an angle:

$$\alpha_{AE} = \phi - \theta + \tan^{-1}\left[\frac{-\tan(\phi - \theta - \varepsilon) + C_{1E}}{C_{2E}}\right] \qquad (3\text{-}27)$$

where:

$$C_{1E} = \sqrt{\tan(\phi - \theta - \varepsilon)\left[\tan(\phi - \theta - \varepsilon) + \cot(\phi - \theta - \beta)\right]\left[1 + \tan(\delta + \theta + \beta)\cot(\phi - \theta - \beta)\right]}$$

$$C_{2E} = 1 + \left\{\tan(\delta + \theta + \beta)\left[\tan(\phi - \theta - \varepsilon) + \cot(\phi - \theta - \beta)\right]\right\}$$

Altough the M-O analysis implies that the total active thrust should act at a point H/3 above the base of a wall of height H, experimental results suggest that it actually acts at a higher points under dynamic loading conditions. The total active thrust, S_{AE}, can be divided into a static component, S_A, and a dynamic component, ΔS_{AE}:

$$S_{AE} = S_A + \Delta S_{AE} \qquad (3\text{-}28)$$

The static component is known to act at H/3 above the base of the wall. Seed & Whitman (1970) recommended that the dynamic component be taken to act at approximately 0.6 H. On this basis, the total active thrust will act at a height h:

$$h = \frac{S_A \cdot H/3 + \Delta S_{AE}(0.6H)}{S_{AE}} \qquad (3\text{-}29)$$

above the base of the wall. The value of h depends on the relative magnitudes of S_A and S_{AE} – it often ends up near to the midheight of the wall. M-O analyses show that k_v, when taken as one-half to two-thirds the value of k_h, affects S_{AE} by less than 10%. Seed and Whitman (1970) concluded that vertical accelerations can be ignored when the M-O method is used to estimate S_{AE} for typical wall designs.

The total passive thrust on a wall retaining a dry cohesionless backfill is given by:

$$S_{PE} = \frac{1}{2} K_{PE} \gamma H^2 (1 - k_v) \qquad (3\text{-}30)$$

where the dynamic passive earth pressure coefficient, K_{PE}, is given by:

$$K_{PE} = \frac{\cos^2(\phi + \beta - \theta)}{\cos\theta \cos^2\beta \cos(\delta - \beta + \theta)\left[1 + \sqrt{\frac{\sin(\delta + \phi)\sin(\phi + \varepsilon - \theta)}{\cos(\delta - \beta + \theta)\cos(\varepsilon - \beta)}}\right]^2} \qquad (3\text{-}31)$$

The critical failure surface for M-O passive conditions is inclined from horizontal by an angle:

$$\alpha_{PE} = \theta - \phi + \tan^{-1}\left[\frac{-\tan(\phi+\theta+\varepsilon)+C_{3E}}{C_{4E}}\right] \qquad (3\text{-}32)$$

where:

$$C_{3E} = \sqrt{\tan(\phi-\theta+\varepsilon)\left[\tan(\phi-\theta+\varepsilon)+\cot(\phi-\theta+\beta)\right]\left[1+\tan(\delta-\theta+\beta)\cot(\phi-\theta+\beta)\right]}$$

$$C_{4E} = 1+\left\{\tan(\delta+\theta-\beta)\left[\tan(\phi-\theta+\varepsilon)+\cot(\phi-\theta+\beta)\right]\right\}$$

The total passive thrust can also be divided (Towhata and Islam, 1987) into static and dynamic components:

$$S_{PE} = S_P + \Delta S_{PE} \qquad (3\text{-}33)$$

where S_{PE} and S_P are computed from equations (3-30) and (3-12), respectively. Note that the dynamic component acts in the opposite direction of the static component, thus reducing the available passive resistance.

From Figure 3-15 to Figure 3-18 the graphical representations of the seismic earth pressure coefficients and the critical failure surfaces in active and passive conditions evaluated with the M-O method for vertical walls retaining a horizontal backfill are plotted. The figures denote a slight influence of the soil-wall friction on the seismic active conditions while, as in the Coulomb method, strong differences exist in the passive case.

Although conceptually quite simple, the M-O analysis provides a useful means of estimating earthquake-induced loads on retaining walls. A positive horizontal acceleration coefficient causes the total active thrust to exceed the static active thrust and the total passive thrust to be less than the static passive thrust. Since the stability of a particular wall is generally reduced by an increase in active thrust and/or a decrease in passive thrust, the M-O method produces seismic loads that are more critical than the static loads that act prior an earthquake. The effects of distributed load and discrete surface loads and irregular backfill surfaces are easily considered by modifying the free-body diagram of the active or passive wedge. In such cases, equations (3-26) and (3-31) no longer apply. The total thrusts must be obtained from the analysis of a number of potential failure planes.

As a pseudostatic extension of the Coulomb analysis, however, the M-O analysis is subject to all of the limitations of pseudostatic analyses as well as the limitations of Coulomb theory. The determination of the appropriate pseudostatic coefficient is difficult and the analysis is not appropriate for soils that experience significant loss of strength during earthquakes (e.g. liquefiable soils). Just as Coulomb theory does under static conditions, the M-O analysis will overpredict the actual total passive thrust, particularly for $\delta > \phi/2$. For these reasons the M-O method should be used and interpreted carefully.

Note that, in Figure 3-17c, the seismic passive earth pressure coefficient is larger than 20 when the yellow horizontal plateau appears.

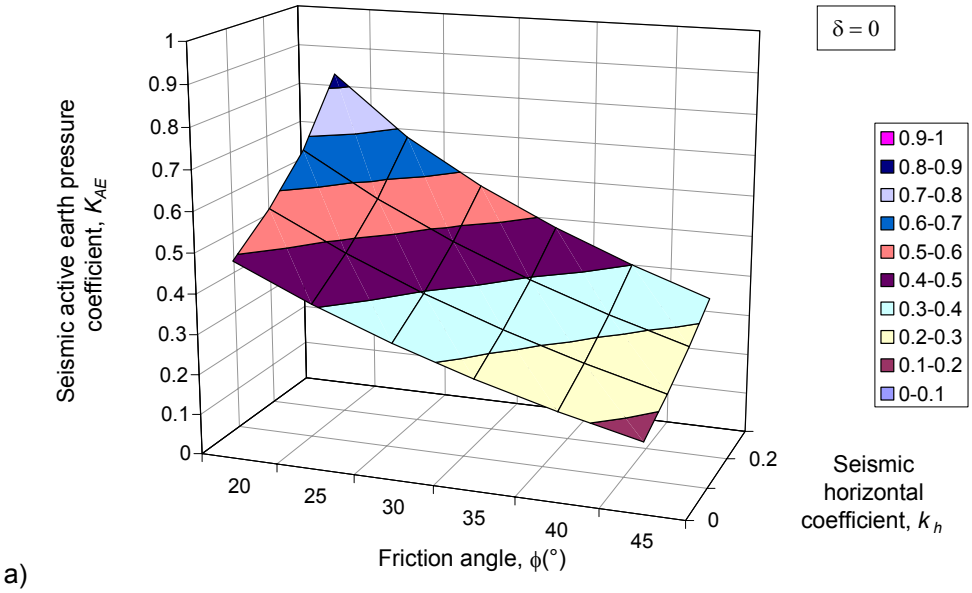

a)

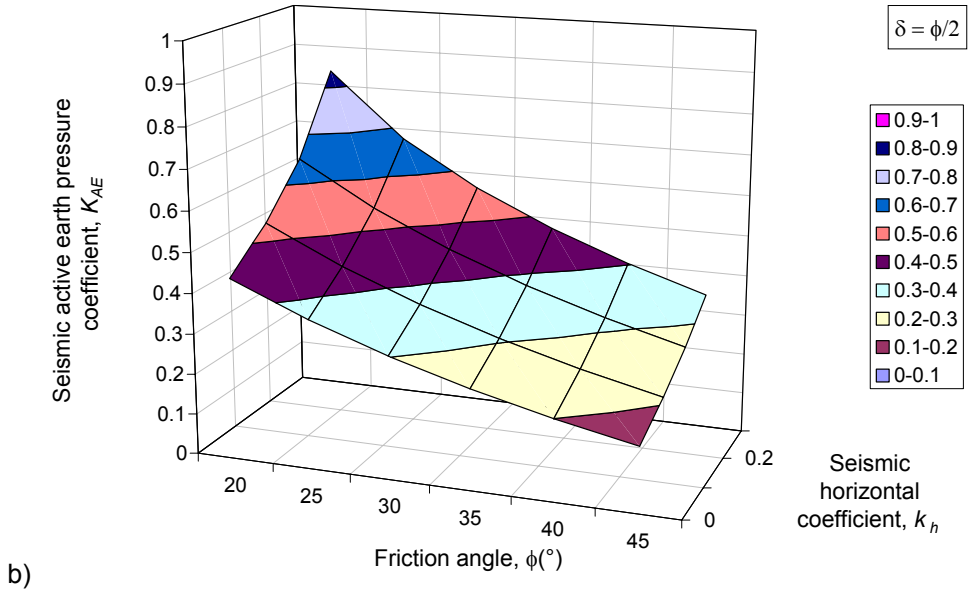

b)

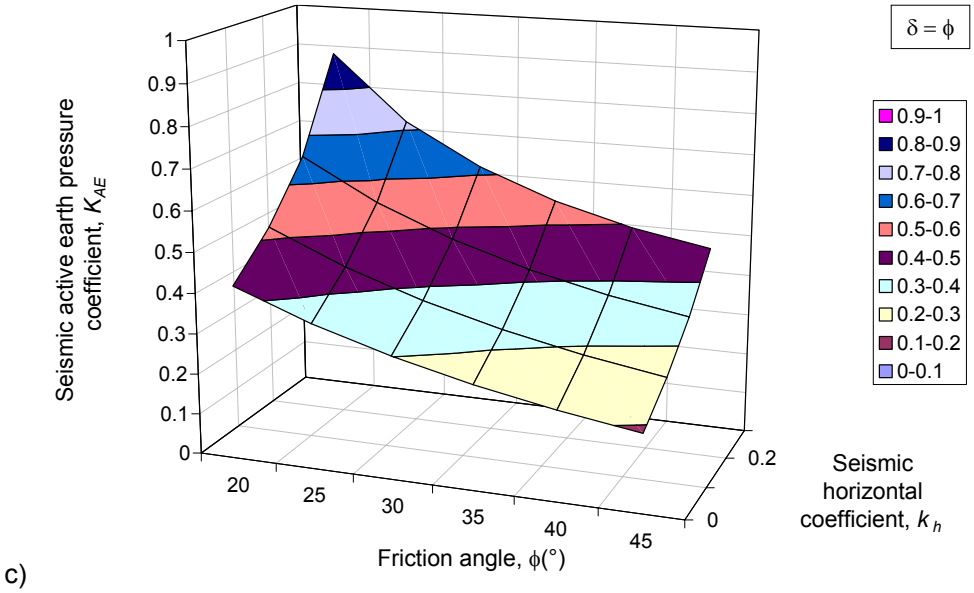

c)

Figure 3-15. *Seismic active earth pressure coefficients for a horizontal backfill sustained by vertical walls (Mononobe-Okabe method): a) δ=0; b) δ=ϕ/2; c) δ=ϕ.*

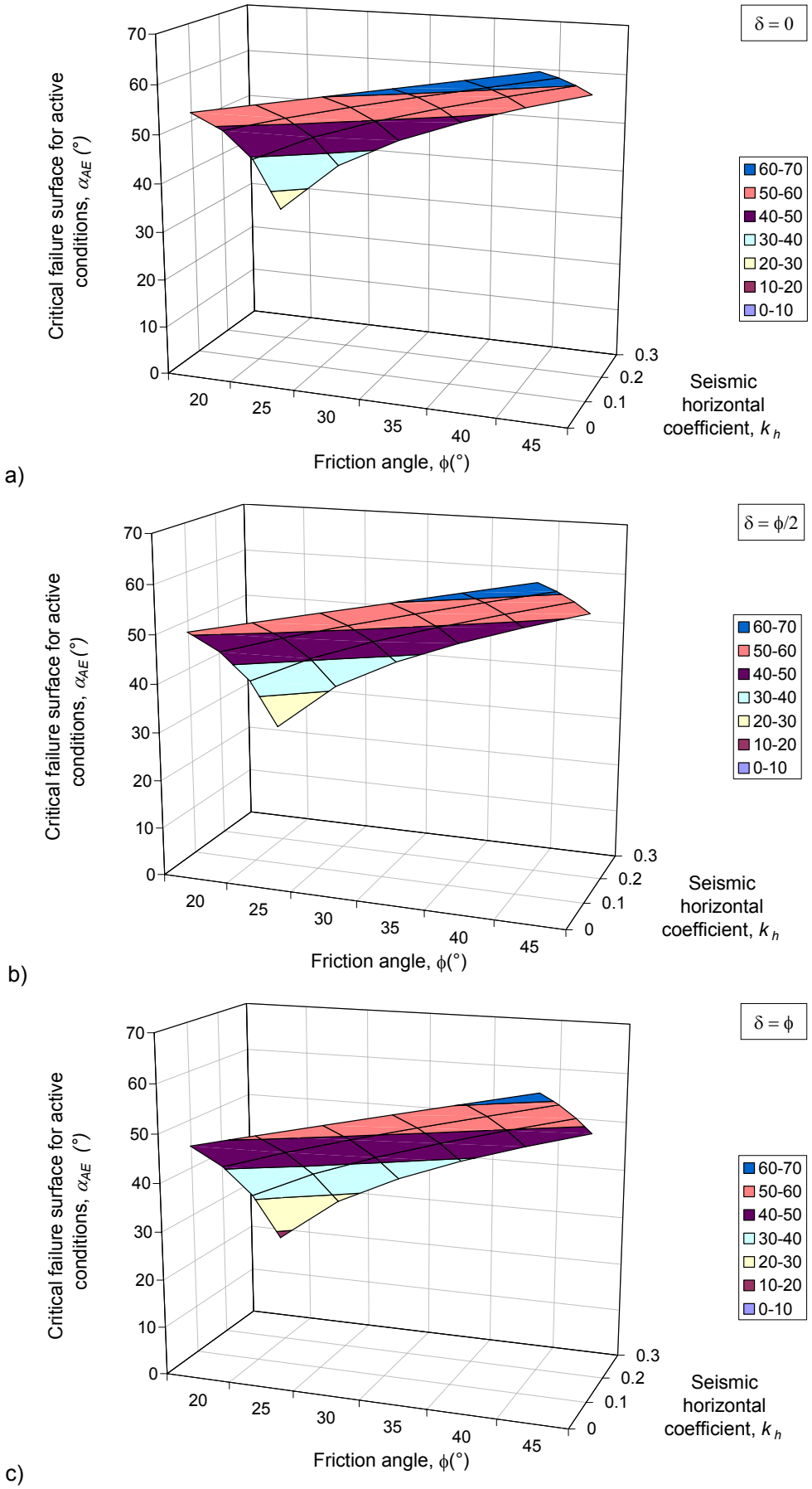

Figure 3-16. *Critical failure surfaces in seismic active conditions for a horizontal backfill sustained by vertical walls (Mononobe-Okabe method): a) δ=0; b) δ=ϕ/2; c) δ=ϕ.*

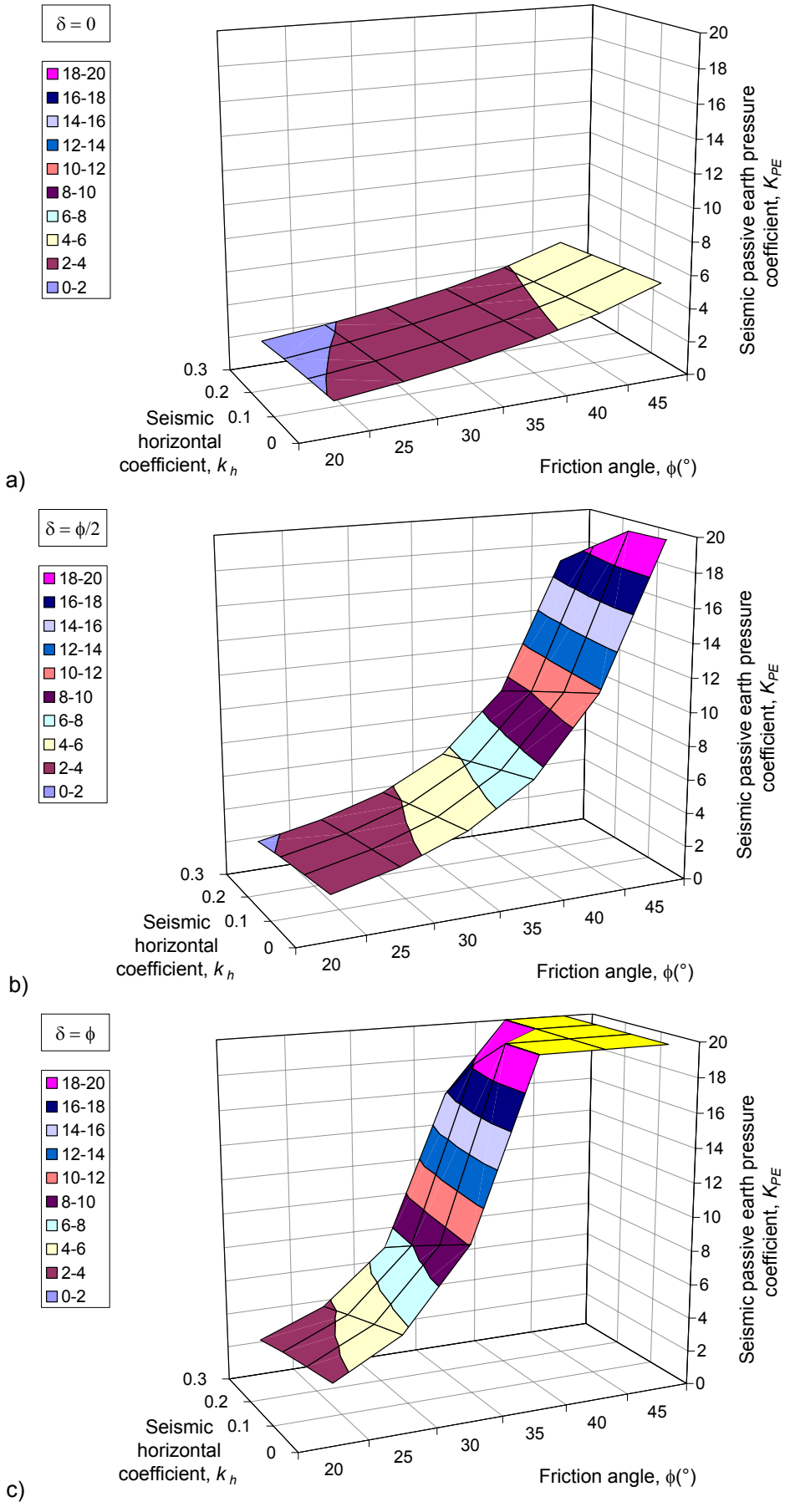

Figure 3-17. *Seismic passive earth pressure coefficients for a horizontal backfill sustained by vertical walls (Mononobe-Okabe method): a) δ=0; b) δ=ϕ/2; c) δ=ϕ.*

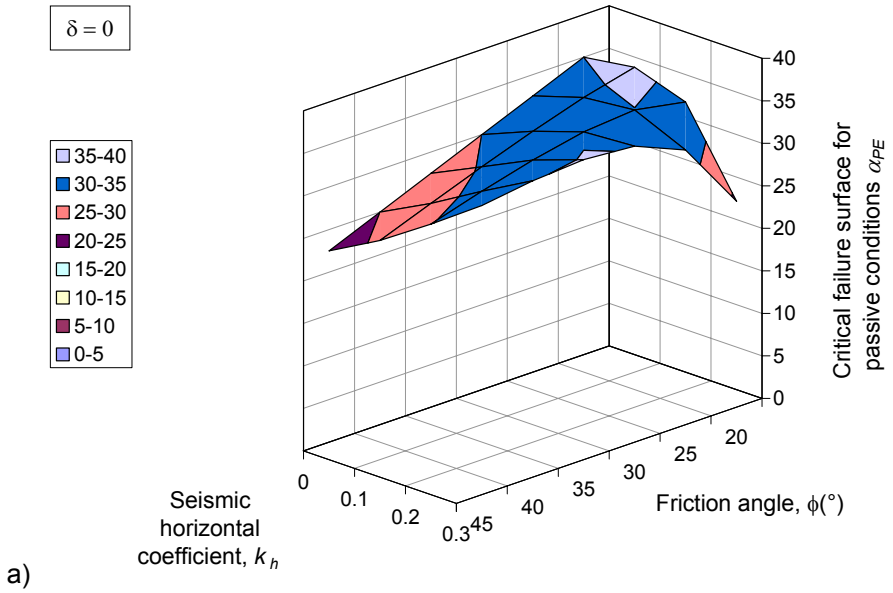

a)

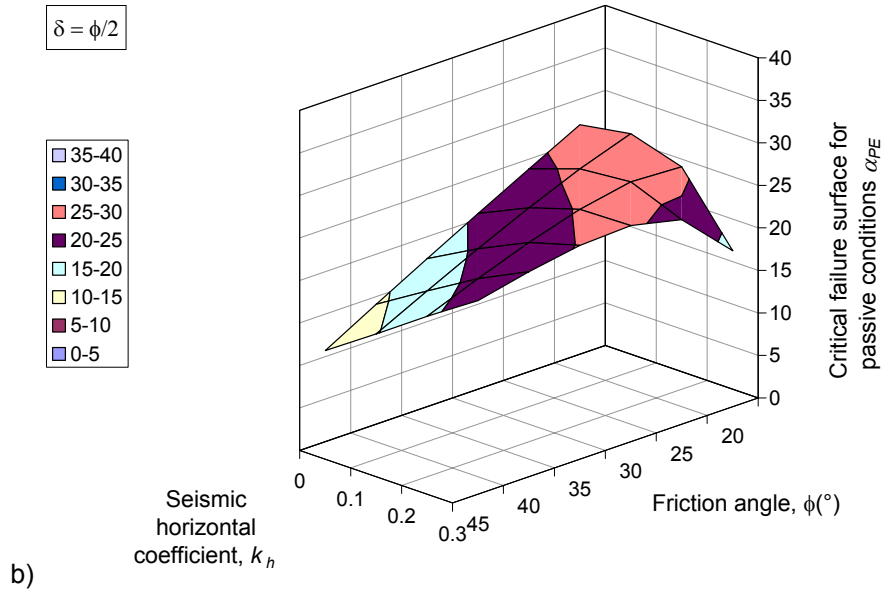

b)

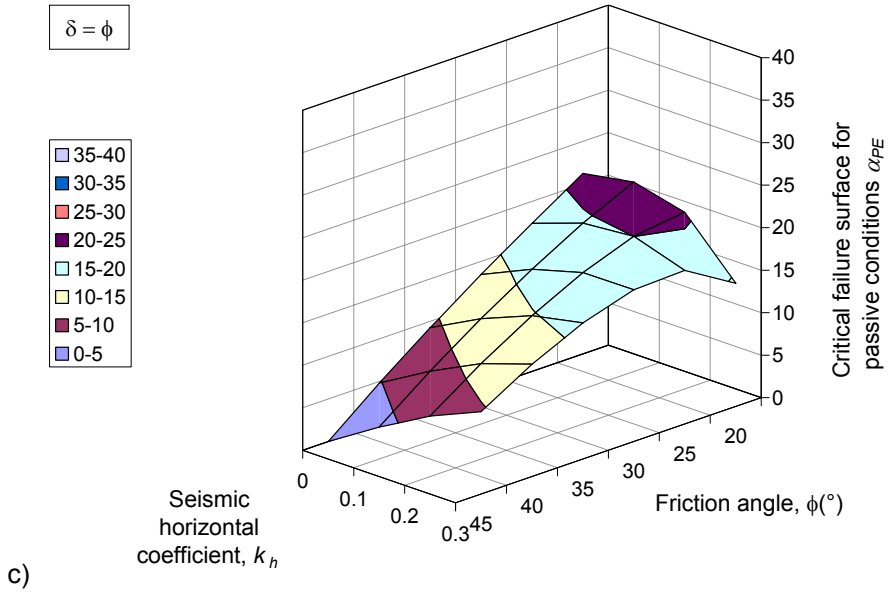

c)

Figure 3-18. *Critical failure surfaces in seismic passive conditions for a horizontal backfill sustained by vertical walls (Mononobe-Okabe method): a) δ=0; b) δ=ϕ/2; c) δ=ϕ.*

3.2.2 Limit analysis methods.

3.2.2.1 Upper bound solution.

By equating the incremental external work to the incremental internal energy dissipation associated to a translational wall movement and a ϕ-spiral log-sandwich mechanism of failure proposed by Chen and Rosenfarb (1973), Chang (1981) has deduced seismic active and passive earth pressure formulations in which the soil thrust can be expressed in terms of equivalent coefficients of seismic earth pressure, K_{AE} and K_{PE}, as:

$$S_E = \frac{1}{2} K_E \gamma H^2 \qquad (3\text{-}34)$$

The seismic active earth pressure coefficient K_{AE} is:

$$K_{AE} = N_{A\gamma} + \frac{2q}{\gamma H} N_{Aq} + \frac{2c}{\gamma H} N_{Ac} \qquad (3\text{-}35)$$

where γ is the unit weight of the backfill material, H the vertical height of the wall, q is the uniform surcharge acting on the surface of the backfill, c is the soil cohesion. $N_{A\gamma}$, N_{Aq} and N_{Ac} are three coefficients for which closed form expressions can be found in Chen & Liu (1990). The most critical K_{AE}-value can be obtained by maximization with respect to ς and χ shown in Figure 3-8.

At the same manner, the seismic passive earth pressure coefficient K_{PE} is given by the following relationship:

$$K_{PE} = N_{P\gamma} + \frac{2q}{\gamma H} N_{Pq} + \frac{2c}{\gamma H} N_{Pc} \qquad (3\text{-}36)$$

Expressions of the three coefficients $N_{A\gamma}$, N_{Aq} and N_{Ac} can be found in Chen & Liu (1990). The most critical K_{PE}-value can be obtained by minimization with respect to ς and χ shown in Figure 3-8.

For practical purposes, the author has calculated some values of the seismic earth pressure coefficients reported in tables (Chang, 1981, as quoted by Chen & Liu, 1990).

In the next Table 3-7 and Table 3-8 some of them are summarized.

Figure 3-19 and Figure 3-20 show the graphical representations of the seismic earth pressure coefficients in active and passive conditions given by the upper bound method for vertical walls retaining a horizontal backfill. As M-O method, the soil-wall friction has a slight influence on the seismic active conditions. For high values of the friction angle ϕ, the differences might become larger in the passive conditions.

The dependence of the seismic coefficient k_h on K_{AE} and K_{PE} is more clear considering the variations of earth pressure coefficients respect to the corresponding static values. For the active case, the increase of K_{AE} is more obvious for denser soils with higher ϕ-values than for the looser soils with lower ϕ-values. The decrease of K_{PE} is more obvious for looser soils than for denser soils in the passive case.

β	ϕ	20°			30°			40°			50°		
	δ	0°	10°	20°	0°	15°	30°	0°	20°	40°	0°	25°	50°
-30°		0.77	0.74	0.76	0.62	0.61	0.67	0.49	0.50	0.62	0.38	0.42	0.65
-15°		0.60	0.56	0.56	0.45	0.42	0.44	0.33	0.32	0.36	0.23	0.23	0.31
0°	$k_h = 0$	0.49	0.45	0.43	0.33	0.30	0.30	0.22	0.20	0.21	0.13	0.13	0.15
15°		0.41	0.37	0.34	0.24	0.21	0.21	0.13	0.12	0.12	0.06	0.06	0.06
30°		0.34	0.29	0.27	0.17	0.14	0.13	0.07	0.05	0.05	0.01	0.01	0.01
-30°		0.84	0.84	0.89	0.69	0.70	0.81	0.56	0.59	0.79	0.44	0.50	0.53
-15°		0.68	0.65	0.66	0.51	0.50	0.53	0.39	0.33	0.45	0.28	0.29	0.41
0°	$k_h = 0.1$	0.57	0.53	0.52	0.40	0.37	0.37	0.27	0.25	0.26	0.17	0.17	0.21
15°		0.49	0.45	0.43	0.31	0.27	0.27	0.18	0.16	0.17	0.09	0.09	0.10
30°		0.44	0.38	0.36	0.23	0.20	0.18	0.10	0.09	0.09	0.04	0.03	0.03
-30°		0.96	1.00	1.12	0.78	0.83	1.02	0.63	0.71	1.07	0.51	0.62	1.58
-15°		0.78	0.78	0.82	0.59	0.60	0.66	0.45	0.47	0.58	0.34	0.37	0.55
0°	$k_h = 0.2$	0.67	0.65	0.65	0.47	0.45	0.47	0.33	0.32	0.36	0.22	0.22	0.28
15°		0.61	0.56	0.55	0.38	0.35	0.35	0.23	0.21	0.23	0.13	0.13	0.15
30°		0.56	0.51	0.48	0.31	0.27	0.26	0.15	0.13	0.14	0.06	0.06	0.06
-30°		1.16	1.30	1.54	0.90	1.01	1.38	0.73	0.87	1.53	0.60	0.77	2.31
-15°		0.95	1.00	1.10	0.70	0.73	0.86	0.53	0.57	0.77	0.40	0.46	0.78
0°	$k_h = 0.3$	0.83	0.84	0.88	0.57	0.56	0.61	0.40	0.40	0.47	0.28	0.29	0.39
15°		0.77	0.75	0.75	0.48	0.45	0.46	0.30	0.28	0.31	0.13	0.17	0.21
30°		0.75	0.70	0.68	0.40	0.36	0.36	0.21	0.19	0.20	0.10	0.09	0.10

Table 3-7. *Values of the seismic active earth pressure coefficient given by the upper-bound method for log-sandwich failure mechanisms (Chang, 1981 as quoted by Chen & Liu, 1990).*

β	ϕ	20°			30°			40°			50°		
	δ	0°	10°	20°	0°	15°	30°	0°	20°	40°	0°	25°	50°
-30°		1.74	2.00	2.29	2.15	2.82	3.77	2.71	4.23	7.45	3.48	7.39	20.18
-15°		1.78	2.16	2.56	2.38	3.42	4.57	3.26	6.08	11.67	4.63	13.12	41.27
0°	$k_h = 0$	2.04	2.58	3.17	3.00	4.71	7.10	4.60	10.09	20.91	7.55	28.68	98.06
15°		2.61	3.45	4.39	4.35	7.42	11.79	7.80	19.67	43.09	15.98	75.20	267.69
30°		3.79	5.27	6.96	7.38	13.67	22.70	16.15	45.47	103.16	43.72	234.22	848.58
-30°		1.66	1.86	2.10	2.09	2.67	3.52	2.66	4.10	7.04	3.45	7.12	19.25
-15°		1.68	1.98	2.33	2.28	3.20	4.52	3.16	5.76	10.97	4.52	12.56	39.42
0°	$k_h = 0.1$	1.89	2.35	2.86	2.82	4.37	6.55	4.38	9.49	19.66	7.27	27.37	93.61
15°		2.38	3.11	3.92	4.04	6.82	10.81	7.36	18.40	40.44	15.27	71.53	255.47
30°		3.39	4.68	6.16	6.77	12.51	20.74	15.11	42.60	96.72	41.63	223.34	809.77
-30°		1.56	1.70	1.87	2.01	2.49	3.24	2.59	3.90	6.61	3.40	6.85	18.32
-15°		1.56	1.78	2.06	2.16	2.96	4.13	3.04	5.41	10.25	4.41	12.01	37.52
0°	$k_h = 0.2$	1.71	2.08	2.50	2.63	4.00	5.95	4.15	8.86	18.33	7.00	25.95	89.09
15°		2.11	2.71	3.39	3.71	6.20	9.78	6.90	17.12	37.57	14.51	67.81	243.13
30°		2.95	4.01	5.24	6.15	11.24	18.66	14.02	39.57	89.78	39.41	211.94	770.53
-30°		1.39	1.46	1.56	1.91	2.30	2.94	2.51	3.68	6.16	3.35	6.56	17.53
-15°		1.37	1.51	1.71	2.02	2.69	3.71	2.91	5.06	9.50	4.29	11.42	35.54
0°	$k_h = 0.3$	1.48	1.73	2.04	2.42	3.59	5.30	3.91	8.20	16.97	6.69	24.51	84.32
15°		1.77	2.21	2.71	3.34	5.50	8.64	6.42	15.73	34.61	13.75	64.09	230.04
30°		2.40	3.19	4.10	5.45	9.89	16.41	12.94	36.27	82.68	37.13	200.35	729.04

Table 3-8. *Values of the seismic passive earth pressure coefficient given by the upper-bound method for log-sandwich failure mechanisms (Chang, 1981 as quoted by Chen & Liu, 1990).*

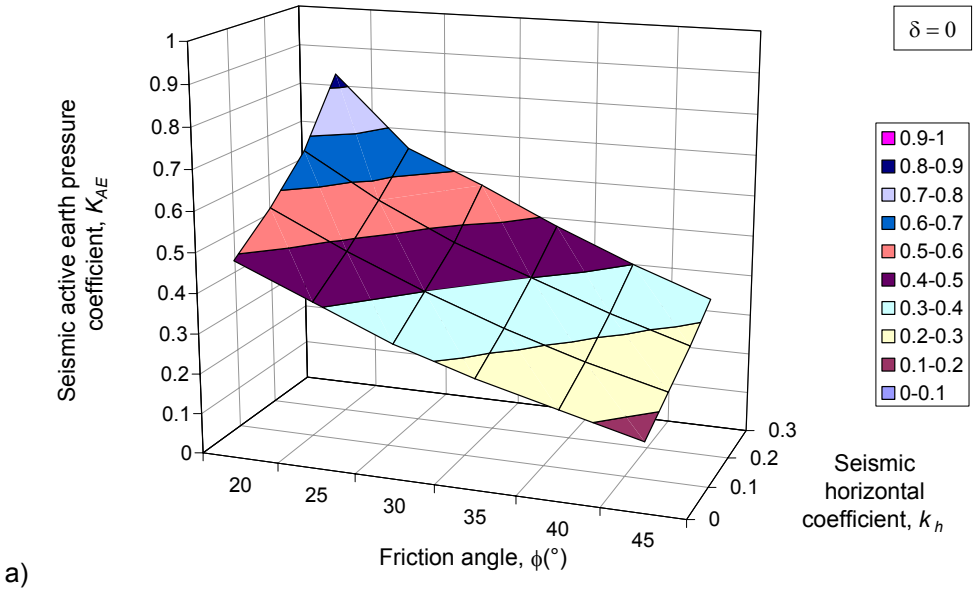

a)

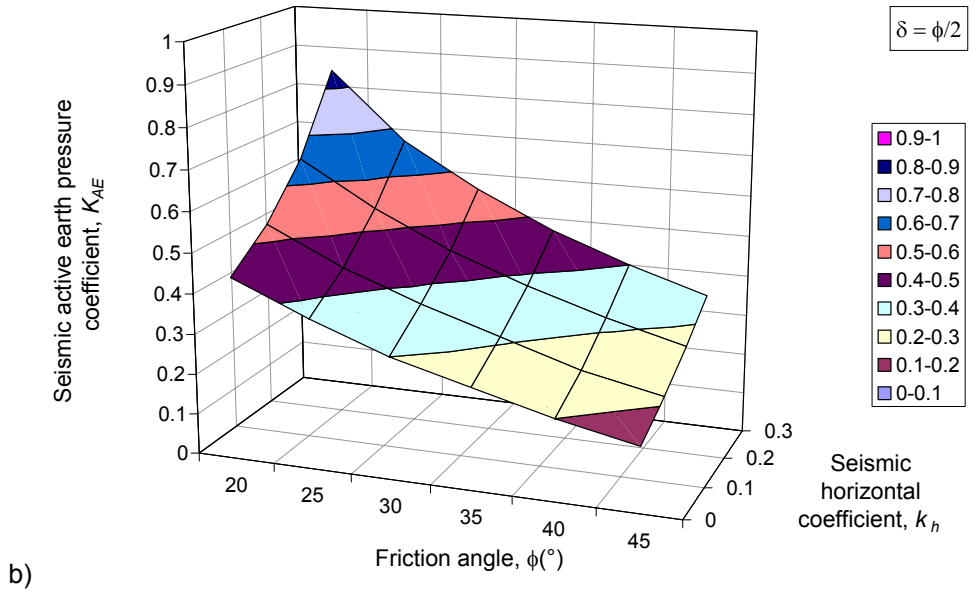

b)

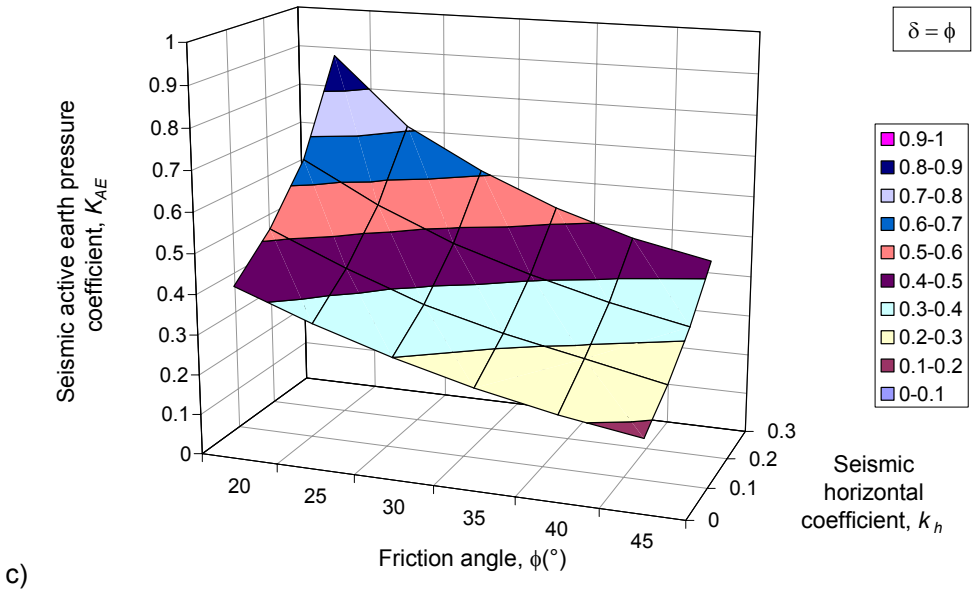

c)

Figure 3-19. *Seismic active earth pressure coefficients for a horizontal backfill sustained by vertical walls (Chang, 1981, as quoted by Chen & Liu, 1990): a) δ=0; b) δ=ϕ/2; c) δ=ϕ.*

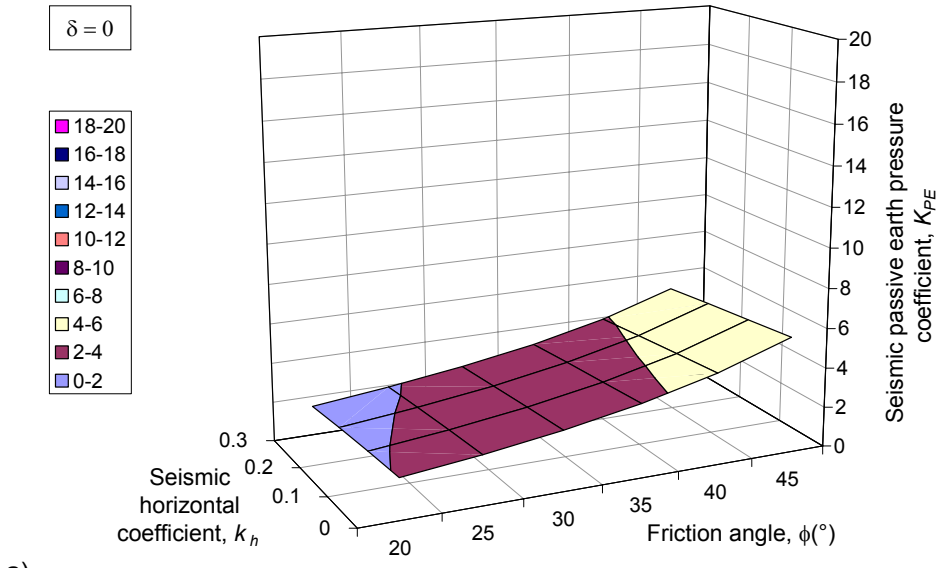

a)

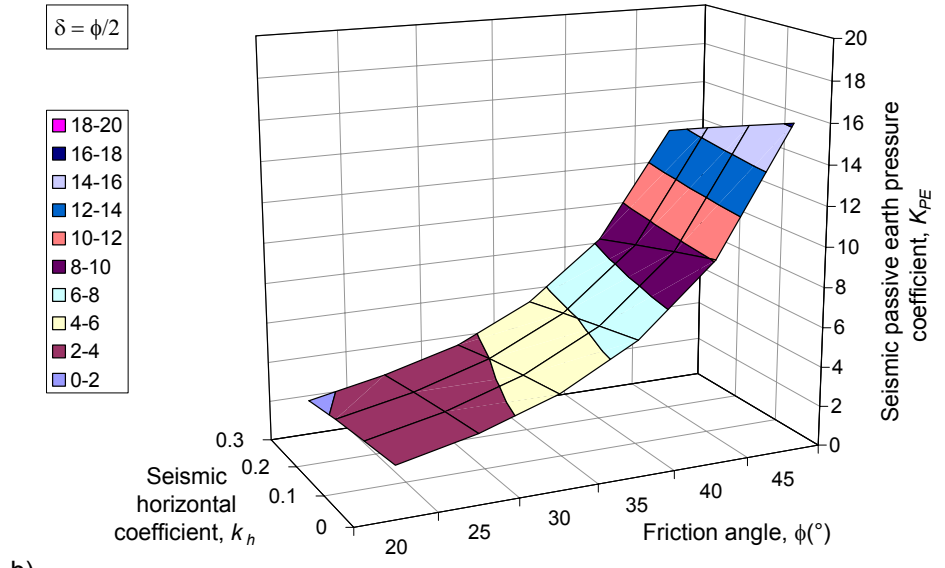

b)

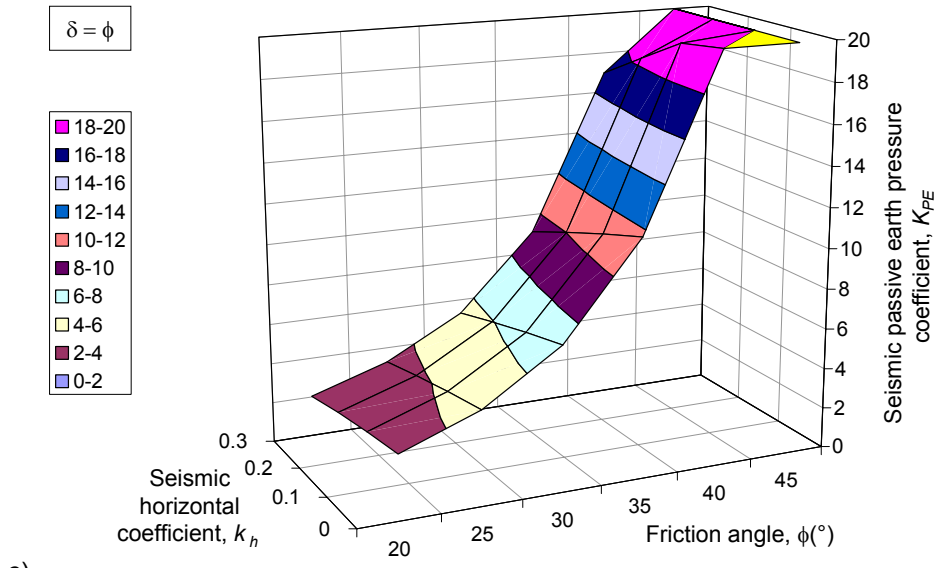

c)

Figure 3-20. *Seismic passive earth pressure coefficients for a horizontal backfill sustained by vertical walls (Chang, 1981, as quoted by Chen & Liu, 1990): a) δ=0; b) δ=ϕ/2; c) δ=ϕ.*

3.2.2.2 Lower bound solution.

Consider a soil surface, sloping at an angle ε with respect to the horizontal, subjected to the vertical body force γ, due to gravity, and to the horizontal body force $k_h\gamma$, which represents the seismic coefficient (positive assumed if the inertia force is towards the backfill). In order to compute the passive resistance on a vertical wall of roughness δ, imagine transforming the problem geometry trough a rigid rotation θ, given by

$$\theta = \tan^{-1} k_h \qquad (3\text{-}37)$$

θ represents the obliquity of the body force per unit volume in the presence of seismic action. Please note that the presence of a vertical component of the inertia forces could be taken into account by assuming

$$\theta = \tan^{-1} \frac{k_h}{1 \pm k_v} \qquad (3\text{-}38)$$

where k_v is the coefficient of vertical acceleration.

The problem of deriving the passive resistance acting on a rough vertical wall in seismic conditions can be dealt with the wall tilted from the vertical by the angle θ and interacting with a backfill of slope ε*= ε – θ. The resulting vertical body force is represented by the vector $\gamma^* = \gamma\sqrt{1+k_h{}^2}$, which can be thought of as a properly scaled gravity body force (in the presence of vertical acceleration it would be $\gamma^* = \gamma\sqrt{(1 \pm k_v)^2 + k_h{}^2}$.

As in static conditions, two regions can be considered, one placed near to the wall in which the stress state is affected from the soil-wall friction and one with the half space stress conditions, divided by a fan of stress discontinuities. By determining the shift between the two extreme Mohr circles of the stress states in the two regions for this problem geometry, Lancellotta (2007) has deduced a closed form for the seismic passive earth pressure coefficient K_{PE}.

$$K_{PE} = \left[\frac{\cos\delta}{\cos(\varepsilon-\theta)-\sqrt{\sin^2\phi-\sin^2(\varepsilon-\theta)}}\cdot\left(\cos\delta+\sqrt{\sin^2\phi-\sin^2\delta}\right)\right]e^{2\theta\tan\phi} \qquad (3\text{-}39)$$

where

$$2\theta = \sin^{-1}\left(\frac{\sin\delta}{\sin\phi}\right)+\sin^{-1}\left[\frac{\sin(\varepsilon-\theta)}{\sin\phi}\right]+\delta+(\varepsilon-\theta)+2\theta \qquad (3\text{-}40)$$

It is useful to remember that the values given by the equation (3-39) represent the normal components to the vertical wall of the seismic passive coefficients. The total earth pressure coefficients can be obtained dividing for cosδ the results of the relationship.

Figure 3-21 shows the graphical representations of the seismic passive earth pressure coefficients evaluated with the lower bound method for vertical walls retaining a horizontal backfill.

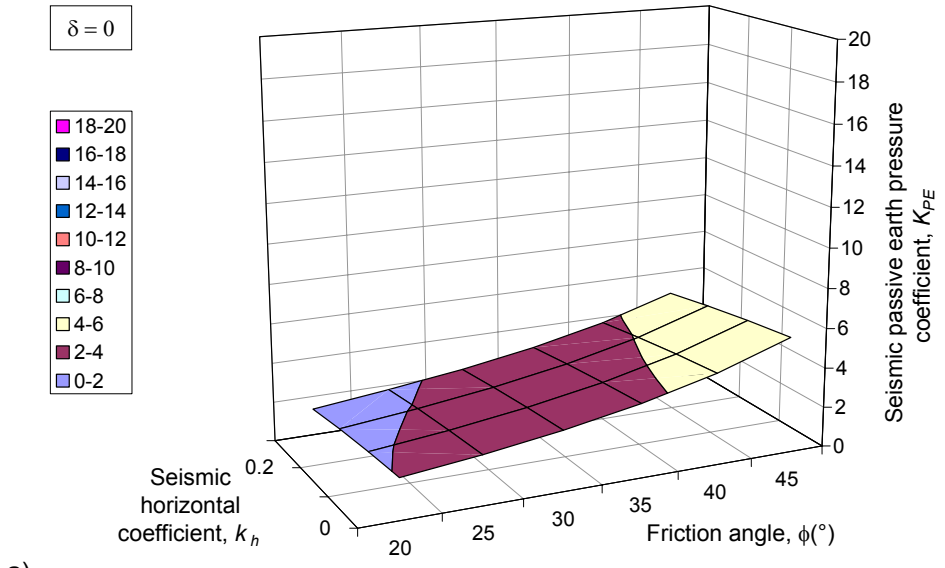

a)

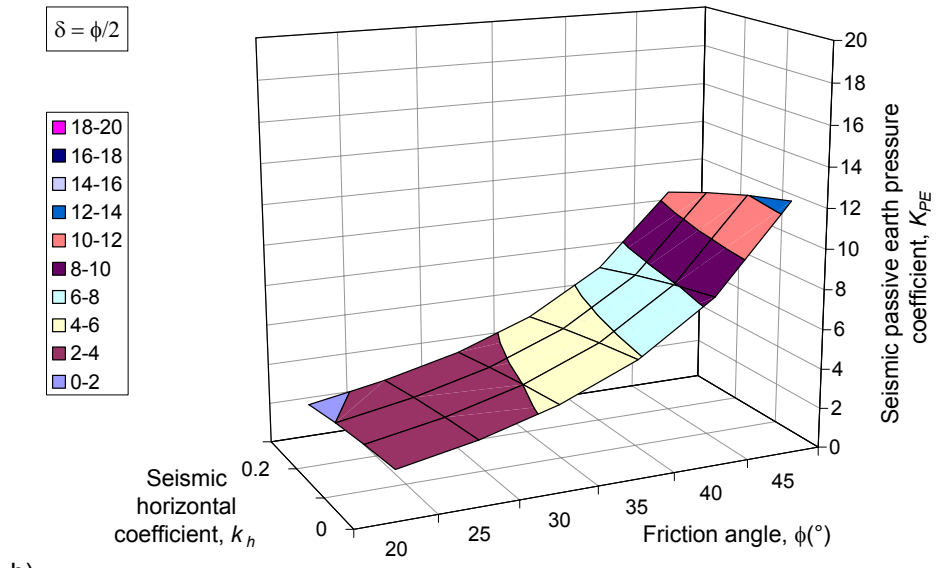

b)

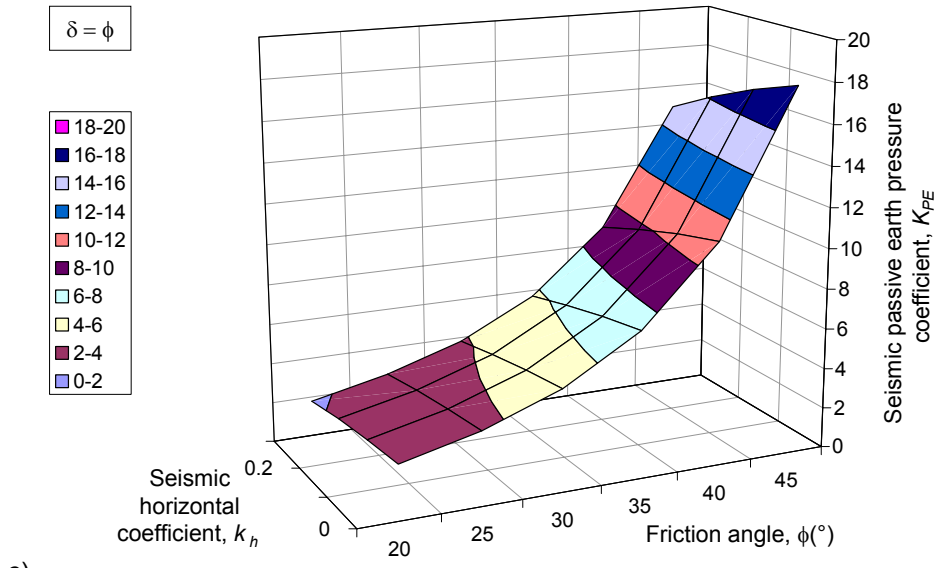

c)

Figure 3-21. *Seismic passive earth pressure coefficients for a horizontal backfill sustained by vertical walls (Lancellotta, 2007): a) δ=0; b) δ=ϕ/2; c) δ=ϕ.*

3.2.3 Comparisons between the different seismic methods.

In Figure 3-22 and Figure 3-23 the values calculated with the different methods previously recalled of the normal components of the seismic active and passive earth pressure coefficients exerted on vertical walls by horizontal backfills are compared.

For the active case, the K_{AEn} values obtained by limit equilibrium and the limit analysis methods are practically identical. This is due to the fact that, when the wall is approximately vertical and the slope angle of the backfill is larger than zero, the most critical failure is practically planar.

For the passive case, the most critical sliding surface is much different from a planar surface as is assumed in the M-O analysis. The K_{PEn} values are seriously overestimated by the M-O method. They are, in most cases, higher than those obtained by the limit analysis. This is especially the case when the wall is rough and the angle of wall repose is large. The condition $\phi = \delta = 40°$ carries out very high K_{PEn} values larger than 20, unreported in Figure 3-23c. For smooth walls, the potential sliding surface is practically planar and the different methods give almost identical results.

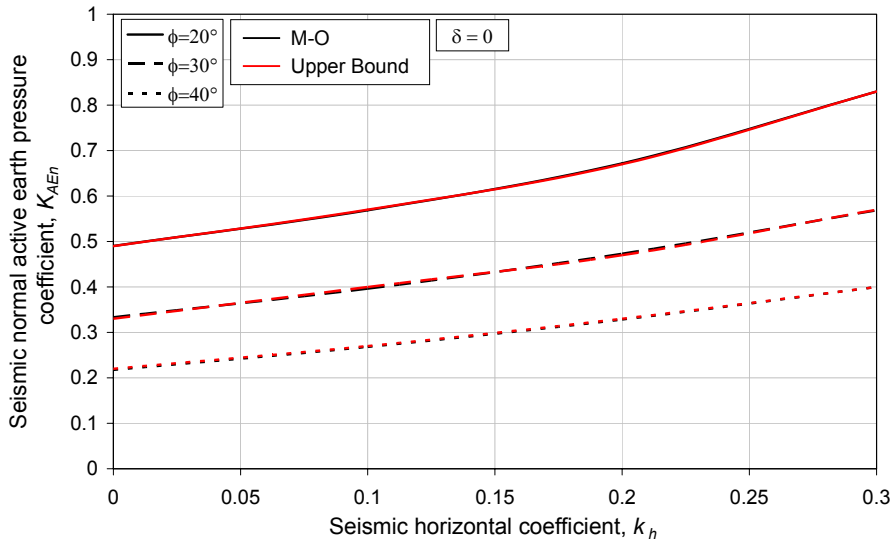

a)

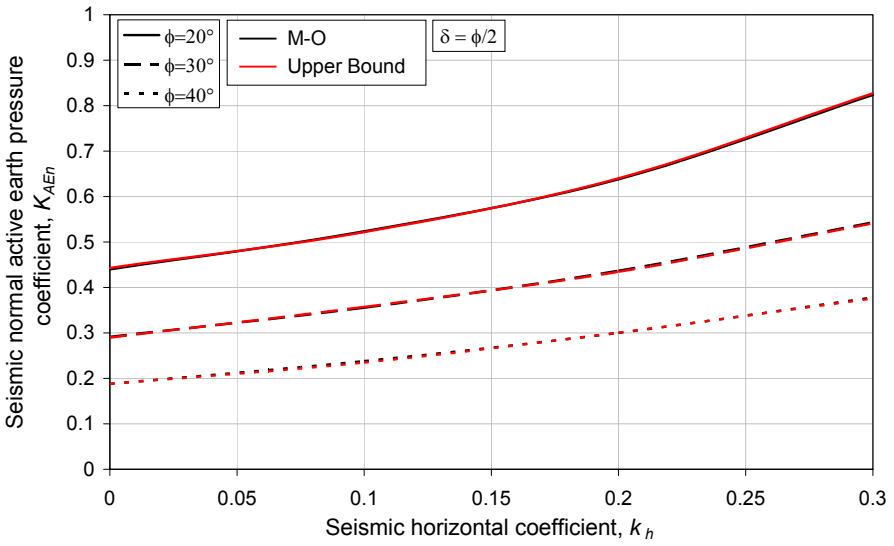

b)

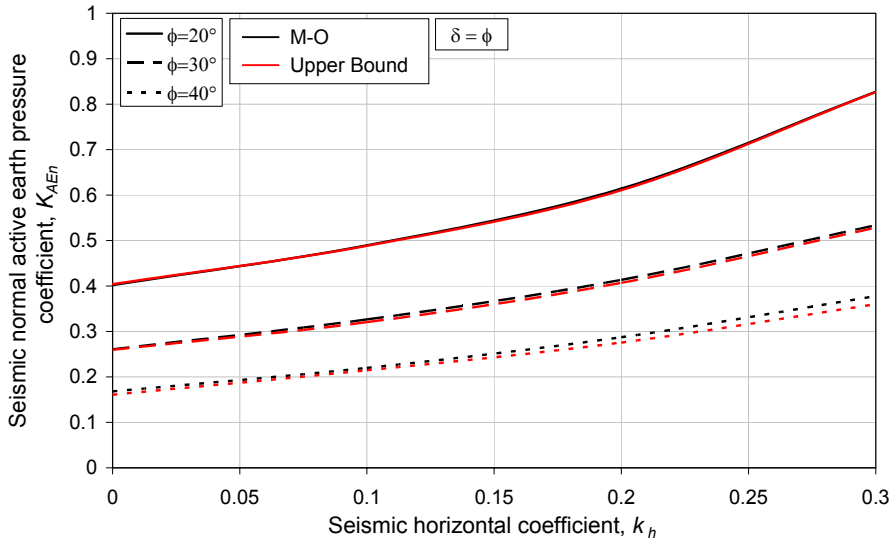

c)

Figure 3-22. *Comparisons between the normal components of the active earth pressure coefficients given by the various methods for horizontal backfills sustained by vertical walls: a) δ=0; b) δ=ϕ/2; c) δ=ϕ.*

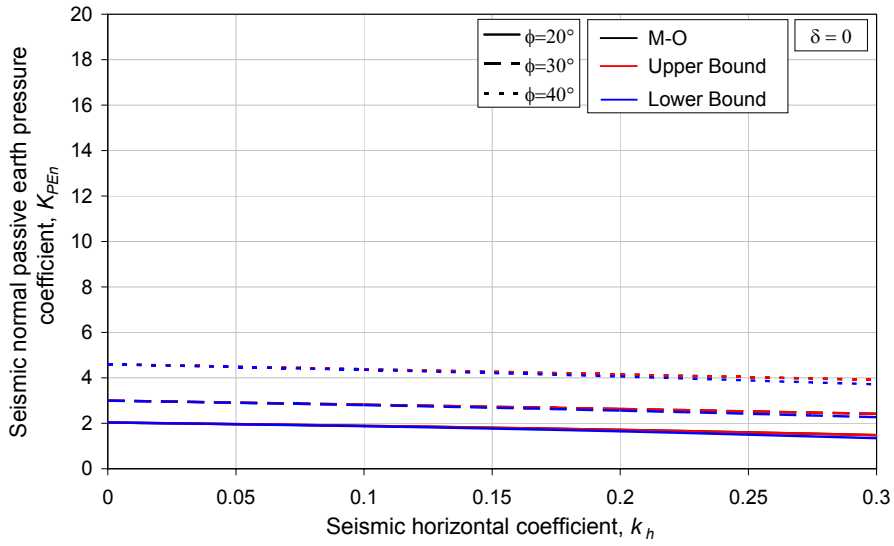

a)

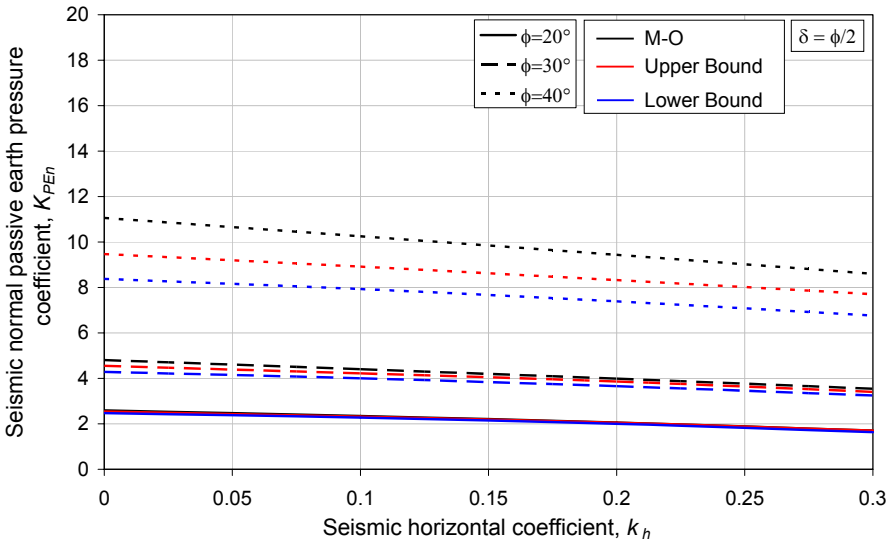

b)

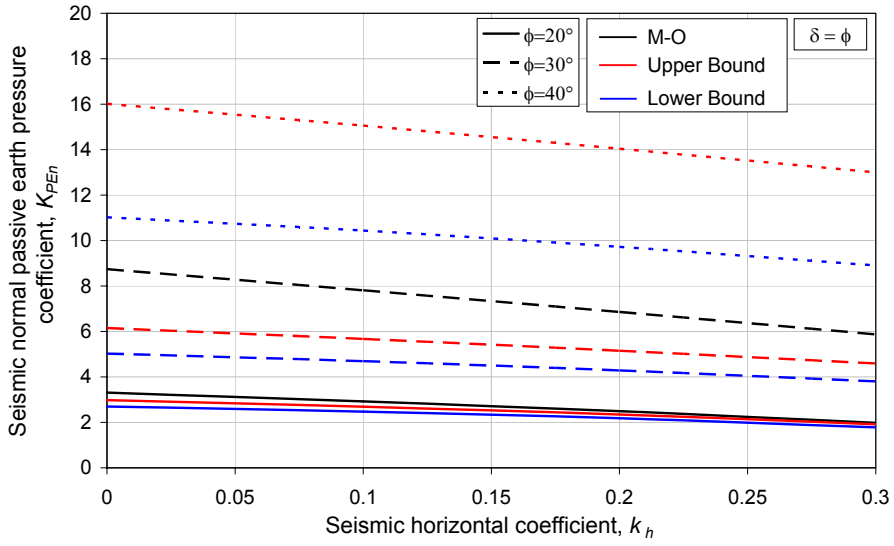

c)

Figure 3-23. *Comparisons between the normal components of the passive earth pressure coefficients given by the various methods for horizontal backfills sustained by vertical walls: a) δ=0; b) δ=ϕ/2; c) δ=ϕ.*

3.3 EFFECTS OF WATER ON WALL PRESSURES.

The procedures for estimation of seismic loads on retaining walls described in the preceding sections have been limited to cases of dry backfills. Most retaining walls are designed with drains to prevent water from building up within the backfill. This is not possible for instance for retaining walls in waterfront areas, where most earthquake-induced wall failures have been observed.

The presence of water plays a strong role in determining the loads on waterfront retaining walls both during and after earthquakes. Water outboard of a retaining wall can exert dynamic pressures on the face of the wall. Water within a backfill can also affect the dynamic pressures that act on the back of the wall. Proper consideration of the effects of water is essential for the seismic design of retaining structures, particularly in waterfront areas. Since few waterfront retaining structures are completely impermeable, the water level in the backfill is usually at approximately the same level as the free water outboard of the wall. Backfill water levels generally lag behind changes in outboard water level – the difference in water level depends on the permeability of the wall and the backfill and on the rate at which the outboard water level changes.

The total water pressures that act on retaining walls in the absence of seepage within the backfill can be divided in two components: hydrostatic pressure, which increases linearly with the depth and acts on the wall before, during and after the earthquake shaking, and hydrodynamic pressure, which results from the dynamic response of the water itself.

3.3.1 Water outboard of wall.

Hydrodynamic water pressure results from the dynamic response of a body of water. For retaining walls, hydrodynamic pressures are usually estimated from Westergaard's solution (Westergaard, 1931) for the case of a vertical, rigid dam retaining a semi-infinite reservoir of water that is excited by harmonic, horizontal motion of its rigid base. Westergaard showed that the hydrodynamic pressure amplitude increased with the square root of water depth when the motion is applied at a frequency lower than the fundamental frequency of the reservoir, $f_0 = V_P/4H$, where V_P is the P-wave velocity of water (about 1400 m/sec) and H is the depth of water in the reservoir (the natural frequency of a 10m-deep reservoir, for example, would be over 35 Hz, well above the frequencies of interest for earthquakes). Westergaard computed the amplitude of the hydrodynamic pressure as:

$$p_w = \frac{7}{8}\frac{a_h}{g}\gamma_w\sqrt{z_w H} \qquad (3\text{-}41)$$

The resultant hydrodynamic thrust is given by:

$$P_w = \frac{7}{12}\frac{a_h}{g}\gamma_w H^2 \qquad (3\text{-}42)$$

The total water pressure on the face of the wall is the sum of the hydrostatic and hydrodynamic water pressures. Similarly, the total lateral thrust due to the water is equal to the sum of hydrostatic and hydrodynamic thrusts.

Another important consideration in the design of a waterfront retaining wall is the potential for rapid drawdown of the water outboard of the wall. Earthquakes occurring near large bodies of water often

induce long-period motion of the water, such as tsunamis or seiches, that cause the water surface to move up and down. While the upward movements of water outboard of a retaining wall will generally tend to stabilize the wall (assuming that it does not rise above the level of the top of the wall), downward movements can create a destabilizing rapid drawdown condtions. When liquefiable soils exist under relatively high levels of initial shear stress, failures can be triggered by very small changes in water level. Such failures, can originate in the soils adjacent to or beneath the retaining structure rather than in the backfill.

3.3.2 Water in backfill.

The presence of water in the backfill behind a retaining wall can influence the seismic loads that act on the wall in three ways:

1. by altering the inertial forces within the backfill
2. by developing hydrodynamic pressures within the backfill
3. by allowing excess pore water pressure generation due to cyclic straining of the backfill soils.

The inertial forces in saturated soils depend on the relative movement between the backfill soil particles and the pore water that surrounds them. If, as is usually the case, the permeability of the soil is small enough (typically $k \leq 10^{-5}$ m/sec or so) that the pore water moves with the soil during the earthquake shaking (no relative movement of soil and water, or restrained pore water conditions), the inertial forces will be proportional to the total unit weight of the soil. If the permeability of the backfill soil is very high, however, the pore water may remain essentially stationary while the soil skeleton moves back and forth (the soil particles move through the pore water in free pore water conditions). In such cases, inertial forces will be proportional to the buoyant (or submerged) unit weight of the soil. Hydrodynamic water pressures can also develop under free pore water conditions and must be added to the computed soil and hydrostatic pressures to obtain the total loading on the wall.

For restrained pore water conditions, the M-O method can be modified to account for the presence of pore water within the backfill (Matsuzawa et al., 1985). Representing the excess of pore water pressure in the backfill by the pore pressure ratio, $r_u = \Delta u/p'_0$, the active soil thrust acting on a yielding wall can be computed from equation (3-25) using:

$$\gamma = \gamma_b(1 - r_u) \qquad (3\text{-}43)$$

$$\theta = \tan^{-1}\left[\frac{\gamma_{sat} k_h}{\gamma_b(1 - r_u)(1 - k_v)}\right] \qquad (3\text{-}44)$$

An equivalent hydrostatic thrust based on a fluid of unit weight $\gamma_{eq} = \gamma_w + r_u \gamma_b$ must be added to the soil thrust. Note that as r_u approaches 1 (as it could in liquefiable backfill), the wall thrust approaches that imposed by a fluid of equivalent unit weight $\gamma_{eq} = \gamma_{sat}$. Subsequent unidirectional movement of a soil that develops high excess pore water pressures may, depending on its residual (or steady state) strength, cause dilation with accompanying pore water pressure reduction and strength gain.

Soil thrusts from partially submerged backfills may be computed using an average unit weight based on the relative volumes of soil within the active wedge that are above and below the phreatic surface (Figure 3-24):

$$\bar{\gamma} = \lambda^2 \gamma_{sat} + \left(1 - \lambda^2\right)\gamma_d \qquad (3\text{-}45)$$

Again, the hydrostatic thrust (and hydrodynamic thrust, if present) must be added to the soil thrust.

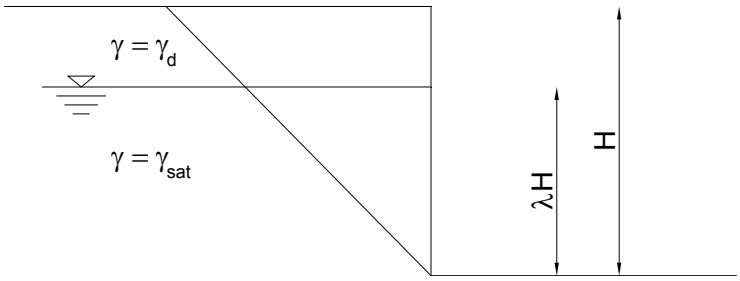

Figure 3-24. *Geometry and notation for partially submerged backfill.*

4 STATIC DESIGN OF EMBEDDED RETAINING WALLS.

Embedded walls are relatively thin walls of steel, reinforced concrete or timber, eventually supported by anchorages, struts and/or passive earth pressure (EN1997-1). The bending capacity of such walls plays a significant role in the support of the retained material while the role of the weight of the wall is usually considered to be insignificant. Examples of such walls include: cantilever steel sheet pile walls, anchored or strutted steel or concrete sheet pile walls, diaphragm walls, etc., as described in Chapter 2.
Limit equilibrium is one of most widespread design method for the analysis of embedded retaining structures. In this procedure, the wall is assumed rigid, the soil has a rigid-perfectly plastic behaviour and the pressures deriving form the interaction depend on the expected movements of the wall. The kinematical mechanism is affected from the constraints applied on the wall. In this section, the various type of embedded retaining walls in relation to the kinematical restraints are separately treated

4.1 FREE CANTILEVER WALLS.

A cantilever sheet pile retaining wall consists of a vertical structural element embedded in the ground below the retained material. The upper part of the wall provides a retaining force due to the wall stiffness and the embedment of the lower part. The embedded cantilever wall obtains its ability to resist the pressure of the retained soil by developing resisting earth pressures on the embedded portion of the wall. Embedded cantilever sheet pile retaining walls are frequently used for temporary and permanent support of excavations up to about 4-5 m high.
The distribution of earth pressure on the embedded part of the wall is dependent on the complex interaction between the wall movement and the ground. Many methods for analysis and design of embedded cantilever walls have been proposed and these have been reviewed by Bica & Clayton (1989). Each method makes various assumptions concerning the distribution of earth pressure on the wall and the deflection or wall movement. Most of the methods follows the limit equilibrium approach based on the classical limiting earth pressure distributions. Model studies on embedded walls have been performed by Rowe (1951), Bransby & Milligan (1975) and Lyndon & Pearson (1984). Bica & Clayton (1992) have produced some empirical charts for the design of cantilever walls.
King (1995) suggested an analytical limit equilibrium approach for dry cohesionless soil, involving different assumptions from the previous methods. One of the assumptions involves the location of the point, near the bottom of the wall, of zero net pressure by means of an empirically determined parameter. Based on the results of centrifuge tests, the author makes a recommendation for an appropriate value of this empirical parameter that, referring to the notation introduced in Figure 4-3, is assumed $z' = 0.35\ d$.
The basis of the limit equilibrium methods is the prediction of the maximum height of excavation for which static equilibrium is maintained. This is known as the limiting equilibrium situation. It is therefore important to be able to accurately evaluate the earth pressure acting on each side of the wall in the limiting equilibrium condition.
The actual distribution and magnitude of earth pressure on an embedded retaining wall is dependent on the complex interaction of the wall and the soil. The general shape of the earth pressure

distribution is shown in Figure 4-1. The common limit equilibrium design and analysis methods are all based on this general shape. Each method makes different simplifications and assumptions that modify the general shape of the pressure distribution to enable a solution to be found.

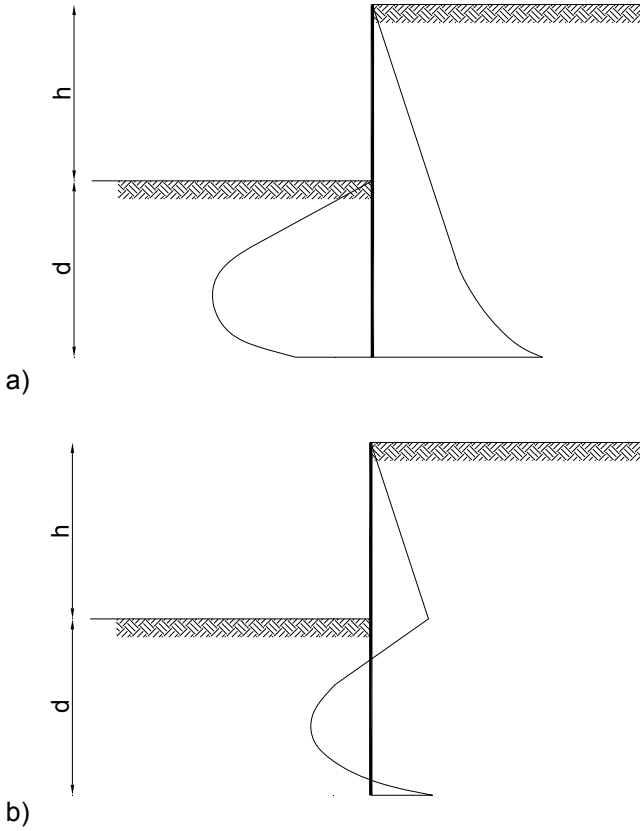

Figure 4-1. *Soil pressure distributions on an embedded cantilever wall: a) pressure distributions; b) net pressure distribution.*

The stability of the cantilever wall is guaranteed from the passive resistance of the soil in which the wall is embedded. In the limit equilibrium methods the wall movement that conducts to limit conditions is constituted by a rigid rotation around a point O placed near to the bottom of the wall. The theoretical earth pressures distributions on the wall are plotted in Figure 4-2.

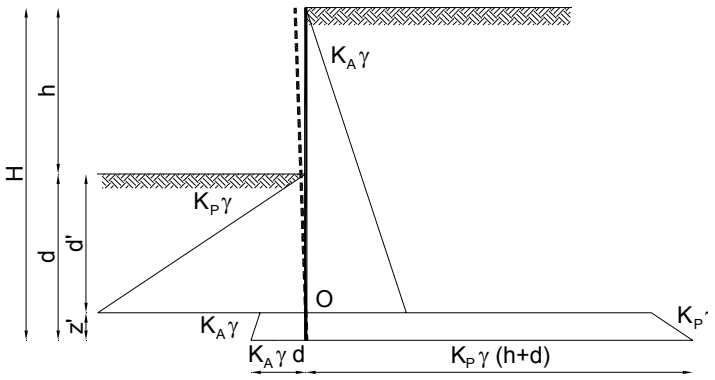

Figure 4-2. *Theoretical earth pressures distributions assumed in limit equilibrium methods.*

To eliminate stresses discontinuities in correspondence of the rotation point and to obtain a simplified shape of the pressures distributions, different simplifications and assumptions were proposed in literature. The main of which are reported in Figure 4-3.

In the first, the net pressure distribution is simplified by a rectilinear shape. It is assumed that the passive resistance below the dredge level is fully mobilized. The rotation point coincides with the zero net pressure point. At the bottom of the wall the soil strengths, active and passive, are mobilized and the net pressure assumes the values reported in Figure 4-3a.

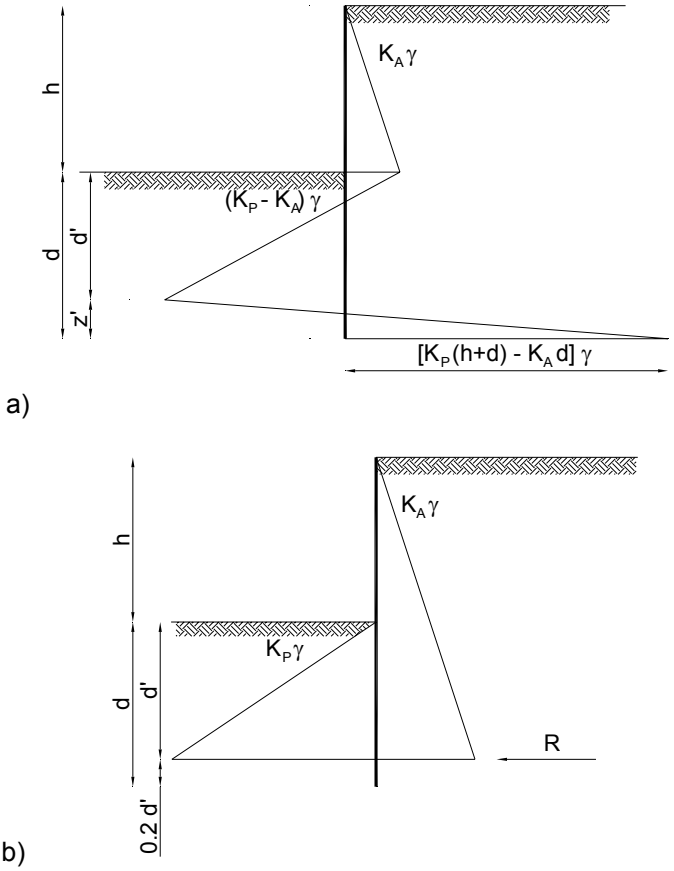

Figure 4-3. *Simplified earth pressures distributions: a) Full Method; b) Blum Method.*

The limit depth *d* can be evaluated imposing translation and moment equilibrium. In this manner, a system of two equations of second and third degree is obtained and the two unknowns, the depth of the point of the inversion of pressures *z'* and the limit depth of embedment *d*, may be calculated using:

$$\frac{z'}{h} = \frac{\frac{K_P}{K_A}\left(\frac{d}{h}\right)^2 - \left(1+\frac{d}{h}\right)^2}{\left(\frac{K_P}{K_A}-1\right)\left(1+2\frac{d}{h}\right)} \qquad (4\text{-}1)$$

$$\frac{z'}{h} = \sqrt{\frac{\frac{K_P}{K_A}\left(\frac{d}{h}\right)^3 - \left(1+\frac{d}{h}\right)^3}{\left(\frac{K_P}{K_A}-1\right)\left(1+2\frac{d}{h}\right)}} \qquad (4\text{-}2)$$

The second method, commonly used in U.K. and described in Padfield & Mair (1984), assumes that the net pressure distribution below the point of rotation can substituted with the net force R applied at a distance *z'* = 0.2·*d'* from the bottom of the wall. Writing the moment equilibrium around the point C, one has an equation of the third degree with the single unknown *d*:

$$d = \frac{1.2h}{\sqrt[3]{K_P / K_A} - 1} \qquad (4\text{-}3)$$

The main problem for the design of embedded walls is then the right choice of the earth pressure coefficients K_A and K_P when the soil-wall friction δ would be considered. It is well-recognized that the Coulomb theory provides unrealistic values of the passive earth pressure coefficient when δ > ϕ'/2. Different suggestions can be found in the literature (Padfield & Mair, 1984; Terzaghi, 1954; Teng, 1962). Since knowledge on this field is limited, in the current practice is commonly adopted δ_A = 2/3 ϕ' for the active case and δ_P = 0, for the passive case. These values are the same that the European codes impose (EN1997-1; EN1998-5). In this manner, passive resistance of soil on the dredge side of reinforced concrete walls, realized with piles or diaphragm, is largely underestimated. Padfield & Mair (1984) state that reasonable values of the soil-wall friction for the calculation of the earth pressure coefficients are δ_A = 2/3 ϕ' and δ_P = 1/2 ϕ'.

Bica & Clayton (1992) have collected a series of experimental data of collapse of embedded walls and have proposed an expression for the preliminary design in simple soil conditions:

$$\frac{d}{h} = FS \cdot \frac{2}{3} e^{-\left[\frac{\phi' - 30°}{18}\right]} \qquad (4\text{-}4)$$

In Figure 4-4, the relationship (4-4) for the case of limit conditions is compared with a series of numerical and experimental results of failure taken from the literature. It can be seen the good agreement between the relationship and the numerical and experimental data given by the different authors.

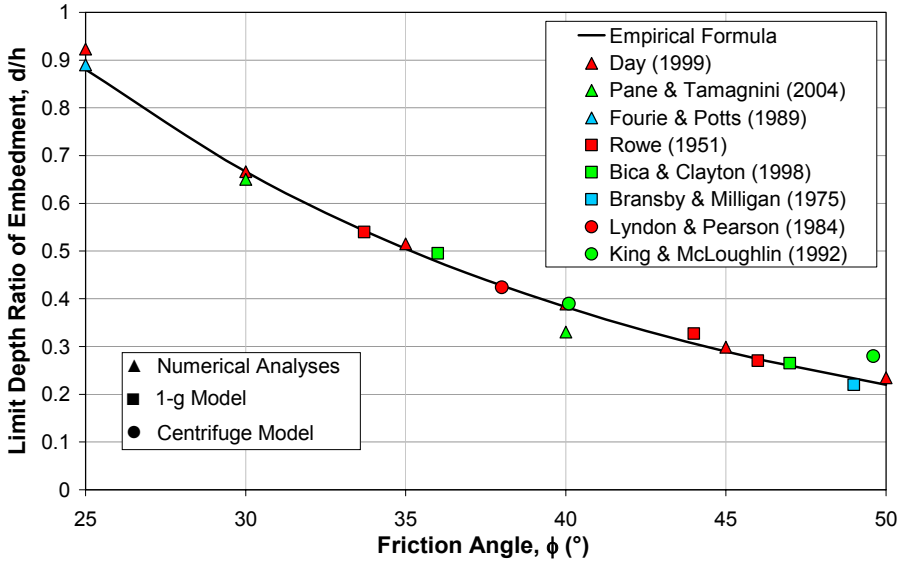

Figure 4-4. *Experimental and numerical limit depth ratios of embedment at collapse for free embedded walls.*

Adopting the Coulomb and Lancellotta theories for the evaluation of the active and passive earth pressure coefficients K_A and K_P, respectively, and assuming the soil-wall friction values suggested by Padfiled & Mair (1984), the full and Blum methods give limit depth ratios of embedment in relation to the soil friction angle ϕ' plotted in Figure 4-5. In the same Figure the *d/h* ratios at failure evaluated with the two limit equilibrium methods and adopting the soil-wall friction angles currently utilized in the design are reported.

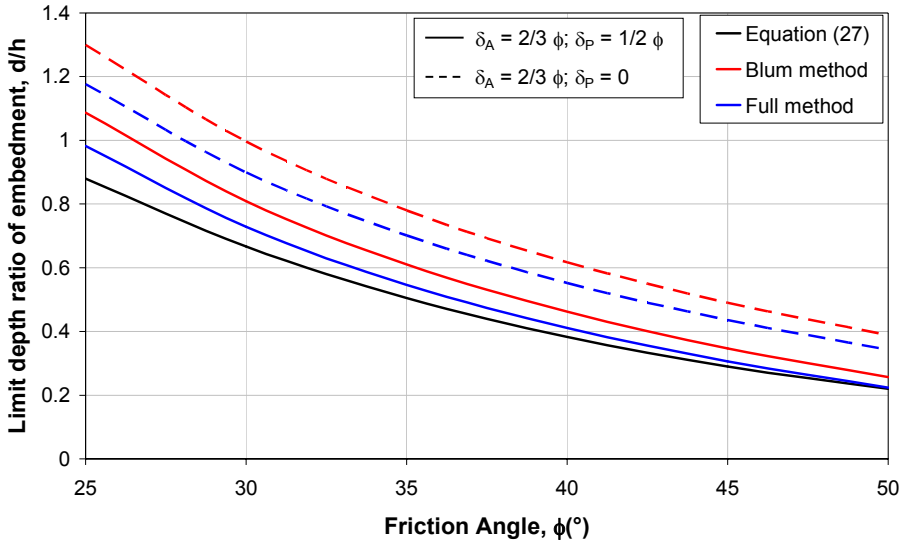

Figure 4-5. *Limit depth ratios of embedment at collapse for free embedded walls computed with limit equilibrium methods.*

It can be noted the large overestimation of the needed depth of embedment *d* when the soil-wall friction is not considered for the calculation of the passive resistances. The Blum method gives more conservative values than the full method for which, if it is applied by adopting Padfield & Mair (1984) indications, the results are close to those experimentally and numerically estimated.

Five methods are used in design to incorporate a factor of safety *FS* against collapse. These involve increasing embedment depth, reducing the strength parameters, reducing the passive pressure coefficient, reducing the net passive pressure or reducing net available passive pressure (Padfield & Mair, 1984). However, no universal procedure has emerged. Major details can be found in Clayton et al. (1993)

The recent European and Italian codes propose the use of the partial factors of safety that increase the magnitude of the actions and reduce the strength of the structure. In particular, for retaining walls, they impose the decreasing of the soil strength parameters, cohesion c' and tangent of the friction angle tanϕ', for effective stress analyses, and undrained shear strength c_u, for total stress analyses. This assumption, for embedded retaining walls, produce a dual effect on the construction safety: an increase of the actions (active earth thrust) and a decrease of the strengths (passive earth thrust).

The maximum bending moment M_{max} acting on the wall depends to the soil and wall properties and to the depth of embedment *d*, for a given retaining height *h*.

Bica & Clayton (1992), on the basis of a collection of experimental results, have proposed the approximated relationship for the computation of M_{max} represented in Figure 4-6 with some numerical and experimental data published in the literature:

$$\frac{M_{max}}{\gamma h^3} = 0.095 \cdot e^{-\left[\frac{\phi'-30°}{16}\right]} \cdot e^{\frac{\left[\frac{d}{h}\frac{2}{3}\right]}{2}} \qquad (4\text{-}5)$$

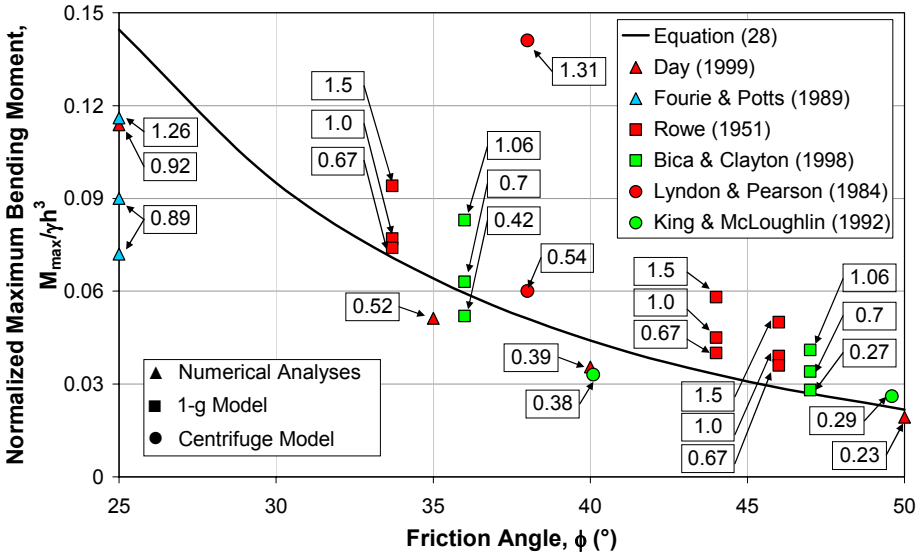

Figure 4-6. *Experimental and numerical normalized maximum bending moment for free embedded walls.*

Near to each point is reported the depth ratio *d/h*. The values given by Equation (4-5) are often conservative when compared with those corresponding to limit conditions for the wall. It can be seen the increase of bending moment with depth of embedment for a fixed value of friction angle. This fact contrasts the design recommendations that M_{max} should be evaluated for a safety factor equal to 1. This factor should be greater than 1 when M_{max} is computed.

Figure 4-7 shows the comparisons between the normalized maximum bending moment $M_{max}/\gamma h^3$ computed with Equation (4-5) and those obtained by the limit equilibrium method with the following expression:

$$M_{max} = \frac{\gamma}{6}\left[K_A (h+x)^3 - K_P x^3\right] \qquad (4\text{-}6)$$

where *x* is the depth from the dredge level in which the shear force is zero:

$$\frac{x}{h} = \frac{1}{\sqrt{K_P/K_A} - 1} \qquad (4\text{-}7)$$

The values obtained by assuming the soil-wall frictions suggested by Padfield & Mair (1984) are lightly underestimated respect to those predicted with the empirical relationship (4-5), while, adopting δ_A = 2/3 ϕ' and δ_P = 0, limit equilibrium provides realistic maximum bending moment at collapse. It should be remembered that, if a safety factor is adopted on the design of the depth of embedment, the actual depth ratio *d/h* should be utilized for the estimation of M_{max}.

The Equations previously recalled are valid for dry homogeneous soils with constant values of K_A and K_P. Limit equilibrium of embedded retaining walls in layered saturated soils is commonly studied by using a hybrid approach in which active and passive horizontal effective stresses are computed

multiplying vertical effective stresses by active and passive earth pressure coefficients given by the theories.

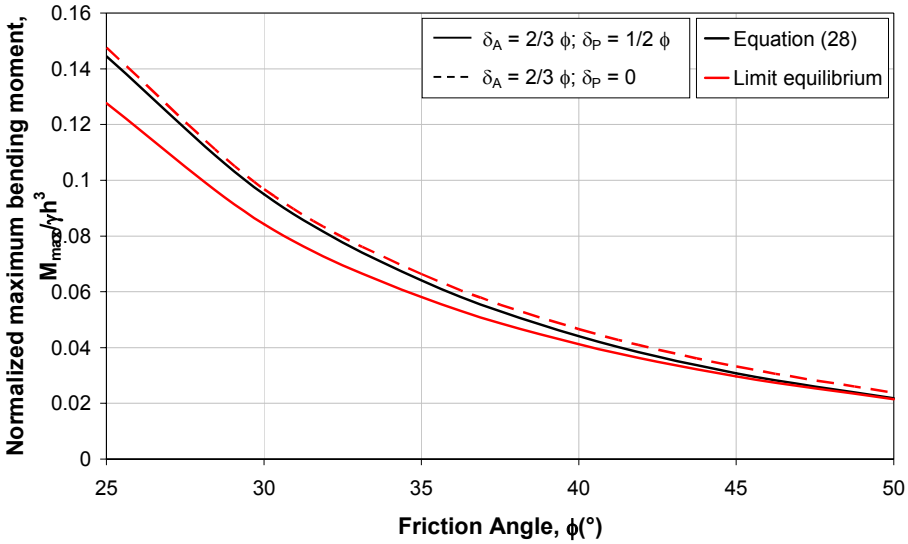

Figure 4-7. *Normalized maximum bending moment for free embedded walls at collapse computed with limit equilibrium method.*

4.2 ANCHORED SHEET-PILE WALLS.

The possible failure modes for anchored sheet-pile walls are:

- rotation about the point at which the anchor tendon joins the sheet piling;
- failure of the wall by bending, between a relatively rigid anchor and a deeply-embedded sheet pile toe;
- failure of the anchor tendon, or of the anchor itself;
- overall rotational failure, involving not only the mass of soil which the sheeting is embedded, but also the soil around the anchor.

In practice, the point on the sheet pile wall at which the anchor is attached will normally move forward sufficiently to ensure the development of the active pressures over much of the back of the wall. Rowe (1952) has estimated that, for typical anchored sheet pile walls, the elastic yield of the anchor coble is of the order of H/1600, while the yield of the anchor block will be about H/800, where H is the height of the wall. All but the softest materials would be expected to achieve active conditions at these displacements.

A large number of methods have been proposed for the design of anchored sheet-pile walls, or "anchored bulkheads" as they are sometimes known. Many of them have fallen into disuse, either because their fundamental principles have been questioned or because their complexity has made them unpopular. Examples of methods commonly in use, in the follow are summarized.

4.2.1 Free earth support method.

According to Tschebotarioff (1973) this is the oldest and most conservative design procedure. This approach often gives an economical design with smaller depths of embedment but larger bending moments, than the fixed earth support method (see the next paragraph). Figure 4-8 shows a typical layout and the limit earth pressure distribution for an anchored sheet-pile wall.

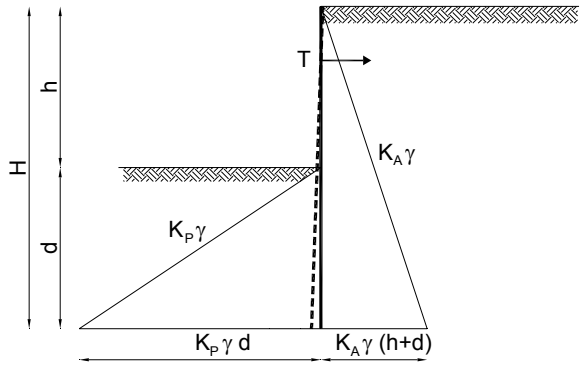

Figure 4-8. *General layout and limit earth pressure distributions for anchored sheet pile wall.*

In the free earth support method the sheets are assumed to be rigid, rotating about point T where support is provided by an underlying anchor. The depth of pile embedment is calculated on the basis of achieving moment equilibrium at the anchor level. The anchor force is then calculated on the basis of horizontal force equilibrium, and the point of maximum bending moment is determined from zero shear force on the shear force diagram. Following the work of Rowe (1952), the design bending moment used to select the sheet-pile section is obtained by reducing the maximum bending moment by a factor which depends on the relative flexibility of the sheet piling with respect to the soil.

As for the cantilever sheet pile walls, a number of different definitions of factor of safety are in use with the *free earth support method*. Clayton et al. (1993) have given a detailed summary of the suggestions.

The design process is as follows:

- determine the soil parameters for the likely height of the sheets.
- estimate tidal range, and the likely lag between the ground water level in the retained soil and in front of the wall;
- calculate the effective horizontal earth pressure using active earth pressure coefficients on the back of the wall;
- calculate the effective horizontal earth pressure using the passive earth pressure coefficients on the front of the wall – these pressures should be divided by a factor of safety of 2, if the method of the passive pressure reduction is used for the analysis;
- calculate the out-of-balance pressure distribution on the wall due to unequal water pressure on either side;
- take moments about the level at which the anchor tie is attached to the sheets, and determine the necessary depth of penetration of the sheet piling to give moment equilibrium;
- resolve horizontally to determine the force applied to the tie;

- calculate the shear force diagram for the sheets, in order to find the position of maximum bending moment – starting from the top of the wall;
- calculate the maximum bending moment at the point of zero shear force;
- in sands or gravels, calculate the relative flexibility of the sheets and the soil, and reduce the bending moment according to the Rowe formulation as presented in the following;
- increase the depth of penetration by 20% to allow for the effects of unintentional excess dredging, unanticipated local scour, and the presence of pockets of exceptionally weak material (Terzaghi, 1954);
- increase the tie force by 10% to allow for horizontal arching;
- design anchors and select tie section.

Since at the outset, the depth of penetration of the sheeting is unknown, the calculations for moment equilibrium about the anchor tie level can be only completed if a depth is assumed or the pressure distributions are expressed in terms of the unknown depth, d.

In practice it is normally easier to adopt the second approach. The condition of moment equilibrium then leads to a cubic equation. The simplest way to determine the correct value of d is by trial and error substitution, starting with a likely value.

The magnitude and the distribution of the bending moment in a sheet pile wall is affected to the its flexibility with respect to the deformability of the retained soil. Rowe (1952, 1957) carried out model tests and provided charts to allow the maximum bending moment calculated from the free earth support method to be reduced in line with his experimental findings. In theory, Rowe's reduction factors can be used for any type of soil, but Skempton (1953), mindful of the fact that they result from model tests, suggested that the amount of the reduction should be as follows:

- Sands: use 1/2 moment reduction from Rowe;
- Silts: use 1/4 moment reduction from Rowe;
- Clays: use no moment reduction.

Rowe identified the stiffness of the sheet piling as:

$$\rho = \frac{H^4}{EI} \qquad (4\text{-}8)$$

where H is the full length of sheet piling (i.e. retained height plus depth of embedment), E is the Young modulus and I the moment of inertia of the sheet piling.

Figure 4-9 shows the Rowe's moment reduction curves for sand. To use these curves, select the relevant soil condition and the wall height, plot a curve of bending moment *vs.* log (ρ) by multiplying the maximum free earth support bending moment for the particular wall by the values of M/M_{max} for different ρ in Figure 4-9. Next select various possible sheet pile sections and calculate log (ρ) and $M_{max} = f\ I\ /\ y$ for each, where f is the permitted maximum stress of the pile material, and y is the distance from the neutral axis to the edge of the section.

Plot the position of each of these sections on the curve. Sections giving points above the operating curve are wasteful, while those below the curve will be overstressed. Ideal sections will fall directly on the curve.

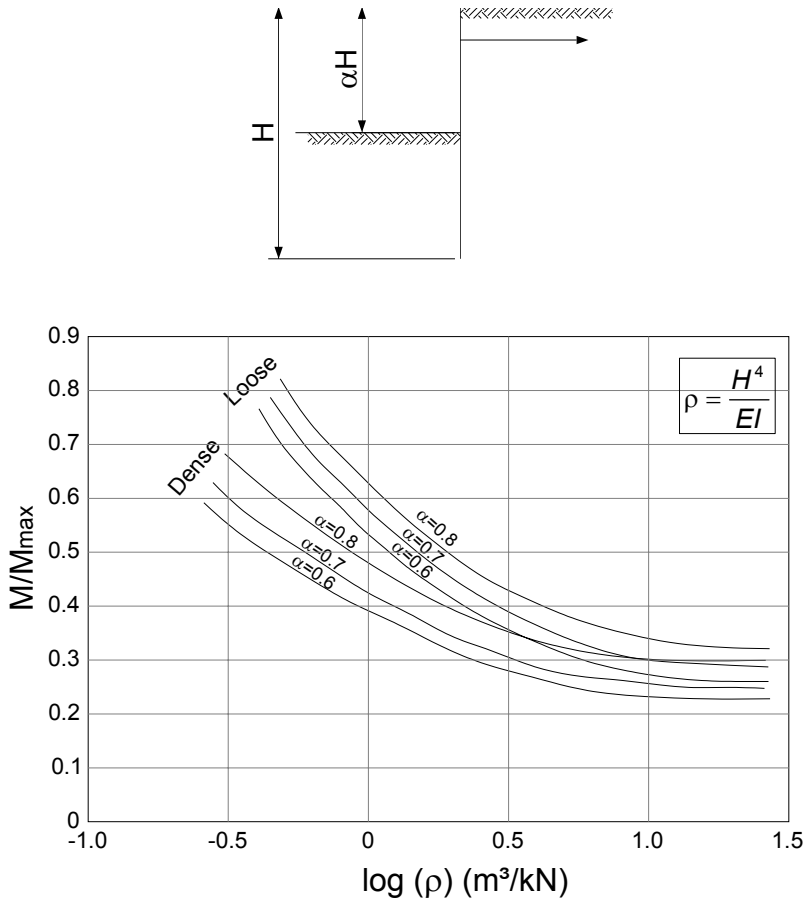

Figure 4-9. *Moment reduction factors proposed by Rowe (1952).*

4.2.2 Fixed earth support method.

This method is derived from the work of Blum (1931). The sheet piling is considered flexible, but driven to sufficient depth that it may be considered fixed at its toe. Blum's general method deals with rigidly and flexibly anchored walls, and with cantilever walls, as it is previously shown. In these methods the stresses on the wall immediately above the toe are replaced by a single force some distance up the wall and the sheet piling is considered to be held vertical at this point. The depth of penetration of the sheeting is found by repetitive calculation until the displacement at the anchor level is correct relative to the point of fixity (at the toe). For routine design the anchor is assumed to be unyielding, and this relative displacement must therefore be zero. Unless carried out by computer, this technique is tedious; therefore a number of simplifications are in common use.

The general method used for fixed earth support design is the "elastic line method". In this method the position of the point C, below of which the sheet pile wall is fixed, is assumed, and the deformation of the sheet pile is assumed to become tangential to the vertical at this point .Successive integration with respect to the depth of the net total pressure diagram leads to the shear force diagram, the bending moment diagram, the slope diagram and the deflection diagram. The position of point C is adjusted until the deflection of the anchor (point T) relative to point C is zero.

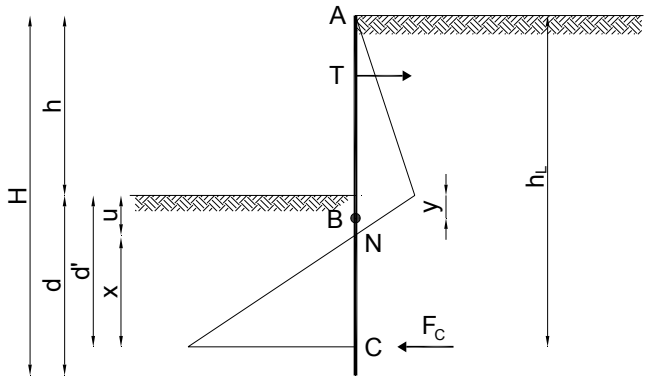

Figure 4-10. *Design of anchored sheet pile by the fixed earth support method.*

From this necessary depth of sheeting may be obtained, since Blum demonstrated that the total required depth of penetration is:

$$d = u + (1.05 \text{ to } 1.20)x \qquad (4\text{-}9)$$

Typically, for convenience, the total required depth of penetration is taken as:

$$d = 1.20(u + x) \qquad (4\text{-}10)$$

As in Tschebotarioff (1973), for the simplified equivalent beam method to be described below, but the actual required depth can be found from:

$$d = u + x + \frac{F_C}{2\gamma' h_L (K_P \cos\delta_P - K_A \cos\delta_A)} \qquad (4\text{-}11)$$

where *u* and *x* are defined in Figure 4-10, γ' is the average buoyant density ($\gamma - \gamma_W$) between the top of the sheet-pile wall and the point C, F_C is the replacement force at C, $K_P\cos\delta_P$ and $K_A\cos\delta_A$ represent the components of earth pressure normal to the wall, h_L is the height of the wall (including embedment of the point C), plus an allowance of $q/K_A\gamma$ for any surcharge q imposed at the top of the wall.

Although in the past the elastic line method has been solved by hand calculation, or graphically, it is now considered too time-consuming for routine use. It is, however, a relatively simple task to program a desktop computer to provide these solutions.

"Blum's equivalent beam method" (Blum, 1931) uses the same simplifying assumptions with regard to the stresses at the toe of the pile as were used for the elastic line method above – the stresses at the pile toe are replaced by a single force some distance above the toe. By carrying out example calculations on uniform soil profiles, Blum was able to establish the relationship between the depth to the point of sheet pile contraflexure (*y*) (where the bending moment is zero – point B in Figure 4-10) and the free height of the wall (*h*, from the dredge level to the top of the wall), as follows

Effective angle of friction of soil, ϕ'	Ratio (depth to point of contraflexure)/(free height of wall) (*y*/*h*)
20°	0.23
25°	0.15
30°	0.08
35°	0.03
40°	-0.007

Table 4-1. *Relationship between the depth to the point of the sheet pile contraflexure (y) and the free height of the wall (h) (Blum, 1931, as quoted in Clayton et al. 1993).*

It is reported by Tschebotarioff (1973) that these values were based on the use of Rankine value for K_A ($\delta_A = 0$) and $K_P = 2/K_A$. Blum is supposed to have used this value for the passive earth pressure coefficient, not because he allowed for the influence of wall friction, but because tests by Franzius (1924) using a hinged wall in a relatively narrow box) had given similar results.

Once the point of contraflexure is known, an imaginary hinge can be inserted at that point on the sheet pile wall, and analysis becomes trivial.

The procedure is:

- by horizontal resolution of forces on span AB, and by taking moments about B, determine the magnitude of the anchor force T, and the force at the hinge F_B;
- Take moments about C, to determine the correct length BC for which the moments about C are zero. Stresses below C are ignored.

  For a uniform soil, with $\gamma' = \gamma - \gamma_W$:

$$F_B(d'-y) = \frac{(d'-y)^3}{6}(K_P - K_A)\gamma' + \frac{(d'-y)^2}{2}\gamma'\left[(K_P - K_A)y - K_A h\right]$$

  For moment equilibrium:

$$(d'-y) = \sqrt{\frac{6F_B}{(K_P - K_A)\gamma'}}$$

- Determine the final depth of embedment (which will also give a factor of safety against failure by forward movement of the piling), approximately:

$$d = 1.2d'$$

- Determine the point of maximum bending moment from the position of zero shear force, by drawing the shear force diagram for span AB;
- Determine the maximum bending moment.

The main problem with this method is the determination of a correct point of contraflexure when soil conditions are non-uniform. For uniform ground conditions B lies approximately level with the point of zero net pressure, N.

5 SEISMIC DESIGN OF EMBEDDED RETAINING WALLS.

The design of retaining walls for seismic conditions is similar, in many aspects, to designing for static conditions. In both cases, potential modes of failure are identified and the wall designed to avoid initiating them. Although the response of retaining walls under seismic loading conditions is much more complex, conventional design procedures make use of simplifying assumptions that render the problem tractable. Several design approaches for embedded retaining walls depending by the analysis type for the desired level of the seismic performance evaluation are described in the following sections. The methods are those obtained by extending the static procedure to the seismic conditions and developed during this work.

5.1 EARTHQUAKE PROVISIONS DESCRIBED IN EUROPEAN AND ITALIAN BUILDING CODES.

Eurocode 8 part 5 (EN 1998-5) states that earth retaining structures must design to fulfil their function during and after an earthquake, without suffering significant structural damages. Permanent displacements, in the form of combined sliding and tilting, the latter due to irreversible deformations of the foundation soil, may be acceptable if it is shown that they are compatible with functional and/or aesthetic requirements. Any established method based on the procedures of structural and soil dynamics, and supported by experience and observations, is in principle acceptable for assessing the safety of an earth retaining structure. The following aspects should be considered in the analyses:

- the generally non-linear behaviour of the soil in the course of its dynamic interaction with the retaining structure;
- the inertial effects associated with the masses of the soil, of the structure, and of all other gravity loads which might participate in the interaction process;
- the hydrodynamic effects generated by the presence of water in the soil behind the wall and/or by the water on the outer face of the wall;
- the compatibility between the deformations of the soil, the wall, and the tiebacks, when present.

It should be underlined that no indications on representative parameters for specifying damage criteria and no limitations on values of the displacements are given.

The basic components that should be included in a pseudo-static analysis consist of the retaining structure and its foundation, of a soil wedge behind the structure supposed to be in a state of active limit equilibrium (if the structure is flexible enough), of any surcharge loading acting on the soil wedge, and, possibly, of a soil mass at the foot of the wall, supposed to be in a state of passive equilibrium.

In the EC8 Part 5, a simplified pseudostatic approach to analyze the safety conditions of retaining walls is described. The seismic increments of earth pressures may be computed with the M-O method. Its application for rigid structures is more prompt than for embedded walls for which the stability is mainly due to the soil passive resistance into the embedded portion. As for the Coulomb theory in static conditions, the M-O theory gives very high values for passive earth pressure coefficient when

the soil-wall friction is considered. For this reason, the evaluation of passive pressure should be conducted assuming zero soil-wall friction.

In the pseudostatic analyses, the seismic actions can be represented by a set of horizontal and vertical static forces equal to the product of the gravity forces and a seismic coefficient. For non-gravity walls, the effects of vertical acceleration can be neglected. In the absence of specific studies, the horizontal seismic coefficient k_h can be taken as:

$$k_h = \frac{S}{r}\frac{a_g}{g} \qquad (5\text{-}1)$$

where S is the soil factor that depends to the seismic zone and considers the local amplification due to stratification of subsoil and topographic effects, a_g is the reference peak ground acceleration on type A ground, g is the gravity acceleration and the factor r is a function of the displacement that the wall can accept. For non gravity walls, the prescribed value is $r = 1$ (EC8 Part 5, Table 7.1).

Furthermore, for walls not higher than 10m, the seismic coefficient can be assumed constant along the height.

The point of application of the force due to the dynamic earth pressures should be taken at mid-height of the wall, in the absence of a more detailed study taking into account of the relative stiffness, the type of movements and the relative mass of the retaining structure.

As previously underlined, this approach suffers of some limitations. Deformability of structure, soil stiffness and damping, natural frequencies of system are neglected. The displacements of the wall and the backfill cannot provide.

Callisto (2006) highlighted some of the limits in the pseudostatic approach as indicated in EC8-5 and specified some preliminary corrections to the code statements.

The new Italian Building Code (NTC, 2008) introduced some innovations on the seismic design of embedded walls to eliminate the discrepancies existing on the application of the pseudostatic analyses for embedded walls.

The pseudostatic analysis of an embedded retaining wall should be carried out assuming that the soil interacting with the wall is subjected to a value of the horizontal acceleration which is:

- constant in space and time (this is implicit in a pseudostatic analysis);
- equal to the peak acceleration expected at the soil surface.

Deformability of the soil can produce amplification of acceleration, that is incorporated into the soil factor S, but that can be better evaluated through a site response analysis.

For many structures, including embedded retaining walls, there may be reasons to question the assumption that the structure should be designed assuming a constant peak acceleration. The validity of the two assumptions (spatial and temporal invariance) will be examined separately for clarity.

Figure 5-1a shows a M-O active wedge which interacts with a vertically propagating harmonic shear wave of frequency f and velocity V_S, characterized by a wavelength $\lambda = V_S/f$ larger than the height of the wedge H. In this case, the variation of the acceleration along the height of the wedge is small, inertial forces (per unit mass) are about constant and the motion of each horizontal element is approximately in phase.

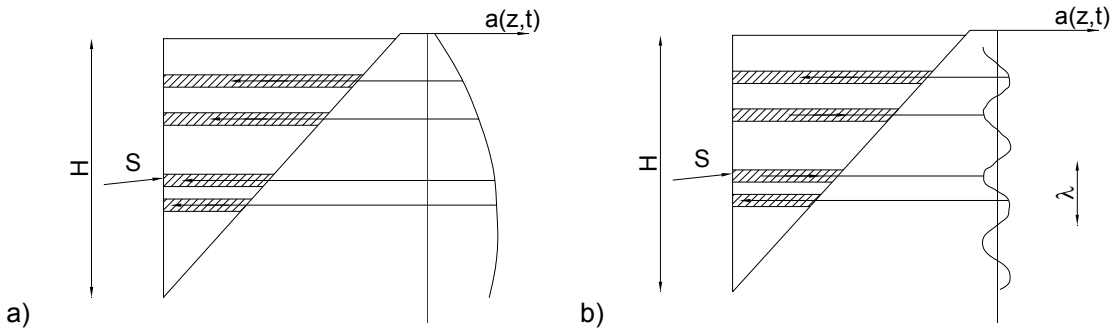

Figure 5-1. *Mononobe-Okabe wedge interacting with harmonic wave characterized by: a) large wavelength; b) small wavelength.*

In Figure 5-1b a case is depicted in which, either because V_S is smaller (the soil is more deformable) or f is larger, λ is small if compared to H. In this case, at a given time t, different horizontal wedge elements are subjected to different inertial forces, and their motion is out of phase. Therefore, at each t the assumption of spatial invariance of the acceleration is no longer valid, and, at each t, the resultant inertial force on the wedge must lead to a smaller resultant force S_{AE} than that predicted with the M-O analysis. Steedman & Zeng (1990) have proposed a method for evaluating the effect of spatial variability of the inertial forces on the values of S_{AE}, maintaining the hypothesis that the wedge is subjected to a harmonic wave.

Figure 5-2 shows some results obtained using this method. Expressing the resultant force by the Equation (2-25) for $k_v = 0$, the calculation results can be expressed in terms of equivalent values of the coefficient of active pressure K_{AE}, plotted as a function of the ratio H/λ, for different values of the amplitude of the shear wave a_g. The equivalent values of K_{AE} can be quite smaller than the corresponding M-O ones (obtained for $H/\lambda = 0$). Values of K_{AE} decrease for increasing wall height, decreasing soil stiffness (quantified by V_S), and increasing frequency of the incident wave.

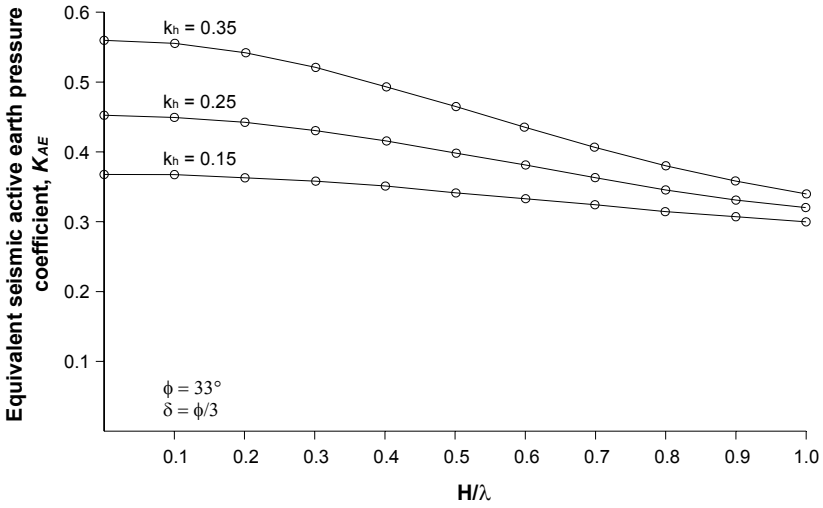

Figure 5-2. *Influence of the ratio between the height of the wall H and the wavelength λ of a harmonic wave on the seismic active earth pressure coefficient (Steedman & Zeng, 1990).*

This approach may be used in practical applications by performing a site response analysis, selecting a value of V_S derived by the average secant shear modulus mobilized along the wall height, and choosing f as the dominant frequency of the seismic motion at a characteristic elevation along the retaining wall.

The assumption of a peak acceleration constant in time for the pseudo-static analysis of an embedded retaining structure is questionable for different ground profiles.

It should be clear that coefficient r in equation (5-1) depends on the displacements that the structure can accept with no loss of strength. That is, it may be acceptable that over a small temporal period during an earthquake the acceleration could be higher than a critical value producing limit conditions, provided that this will lead to acceptable displacements and that these displacements do not produce any strength degradation. This is equivalent to state that the behaviour of the structure should be ductile, i.e. that strength should not drop as the displacements increase.

To account for these aspects, in the latest Italian Building Code NTC two coefficients were introduced. In the absence of specific studies, the seismic horizontal coefficient k_h can be estimated with the relationship:

$$k_h = \alpha \cdot \beta \cdot \frac{Sa_g}{g} \qquad (5\text{-}2)$$

where $\alpha \leq 1$ and $\beta \leq 1$ are factors for the deformability of the soil that interacts with the wall and for the capability of the structure to accept displacements without losses of strength, respectively. Their values are reported in the next Figure 4-7 and Figure 5-6.

The points of application of the forces due to the dynamic earth pressures can be assumed to be the same of the static earth thrusts, if the wall can accept displacements. Instead, they should be taken to lie at mid-height of the wall, in the absence of more detailed studies, accounting for the relative stiffness, the type of movements and the relative mass of the retaining structure.

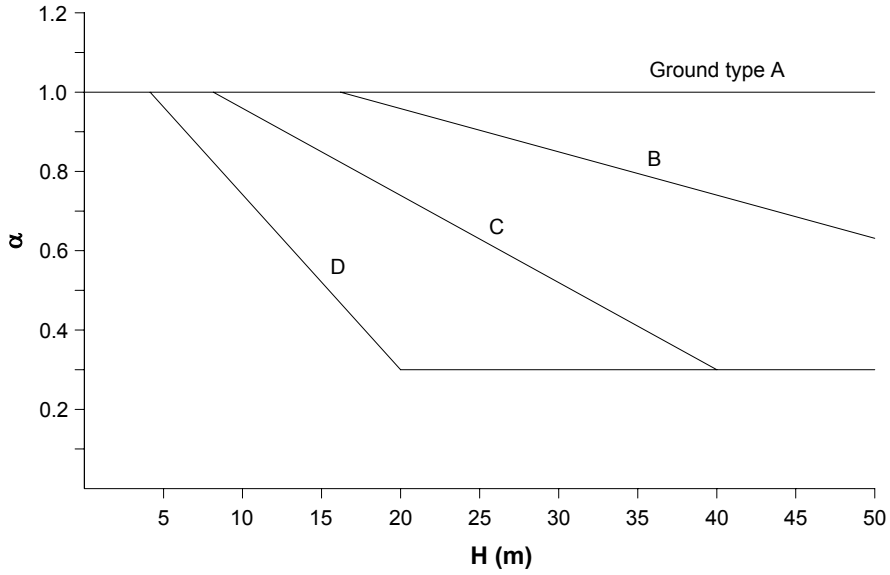

Figure 5-3. *Diagram for the evaluation of the deformability factor α (NTC, 2008).*

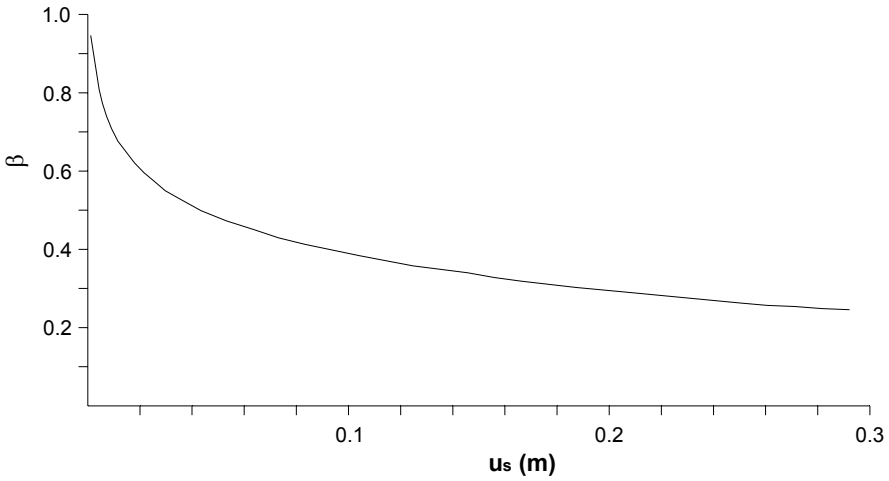

Figure 5-4. *Diagram for the evaluation of displacements factor β (NTC, 2008).*

5.2 PERFORMANCE-BASED DESIGN METHODOLOGY AND DAMAGE CRITERIA.

An evolving design philosophy for many type of constructions in seismically active regions reflect the observations that:

- deformations in ground and foundation soils and the corresponding structural deformation and stress states are key design parameters;
- conventional limit equilibrium-based methods are not well suited to evaluating these parameters;
- some residual deformation may be acceptable.

Performance-based design is a methodology, which was born from the lessons learned from earthquakes in the 1990s (SEAOC, 1995; Iai and Ichii, 1998; Steedman, 1998). The goal is to overcome the limitations present in conventional seismic design. Conventional building code seismic design is based on providing capacity to resist a design seismic force, but it does not provide information on the performance of a structure when the limit of the force-balance is exceeded. If we demand that limit equilibrium not be exceeded in conventional design for the relatively high intensity ground motions associated with a very rare seismic event, the construction/retrofitting cost will most likely be too high. If force-balance design is based on a more frequent seismic event, then it is difficult to estimate the seismic performance of the structure when subjected to ground motions that are greater than those used in design.

In performance-based design, the acceptable level of damage, i.e. the damage criteria, should be specified in engineering terms such as displacements, limit stress state and ductility/strain limit based on the function and seismic response of the structure.

Seismic performance of a sheet pile wall may be specified basing on serviceability and in terms of structural damage regarding stress states as well as displacements. Parameters for specifying damage criteria are as follows (referring to Figure 4-7 - PIANC, 2001).

Displacements:

- sheet pile wall: horizontal displacements, settlements, differential displacements, tilting;
- apron: settlements, differential settlements;
- anchor: differential settlements, ground surface cracking at anchor, pull-out displacements of battered pile anchors.

Stresses:

- sheet pile wall (above and below the dredge level);
- tie-rod (including joints);
- anchor.

Damage criteria should be established by choosing and specifying appropriate parameters from those mentioned above.

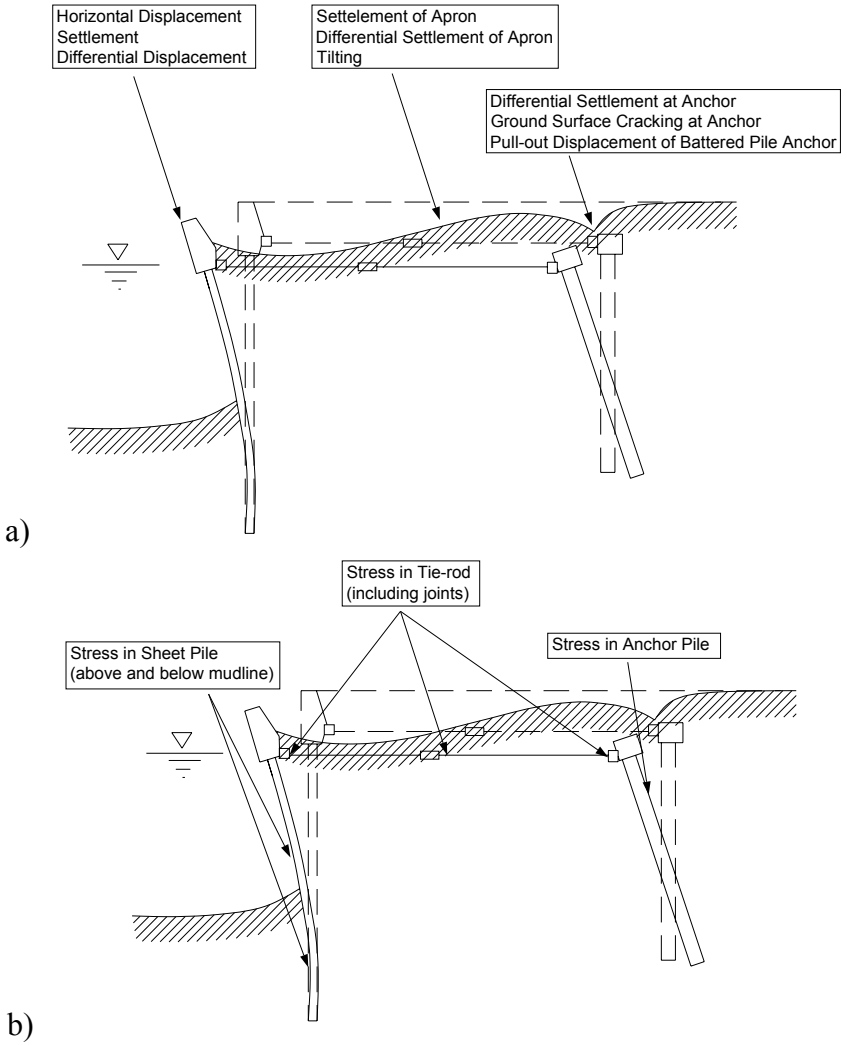

Figure 5-5. *Parameters for specifying damage criteria: a) respect to displacements; b) respect to stresses (PIANC, 2001).*

The preferred sequence to reach ultimate states with increasing level of seismic load should be appropriately specified for a sheet pile wall. If a damaged anchor is more difficult to restore than a sheet pile, the appropriate sequence may be given as follows (refer to Figure 5-6 – PIANC, 2001).

1. Displacement of anchor

2. Yield at sheet pile wall (above the dredge level)
3. Yield at sheet pile wall (below the dredge level)
4. Yield at anchor
5. Yield at tie-rod

If a damaged sheet pile wall is more difficult to restore than an anchor, the yield at anchor should precede the yield at sheet pile wall.

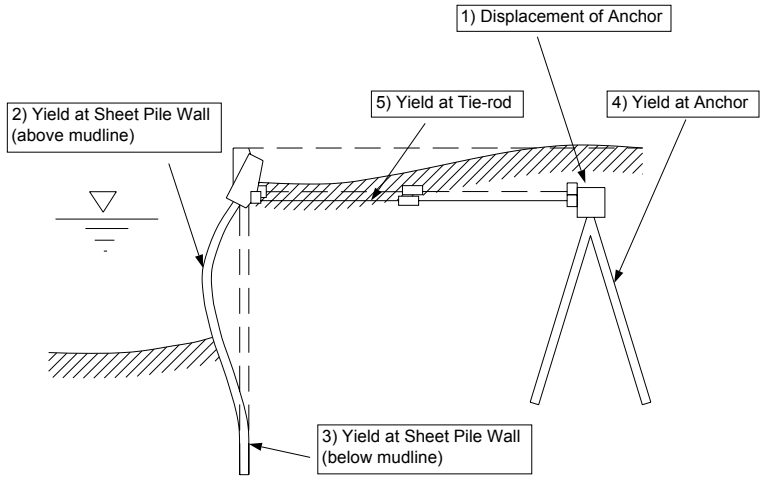

Figure 5-6. *Preferred sequence for yield of sheet pile wall (PIANC, 2001).*

It could be noted that the yield of soil for passive state is not considered in the sequence and maybe might be included in the list. However, different and unclear opinions on this point exist in scientific community.

On the basis of these concepts, the damage criteria for a sheet pile wall can be established by referring to Table 3-1. The most restrictive conditions among displacements and stresses should define the damage criteria. Structural damage to the embedded portion of a sheet pile is generally difficult to restore, and thud necessitates higher seismic resistance. Brittle fracture of a sheet pile wall, rupture of a tie-rod, and the collapse of anchor should be avoided.

Other damage and serviceability criteria can be found in some seismic codes (e.g., Port and Harbour Research Institute, 1997; Ministry of Transport, Japan, 1999; ASCE-TCLEE, Werner, 1998).

Damage criteria	***Component***	***Level of damage***	***Serviceable***	***Repairable***	***Near Collapse***	***Collapse***
		Damage Parameters				
Residual displacements	Sheet pile wall	Normalized residual horizontal displacement (u_x/h)	Less than 1.5%	N/A	N/A	N/A
		Residual tilting towards the excavation side	Less than 3°	N/A	N/A	N/A
	Apron	Differential settlement on apron	Less than 0.03÷0.1m	N/A	N/A	N/A
		Differential settlement between apron and non-apron areas	Less than 0.3÷0.7m	N/A	N/A	N/A
		Residual tilting towards the excavation side	Less than 2÷3°	N/A	N/A	N/A
Peak response stresses/strains	Sheet pile wall	Above the dredge level	Elastic	Plastic (less than the ductility factor/strain limit above the dredge level)	Plastic (less than the ductility factor/strain limit above the dredge level)	Plastic (beyond the ductility factor/strain limit above the dredge level)
		Below the dredge level	Elastic	Elastic	Plastic (less than the ductility factor/strain limit below the dredge level)	Plastic (beyond the ductility factor/strain limit below the dredge level)
	Tie-rod		Elastic	Elastic	Plastic (less than the ductility factor/strain limit for tie-rod)	Plastic (beyond the ductility factor/strain limit for tie-rod)
	Anchor		Elastic	Elastic	Plastic (less than the ductility factor/strain limit for anchor)	Plastic (beyond the ductility factor/strain limit for anchor)

Table 5-1. *Damage criteria for sheet pile wall (adapted from PIANC, 2001).*

5.3 SEISMIC ANALYSIS OF EMBEDDED RETAINING WALLS.

Seismic analysis of many type of constructions is accomplished in three steps that include assessment of the regional seismicity, the geotechnical hazards and soil structure interaction analysis. The first step is to define the earthquake motions at the bedrock. This is typically accomplished by seismic hazard analysis based on geologic, tectonic and historical seismicity data available for the region of interest. The second step involves the following two interrelated aspects of dynamic soil response: 1) an evaluation of local site effects for obtaining the earthquake motions at or near the ground surface; 2) an assessment of the liquefaction resistance of the near surface sandy soils and the associated potential for ground failures. Once the ground motion and geotechnical parameters have been established, then seismic analysis of the construction can proceed.

As in all engineering disciplines, reasonable judgement is required in specifying appropriate methods of analysis and design, as well as in the interpretation of the results of the analysis procedures. This is particularly important in seismic design, given the multidisciplinary input that is required for these evaluations, and the influence of this input on the final design recommendations.

5.3.1 Type of analysis.

The objective of analysis in performance-based design is to evaluate the seismic response of the embedded retaining walls with respect to allowable limits (e.g. displacements, stress, ductility/strain). Higher capability in analysis is generally required for a higher performance grade facility. The selected analysis methods should reflect the analytical capability required in the seismic performance evaluation.

A variety of analysis methods are available for evaluating the local site effects, liquefaction potential and the seismic response of retaining walls. These analysis methods are broadly categorized based on a level of sophistication and capability as follows (PIANC, 2001):

1. Simplified analysis: appropriate for evaluating approximate threshold limit for displacements and/or elastic response limit and an order-of-magnitude estimate for permanent displacements due to seismic loading.
2. Simplified dynamic analysis: possible to evaluate extent of displacement/stress/ductility/strain based on assumed failure modes.
3. Dynamic analysis: possible to evaluate both of failure modes and the extent of displacement/stress/ductility/strain.

In principle, the structures characterized by a higher performance grade should be studied using more sophisticated methods. Less sophisticated methods may be allowed for preliminary design, screening purposes or response analysis for low levels of excitation.

Table 5-2 shows the input parameters and the outputs of the various type of seismic analysis of embedded walls. It should be noted that the reliability of the results depends not only on the type of analysis, but also on the reliability of the input parameters. It is ideal to use input data based on through geotechnical investigations for more sophisticated analysis.

Type of Analysis	***Simplified Analysis***	***Simplified Dynamic Analysis***		***Dynamic Analysis***
Method	*Pseudo-static/empirical methods*	*Newmark type method*	*Simplified chart based on parametric studies*	*FEM/FDM*
Design Parameters	k_h: equivalent seismic coefficient k_{crit}: threshold seismic coefficient	Empirical equations: a_{max}: peak acceleration V_{max}: peak velocity Time history analysis: time histories of earthquake motions a_{crit}: threshold acceleration	a_g: peak acceleration at the bedrock Cross section of wall Index properties of soil including SPT *N*-values	Time histories of earthquake mations at the bottom of analysis domain Cross section of wall For equivalent linear geotechnical analysis: $G/G_0(\gamma)$ and $D(\gamma)$ curves For nonlinear geotechnical analysis: undrained cyclic properties and G, K: shear and bulk modulus, in addition to the geotechnical parameters for pseudo-static and simplified analyses
Input Parameters	Results of site response analysis, including a_{max} and liquefaction potential assessment Cross section of wall Geotechnical parameters, including cohesion c, friction angle ϕ and soil-wall friction angle; ground water level			
Analysis Output	Threshold limit Order-of-magnitude displacement	Wall displacement Stress/ductility		Response/failure modes Peak and residual displacements, stress/ductility

Table 5-2. *Inputs and outputs of analyses (adapted from PIANC, 2001).*

5.3.2 Simplified analysis.

Simplified analysis of retaining structures is based on the conventional force-balance approach, sometimes combined with statistical analysis of case history data. The methods in this category are often those adopted in conventional seismic design codes and standards. In simplified analysis, retaining walls can be idealized as rigid blocks of soil and structural masses. The rigid block analysis is typically applied for gravity and sheet pile walls.

Effects of earthquake motions in simplified analysis are represented by a peak ground acceleration a_{max} or an equivalent seismic coefficient k_h for use in conventional pseudo-static design procedures. These parameters are obtained from the simplified analysis of local site effects. A capacity to resist the seismic force is evaluated based on structural and geotechnical conditions, often in terms of a threshold acceleration a_{crit} or a threshold seismic coefficient k_{crit}, beyond which the rigid blocks of soil and structural masses begin to move. When soil liquefaction is an issue, the geometric extent of liquefaction must also be considered in the analysis.

Results of the simplified analysis are appropriate for evaluating the approximate threshold level of damage, which ensures at least the repairable state of structural performance for the earthquake related to serviceability criteria. Whether or not the approximate threshold level ensures the serviceable state of structural performance depends on the details in evaluating the design parameters for the pseudo-static method. Order-of-magnitude displacement is also obtained by the pseudo-static method combined with statistical analysis of case history data. This, however is a crude approximation and should be used only for the preliminary design stage or low levels of excitation.

There is a significant difference between the conventional design concept and the performance-based design approach. In the former, especially when referring to the simplified analysis, an equivalent seismic coefficient is used as an input parameter representing adequately the ensemble of ground motions, and a factor of safety is applied to determine the dimensions of the structure. In the latter, the design is based on the seismic performance of the structure evaluated appropriately through response analysis for a variety of input earthquake motions. The ensemble of the seismic responses, rather than the ensemble of the input motions, is used as a basis for accomplishing the design in the performance-based method. For each response analysis, input parameters most appropriate are those well defined in terms of applied mechanics, such as a peak ground acceleration for the simplified analysis and/or an equivalent parameter clearly defined in terms of peak ground acceleration. Consequently, no factor of safety should be applied to input data used in seismic analysis for evaluating the threshold level of the structure.
The simplified analyses for the evaluation of the seismic performance of free and anchored embedded walls are separately presented in the following. The methodologies were derived from the current procedure adopted for the static analyses and extended to the seismic conditions.

5.3.2.1 Free embedded retaining walls.

As demonstrated in the previous chapter for the static conditions, the Blum method allows to conservative depths of embedment respect to the empirical relationship proposed by Bica & Clayton (1992) if applied adopting the Padfield & Mair (1984) suggestions on the soil-wall friction angles values for active and passive conditions. It seems to be reasonable the extension of this simplified procedure for evaluating the safety conditions of a cantilever retaining wall.
In the pseudostatic analyses of a free embedded wall, the seismic actions can be represented by a set of horizontal static forces equal to the product of the gravity forces and an equivalent seismic coefficient k_h. In the absence of specific studies, the horizontal seismic coefficient k_h can be evaluated according to (5-1). Different opinions exist in the literature on the point of application of the force due to dynamic earth pressures. The Italian Building Code (NTC, 2008) states that the points of application of the seismic thrust increments can be assumed to be the same of the static earth thrusts, if the wall can accept displacements. When the wall movements are constrained, instead, the seismic increments of the earth thrusts should be taken to lie at mid-height of the wall, in the absence of more detailed studies in which the relative stiffness, the type of movements, the relative mass of the retaining structure and the joint systems acting on the wall are taken into account.
For the cantilever walls, the free displacements condition can be assumed and, then, the seismic increments of the earth pressures reported in Figure 5-7 can be adopted for the simplified analysis.
The values of seismic earth pressure coefficients K_{AE} and K_{PE} can be evaluated adopting the formulations presented in the previous Chapter 3. For soil-wall friction angles δ larger than $\phi'/2$, the soil passive resistance should be determined considering the nonplanarity of the sliding surfaces (i.e. limit analysis solutions). The active pressure coefficient K_{AE} is currently calculated with the M-O method by assuming realistic values of δ_A that accounts for the actual behaviour of the soil-wall interface subjected to cyclic loadings. In the practical applications, for static analysis of cast-in-place reinforced concrete wall (sheet pile or diaphragm), it is assumed $\delta = \phi'$. To account for the degradation

of the contact due to cyclic loading, reasonable values of the soil-wall friction angle suggested in the literature (Padfield & Mair, 1984) are $\delta = 2/3\phi'$. The passive pressure coefficient K_{PE}, instead, is currently evaluated by adopting the M-O method for a zero value of the soil-wall friction angle $\delta_P = 0$ or by using the Chang (1981) tables. More recently, Lancellotta (2007) has given an analytical expression for the evaluation of the K_{PE} coefficient that represents a conservative value of the soil passive resistance.

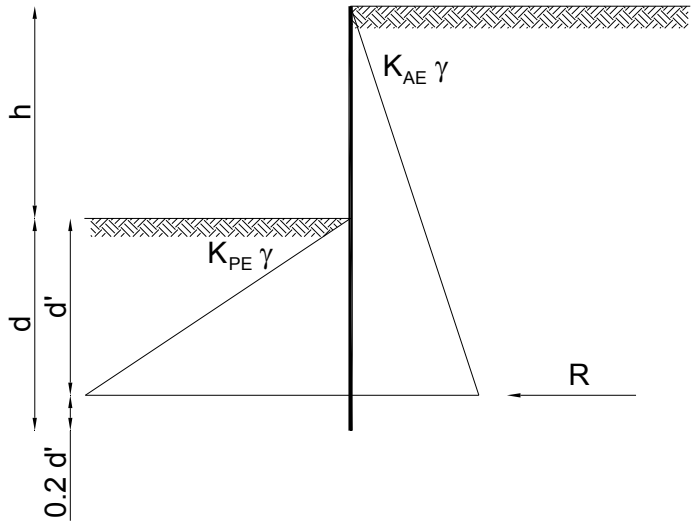

Figure 5-7. *Seismic earth pressures acting on a free embedded wall according to Italian Building code (NTC, 2008) for a pseudo-static analysis adopting the Blum method.*

In this work, the seismic coefficients K_{AE} and K_{PE} were calculated by means of the M-O and Lancellotta methods, respectively, and adopting $\delta_A = 2/3\phi'$ and $\delta_P = \phi'/2$.
On the basis of the previous considerations, the moment equilibrium about the point C near to the bottom of the wall in seismic conditions gives the following relationships between the earth pressure coefficients and the limit depth ratio of embedment:

$$\frac{d}{h} = \frac{1.2}{\sqrt[3]{K_{PE}/K_{AE}} - 1} \qquad (5\text{-}3)$$

Similarly to the static conditions, the maximum bending moment can be computed with the expression

$$M_{max} = \frac{\gamma}{6}\left[K_{AE}(h+x)^3 - K_{PE}x^3\right] \qquad (5\text{-}4)$$

where x is the depth of the zero shear force from the dredge level:

$$\frac{x}{h} = \frac{1}{\sqrt{K_{PE}/K_{AE}} - 1} \qquad (5\text{-}5)$$

The values of the ratio between the depth of embedment and the height of excavation d/h and the normalized bending moment $M_{max}/\gamma h^3$ evaluated by means of the equations (**5-3**) and (**5-4**) are reported in the next Figure 5-8 and Figure 5-9.

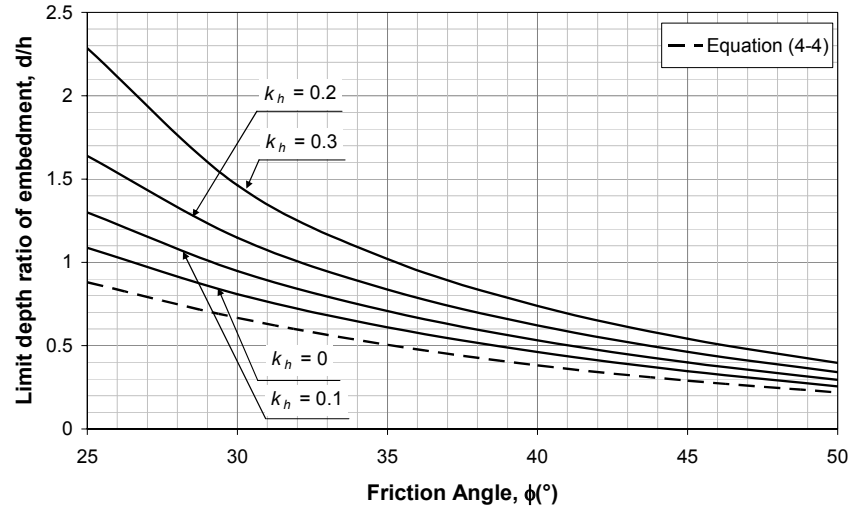

Figure 5-8. *Limit depth ratio of embedment computed by the Blum method in seismic conditions of a free embedded wall.*

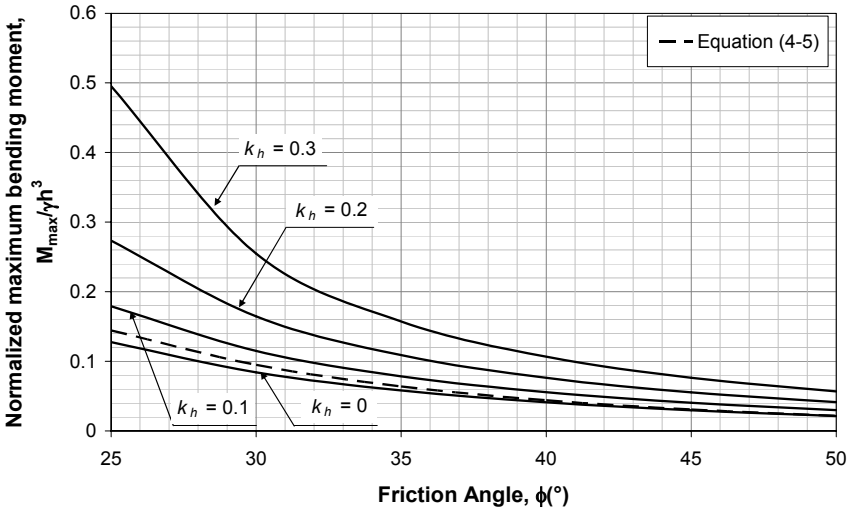

Figure 5-9. *Normalized maximum bending moment computed by the Blum method in seismic conditions of a free embedded wall.*

As observed in the previous Chapter 4, for the assumed values of the soil-wall friction angles, the maximum bending moment calculated by the Blum method are slightly lower than those given by the empirical relationship (4-5). But, it useful to remember that the (4-5) derives from an interpolation of experimental and numerical data that can not be referred to the limit equilibrium conditions.

The previous charts can be used for the preliminary design of free embedded RC walls. Remembering that the factors of safety are not introduced in the analysis, the soil friction angle ϕ' should be interpreted as the design value ϕ'_d. Adopting the partial factors of safety, ϕ'_d may be estimated as

$$\phi'_d = \arctan\left(\frac{\tan\phi'}{\gamma_{\phi'}}\right) \qquad (5\text{-}6)$$

where the partial coefficient $\gamma_{\phi'}$ is taken equal to 1.25 (EC8-5; NTC, 2008).

In the view of the performance-based design, the threshold seismic coefficient k_{crit} can be evaluated by entering into the charts of with the couple (ϕ'; d/h) in Figure 5-8 and ((ϕ'; $M_y/\gamma h^3$) that characterize the

problem of interest (M_y is the yielding moment of the wall with respect to the examined limit state) and estimating the reference curves with constant value of k_h.

The factors of safety FS against the earthquake for rotational and structural failure modes are defined by (PIANC, 2001):

$$FS = \frac{k_{crit}}{k_h} \qquad (5\text{-}7)$$

The displacements of the wall can be then estimated by using empirical relationships and charts.

Richards & Elms (1979) proposed a method for the seismic design of gravity walls based on allowable permanent wall displacements. Using the results of sliding block analyses in the same manner as Newmark (1965) and Franklin and Chang (1977), the authors proposed the following expression for permanent block displacement:

$$u_x = 0.087 \frac{v_{\max}^2 a_{\max}^3}{a_{crit}^4} \qquad \frac{a_{crit}}{a_{\max}} \geq 0.3 \qquad (5\text{-}8)$$

where v_{max} is the peak ground velocity, a_{max} is the peak ground acceleration and $a_{crit} = k_{hcrit} \cdot g$ is the yield acceleration for the wall-backfill system.

Whitman & Liao (1985) identified several modelling errors that result from the simplifying assumptions of the Richards & Elms procedure. The most important of these are neglect of the backfill dynamic response, the kinematic factors, the tilting mechanisms and the vertical accelerations. Finite element analyses of the effects of the dynamic response of the backfill on wall displacements (Nadim, 1982), for example, show that amplification occurs when input motions coincide with the natural period of the backfill and produce considerably greater permanent displacement than the rigid-block model used by Richards & Elms. Analyses in which the backfill wedge and wall were treated as separate blocks (Zarrabi-Kashani, 1979) show that the kinematic requirements of horizontal and vertical displacement of the backfill wedge cause systematically smaller displacements than the single-block model of Richards and Elms. Studies of combined tilting and sliding (Nadim, 1980; Siddharthan et al., 1992) indicate that tilting mechanisms generally increase wall displacements over those produced by sliding-only models such as that of Richards & Elms. Consideration of vertical accelerations produces slightly larger displacements than when they are neglected, at least for motions with high peak horizontal acceleration (a_{max} greater than about 0.5g) and $a_{crit}/a_{max} \geq 0.4$ (Whitman & Liao, 1985). Whitman & Liao quantified and combined the effects of each of these sources of modelling error to describe the total modelling error by a lognormally distributed random variable with mean value, $\overline{M}$, and standard deviation, $\sigma_{\ln M}$.

Using the results of sliding block analyses of 14 ground motions by Wong (1982), Whitman & Liao found that the permanent displacements were lognormally distributed with mean value

$$\overline{u_x} = \frac{37 v_{\max}^2}{a_{\max}} \exp\left(\frac{-9.4 a_{crit}}{a_{\max}}\right) \qquad (5\text{-}9)$$

Uncertainty due to statistical variability of ground motions was characterized by a lognormally distributed random variable, Q, with a mean value of $\overline{Q}$ and standard deviation, $\sigma_{\ln Q}$.

The effects of uncertainty in soil properties, specifically the friction angles, on permanent displacement were also investigated. Using standard deviations of σ_ϕ = 2 to 3° for soil friction angles and σ_δ = 5° for wall-soil interface friction angles, the computed yield acceleration was defined as a random variable with mean value $\bar{a}_{crit}$ and standard deviation $\sigma_{a_{crit}}$. The mean value $\bar{a}_{crit}$ is the yield acceleration computed using the mean values of ϕ and δ.

Combining all the sources of uncertainty, the permanent displacement can be characterized as a lognormally distributed random variable with mean value

$$\overline{u_x} = \frac{37 v_{\max}^2}{a_{\max}} \exp\left(\frac{-9.4\bar{a}_{crit}}{a_{\max}}\right)\overline{Q}\overline{M} \qquad (5\text{-}10)$$

and variance

$$\sigma^2_{\ln u_x} = \left(\frac{9.4g}{a_{\max}}\right)^2 \sigma^2_{a_{crit}} + \sigma^2_{\ln M} + \sigma^2_{\ln Q} \qquad (5\text{-}11)$$

Suggested values of the means and standard deviations of the ground motion, soil resistance and model error factors are shown in Table 5-3.

Factor	Mean	Standard Deviation
Model error	$\overline{M} = 3.5$	$\sigma_{\ln M} = 0.84$
Soil resistance	$\bar{a}_{crit} = a_{crit}\left(\bar{\phi};\bar{\delta}\right)$	$\sigma_{a_{crit}} = 0.04$ to 0.065
Ground motion	$\overline{Q} = 1$	$\sigma_{\ln Q} = 0.58$ to 1.05

Table 5-3. *Mean and standard deviation values for gravity walls displacement analysis (after Whitman & Liao, 1985).*

5.3.2.2 Anchored sheet pile walls.

The design of anchored bulkheads in waterfront areas is strongly influenced by liquefaction hazards. If widespread liquefaction occurs, experience indicates that bulkhead failures are very likely. Consequently, steps should be taken prior to construction to ensure that such liquefaction will not occur. Permanent seaward movements of anchored bulkheads in the absence of widespread liquefaction, however, has also been observed. Conventional design procedures seek to minimize this type of damage using pseudostatically determined design pressures.

A widespread design procedure uses the free earth support method and Rowe's moment reduction method, with earthquake effects represented by pseudostatic inertial forces. A brief summary of the procedure is presented below; a detailed description with a worked example may be found in Ebeling & Morrison (1993).

- Design the anchored bulkhead for static loading conditions.
- Select pseudostatic accelerations a_h and a_v.
- Compute the active soil thrust on the back of the wall using the M-O method. The active wedge is assumed to originate at the bottom of the wall.

- Compute the passive soil thrust acting on the front of the wall using a method that accounts for the nonplanarity of the sliding surfaces. The passive wedge is also assumed to originate at the bottom of the wall.
- Compute the minimum required depth of wall penetration by summing moments about the wall-tie rod connection. All water pressures (hydrostatic, hydrodynamic and excess pore water, if present) must be included.
- Compute the required anchor resistance by summing the horizontal forces acting on the wall. All water pressures (hydrostatic, hydrodynamic and excess pore water, if present) must be included. The computed anchor resistance is termed the free earth support anchor resistance.
- Compute the distribution of bending moments over the height of the wall. All water pressures (hydrostatic, hydrodynamic and excess pore water, if present) must be included. The maximum bending moment is termed the free earth support moment.
- Compute the design bending moment as the product of the free earth support moment and Rowe's moment reduction factor (Rowe, 1952).
- Set the design tie-rod force at a level 30% greater than the free earth support anchor resistance.
- Determine the required size of the anchor block to satisfy horizontal force equilibrium considering the active and passive pressures, as well as all water pressures, on both sides of the block. The effects of any water pressures on the bottom and top surfaces of the anchor block should also be considered.
- Locate the anchor block at a sufficient distance behind the wall that the active wedge behind the wall dose not intersect the passive wedge in front of the anchor block. Since the active and passive failure surfaces are flatter for seismic loading than for static loading, seismic design may require a considerably longer tie-rod than static design.
- Check the effects of redistribution of any earthquake-induced excess pore water pressures after earthquake shaking has ended.

Case histories of anchored bulkhead performance (neglecting cases in which widespread liquefaction was observed) suggest that anchored bulkhead damage levels can be predicted approximately wth the aid of two dimensionless indices: the *effective anchor index (EAI)* and the *embedment participation index (EPI)* (Gazetas *et al.*, 1990).

Referring to Figure 5-10a, the effective anchor index describes the relative magnitude of the available anchor capacity as

$$EAI = \frac{g}{h} \qquad (5\text{-}12)$$

where g is the horizontal distance between the active wedge and the tie-rod anchor connection and h is the height of the wall. The critical active failure plane is taken to originate at the effective point of rotation of the wall, which can be located using soil-structure interaction analysis or estimated as

$$f = \left(\frac{1 + k'_e}{2} - \frac{\phi' - 20^\circ}{50^\circ} \right) h \le g \qquad (5\text{-}13)$$

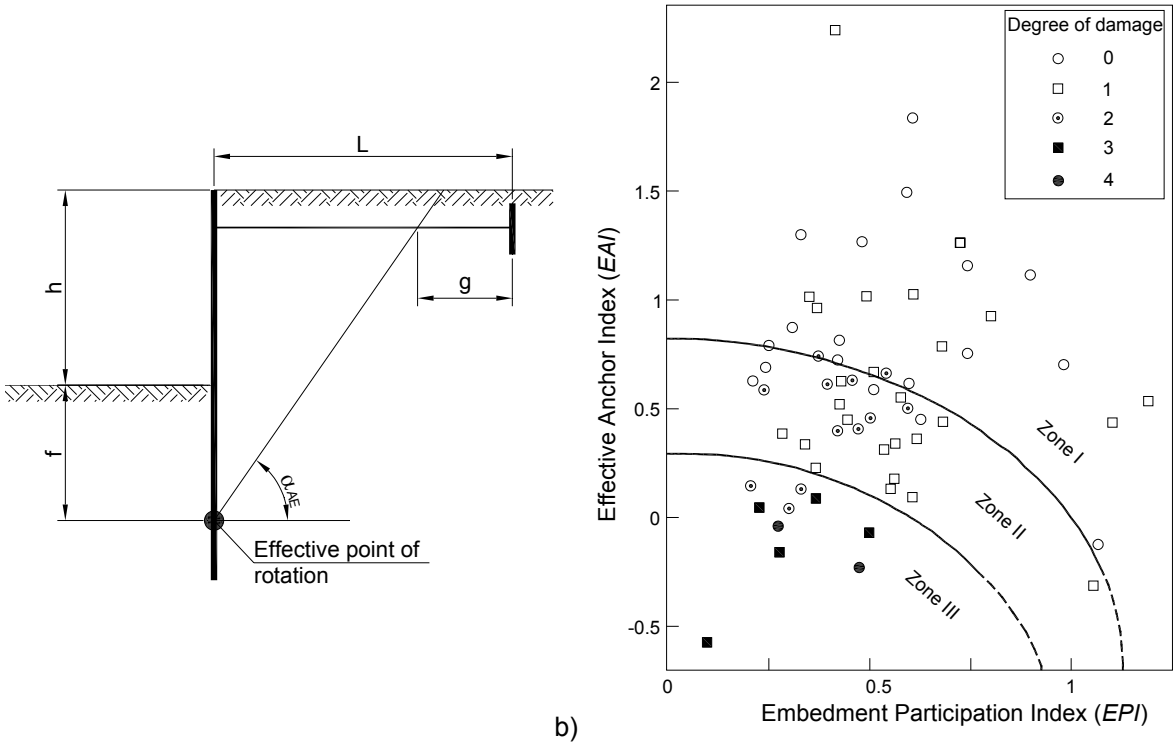

a) b)

Figure 5-10. *a) Geometry and notation for evaluation of anchored bulkhead design; b) Correlation between damage levels and dimensionless anchored bulkhead indices. After Gazetas et al. (1990). Empirical design method for waterfront anchored sheet pile walls, Design and Performance of Earth Retaining Structures (ASCE)*

where

$$k'_e = \begin{cases} \dfrac{k_h}{1-k_v} & \text{above the water table} \\ \dfrac{(a_h/g)_{\max}}{1-2(a_h/g)_{\max}/3} & \text{below the water table} \end{cases}$$

The inclination of the critical active failure plane can be approximated (Dennehy, 1985) as

$$\alpha_{AE} \approx 45° + \frac{\phi}{2} - 135°(k'_e)^{1.75} \qquad (5\text{-}14)$$

for $0.10 \le k'_e \le 0.50$ and $25° \le \phi' \le 35°$. Beyond these ranges equation (5-14) can be used to estimate the inclination of the active wedge. The embedment participation index is defined as

$$EPI = \frac{F_{PE}}{F_{AE}}\left(1+\frac{f}{f+h}\right) \qquad (5\text{-}15)$$

where F_{AE} and F_{PE} are the potential active and passive thrusts, respectively. For uniform backfill and foundation soils,

$$EPI = \frac{K_{PE}}{K_{AE}} r^2(1+r) \qquad (5\text{-}16)$$

where r = f/(f+h). Values of *EAI* and *EPI* have been computed for 75 bulkheads for which degrees of damage in earth quake have been categorized as indicated in Table 5-4 (Gazetas *et al.*, 1990)

Comparison of degrees of damage with *EAI* and *EPI* showed significant trends in the characteristics of anchored bulkheads that performed well and those that performed poorly. As illustrated in Figure 5-10b, anchored bulkheads with high *EAI* and *EPI* values (zone I) generally suffered little or no damage. Anchored bulkheads with low *EAI* and *EPI* values (zone III) usually suffered severe damage. Moderate damage was generally associated with intermediate combinations of *EAI* and *EPI* (zone II).

Degree of damage	***Description of damage***	***Permanent horizontal displacement at top of sheet pile (cm)***
0	No damage	< 2
1	Negligible damage to the wall itself; noticeable damage to related structures	2-10
2	Noticeable damage to the wall	10-30
3	General shape of anchored sheet pile preserved, but significantly damaged	30-60
4	Complete destruction	> 60

Table 5-4. *Qualitative and quantitative descriptions of reported degrees of damage to anchored bulkhead during earthquakes (Gazetas et al., 1990).*

The chart of Figure 5-10b is a very useful tool for checking the design of anchored bulkheads in waterfront areas.

The displacements of the retaining system can be then estimated by using empirical relationships and charts depending on the liquefaction potential of the site.

For anchored sheet pile walls in non-liquefiable sites, a set of empirical equations were derived through regression analysis to define horizontal displacement u_x, settlement u_y and normalized horizontal displacement u_x/h (Uwabe, 1983).

$$u_x(cm) = -1.6 + 34.9(1/FS) \quad (5\text{-}17)$$

$$u_y(cm) = -5.3 + 14.7(1/FS) \quad (5\text{-}18)$$

$$u_x/h(\%) = -1.5 + 5.8(1/FS) \quad (5\text{-}19)$$

When site contain saturated loose to medium sandy soils, it is necessary to consider the consequences of liquefaction. The simplified geometries of the loose saturated sand relative to the cross section of the wall characterized by liquefiable soil behind the wall only, liquefiable backfill and liquefiable soil both in backfill and foundation were used for classifying the case histories for anchored sheet pile walls. Table 5-5 shows some case history data with supplemental information shown in Figure 5-11 (Iai *et al.*, 1998). A summary of the normalized horizontal displacements of anchored sheet pile walls at liquefaction sites are shown in Table 5-6. The intensity of the earthquake motion is equivalent to the design seismic coefficient.

From the Table 5-6, it is possible to obtain a rough estimate of displacements based on the wall height.

Port	***Seismic coefficient k_h***	***Water depth (m)***	***Earthquake/ Magnitude/ Year***	***PGA (g)***	***Acceleration Level***	***Soil Conditions***	***Horizontal Displacements, u_x (m)***	***Normalized Horizontal Displacements, u_x/h***
Akita Port Ohama No.2	0.10	-10.0	Nihonkai-Chubu M = 7.7 1983	0.209	Design seismic coefficient	Loose sand behind the wall only	1.72	14%
Akita Port Ohama No.3	0.10	-10.0	Nihonkai-Chubu M = 7.7 1983	0.209	Design seismic coefficient	Loose sand behind the wall only	0.82	7%
Ishinomaki Port Shiomi wharf	0.10	-4.5	Miyagiken-Oki M = 7.4 1978	0.287	Design seismic coefficient	Loose sand at backfill	1.16	16%
Hakodate Port Benten wharf	0.15	-8.0	Hokkaido-Nansei-Oki M = 7.8 1993	0.113	Design seismic coefficient	Loose sand at both backfill and foundation	5.21	46%

Table 5-5. *Case histories of seismic performance of retaining walls at liquefied sites (PIANC, 2001).*

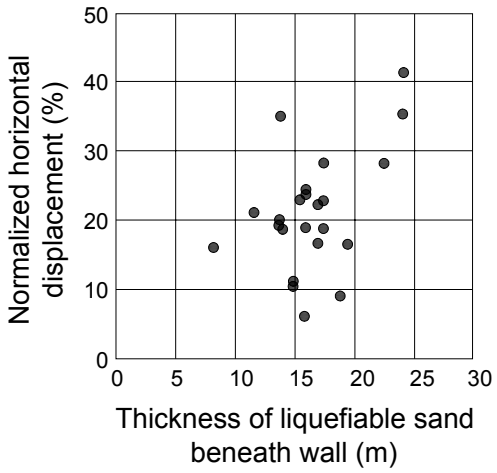

Figure 5-11. *Normalized horizontal displacements correlated with thickness of loose soil deposit below the wall (after Iai et al., 1998).*

	Normalized Horizontal Displacements, u_x/h (%)			
	0-5	5-15	15-25	25-50
Non-liquefaction	■			
Loose sand behind the wall only		■		
Loose sand at backfill including anchor			■	
Loose sand at both backfill and foundation				■

Table 5-6. *Normalized horizontal displacements of anchored sheet pile walls at liquefied sites during design level earthquake motion (PIANC, 2001).*

5.3.3 Simplified dynamic analysis.

Simplified dynamic analysis is similar to simplified analysis, idealizing a structure by a sliding rigid block (Newmark analysis). In simplified dynamic analysis, displacement of the sliding block is computed by integrating the acceleration time history that exceeds the threshold limit for sliding over the duration until the block ceases sliding.

Effects of earthquake are generally represented by a set of time histories of seismic motion at the base of the structure. The time histories of earthquake motion are obtained from the simplified dynamic analysis of local site effects. In the sliding block analysis, structural and geotechnical conditions are represented by a threshold acceleration for sliding. A set of empirical equations obtained from a statistical summary of sliding block analysis is available (Richards & Elms, 1979; Whitman & Liao, 1984; Towhata & Islam, 1987; Steedman, 1998). In these equations, peak ground acceleration and velocity are used to represent the effect of earthquake shaking.

It should be noted that the procedure commonly used for the gravity walls poses two difficulties when applied to the flexible embedded wall cases. First, the active earth pressure may not be accurate because of the flexible nature of the sheet pile wall. Second, the inertia force on and bottom friction at the wall, i.e. two of major parameters for gravity wall analysis, are not the major parameters in the sheet pile-backfill soil system. These problems are solved by idealizing the movement of the sheet

pile-backfill system, assuming united rigid block motion of the wall and backfill (Towhata & Islam, 1987). The driving force is the inertia force acting on the soil wedge and the resistance force includes the passive earth pressures in front of the wall and the shear resistance along the failure surface of the soil wedge.

By expressing the dynamic earth pressure coefficients K_{AE} and K_{PE} and the ultimate anchor resistance T_E as functions of K_A, K_P and T_S before the earthquake (Seed and Whitman, 1970)

$$K_{AE} = K_A + \Delta K_{AE} = K_A + \frac{3}{4}k_h \qquad (5\text{-}20)$$

$$K_{PE} = K_P + \Delta K_{PE} = K_P - \frac{17}{8}k_h \qquad (5\text{-}21)$$

$$T_E = T_S + \frac{K_{PE} - K_{AE}}{K_P - K_A} \qquad (5\text{-}22)$$

the threshold horizontal seismic coefficient is obtained as (Towhata and Islam, 1987)

$$k_{crit} = \frac{a\tan\alpha_{AE} - b + \tan(\phi - \alpha_{AE})(1 + b\tan\alpha_{AE})}{1 + c\tan\alpha_{AE}} \qquad (5\text{-}23)$$

where

$$a = \frac{mT_S + P_P + 1/2\,\gamma_w(h_w + d)^2 + \Delta U_P}{W_m} \qquad (5\text{-}24)$$

$$b = \frac{1/2\,\gamma_w(h_w + d)^2\tan\phi + \Delta U_A \sin\alpha_{AE}}{W_m}\tan\theta \qquad (5\text{-}25)$$

$$c = \frac{1}{W_m}\left[\frac{23mnT_S}{8(K_P - K_A)} + \frac{17P_P\gamma_{sat}}{8K_P\gamma'} + \frac{7}{12}\gamma_w h_w^2\right] \qquad (5\text{-}26)$$

$$W_m = \frac{1}{2}\left[\gamma_{sat}(h_w + d)^2 + \gamma(h - h_w)(h + 2d + h_w)\right] \qquad (5\text{-}27)$$

and

m = 0 for no anchor capacity, 1 for full anchor capacity (dependant on the amount of excess pore pressure generation around the anchor)

P_P = static passive earth thrust

ΔU = excess pore water pressure due to cyclic shearing; subscripts A and P denote pressures within the active and passive soil wedges

n = 1 when the anchor block is above the water table, and γ/γ' when the anchor is completely submerged.

The ground water table behind the wall is the same as that of the excavation side.

Using the threshold seismic coefficient k_{crit} defined for the sheet pile-backfill system, displacement of the wall is computed based on Newmark's sliding block approach.

5.3.4 Pushover analysis.

A more sophisticated method for the evaluation of k_{crit} for an embedded retaining wall is based on nonlinear FEM/FDM pseudostatic analysis. The procedure can be included in the framework of the "*pushover analyses*". The first application was proposed by Visone & Santucci de Magistris (2007).

Pushover analysis is a static nonlinear procedure in which the magnitude of the structural loading is incrementally increased in accordance with a certain predefined pattern. With the increase of the loading magnitude, weak links and failure modes of the structure can be found. The sequence of yields in the structure and the transition from elastic to the ultimate state response may also be identified. Static pushover analysis is a consolidated methodology in the structural engineering for evaluation of the real strength of the structures and it promises to be a useful and effective tool in the view of the performance-based design philosophy.

In geotechnical engineering, only few applications of pushover analyses can be found in the literature (e.g. Pile-supported wharves – PIANC, 2001). This is maybe due to the difficulties to recognize the vibration modes of the geotechnical system.

The methodology requires the numerical modelling of the problem by means of FE or FD simulations. For this scope, the soil can be modelled adopting subgrade reaction method (FE1D analysis) or as an elasto-plastic continuum.

The static conditions of the soil-wall system should be studied to take into account the nonlinearities of the soil and wall behaviours. Then, starting from the deformed configuration, the seismic loadings are applied to the structure through pressure distributions on the wall towards the excavation.

The aspects that should be considered in this type of analysis are:

- geometrical nonlinearities: when the system reach the collapse the small deformations hypothesis is violated, hence, the calculation need continuous updating of the configuration;
- material nonlinearities: the stress-strain behaviour of the soil, the structural element, the soil-structure interface and of the other elements (anchors, props, etc.) should be represented with suitable constitutive models that implement plasticity;
- load advancement to the ultimate level: the external load should be applied incrementally in order to obtain a load-displacement relationship that permits to detect the displacements of the system when it is subjected to design actions (seismic demand).

The main results of the analysis are load-displacements curves that represent the capacity of the system to resist seismic actions (seismic capacity).

In the present research, two different linear pressures distributions are considered.

1. Triangular (TRD), with a maximum p_{max} at the base of the wall, suitable for low frequencies motions, as shown for instance by Steedman & Zeng (1990). This distribution agrees with the provisions given by the Italian Building code (NTC, 2008).
2. Rectangular (RTD), following the indications found in EC8-5.

Thus, dynamic thrust increments are equal to:

$$S_E = \frac{1}{2} p_{\max} H \qquad \text{TRD} \qquad (5\text{-}28)$$

$$S_E = p_{\max} H \qquad \text{RTD} \qquad (5\text{-}29)$$

acting at H/3, H/2 and 0.6 H from the base of the wall having a total height H = h +d.
These values can be normalized with respect to the weight W of the active soil wedge and the weight W_w of the wall, in order to obtain the seismic horizontal coefficient k_{crit}

$$k_{crit} = \frac{a_{crit}}{g} = \frac{S_E}{W + W_w} \qquad (5\text{-}30)$$

beyond which the rigid block of soil-wall system begin to move.
For a uniform subsoil, assuming a critical planar surface inclined of an angle α_{crit} respect to the horizontal plane, W can be evaluated by the following expression

$$W = \frac{1}{2}\gamma H^2 \tan(90° - \alpha_{crit}) \qquad (5\text{-}31)$$

while, for a rectangular diaphragm with a thickness s, W_w is

$$W_w = \gamma_{RC} \cdot s \cdot H \qquad (5\text{-}32)$$

having indicated with γ_{RC} the unit weight of the wall.
Hence, the expressions of k_{crit} are

$$k_{crit} = \frac{p_{max}}{\gamma H \tan(90° - \alpha_{crit}) + 2\gamma_{RC} s} \qquad \text{TRD} \qquad (5\text{-}33)$$

$$k_{crit} = \frac{2p_{max}}{\gamma H \tan(90° - \alpha_{crit}) + 2\gamma_{RC} s} \qquad \text{RTD} \qquad (5\text{-}34)$$

For a given geometry of a retaining wall, the value of k_{crit} can be obtained by a pseudostatic numerical analysis in which, starting from the static deformed configuration after the excavation, an incremental load is applied on the structure until the failure is reached. As illustrated in the Chapter 3, the α_{crit} value depends on the seismic coefficient k_h. A simple trial and error procedure is sufficient to determine step by step k_h and α_{crit}.
Another possible strategy to evaluate the threshold seismic acceleration a_{crit} with FE or FD methods is that to apply on the mesh nodes of the 2D numerical model an incremental horizontal acceleration a_h. The critical value a_{crit} of the soil-wall system can be defined as the value that corresponds to the condition for which the pseudostatic equilibrium is not satisfied. This type of analysis requires some precautions when the numerical model is defined.
In the next Chapter, examples of application of the procedure to free embedded walls by using a 2D finite element code will be presented.

5.3.5 Dynamic analysis.

Dynamic analysis is based on soil-structure interaction, generally using FE or FD methods. In this category of analysis, effects of earthquake are represented by a set of time histories of seismic motion at the base of the analysis domain chosen for the soil-structure system. A structure is idealized either as linear or as nonlinear, depending on the level of earthquake motion relative to the elastic limit of the structure. Soil is idealized either by equivalent linear or by an effective stress model, depending on the expected strain level in the soil deposit during the design earthquake.

Fairly comprehensive results are obtained from soil-structure interaction analysis, including failure modes of the soil-structure system and the extent of the displacement/stress/strain states. Since this category of analysis is often sensitive to a number of factors, it is especially desirable to confirm the applicability by using a suitable case history or a suitable model test result.
Before to conduct any dynamic analysis of geotechnical systems, the seismic response of the numerical models should be tested by comparing its results with the physical model data or with theoretical solution of the dynamic problems in order to confirm the rightness of the calculation parameters and the modelling techniques.
An extensive parametric study on the seismic response of FE models by using PLAXIS code (Brinkgreve, 2002) has been conducted. The results obtained by the research are described in the Annex B. Here, some of the main aspects of the numerical modelling with the finite element method for dynamic soil-structure interaction are summarized.

5.3.5.1 Numerical integration methods.

The most general approach for the solution of the dynamic response of mechanical systems id the direct numerical integration of the dynamic equilibrium equations. This involves, after the solution is defined at time zero, the attempt to satisfy dynamic equilibrium at discrete points in time. Most methods use equal time intervals at *dt*, 2*dt*, 3*dt*, N*dt*. Many different numerical techniques have been proposed in the literature. However, all approaches can fundamentally be classified as either *explicit* or *implicit* integration methods.
Explicit methods do not involve the solution of a set of linear equations at each time step. Basically, these methods use the differential equation at time "*t*" to predict a solution at time "*t*+*dt*". For most real systems, which contain stiff elements, a very small time step is required in ordr to obtain a stable solution. Therefore, all explicit methods are conditionally stable with respect to the size of the time step.
Implicit methods attempt to satisfy the differential equation at time "*t*" after the solution at time "*t*-*dt*" is found. These methods require the solution of a set of linear equations at each time step. However, larger time steps may be used. Implicit methods can be conditionally or unconditionally stable.
There exist a large number of accurate, higher-order, multi-step methods that have been developed for the numerical solution of differential equations. These multistep methods assume that the solution is a smooth function in which the higher derivatives are continuous. The exact solution of many nonlinear systems requires that accelerations, the second derivative of the displacements, are not smooth functions. This discontinuity of the acceleration is caused by the nonlinear hysteresis of most materials, interfaces, etc. Therefore, only single-step, implicit, unconditional stable methods represents an useful tool for the step-by-step seismic analysis of constructions.
Newmark (1959) presented a family of single-step integration methods for the solution of dynamic problems for both blast and seismic loading. During the past 40 years Newmark's method has been applied to the dynamic analysis of many practical engineering structures. In addition, it has been modified and improved by many other researchers. In order to illustrate the use of this family of numerical integration methods consider the solution of the linear dynamic equilibrium equations written in the following form:

$$\mathbf{M}\ddot{\mathbf{u}}^t + \mathbf{C}\dot{\mathbf{u}}^t + \mathbf{K}\mathbf{u}^t = \mathbf{F}^t \qquad (5\text{-}35)$$

The direct use of Taylor's series provides a rigorous approach to obtain the following two additional equations:

$$\mathbf{u}^t = \mathbf{u}^{t-dt} + dt\dot{\mathbf{u}}^{t-dt} + \frac{dt^2}{2}\ddot{\mathbf{u}}^{t-dt} + \frac{dt^3}{6}\dddot{\mathbf{u}}^{t-dt} + \ldots \qquad (5\text{-}36)$$

$$\dot{\mathbf{u}}^t = \dot{\mathbf{u}}^{t-dt} + dt\ddot{\mathbf{u}}^{t-dt} + \frac{dt^2}{2}\dddot{\mathbf{u}}^{t-dt} + \ldots \qquad (5\text{-}37)$$

Newmark truncated these equations and expressed them in the following form:

$$\mathbf{u}^t = \mathbf{u}^{t-dt} + dt\dot{\mathbf{u}}^{t-dt} + \frac{dt^2}{2}\ddot{\mathbf{u}}^{t-dt} + \alpha_N dt^3 \dddot{\mathbf{u}}^{t-dt} \qquad (5\text{-}38)$$

$$\dot{\mathbf{u}}^t = \dot{\mathbf{u}}^{t-dt} + dt\ddot{\mathbf{u}}^{t-dt} + \beta_N dt^2 \dddot{\mathbf{u}}^{t-dt} \qquad (5\text{-}39)$$

α_N and β_N are two coefficients that control the accuracy of the numerical integration. If the acceleration is assumed to be linear within the time step, the following equation can be written:

$$\dddot{\mathbf{u}} = \left(\frac{\ddot{\mathbf{u}}^t - \ddot{\mathbf{u}}^{t-dt}}{dt}\right) \qquad (5\text{-}40)$$

The substitution of equation (5-40) into equations (5-38) and (5-39) produces Newmark's equations in standard form:

$$\mathbf{u}^t = \mathbf{u}^{t-dt} + dt\dot{\mathbf{u}}^{t-dt} + \left(\frac{1}{2} - \alpha_N\right)dt^2\ddot{\mathbf{u}}^{t-dt} + \alpha_N dt^2\ddot{\mathbf{u}}^t \qquad (5\text{-}41)$$

$$\dot{\mathbf{u}}^t = \dot{\mathbf{u}}^{t-dt} + (1-\beta_N)dt\ddot{\mathbf{u}}^{t-dt} + \beta_N dt^2\ddot{\mathbf{u}}^t \qquad (5\text{-}42)$$

Newmark used equations (5-41), (5-42) and (5-35) iteratively, for each time step, for each displacement DOF of the system. The term $\ddot{\mathbf{u}}^t$ was obtained from equation (5-35) by dividing the equation by the mass associated with the DOF.

Wilson (1962) formulated Newmark's method in matrix notation, added stiffness and mass proportional damping and eliminated the need for iteration by introducing the direct solution of equations at each time step. This requires that equations (5-41) and (5-42) be rewritten in the following form:

$$\ddot{\mathbf{u}}^t = c_0\left(\mathbf{u}^t - \mathbf{u}^{t-dt}\right) + c_2\dot{\mathbf{u}}^{t-dt} + c_3\ddot{\mathbf{u}}^{t-dt} \qquad (5\text{-}43)$$

$$\dot{\mathbf{u}}^t = c_1\left(\mathbf{u}^t - \mathbf{u}^{t-dt}\right) + c_4\dot{\mathbf{u}}^{t-dt} + c_5\ddot{\mathbf{u}}^{t-dt} \qquad (5\text{-}44)$$

where the constants c_0 to c_5 are defined as:

$$c_0 = \frac{1}{\alpha_N dt^2};\ c_1 = \frac{\beta_N}{\alpha_N dt};\ c_2 = \frac{1}{\alpha_N dt};\ c_3 = \alpha_N - \frac{1}{2};\ c_4 = 1 + \frac{\alpha_N}{\beta_N};\ c_5 = dt\left[1 + \beta_N\left(\alpha_N - \frac{1}{2}\right) - \beta_N\right]$$

The substitution of equations (5-43) and (5-44) into equation (5-35) allows the dynamic equilibrium of the system at time "*t*" to be written in terms of the unknown node displacements $\mathbf{u}^t$.

$$(c_0\mathbf{M} + c_1\mathbf{C} + \mathbf{K})\mathbf{u}^t = \mathbf{F}^t + \mathbf{M}\left(c_2\mathbf{u}^{t-dt} - c_3\dot{\mathbf{u}}^{t-dt} - c_1\ddot{\mathbf{u}}^{t-dt}\right) + \mathbf{C}\left(c_1\mathbf{u}^{t-dt} - c_4\dot{\mathbf{u}}^{t-dt} - c_5\ddot{\mathbf{u}}^{t-dt}\right) \qquad (5\text{-}45)$$

The Newmark direct integration algorithm can be summarized as follows:

I. INITIAL CALCULATION

1. Form static stiffness matrix **K**, mass matrix **M** and damping matrix **C**
2. Specify integration parameters α_N and β_N
3. Calculate integration constants c_0 to c_5
4. Form effective stiffness matrix $\overline{\mathbf{K}} = \mathbf{K} + c_0\mathbf{M} + c_1\mathbf{C}$
5. Triangularize effective stiffness matrix $\overline{\mathbf{K}} = \mathbf{L}\mathbf{D}\mathbf{L}^T$
6. Specify initial conditions $\mathbf{u}_0$, $\dot{\mathbf{u}}_0$ $\ddot{\mathbf{u}}_0$

II. FOR EACH TIME STEP

1. Calculate effective load vector

$$\overline{\mathbf{F}}^t = \mathbf{F}^t + \mathbf{M}\left(c_2\mathbf{u}^{t-dt} - c_3\dot{\mathbf{u}}^{t-dt} - c_1\ddot{\mathbf{u}}^{t-dt}\right) + \mathbf{C}\left(c_1\mathbf{u}^{t-dt} - c_4\dot{\mathbf{u}}^{t-dt} - c_5\ddot{\mathbf{u}}^{t-dt}\right)$$

2. Solve for node displacement vector at time *t*

$\mathbf{L}\mathbf{D}\mathbf{L}^T\mathbf{u}^t = \overline{\mathbf{F}}^t$ forward and back-substitution only

3. Calculate node velocities and accelerations at time *t*

$$\dot{\mathbf{u}}^t = c_1\left(\mathbf{u}^t - \mathbf{u}^{t-dt}\right) + c_4\dot{\mathbf{u}}^{t-dt} + c_5\ddot{\mathbf{u}}^{t-dt}$$

$$\ddot{\mathbf{u}}^t = c_0\left(\mathbf{u}^t - \mathbf{u}^{t-dt}\right) + c_2\dot{\mathbf{u}}^{t-dt} + c_3\ddot{\mathbf{u}}^{t-dt}$$

4. Go to Step II.1 with $t = t+dt$

Note that the constants c_0 need to be calculated only once. Also, for linear systems, the effective dynamic stiffness matrix $\overline{\mathbf{K}}$ is formed and triangularized only once.

For zero damping Newmark's method is conditionally stable if

$$\beta_N \geq \frac{1}{2}, \quad \alpha_N \leq \frac{1}{2}, \quad dt \leq \frac{1}{\omega_{\max}\sqrt{\frac{\beta_N}{2} - \alpha_N}} \qquad (5\text{-}46)$$

where ω_{max} is the maximum circular frequency of interest.

Newmark's method is unconditionally stable if

$$2\alpha_N \geq \beta_N \geq \frac{1}{2} \qquad (5\text{-}47)$$

However, if β_N is greater than 1/2 , errors are introduced. These errors are associated with "numerical damping" and "period elongation".

If α_N = 1/4 and β_N = 1/2 the Newmark's method becomes the so-called *constant average acceleration method*. It is identical to the trapezoidal rule that has been used to numerically evaluate the second order differential equations for approximately 100 years. It can easily be shown that this method conserves energy for free vibration problem, **Mü + Ku = 0**, for all possible time steps. Therefore, the sum of the kinematic and strain energy is constant.

$$2E = \dot{\mathbf{u}}^{t\,T}M\dot{\mathbf{u}}^t + \mathbf{u}^{t\,T}K\mathbf{u}^t = \dot{\mathbf{u}}^{t-dt\,T}M\dot{\mathbf{u}}^{t-dt} + \mathbf{u}^{t-dt\,T}K\mathbf{u}^{t-dt} \qquad (5\text{-}48)$$

Wilson (1973) made unconditionally stable the general Newmark's method by the introduction of a θ factor. The introduction of θ is motivated by the observation that an unstable solution tends to oscillate about the true solution. Therefore, if the numerical solution is evaluated within the time increment, the spurious oscillations are minimized. This can be accomplished by a simple modification to the Newmark method by using a time step defined by

$$dt' = \theta dt \tag{5-49}$$

and a load defined by

$$R^{t'} = R^{t-dt} + \theta\left(R^{t} - R^{t-dt}\right) \tag{5-50}$$

where θ ≥ 1.0. After the acceleration $\ddot{\mathbf{u}}^{t}$, vector is evaluated by Newmark's method at the integration time step θ*dt*, values of node accelerations, velocities and displacements are calculated from the following fundamental equations:

$$\ddot{\mathbf{u}}^{t} = \ddot{\mathbf{u}}^{t-dt} + \frac{1}{\theta}\left(\ddot{\mathbf{u}}^{t'} - \ddot{\mathbf{u}}^{t-dt}\right) \tag{5-51}$$

$$\dot{\mathbf{u}}^{t} = \dot{\mathbf{u}}^{t-dt} + (1-\beta_N)dt\ddot{\mathbf{u}}^{t-dt} + \beta_N dt\ddot{\mathbf{u}}^{t} \tag{5-52}$$

$$\mathbf{u}^{t} = \mathbf{u}^{t-dt} + dt\dot{\mathbf{u}}^{t-dt} + \frac{dt^2}{2}(1-2\alpha_N)\ddot{\mathbf{u}}^{t-dt} + \alpha_N dt^2\ddot{\mathbf{u}}^{t} \tag{5-53}$$

The use of the θ factor tends to numerically damp out the high modes of the system. If θ equals to 1.0 Newmark's method is not modified. However, for problems where the higher mode response is important, the errors that are introduced can be large. In addition, the dynamic equilibrium equations are not exactly satisfied at time *t*. Therefore, the author no longer recommends the use of the θ factor. At the time of the introduction of the method, it solved all problems associated with stability of the Newmark family methods. However, during the past twenty years new and more accurate numerical methods have been developed. An example is the α-method (or HHT method) proposed by Hilber et al. (LUSAS, 2000). that uses the Newmark method to solve the following modified equations of motion:

$$\mathbf{M}\ddot{\mathbf{u}}^{t} + (1-\alpha)\mathbf{C}\dot{\mathbf{u}}^{t} + (1-\alpha)\mathbf{K}\mathbf{u}^{t} = (1-\alpha)\mathbf{F}^{t} + \alpha\mathbf{F}^{t} - \alpha\mathbf{C}\dot{\mathbf{u}}^{t\text{-}dt} - \alpha\mathbf{K}\mathbf{u}^{t-dt} \tag{5-54}$$

With α equals to zero the method reduces to the constant acceleration method. It produces numerical energy dissipation in the higher modes that increases with α. If the numerical parameters α, α_N and β_N are selected such that

$$0 \le \alpha \le \frac{1}{3}; \quad \alpha_N = \frac{(1+\alpha)^2}{4}; \quad \beta_N = \frac{1}{2} + \alpha \tag{5-55}$$

an unconditionally stable, second-order accurate scheme results.

It is apparent that a large number of different direct numerical integration methods are possible by specifying different integration parameters. A few of the most commonly used methods are summarized in Table 5-7.

For SDOF systems the central difference method is most accurate and the linear acceleration method is more accurate than the average acceleration method.

Method	α_N	β_N	***Accuracy***
Central Difference (Explicit)	0	1/2	Excellent for small *dt* Unstable for large *dt*
Linear Acceleration	1/6	1/2	Very good for small *dt* Unstable for large *dt*
Average Acceleration	1/4	1/2	Good for small *dt* No energy dissipation
Modified Average Acceleration	1/4	1/2	Good for small *dt* Energy dissipation for large *dt*
Fox-Goodwin	1/12	1/2	Fourth-order accurate Conditionally stable

Table 5-7. *Summary of Newmark's family integration methods.*

For MDOF systems the average acceleration method does not introduce numerical dissipation. If the Newmark integration parameters α_N and β_N are selected according to the equation (5-55), the energy dissipation introduced into the dynamic analysis of subsoil layers for $\alpha > 0$ can be considered as a stiffness proportional damping, as shown in the Annex B.

The basic Newmark constant acceleration method can be extended to nonlinear dynamic analysis. This requires that iteration must be performed at each time step in order to satisfy equilibrium. Also, the incremental stiffness matrix must be formed and triangularized at each iteration or at selective points in time. Many different numerical tricks, including element by element methods, have been developed in order to minimize the computational requirements. Also, the triangularization of the effective incremental stiffness matrix may be avoided by the introduction of iterative solution methods.

5.3.5.2 Critical time steps.

To avoid unreliable numerical responses, before to conduct any type of dynamic analysis, a careful evaluation of the critical time step dt_{crit} for the system should be performed.

The stability condition for an elastic solid discretized into elements of size *dx* is

$$dt < \frac{dx}{c} \qquad (5\text{-}56)$$

where *c* is the maximum speed at which information can propagate.

For a single mass-spring element, the stability condition is

$$dt < 2\sqrt{\frac{m}{k}} \qquad (5\text{-}57)$$

where *m* is the mass and *k* is the stiffness.

In a general system, consisting of solid material and arbitrary networks of interconnected masses and springs, the critical time step is related to the smallest natural period of the system, T_{min}:

$$dt < \frac{T_{\min}}{\pi} \qquad (5\text{-}58)$$

For a finite element mesh, the critical time step depends on the maximum frequency and on the refinement degree of the discretization. In general, the following expression can be used for a single element (Pal, 1998 as quoted by Brinkgreve, 2002):

$$dt_{crit} = \frac{B}{\alpha\sqrt{V_P}\sqrt{1+\frac{B^4}{4S^2}-\frac{B^2}{2S}\left(1+\frac{1-2\nu}{4}\frac{2S}{B^2}\right)}} \qquad (5\text{-}59)$$

The factor α depends on the element type. For a 6-node-element $\alpha = 1/\left(6\sqrt{c_6}\right)$, with c_6 = 5.1282 and for a 15 node-element $\alpha = 1/\left(19\sqrt{c_{15}}\right)$, with $c_{15} \approx 4.9479$ (Zienkiewicz and Taylor, 1991). V_P and v are the compression waves velocity and the Poisson ratio of the element. B and S are the average length and the surface of the element. In a finite element model the critical time step is equal to the minimum value of dt_{crit} according to (5-59) all over the elements. This time step is chosen to ensure that a wave during a single step does not move a distance larger than the minimum dimension of an element.

5.3.5.3 Numerical modelling of soil damping.

In nonlinear time-domain response models, there are generally two sources of damping. One source is hysteretic damping (frequency independent) associated with the area bounded by hysteretic stress-strain loops. When Masing (1926) and extended Masing rules (Pyke, 1979; Wang et al., 1980; Vucetic 1990) are used to represent the unload-reload behaviour of soil, zero damping is encountered at small strains, where the backbone curve is linear. The zero damping condition is incompatible with soil behaviour measured in the laboratory at small strains (e.g. Hardin & Drnevich, 1972; Tatsuoka *et al.* 1978) and can result in overestimation of propagated ground motion. One solution to this problem is to add velocity-proportional viscous damping in the form of dashpots embedded within the material elements. It should be noted that the nature of soil damping at small strains is neither perfectly hysteretic nor perfectly viscous (Vucetic & Dobry 1986; Lanzo & Vucetic 1999). The incorporation of hysteretic or viscous damping schemes into nonlinear codes is merely a convenient approximation for simulation purposes, and is required to ensure numerical stability of lumped mass solutions.

A very common type of damping used in the nonlinear time domain analysis is to assume that the damping matrix **C** is proportional to the mass **M** and stiffness **K** matrices by means of two coefficients, α_R and β_R.

$$\mathbf{C} = \alpha_R\mathbf{M} + \beta_R\mathbf{K} \qquad (5\text{-}60)$$

This type of damping is normally referred to as Rayleigh damping. In mode superposition analysis the damping matrix must have the following properties in order for the modal equations to be uncoupled:

$$2\omega_n\zeta_n = \phi_n^T\mathbf{C}\phi_n \qquad (5\text{-}61)$$

Due to the orthogonality properties of the mass and stiffness matrices, this equation can be rewritten as

$$2\omega_n\zeta_n = \alpha_R + \beta_R\omega_n^2 \qquad \text{or} \qquad \zeta_n = \frac{1}{2}\left(\frac{\alpha_R}{\omega_n} + \beta_R\omega_n\right) \tag{5-62}$$

It is apparent that modal damping can be specified exactly at only two frequencies in order to solve for α_R and β_R in the above equation. The use of stiffness proportional damping has the effect of increasing the damping in the higher modes of the system for which there is no physical justification and can result in significant errors for impact type of problems. Therefore, the use of Rayleigh type of damping is not the best way to simulate damping in the soil but it is often introduced in numerical codes as it is straightforward to implement.

Different procedures were proposed for the evaluation of the Rayleigh damping coefficients (Park & Hashash, 2004; Lanzo et al., 2004). On the base of the parametric study described in detail in the Annex B, it may be concluded that, for geotechnical earthquake engineering problems, the full Rayleigh damping formulation is more accurate than the simplified forms to model the soil viscous damping. In this procedure, the choice of α_R and β_R is based on the solution of the following linear system

$$\begin{bmatrix}\alpha_R \\ \beta_R\end{bmatrix} = \frac{2\zeta}{\omega_n + \omega_m}\begin{bmatrix}\omega_n\omega_m \\ 1\end{bmatrix} \tag{5-63}$$

where ζ, the modal damping ratio, can be identified as the soil damping ratio at low strain level, D_0, ω_n and ω_m are two significant circular natural frequencies of the system that can be fixed as two of the first three natural frequencies, in most of cases.

5.3.5.4 Boundary conditions for dynamic soil-structure interaction analyses.

The modelling of geomechanics problems involves media which, at the scale of the analysis, are better represented as unbounded. Deep underground excavations are normally assumed to be surrounded by an infinite medium, while surface and near-surface structures are assumed to lie on a half-space. Numerical methods relying on the discretization of a finite region of space require that appropriate conditions be enforced at the artificial numerical boundaries. In static analyses, fixed or elastic boundaries (e.g., represented by boundary-element techniques) can be realistically placed at some distance from the region of interest. In dynamic problems, however, such boundary conditions cause the reflection of outward propagating waves back into the model and do not allow the necessary energy radiation. The use of a larger model can minimize the problem, since material damping will absorb most of the energy in the waves reflected from distant boundaries. However, this solution leads to a large computational burden. The alternative is to use quiet (or absorbing) boundaries. Several formulations have been proposed. One of most widespread is the use of viscous boundaries developed by Lysmer and Kuhlemeyer (1969). It is based on the use of independent dashpots in the normal and shear directions at the model boundaries. The method is almost completely effective at absorbing body waves approaching the boundary at angles of incidence greater than 30°. For lower angles of incidence, or for surface waves, there is still energy absorption, but it is not perfect. However, the scheme has the advantage that it operates in the time domain. Its effectiveness has been demonstrated in both finite-element and finite-difference models (Kunar et al., 1977). A variation of the technique proposed by White et al. (1977) is also widely used. More efficient energy absorption

(particularly in the case of Rayleigh waves) requires the use of frequency-dependent elements, which can only be used in frequency-domain analyses (e.g., Lysmer and Waas 1972). These are usually termed "consistent boundaries," and involve the calculation of dynamic stiffness matrices coupling all the boundary degrees-of-freedom. Boundary element methods may be used to derive these matrices (e.g., Wolf 1985). A comparative study of the performance of different types of elementary, viscous and consistent boundaries was documented by Roesset and Ettouney (1977).

The quiet-boundary scheme proposed by Lysmer and Kuhlemeyer (1969) involves dashpots attached independently to the boundary in the normal and shear directions. The dashpots provide viscous normal and shear tractions given by:

$$\sigma_n = -c_1 \rho V_P \dot{u}_x \qquad (5\text{-}64)$$

$$\tau = -c_2 \rho V_S \dot{u}_y \qquad (5\text{-}65)$$

where ρ is the mass density of the material, V_P and V_S are the compression and shear wave velocities, $\dot{u}_x$ and $\dot{u}_y$ are the normal and shear components of the velocity at the boundary, c_1 and c_2 are relaxation coefficients.

Only few suggestions exist in literature for the choice of these parameters (e.g., Lysmer and Kuhlemeyer, 1969). Such constraints are introduced in the model simply by adding frequency-independent terms to the damping matrix of the system.

Dynamic analysis starts from some in-situ condition. If a velocity boundary is used to provide the static stress state, this boundary condition can be replaced by a quiet boundary; the boundary reaction forces will be automatically calculated and maintained throughout the dynamic loading phase. Note that the boundaries must not be freed before applying the quiet boundary condition, otherwise the reaction forces will be lost.

Quiet boundaries are best-suited when the dynamic source is within a mesh while should not be used alongside boundaries of a calculation domain when the dynamic source is applied as a boundary condition at the top or base, because the wave energy will "leak out" of the sides. In this situation, other types of boundary conditions should be adopted such as perfectly matched layers (Berenger, 1994), infinite elements (Kramer, 1996; Ross, 2004), free-field boundaries (Cundall et al., 1980).

The numerical study described in the Annex B by using the FE code PLAXIS on homogeneous linear visco-elastic layers crossed by vertical shear waves has shown that the simple assumption of the lateral adsorbent boundaries is not able to reproduce the expected seismic response of the subsoil. The more accurate solutions were found by adopting the finite element models sketched in Figure 5-12. These models are characterized by a central domain with a refined mesh, in which the interest of the study is concentrated, and two lateral domains with a coarse mesh, that have the only aim to minimize the effects of spurious waves reflected on the boundaries. The boundary conditions are the following:

1. LOWER BOUNDARY: fixed nodes with a prescribed acceleration (for rigid bedrock) or shear stress (for elastic bedrock) time history, that is decreased linearly from the central part to the vertical boundaries until zero
2. LATERAL BOUNDARIES: fixed nodes
3. UPPER BOUNDARY: free surface conditions.

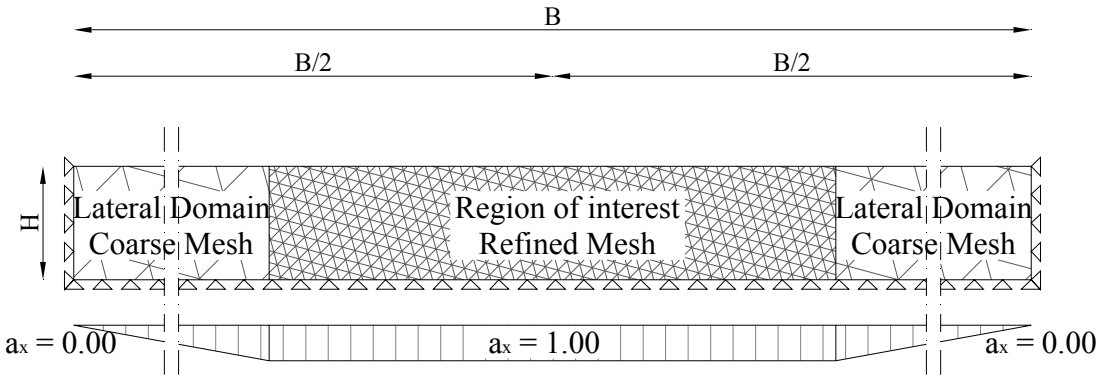

Figure 5-12. *Sketch of numerical models able to minimize the reflected waves on lateral boundaries.*

Mesh dimension ratios *B*/2*H* between the half-width, *B*/2, and the height, *H*, of the model of order of 15 allow numerically simulating the free field conditions.

6 CASE STUDY: CANTILEVER DIAPHRAGMS EMBEDDED IN DRY LOOSE AND DENSE SAND LAYERS.

In this chapter, the seismic responses of cantilever diaphragms embedded in dry loose and dense LB sand layers and subjected to the accelerometer registrations of the Tolmezzo and Sturno Stations during the Friuli 1976 and Irpinia 1980 earthquakes, respectively, are studied by using the various types of analyses described in the previous chapter. The geometrical schemes of two centrifuge models are considered. The results of different methods are presented and compared. The nonlinear static and dynamic analyses were performed by using the FE code PLAXIS v.8.2 (Brinkgreve, 2002). In order to verify the free-field motions estimated by the complete dynamic analyses and to compute the site amplification for the simplified dynamic analyses, the codes EERA (Bardet et al., 2000) and NERA (Bardet and Tobita, 2001) were used.

6.1 DESCRIPTION OF THE EXAMINED PROBLEMS.

6.1.1 Geometries.

The geometry of the examined problems is plotted in Figure 5-1. They are constituted by cantilever walls with a total length of H = 8 meters and thickness of s = 0.6m and s = 1.0m embedded for 4 meters into dry loose (D_r = 20%) and dense (D_r = 80%) layers of Leighton Buzzard sand. The height of excavation is equal to h = 4 meters. The sandy layers have a thickness of 16m and are based on a very stiff bedrock that was assumed as rigid in the analyses. For simplicity, potential loadings on the backfill are not considered and the conditions of unbounded media is supposed at the sides of the wall.

The water level is assumed at or below the bedrock, in order to leave out effects of dynamic pore pressures in the calculation.

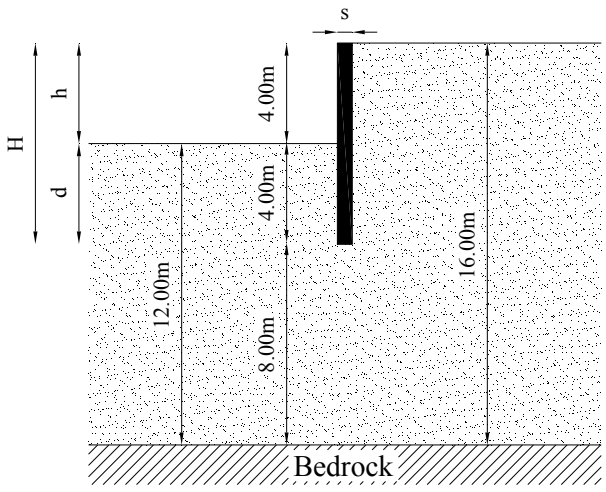

Figure 6-1. *Geometry of the examined problem.*

6.1.2 Soil properties.

The physical and mechanical properties of the sand layers are referred to those experimentally determined by means of the laboratory tests on loose and dense samples described in the Annex A. Table 3-1 shows the parameters adopted in the analyses.

Parameters	Symbol	LOOSE SAND	DENSE SAND
Relative density	D_r	20%	80%
Void ratio	e	0.934	0.693
Unit weight (kN/m^3)	γ	13.44	15.35
Cohesion (kPa)	c'	$5x10^{-4}$	$5x10^{-4}$
Friction angle	ϕ'	33°	40°
Dilatancy angle	ψ	0°	10°

Table 6-1. *Physical and mechanical parameters of LB sand layers.*

The adopted stiffness and damping profiles derive from the experimental measurements of the initial shear modulus G_0 and damping ratio D_0 during the isotropic compressions of the torsional shear tests. In particular, adopting the relationships (A-11) and (A-14) particularized for the assumed relative densities of the sand layers and fixing the earth pressure coefficient at rest k_0 = 0.5, both for loose and dense sand, the estimated shear wave velocity and damping ratio profiles are those reported in Figure 6-2.

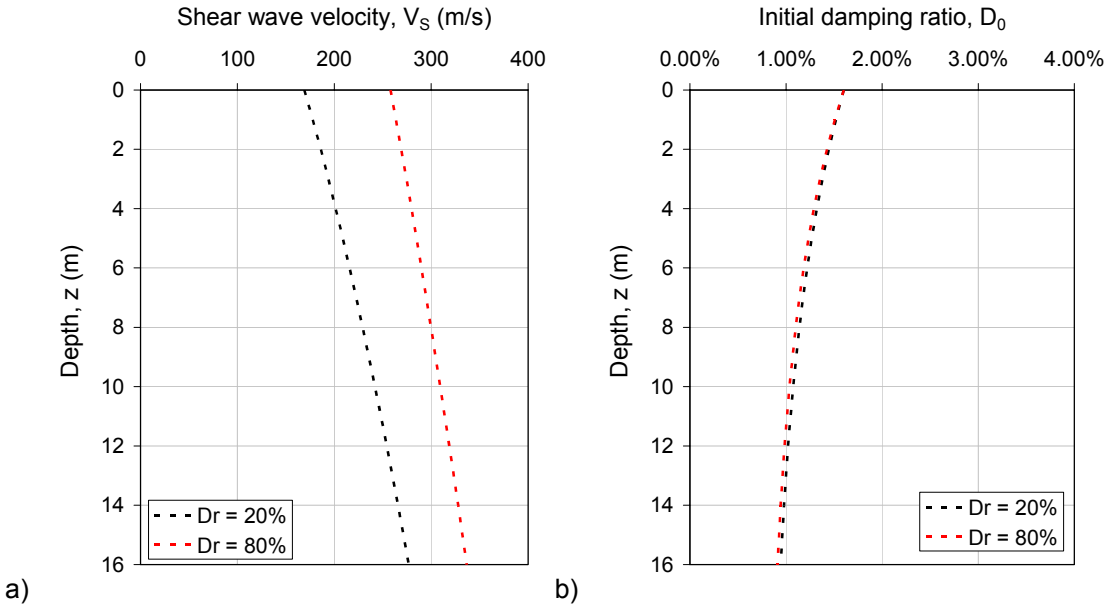

Figure 6-2. *Shear wave velocity (a) and damping ratio (b) profiles for loose (D_r = 20%) and dense (D_r = 80%) LB sand layers.*

To take into account the nonlinear behaviour of the sand, on the base of the results of the cyclic torsional shear tests, the decay curves shown in Figure 6-3 are assumed in the analyses.

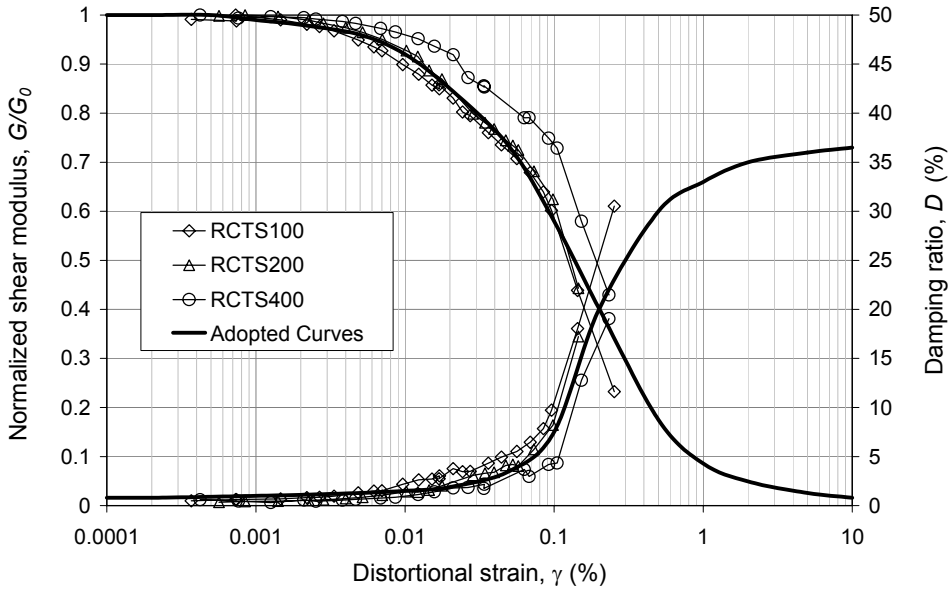

Figure 6-3. *Assumed decay curves of the LB sandy layers, both for loose and dense state.*

The adopted curves are close to those measured during the tests with lower mean effective stress (RCTS100 and RCTS200) that simulate better the actual stress state of the soil interacting with the walls.

6.1.3 Diaphragms properties.

The diaphragms are schematized as rigid in simplified analyses and as linear elastic plates in the complete analyses, where the soil-structure interaction can be modelled.

In PLAXIS, for the elastic behaviour an axial stiffness, *EA*, and a flexural rigidity, *EI*, should be specified as material properties. For plane strain models the values of *EA* and *EI* relate to a stiffness per unit width in the out-of-plane direction. Hence, the axial stiffness, *EA*, is given in force per unit width and the flexural rigidity, *EI*, is given in force length squared per unit width. From the ratio of *EI* and *EA* an equivalent thickness for an equivalent plate (s_{eq}) is automatically calculated from the equation:

$$s_{eq} = \sqrt{12\frac{EI}{EA}} \qquad (6\text{-}1)$$

For the modelling of plates, PLAXIS uses the Mindlin beam theory as described in Bathe (1982). This means that, in addition to bending, shear deformation is taken into account. The shear stiffness of the plate is determined from:

$$\text{SHEAR STIFFNESS} = \frac{5EA}{12(1+\upsilon)} = \frac{5E(s_{eq}\cdot 1m)}{12(1+\upsilon)} \qquad (6\text{-}2)$$

This implies that the shear stiffness is determined from the assumption that the plate has a rectangular cross-section. In the case of modelling a solid wall, this will give the correct shear deformation. However, in the case of steel profile elements, like sheet-pile walls, the computed shear deformation may be too large. You can check this by judging the value of s_{eq}. For steel profile elements, s_{eq} should

be at least of the order of a factor 10 times smaller than the length of the plate to ensure negligible shear deformations.

In addition to the above stiffness parameters, a Poisson's ratio, v, is required. For thin structures with a certain profile or structures that are relatively flexible in the out-of-plane direction (like sheet-pile walls), it is advisable to set Poisson's ratio to zero. For real massive structures (like concrete walls) it is more realistic to enter a true Poisson's ratio of the order of 0.15. Since PLAXIS considers plates (extending in the out-of-plane direction) rather than beams (one-dimensional structures), the value of Poisson's ratio will influence the flexural rigidity of the plate as follows:

$$\text{Input value of flexural rigidity} \quad EI \tag{6-3}$$

$$\text{Observed value of flexural rigidity} \quad \frac{EI}{1-\upsilon^2} \tag{6-4}$$

The stiffening effect of Poisson's ratio is caused by the stresses in the out-of-plane direction (σ_{zz}) and the fact that strains are prevented in this direction.

Furthermore, in a material set for plates a specific weight *w* can be specified, which is entered as a force per unit area. For relatively massive structures this force is, in principle, obtained by multiplying the unit weight of the plate material by the thickness of the plate. Note that in a finite element model, plates are superimposed on a continuum and therefore 'overlap' the soil. To calculate accurately the total weight of soil and structures in the model, the unit weight of the soil should be subtracted from the unit weight of the plate material. For sheet-pile walls the weight (force per unit area) is generally provided by the manufacturer. This value can be adopted directly since sheet-pile walls usually occupy relatively little volume.

6.1.4 Seismic input motions.

To highlight the influence of the input motion on nonlinear seismic responses of the examined problems, two earthquake signals were considered.

The first is the WE component of the accelerometer registration at Tolmezzo Station for the main shock of the earthquake of Friuli (Italy) on May 6th, 1976, denoted as TMZ-270. The data were sampled at 200 Hz for a total number of 7279 registration points. The horizontal peak acceleration, equal to 0.315 g, was reached at the time t=3.935 s. Most of the energy is included into a frequency range between 0.8 and 5 Hz, with a predominant frequency of 1.5 Hz. The Arias intensity is 1.20 m/s and the significant duration (Trifunac and Brady, 1975) is 4.92 s. The time-history of acceleration and the Fourier spectrum of amplitude are reported in Figure 6-4.

The second is the WE component of the accelerometer registration at Sturno Station for the main shock of the earthquake of Irpinia (Italy) on November 23rd, 1980, denoted as STU-270. The sampling frequency is 400 Hz for a total number of 15737 registration points. The horizontal peak acceleration, equal to 0.321g, was reached at the time t = 5.2375 s. The predominant frequency is 0.44 Hz. The Arias intensity and the significant duration are 1.39 m/s and 15.2 s, respectively. The acceleration time-history and the Fourier spectrum of amplitude are plotted in Figure 6-5.

Even if the two considered seismic motions have similar maximum acceleration, they are characterized by different frequency contents.

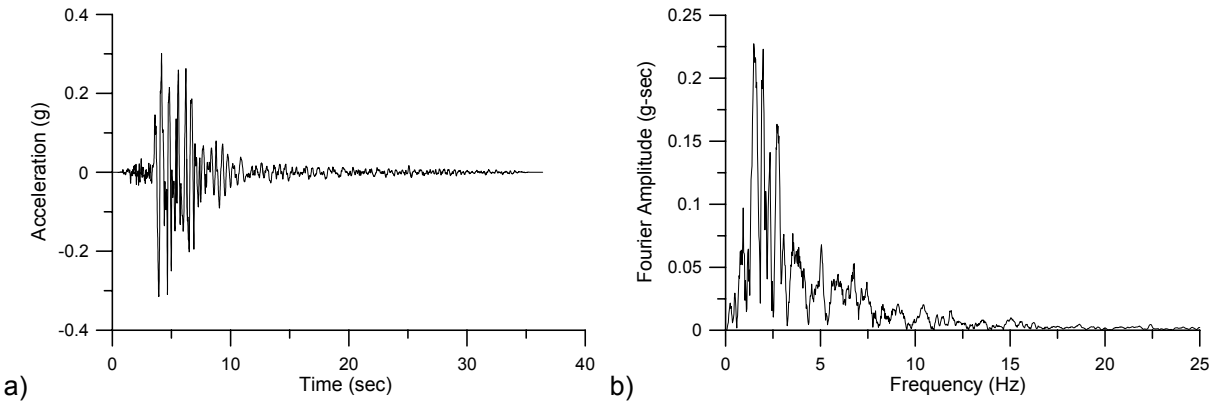

Figure 6-4. *TMZ-270 Seismic input signal: a) acceleration time-history; b) Fourier spectrum.*

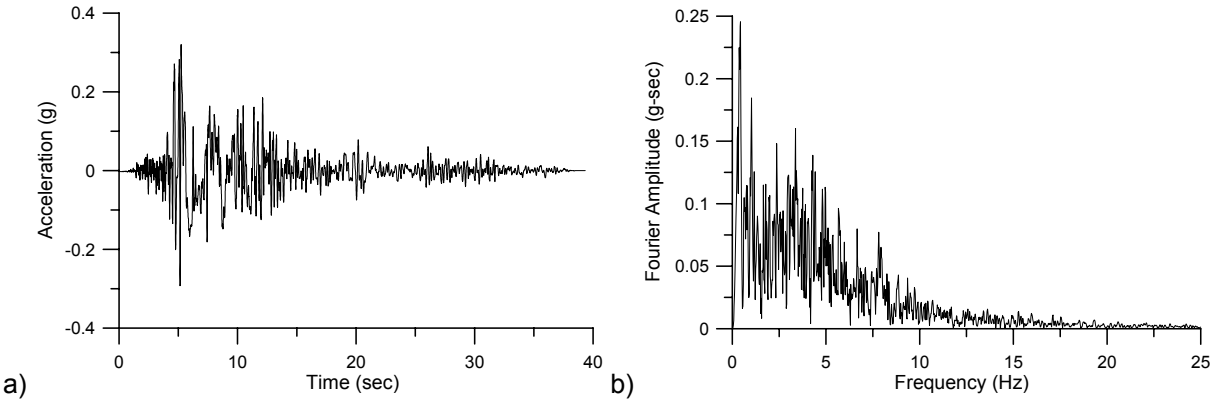

Figure 6-5. *STU-270 Seismic input signal: a) acceleration time-history; b) Fourier spectrum.*

6.1.5 Analyses program.

In order to simplify the notation for the description of the results of the different types of analyses, in the following, the analysis codes reported in Table 6-2 will be used. In the adopted acronyms, the first letter indicates the sandy layer (loose or dense), the three numbers remember the thickness of the wall and the last three letters stay for the considered earthquake motion.

ANALYSIS CODE	SAND	WALL	EARTHQUAKE MOTION
L060TMZ	LOOSE	*s* = 0.60m	TMZ-270
L100TMZ	LOOSE	*s* = 1.00m	TMZ-270
L060STU	LOOSE	*s* = 0.60m	STU-270
L100STU	LOOSE	*s* = 1.00m	STU-270
D060TMZ	DENSE	*s* = 0.60m	TMZ-270
D100TMZ	DENSE	*s* = 1.00m	TMZ-270
D060STU	DENSE	*s* = 0.60m	STU-270
D100STU	DENSE	*s* = 1.00m	STU-270

Table 6-2. *Analyses program.*

6.2 SIMPLIFIED ANALYSES.

The first step for the prediction of the seismic behaviour of an embedded retaining walls is the calculation of the critical seismic coefficient k_{crit}, for example, by using a pseudostatic approach of the limit equilibrium method. In this type of analysis, a widespread practice is the neglecting of the wall weight in the forces limit equilibrium. Then, k_{crit} depends only on the soil strength and, for the two wall, s = 0.6m and s = 1.0m, assumes an unique value.

With a simple trial and error procedure in which:

- a tentative value of the seismic coefficient k_h was fixed
- the seismic earth pressure coefficients K_{AE} and K_{PE} were evaluated by means of the M-O and Lancellotta methods, as described in the previous chapter
- the limit depth ratio d/h was estimated by adopting the equation (5-3), till to have the assigned value of d/h = 1

for the examined problems, the following critical seismic coefficient k_{crit} were calculated:

ANALYSIS CODE	SAND	WALL	k_{crit}	$\Delta M_{max}/\gamma h^3$
L060TMZ	LOOSE	s = 0.60m	0.228	0.074
L100TMZ	LOOSE	s = 1.00m	0.228	0.074
L060STU	LOOSE	s = 0.60m	0.228	0.074
L100STU	LOOSE	s = 1.00m	0.228	0.074
D060TMZ	DENSE	s = 0.60m	0.447	0.146
D100TMZ	DENSE	s = 1.00m	0.447	0.146
D060STU	DENSE	s = 0.60m	0.447	0.146
D100STU	DENSE	s = 1.00m	0.447	0.146

Table 6-3. *Seismic capacities of the retaining walls predicted by the pseudostatic limit equilibrium method.*

In Table 6-3 the normalized seismic increments of maximum bending moment $\Delta M_{max}/\gamma h^3$ were also reported. The values were estimated as the difference the static and the seismic prediction of the bending moments.

To assess the earthquake-induced displacements, the seismic horizontal coefficient k_h related to each seismic motion should be estimated. For this aim, the indications of the New Italian Building code (NTC-2008) are considered. Both of loose and dense sand layers can be classified as soil type C (180 m/s < V_{S16} < 360 m/s) at which a soil factor S = 1.5 corresponds (maximum value for the category). The α-value can be assumed equal to α = 1 (for H < 10m and ground type C, see Figure 5-3) while the β-value, assuming the acceptable limit displacement $u_x = 0.005\ H = 0.005 \cdot 8.00\text{m} = 4$ cm, may be fixed as β = 0.55 (see Figure 5-4). The expression (5-2) allows computing the seismic coefficients k_h for TMZ-270 and STU-270 earthquake motions given in Table 6-4. In the same Table, the seismic performances of the walls predicted by the simplified analyses are also summarized. The seismic factors of safety, FS, were estimated by means of equation (5-7) while the relationship (5-17)

proposed by Uwabe (1983) for anchored sheet pile walls in nonliquefiable sites was used to evaluate the horizontal displacements u_x, normalized with respect to the height of excavation h.

ANALYSIS CODE	k_{crit}	$\Delta M_{max}/\gamma h^3$	k_h	FS = k_{crit} / k_h	u_x/h
L060TMZ	0.228	0.074	0.260	0.877	9.55%
L060STU	0.228	0.074	0.264	0.864	9.70%
L100TMZ	0.228	0.074	0.260	0.877	9.55%
L100STU	0.228	0.074	0.264	0.864	9.70%
D060TMZ	0.447	0.146	0.260	1.719	4.68%
D060STU	0.447	0.146	0.264	1.693	4.75%
D100TMZ	0.447	0.146	0.260	1.719	4.68%
D100STU	0.447	0.146	0.264	1.693	4.75%

Table 6-4. *Seismic performances of the retaining walls predicted by the simplified analyses.*

6.3 SIMPLIFIED DYNAMIC ANALYSES.

A simplified dynamic analysis of a retaining wall is composed by a pseudostatic analysis, by means of which the critical acceleration is estimated, and a pseudodynamic analysis, that allows computing the earthquake-induced displacements of the system when subjected to a given input motion.

6.3.1 Pseudostatic analyses.

As previously mentioned, in the current design of the embedded walls, the inertia forces related to the masses of the structure are not considered in the forces balance. In the simplified dynamic analysis, the earthquake-induced displacements should be predicted with more accuracy than with the simplified methods. Then, the calculation of the critical acceleration of the system can not leave out of consideration these forces in the limit equilibrium conditions.

Considering them, the two walls present different seismic performances. In Table 6-5 the seismic capacities of the examined retaining systems are carried out.

It can be seen the worst behaviour of the more stiff wall (s = 1.0m) than the deformable one (s = 0.6m), both in terms of the critical seismic coefficient and the maximum bending moment.

In order to show the influence of the wall inertia forces on the seismic performances of the structures, the normalized displacements predicted by the empirical relationship (5-19) were recalculated and reported in Table 6-6.

ANALYSIS CODE	SAND	WALL	k_{crit}	$\Delta M_{max}/\gamma h^3$
L060TMZ	LOOSE	*s* = 0.60m	0.167	0.093
L100TMZ	LOOSE	*s* = 1.00m	0.140	0.100
L060STU	LOOSE	*s* = 0.60m	0.167	0.093
L100STU	LOOSE	*s* = 1.00m	0.140	0.100
D060TMZ	DENSE	*s* = 0.60m	0.370	0.159
D100TMZ	DENSE	*s* = 1.00m	0.328	0.178
D060STU	DENSE	*s* = 0.60m	0.370	0.159
D100STU	DENSE	*s* = 1.00m	0.328	0.178

Table 6-5. *Seismic capacities of the retaining walls predicted by the pseudostatic limit equilibrium method considering the inertia forces due to the wall masses.*

ANALYSIS CODE	k_{crit}	$\Delta M_{max}/\gamma h^3$	k_h	FS = k_{crit} / k_h	u_x/h
L060TMZ	0.167	0.093	0.260	0.642	13.19%
L100TMZ	0.140	0.100	0.260	0.538	15.82%
L060STU	0.167	0.093	0.264	0.633	13.38%
L100STU	0.140	0.100	0.264	0.530	16.06%
D060TMZ	0.370	0.159	0.260	1.423	5.73%
D100TMZ	0.328	0.178	0.260	1.262	6.51%
D060STU	0.370	0.159	0.264	1.402	5.82%
D100STU	0.328	0.178	0.264	1.242	6.62%

Table 6-6. *Seismic performances of the retaining walls predicted by the simplified analyses accounting for the wall weight.*

6.3.2 Free field motions.

Before to conduct any type of dynamic analysis, a good practice is to perform local site response analyses in order to highlight the amplification of the seismic motion due to the stratigraphic conditions. In this study, various type of ground response analyses were carried out by assuming different soil constitutive models and integration techniques. The results are presented and compared in this subsection.

The computer codes used in the analyses are the following:

- EERA (Bardet et al., 2000), that stands for Equivalent-linear Earthquake site Response Analysis. It is a modern implementation of the well-known concepts of the equivalent linear site response analysis that was first implemented in the SHAKE code (Schnabel et al., 1972). The input and output are fully integrated with the spreadsheet program MS-Excel. This code permits to perform frequency domain analyses for linear and equivalent linear stratified subsoils. The bedrock can be modelled as rigid, if the option “inside” is selected in the Profile

spreadsheet of the program, or as elastic, by assigning its properties to the last layer and selecting the option “outcrop” in the Profile spreadsheet. In order to transform the signal from the outcropping rock to the bedrock, placed at the bottom of the soil layer, EERA applies a suitable transfer function to the input signal.

- NERA (Bardet and Tobita, 2001), that stands for Nonlinear Earthquake site Response Analysis. It allows solving the 1-D vertical shear wave propagation in a nonlinear hysteretic medium in the time domain. The constitutive model implemented in NERA is that proposed by Iwan (1967) and Mroz (1967), IM model, which simulates nonlinear stress-strain curves using a series of n mechanical elements, having different stiffness k_i and sliding resistance R_i. The IM model assumes that the hysteretic stress-strain loop follows the Masing rules. For this reason, the damping ratio curves directly derive from the $G/G_{max}(\gamma)$ curves and, then, they can not be defined independently as in the case of the equivalent linear model. Therefore, the damping ratio curves that derive from the IM model are shown and compared with the assumed curves in the previously presented Figure 3. The central difference method is used to perform the 1-D time domain analyses by adopting a finite difference formulation.
- PLAXIS (Brinkgreve, 2002) that is a commercial finite element code. It allows performing stress-strain analyses for various types of geotechnical systems. An earthquake analysis can be performed by imposing an acceleration time-history at the base of the FE model and solving the equations of motion in the time domain by adopting a Newmark type implicit time integration scheme. Different material models can be chosen to describe the soil behaviour. In this study, only the linear elastic and the Mohr-Coulomb models were considered.

6.3.2.1 Linear analyses.

As described in the Annex B, to rightly define the Rayleigh damping parameters for the time domain analyses, the natural frequencies of the layers should be estimated. For this reason, linear analyses were performed by means of the code EERA. Figure 6-6 shows the discretized subsoil profiles adopted in the frequency domain analyses, in the following abbreviated as FDA, while the calculated natural frequencies are summarized in Table 6-7.

Choosing f_1 and f_2 as target frequencies in the relationship (B-11), for the assumed profiles, the corresponding Rayleigh parameters profiles are those plotted in Figure 6-7.

To ensure the rightness of α_R and β_R values and the effectiveness of the lateral boundary conditions presented in the Annex B, the amplification functions of the two sandy layers calculated by the linear time domain analyses, marked as TDA, and the FDA are compared in Figure 6-8. The numerical results of the time domain analyses were obtained by the code PLAXIS assuming a constant acceleration scheme for the time integration ($\alpha = 0$; $\alpha_N = 0.25$; $\beta_N = 0.5$) and a mesh dimension ratio B/2H = 15. The average element size in the central part of the calculation domain was fixed according to Kuhlemeyer and Lysmer (1973). Obviously, because the soil was modelled as linear elastic, the amplification functions do not depend to the input motion.

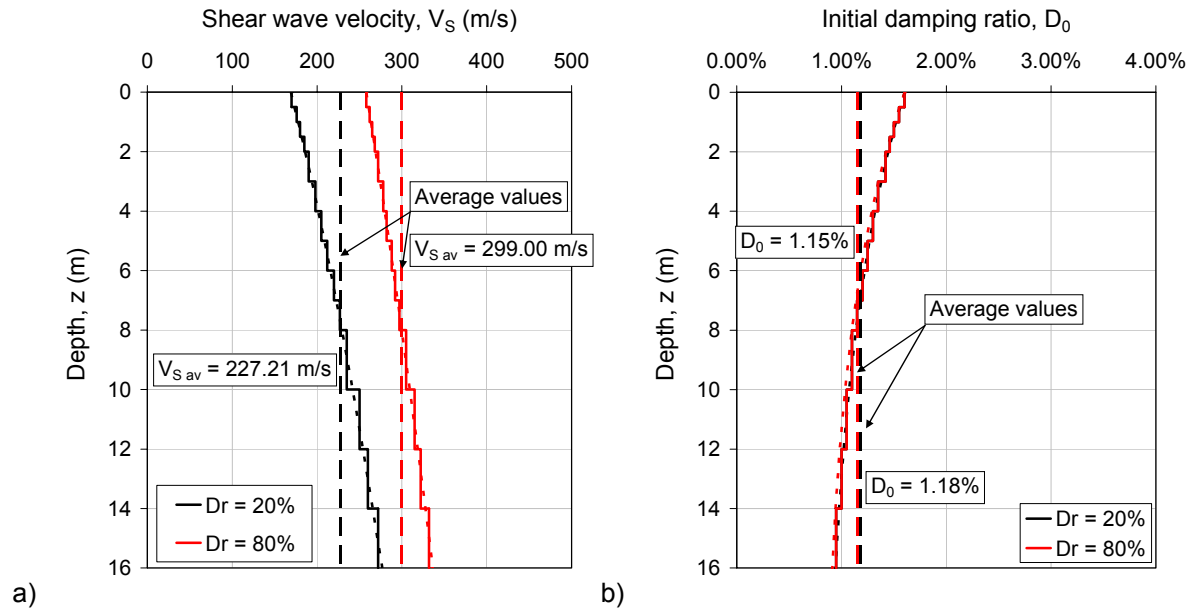

Figure 6-6. *Shear wave velocity (a) and damping ratio (b) profiles for loose (D_r = 20%) and dense (D_r = 80%) LB sand layers adopted in the linear frequency domain analyses.*

	Frequencies (Hz)			Circular frequencies		
SAND	**f_1**	**f_2**	**f_3**	**ω_1**	**ω_2**	**ω_3**
LOOSE	3.84	10.59	17.52	24.13	66.54	110.08
DENSE	4.89	14.02	23.29	30.72	88.09	146.34

Table 6-7. *Natural frequencies of the LB sandy layers obtained by means of linear frequency domain analyses.*

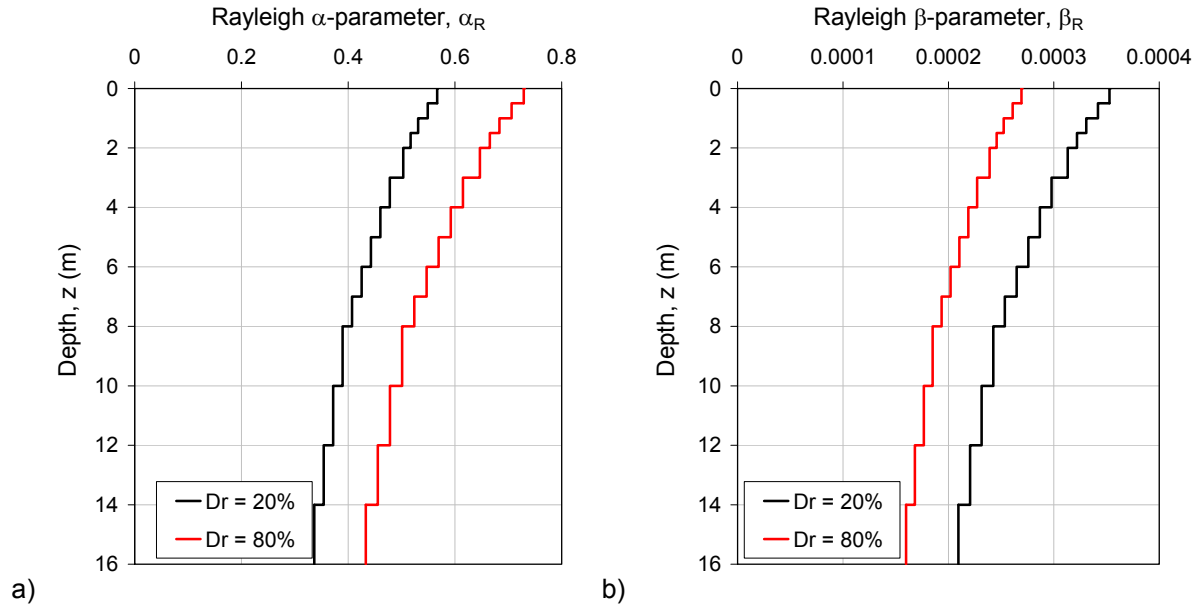

Figure 6-7. *Rayleigh α (a) and β (b) damping parameters profiles for loose (D_r = 20%) and dense (D_r = 80%) LB sand layers adopted in the time domain analyses.*

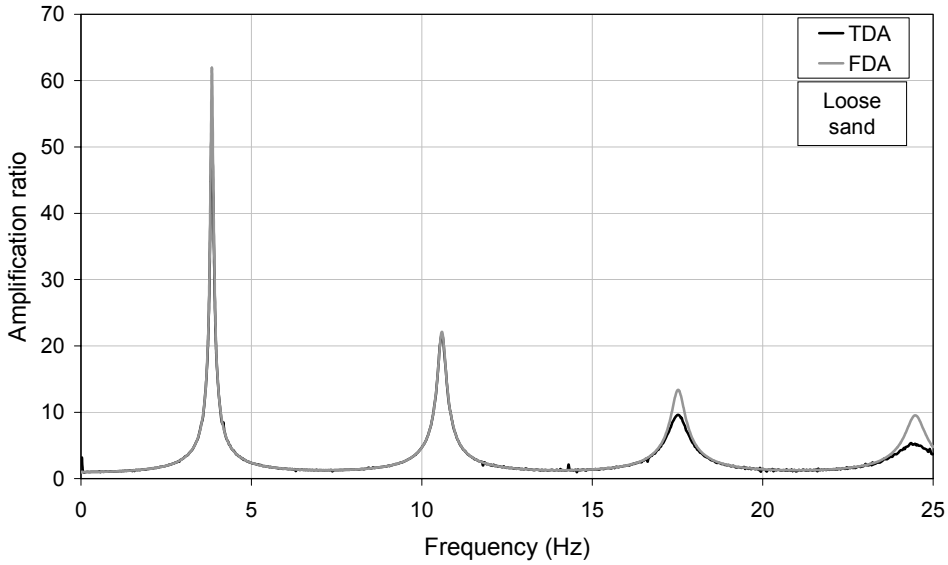

a)

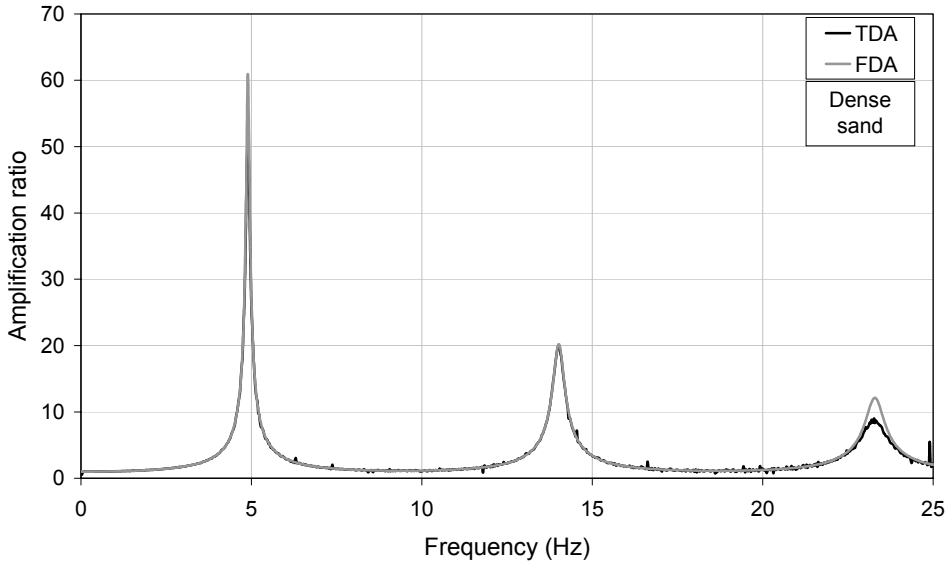

b)

Figure 6-8. *Comparisons between the linear time (TDA) and frequency (FDA) domain analyses in terms of amplification functions of the loose (a) and the dense (b) sand layers.*

It can be seen the perfect agreement between the natural frequencies estimated by the TDA and the FDA. The differences between the two types of analyses exist only on the amplification peaks greater than the second. This is a consequence of the choice of the target frequencies for the definition of the Rayleigh damping parameters. However, the discrepancies can be considered acceptable, as demonstrated by the maximum acceleration profiles shown in Figure 6-9 and Figure 6-10. It seems that, for the loose stratum, the soil amplification is larger for the TMZ-270 seismic motion while, for the dense layer, STU-270 earthquake induces larger maximum accelerations near to the surface.

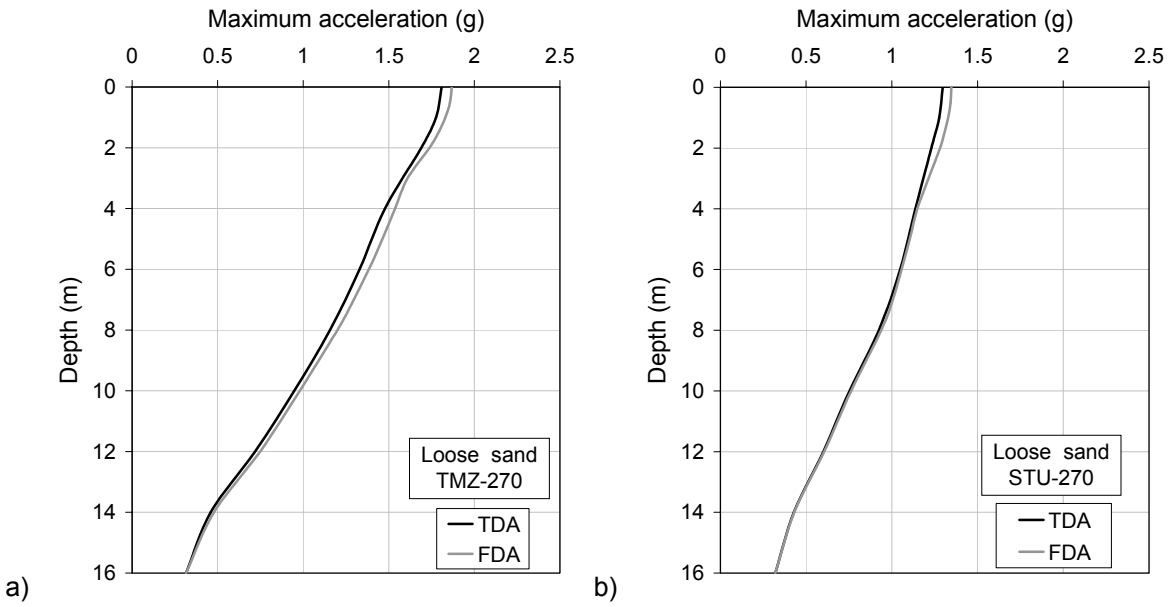

Figure 6-9. *Maximum acceleration profiles computed by the linear analyses for loose sand layer: a) TMZ-270 input motion; b) STU-270 input motion.*

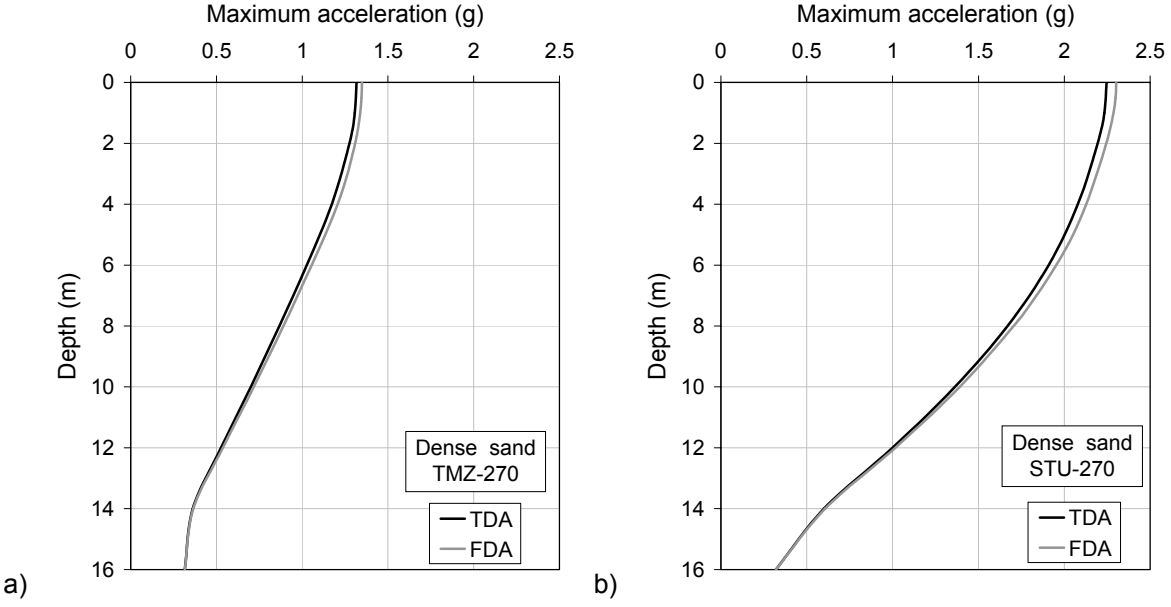

Figure 6-10. *Maximum acceleration profiles computed by the linear analyses for dense sand layer: a) TMZ-270 input motion; b) STU-270 input motion.*

6.3.2.2 Equivalent linear and nonlinear analyses.

The experimental results of the laboratory tests performed on the LB sand and described in the Annex A have shown the influence of the shear strain level on the shear modulus and the damping ratio of the Leighton Buzzard sand 100/170. To take into account the nonlinear behaviour of the sand, here, three different approaches were considered:

- Equivalent Linear (Seed and Idriss, 1968): it was first implemented in the code SHAKE (Schnabel et al., 1972) and then in the EERA. First, in the equivalent linear method, the shear modulus G is taken as the secant value G_{sec}, in relation to the shear strain amplitude γ, and

the damping ratio D is the value that produces the same energy loss in a single cycle as the hysteresis stress-strain loop of the irreversible soil behaviour. Then, the equivalent parameters G and D are modified considering the proper strain levels that develops at each soil layer, using an iterative procedure.

- IM model (Iwan, 1967; Mroz, 1967): it simulates nonlinear stress-strain curves using a series of *n* mechanical elements, having different stiffness k_i and sliding resistance R_i. The IM model assumes that the hysteretic stress-strain loop follows the Masing rule. For this reason, the damping ratio curves directly derive from the $G/G_{max}(\gamma)$ curves and then, they can not be defined independently as in the case of the linear equivalent model. Therefore, the damping ratio curve that derive from the IM model is shown in Figure 6-11.
- MC model (as quoted in Brinkgreve, 2002): Mohr-Coulomb model is a linear elastic-perfectly plastic constitutive law. The yield condition is an extension of Coulomb's friction law to general states of stress (Smith and Griffith, 1982). In fact, this condition ensures that Coulomb's friction law is obeyed in any plane within a material element. Three of the five model parameters define the yield function (friction angle, ϕ, and cohesion, *c*) and the plastic potential (dilatancy angle, ψ). The other two (Young modulus, *E*, and Poisson ratio, ν) individuate the elastic behaviour of the medium. The decay of *G* at a fixed depth *z* can be described by means of a trilinear curve: two horizontal lines characterized by $G = G_0$ and $G = 0$ connected by a vertical line in correspondence of a shear strain level γ_f depending on the model parameters and the stress state acting at *z*. The damping ratio *D* is zero when the plasticity is not involved in the deformation process, while depends also on the induced distortional strain level γ_{max}, when $\gamma_{fmax} > \gamma_f$.

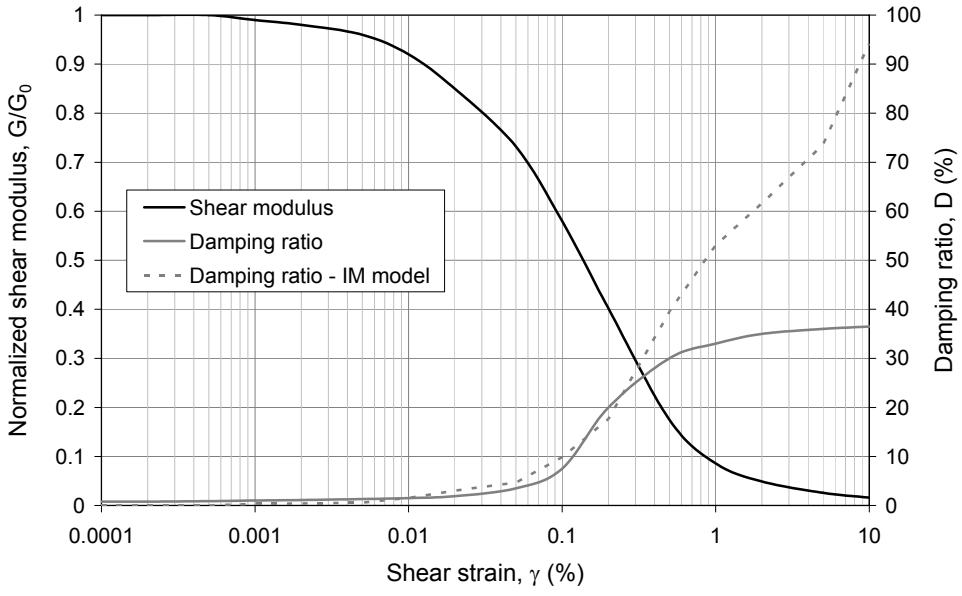

Figure 6-11. *Decay curves of loose and dense sand adopted in the site response analyses.*

Figure 6-12 and Figure 6-13 plots the comparisons between the free field motions computed by the different analyses in terms of response spectra and maximum acceleration profiles, both for TMZ-270 and STU-270 and for loose and dense sand layers.

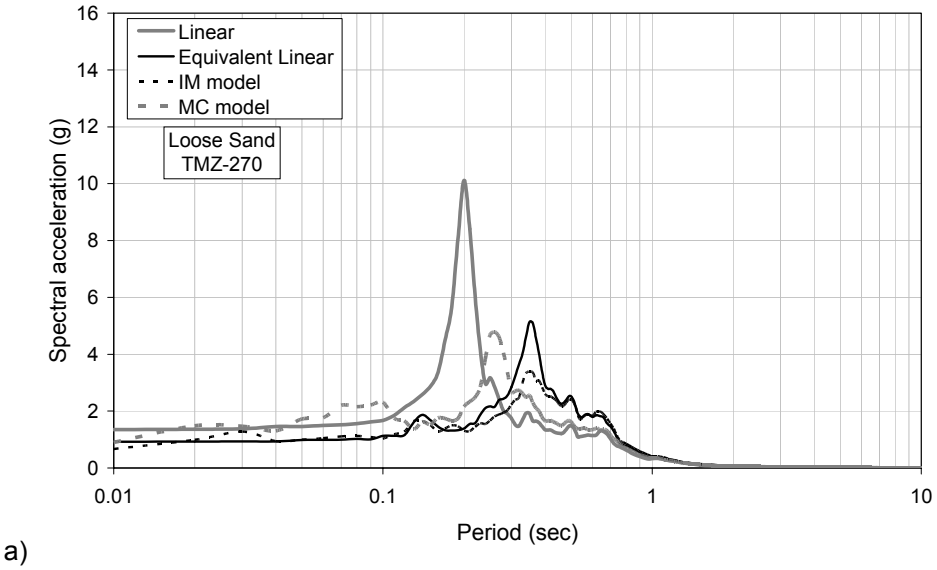

a)

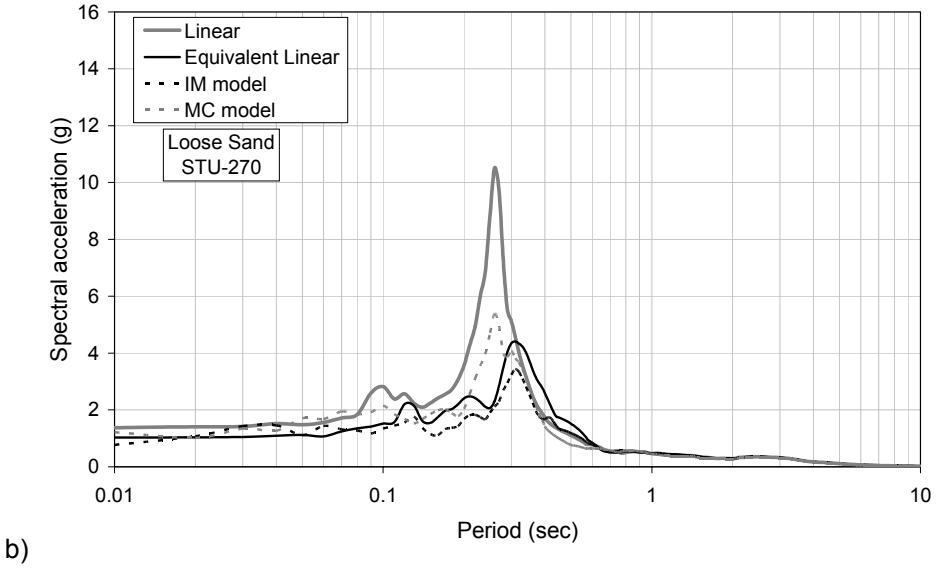

b)

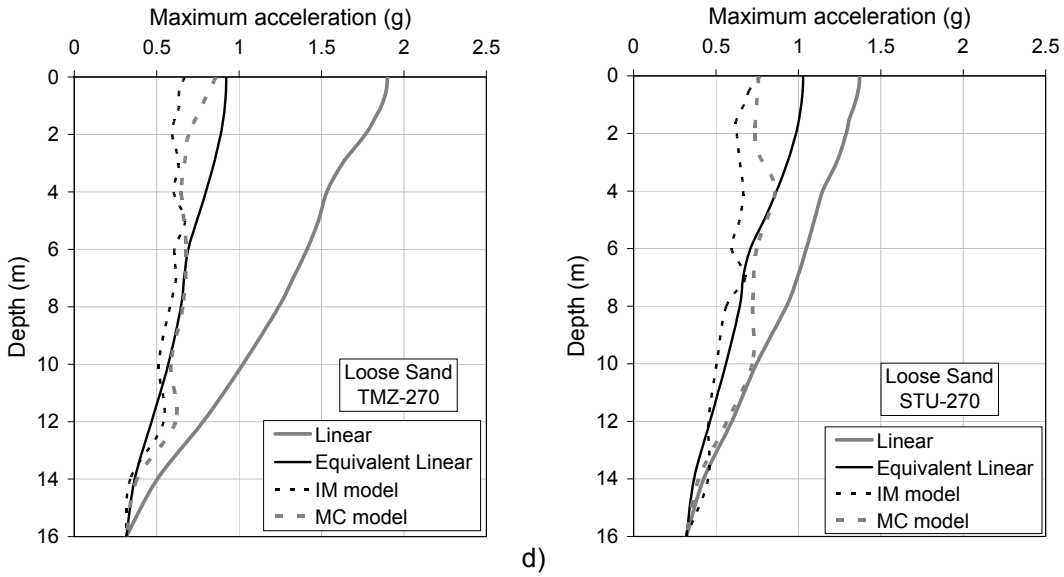

c) d)

Figure 6-12. *Comparisons between the calculated free field motions for loose sand layer: a) response spectrum at surface for TMZ-270; b) response spectra at surface for STU-270; c) maximum acceleration profiles for TMZ-270; d) maximum acceleration profiles for STU-270.*

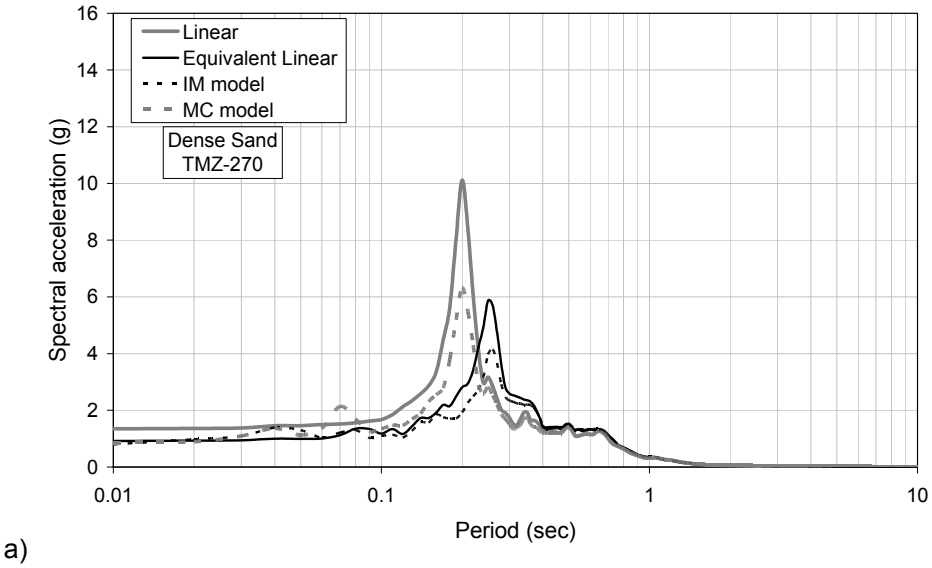

a)

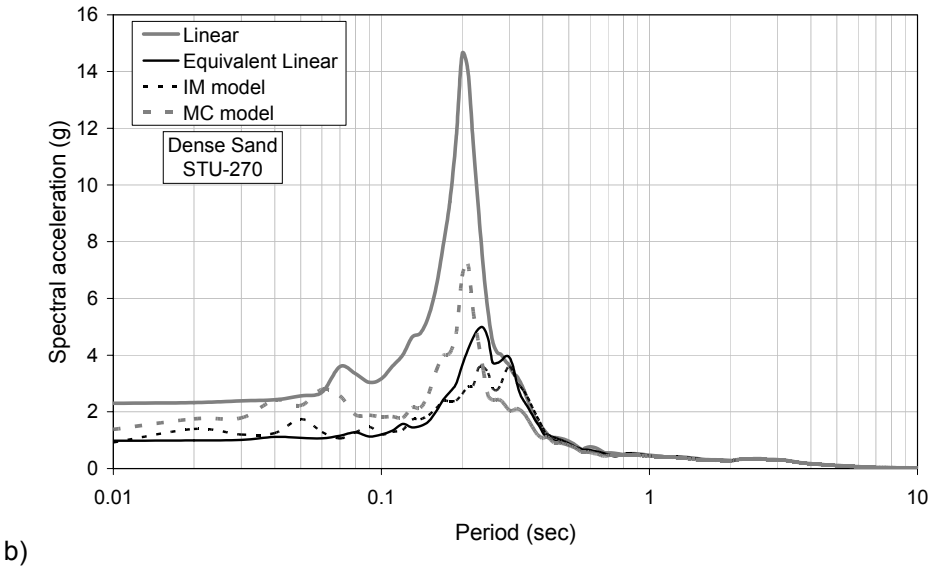

b)

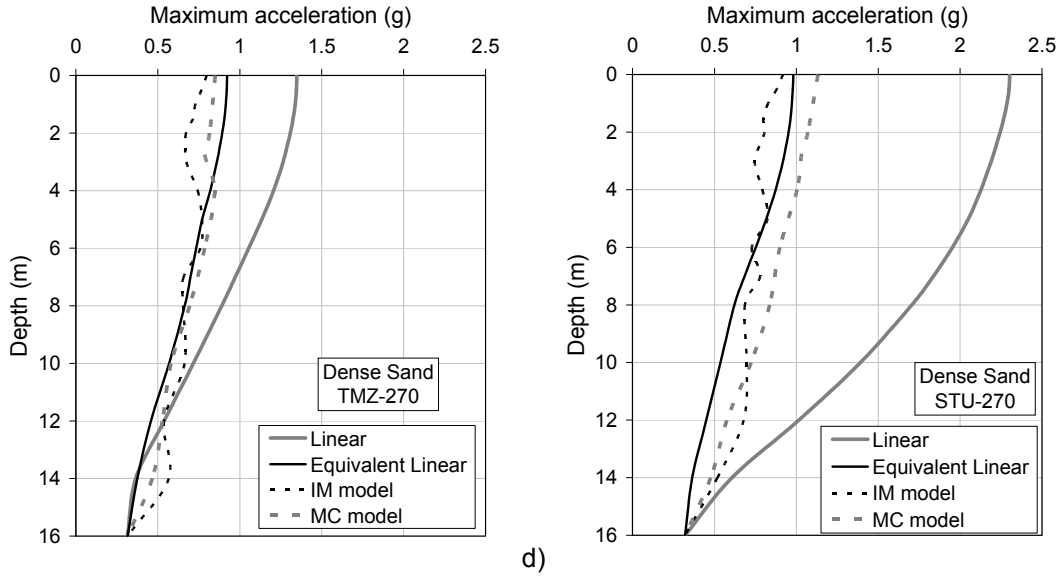

c) d)

Figure 6-13. *Comparisons between the calculated free field motions for dense sand layer: a) response spectrum at surface for TMZ-270; b) response spectra at surface for STU-270; c) maximum acceleration profiles for TMZ-270; d) maximum acceleration profiles for STU-270.*

While the surface motions of dense sand estimated by the equivalent linear and nonlinear analyses are quite similar, for loose sand the three types of analyses provide different results.

6.3.3 Pseudodynamic analyses: Newmark sliding block analyses.

A possible way to compute the seismic displacements of the retaining walls is the use of the critical acceleration a_{crit} deriving from the limit equilibrium condition and of the surface motion computed by local site response analyses as input for Newmark sliding block analyses. Different authors have highlighted the difficulties and the limitations connected to this type of analysis when applied to the flexible earth retaining structures (see for instance Callisto, 2006).
However, in the next Table 6-8 the results obtained by the sliding block analyses using as input motions those computed by the three abovementioned nonlinear approaches are summarized.

FREE-FIELD MOTION	**COMPUTER CODE**		**EERA**	**NERA**	**PLAXIS**
	NONLINEAR APPROACH		**Equiv. Lin.**	**IM model**	**MC model**
ANALYSIS CODE	k_{crit}	$\Delta M_{max}/\gamma h^3$	u_x/h	u_x/h	u_x/h
L060TMZ	0.228	0.074	10.23%	6.70%	1.95%
L100TMZ	0.228	0.074	10.23%	6.70%	1.95%
L060STU	0.228	0.074	6.30%	4.35%	4.73%
L100STU	0.228	0.074	6.30%	4.35%	4.73%
D060TMZ	0.447	0.146	1.53%	0.68%	0.08%
D100TMZ	0.447	0.146	1.53%	0.68%	0.08%
D060STU	0.447	0.146	1.55%	0.83%	0.10%
D100STU	0.447	0.146	1.55%	0.83%	0.10%

Table 6-8. *Seismic performances of the retaining walls predicted by the simplified dynamic analyses.*

FREE-FIELD MOTION	**COMPUTER CODE**		**EERA**	**NERA**	**PLAXIS**
	NONLINEAR APPROACH		**Equiv. Lin.**	**IM model**	**MC model**
ANALYSIS CODE	k_{crit}	$\Delta M_{max}/\gamma h^3$	u_x/h	u_x/h	u_x/h
L060TMZ	0.167	0.093	14.58%	10.78%	6.50%
L100TMZ	0.140	0.100	17.23%	13.23%	9.90%
L060STU	0.167	0.093	9.75%	8.38%	19.18%
L100STU	0.140	0.100	12.33%	11.40%	31.00%
D060TMZ	0.370	0.159	2.55%	1.43%	0.13%
D100TMZ	0.328	0.178	3.30%	2.08%	0.45%
D060STU	0.370	0.159	2.93%	1.73%	0.53%
D100STU	0.328	0.178	4.13%	2.55%	1.43%

Table 6-9. *Seismic performances of the retaining walls predicted by the simplified dynamic analyses accounting for the wall weight.*

Table 6-9 shows the same results considering the inertia forces associated to the wall masses in the force balance at limit equilibrium conditions.
It can be noted the large discrepancies between the seismic displacements calculated by the different adopted nonlinear approaches for free-field motion estimation that corresponds to each scheme. The effects of the TMZ earthquake in terms of wall displacements predicted by the Newmark analyses are more disastrous than for STU input motion if the surface motion computed by the equivalent linear method and the IM model are used. On the contrary, if the seismic response of the MC material layer is adopted, strong damages are registered for STU signal.

6.4 PUSHOVER ANALYSES.

As described in the previous Chapter 5, two types of pseudostatic analyses can be performed to evaluate the seismic threshold coefficients of the embedded diaphragms.
The first procedure is constituted by a pseudostatic stress-strain analysis in which, starting from the deformed configuration after the excavation, the horizontal acceleration a_h applied to each node of the discrete model is increased until reaching the collapse of the excavation (HAIP, Horizontal Acceleration Increasing Procedure). The results can be easily summarized in diagrams in which the evolution of maximum horizontal and vertical displacements and of the maximum bending moment acting on the wall are related to the increasing seismic level.
In the second procedure, the seismic loadings are modelled by means of pseudostatic forces acting on the diaphragm. In this research, the two shapes of loading (TRD, triangular distribution, and RTD, rectangular distribution) described in the previous Chapter were considered and applied on the wall after the excavation. The seismic pressures are increased until to the equilibrium condition can not be reached in the analysis. As for the HAI procedure, the horizontal seismic coefficient k_h can be related to the normalized seismic increments of displacements and normalized maximum bending moment. The k_h values are evaluated by means of the equations (5-33) and (5-34) with an iterative trial and error procedure for each step of calculation.

6.4.1 Finite element modelling.

A sketch of the finite element models used in the pushover analyses is plotted in Figure 6-14. They are constituted by rectangular domains 80m wide and 16m high with fixed nodes along the boundaries. The subsoils are subdivided into 14 layers having the same thicknesses used in the site response analyses. Each layer of loose and dense sand was modelled with a MC model characterized by the mechanical parameters reported in the Table 6-10 and Table 6-11.
Soil-wall friction was simulated by adopting an interface element with a R_{int} parameter equal to:

$$R_{\text{int}} = \frac{\tan\delta}{\tan\phi} \qquad (6\text{-}5)$$

The initial stress generation was executed by the k_0-procedure in which the value of k_0 was fixed to 0.5, both for loose and dense sand layers.
The walls were schematized as linear elastic plates having the properties summarized in Table 6-12.

DEPTH (m)	E (MPa)	ν	α_R	β_R	ϕ	c (kPa)	ψ	R_{int}
0.00 – 0.50	99.01	0.25	0.567	3.529×10^{-4}	33°	5×10^{-4}	0°	0.622
0.50 – 1.00	106.12	0.25	0.549	3.419×10^{-4}	33°	5×10^{-4}	0°	0.622
1.00 – 1.50	111.00	0.25	0.531	3.309×10^{-4}	33°	5×10^{-4}	0°	0.622
1.50 – 2.00	117.25	0.25	0.517	3.221×10^{-4}	33°	5×10^{-4}	0°	0.622
2.00 – 3.00	123.67	0.25	0.503	3.132×10^{-4}	33°	5×10^{-4}	0°	0.622
3.00 – 4.00	134.31	0.25	0.478	2.978×10^{-4}	33°	5×10^{-4}	0°	0.622
4.00 – 5.00	143.97	0.25	0.460	2.868×10^{-4}	33°	5×10^{-4}	0°	0.622
5.00 – 6.00	153.97	0.25	0.443	2.757×10^{-4}	33°	5×10^{-4}	0°	0.622
6.00 – 7.00	165.81	0.25	0.425	2.647×10^{-4}	33°	5×10^{-4}	0°	0.622
7.00 – 8.00	176.53	0.25	0.407	2.537×10^{-4}	33°	5×10^{-4}	0°	0.622
8.00 – 10.00	189.20	0.25	0.390	2.427×10^{-4}	33°	5×10^{-4}	0°	0.622
10.00 – 12.00	214.12	0.25	0.372	2.316×10^{-4}	33°	5×10^{-4}	0°	0.622
12.00 – 14.00	231.59	0.25	0.354	2.206×10^{-4}	33°	5×10^{-4}	0°	0.622
14.00 – 16.00	253.46	0.25	0.336	2.096×10^{-4}	33°	5×10^{-4}	0°	0.622

Table 6-10. *MC model parameters of loose sand layers.*

DEPTH (m)	E (MPa)	ν	α_R	β_R	ϕ	c (kPa)	ψ	R_{int}
0.00 – 0.50	260.45	0.25	0.729	2.693×10^{-4}	40°	5×10^{-4}	10°	0.599
0.50 – 1.00	268.58	0.25	0.706	2.609×10^{-4}	40°	5×10^{-4}	10°	0.599
1.00 – 1.50	274.77	0.25	0.683	2.525×10^{-4}	40°	5×10^{-4}	10°	0.599
1.50 – 2.00	281.03	0.25	0.665	2.458×10^{-4}	40°	5×10^{-4}	10°	0.599
2.00 – 3.00	289.48	0.25	0.647	2.390×10^{-4}	40°	5×10^{-4}	10°	0.599
3.00 – 4.00	302.39	0.25	0.615	2.272×10^{-4}	40°	5×10^{-4}	10°	0.599
4.00 – 5.00	311.15	0.25	0.592	2.188×10^{-4}	40°	5×10^{-4}	10°	0.599
5.00 – 6.00	324.54	0.25	0.569	2.104×10^{-4}	40°	5×10^{-4}	10°	0.599
6.00 – 7.00	333.61	0.25	0.547	2.020×10^{-4}	40°	5×10^{-4}	10°	0.599
7.00 – 8.00	345.14	0.25	0.524	1.936×10^{-4}	40°	5×10^{-4}	10°	0.599
8.00 – 10.00	363.98	0.25	0.501	1.852×10^{-4}	40°	5×10^{-4}	10°	0.599
10.00 – 12.00	388.24	0.25	0.478	1.767×10^{-4}	40°	5×10^{-4}	10°	0.599
12.00 – 14.00	405.69	0.25	0.456	1.683×10^{-4}	40°	5×10^{-4}	10°	0.599
14.00 – 16.00	431.27	0.25	0.433	1.599×10^{-4}	40°	5×10^{-4}	10°	0.599

Table 6-11. *MC model parameters of dense sand layers.*

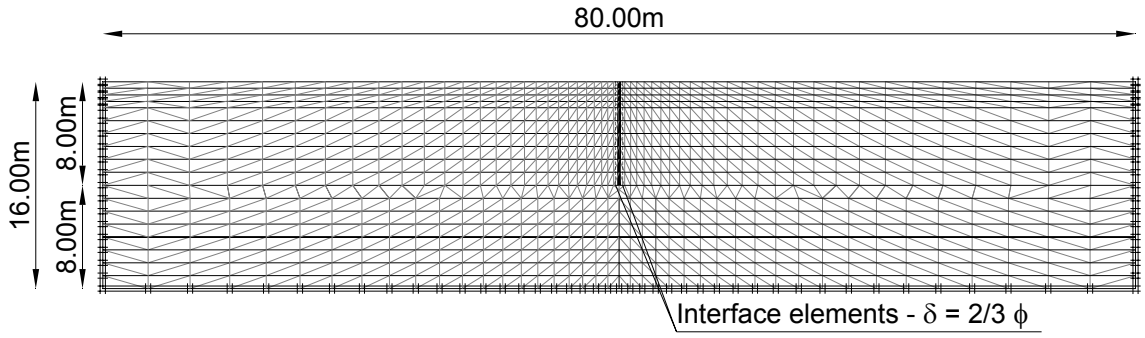

Figure 6-14. *Sketch of the FE models used in the pushover analyses.*

ANALYSIS CODE	Thickness, s(m)	EA (kNm^2/m)	EI (kNm^2/m)	w (kN/m^3/m)	ν
L060TMZ	0.60	18 x 10^6	5.4 x 10^5	6.94	0.00
L100TMZ	1.00	30 x 10^6	25 x 10^5	11.56	0.00
L060STU	0.60	18 x 10^6	5.4 x 10^5	6.94	0.00
L100STU	1.00	30 x 10^6	25 x 10^5	11.56	0.00
D060TMZ	0.60	18 x 10^6	5.4 x 10^5	5.79	0.00
D100TMZ	1.00	30 x 10^6	25 x 10^5	9.65	0.00
D060STU	0.60	18 x 10^6	5.4 x 10^5	5.79	0.00
D100STU	1.00	30 x 10^6	25 x 10^5	9.65	0.00

Table 6-12. *Elastic properties of plates.*

The excavation process was executed by removing the material clusters in front of the wall. The simulation was organized into 5 calculation phases: in the first, the plate and the interface elements were activated; from phase 2 to phase 5, the soil layers of 1.00m thick were removed. After of them, the pseudostatic analyses were carried out. The numerical calculations were performed with the updating of the mesh during the deformation processes because it needs everytime the analysis should reach the failure conditions.

6.4.2 Configurations at the end of excavation.

Because the deformed configuration after the excavation represents the initial stress-strain scheme on which the seismic loadings act, it is interesting to analyze the static conditions of the walls after the excavations.

Figure 6-15 and Figure 6-16 plot the normal interface stresses and the bending moments acting on the walls embedded in the dry loose and dense sand layers. The numerical results are compared with those predicted by the limit equilibrium method (LE). The active and passive earth pressures were calculated by the Coulomb and Lancellotta theories accounting for the assigned soil-wall friction angle, as described in the Chapter 3. It can be seen the good agreement between the theoretical and the numerical normal stresses. While the positions along the walls is well predicted, the values of the maximum bending moments is underestimated by the LE method. This is due to the greater normal

stresses on active sides related to the different mobilization degrees of the shear strength along the interface elements, as shown by the relative shear strength distributions on the walls (red diagrams at the left of the interface stresses distributions).

In static conditions, the stress-strain behaviour of the two walls can be retained the same, both in terms of maximum bending moment and earth pressure distributions.

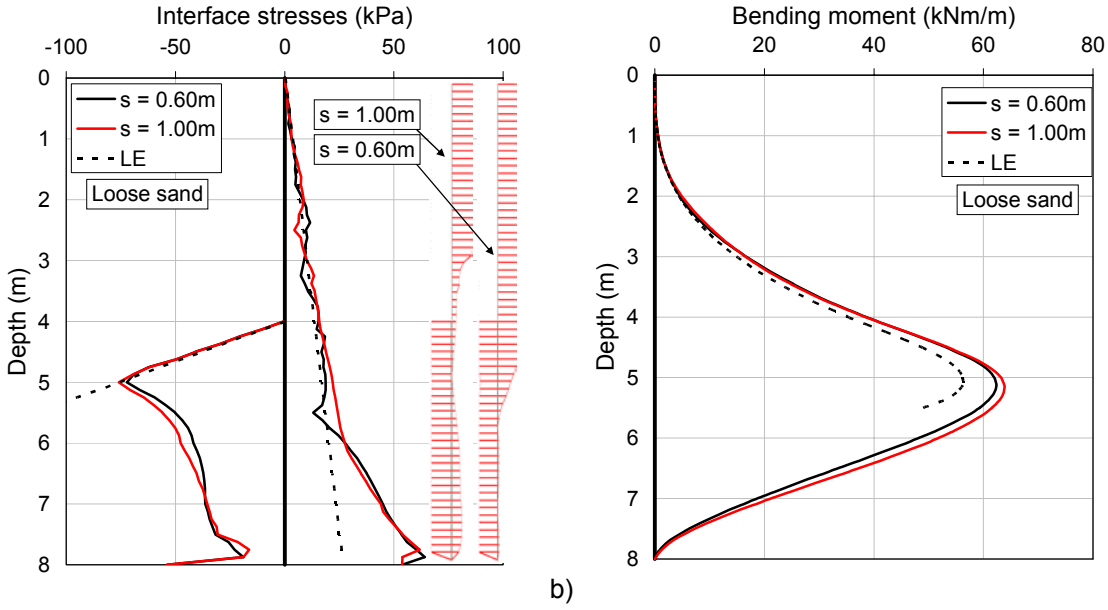

Figure 6-15. *Interface stresses (a) and bending moment (b) on walls in loose sand at the end of excavation.*

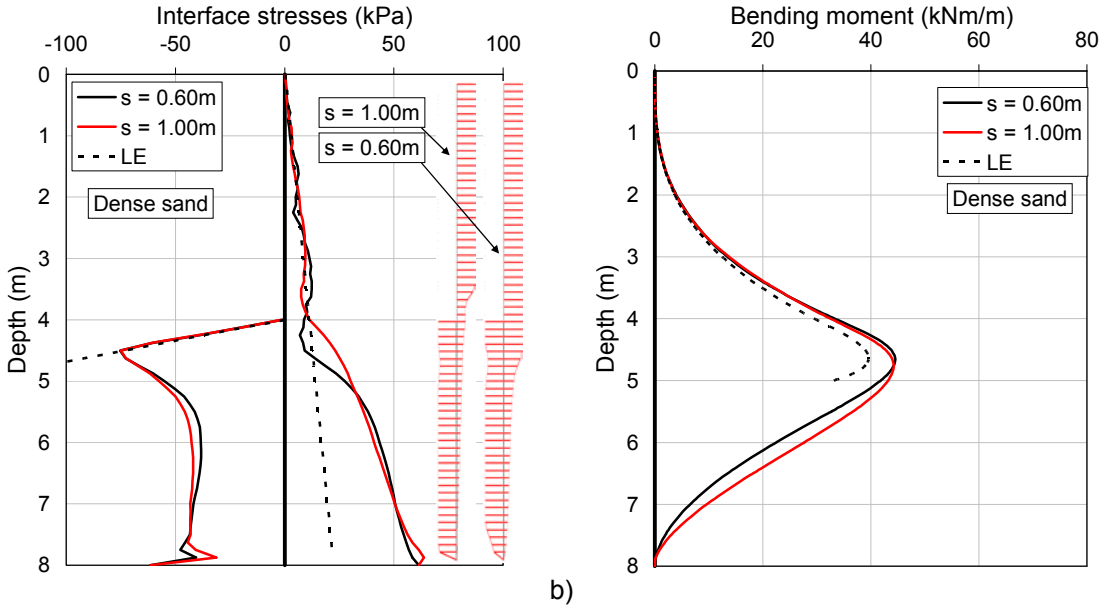

Figure 6-16. *Interface stresses (a) and bending moment (b) on walls in dense sand at the end of excavation.*

Some discrepancies exist on the horizontal displacements of the walls, as reported in Figure 6-17. The total kinematical mechanism was divided into a flexural mechanism, that coincides with the elastic line of the plates obtained by the double integration of the bending moment distribution, and a rigid

mechanism, given by the difference between the total and flexural mechanisms. As expected, the displacements of the stiff diaphragm are lower than those of the deformable one, both in loose and dense sand. However, it can be recognized that the wall movements are more affected from the soil stiffness and strength than the plate properties.

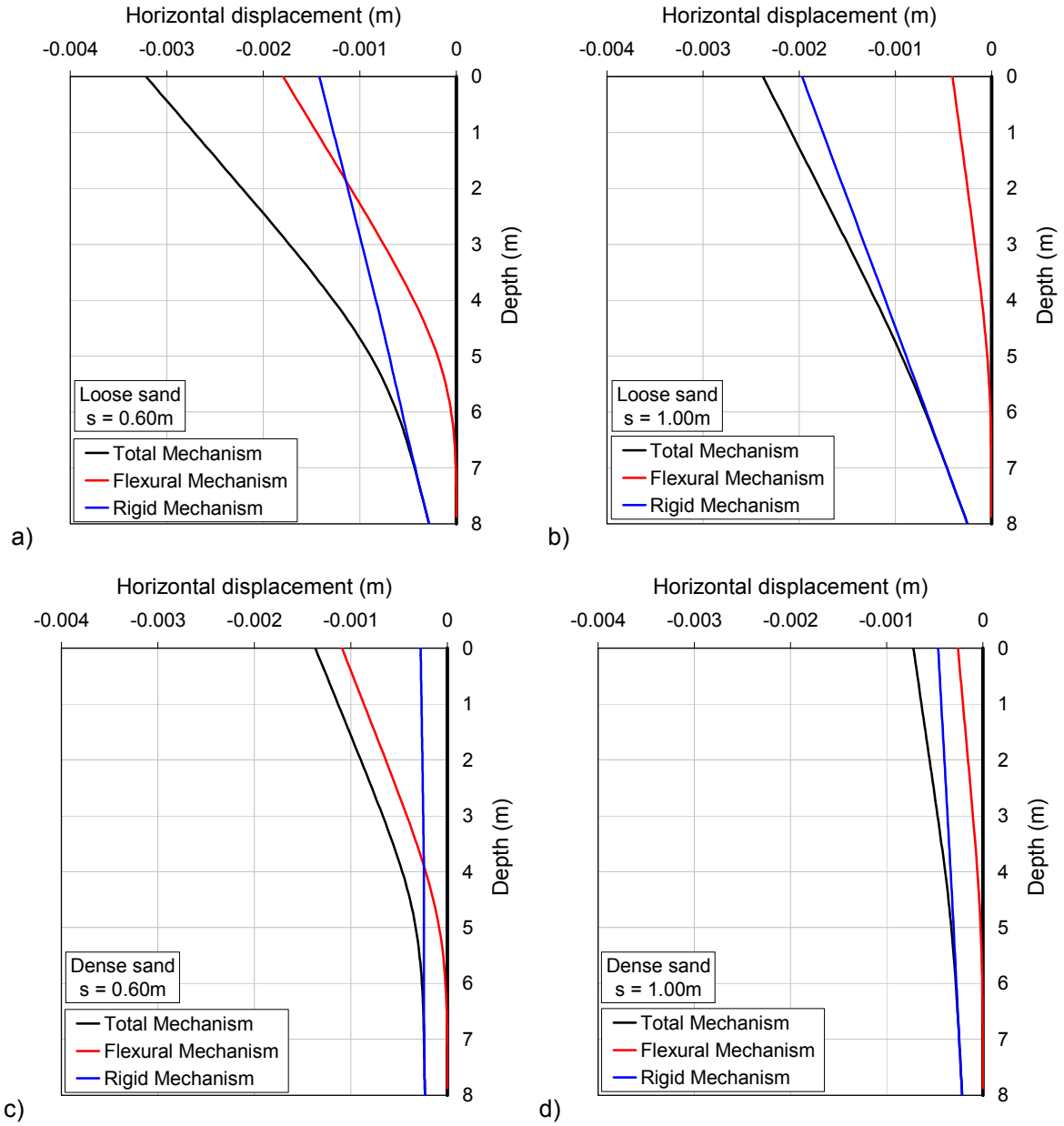

Figure 6-17. *Horizontal displacements of the walls at the end of excavation: a) loose sand, s = 0.60m; b) loose sand, s = 1.00m; c) dense sand, s = 0.60m; d) dense sand, s = 1.00m*

In order to show the soil movements near the excavation, in Figure 6-18 was plotted the shading of the horizontal displacements estimated at the end of excavation phases for the deformable wall (s = 0.60m) embedded in the loose sand layer.

It can be recognized the formation of the active wedge behind the wall for an heigth lower than that corresponds to the limit condition. The soil volume involved in the movements extends for 3 times the heigth of excavation, *h*, on active side, and 2.5 times *h* on passive side.

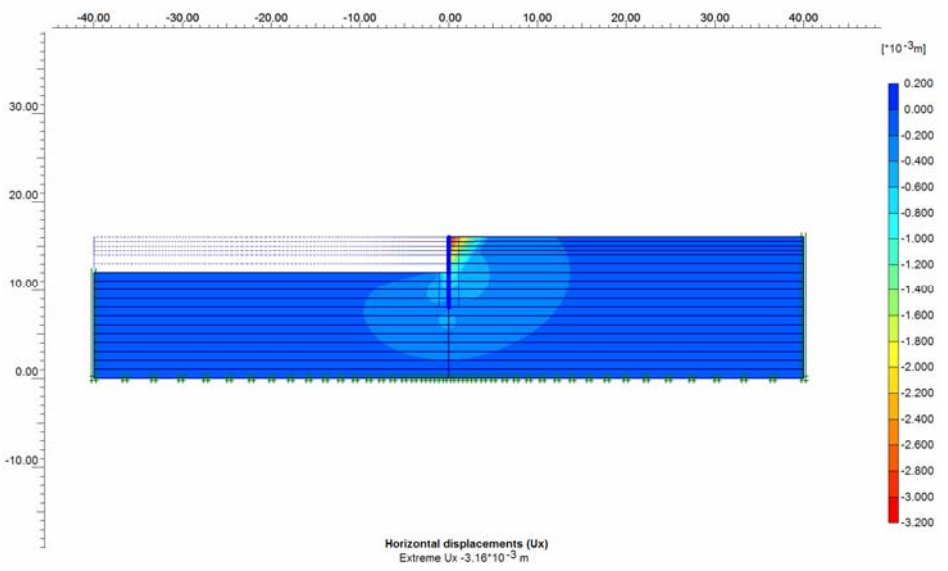

Figure 6-18. *Shading of horizontal displacements at the end of excavation (loose sand, s = 0.60m).*

6.4.3 Pseudostatic loadings.

As described above, there are two pseudostatic procedures to apply the seismic loadings on the walls by means of 2D finite element modelling. In the first, HAIP, the horizontal accelerations of the mesh nodes were increased till to reach the condition at which the numerical calculation can not advance. This condition is assumed as the limit condition for the system. The second procedure consists to apply a distributed loading, with a triangular (TRD) or a rectangular (RTD) distribution, as reported in Figure 6-19, on the entire length of the wall. The collapse loading corresponds to the value at which the analysis can not achieve the static equilibrium. The loading systems can be converted to horizontal accelerations by means of equations (5-33) and (5-34).

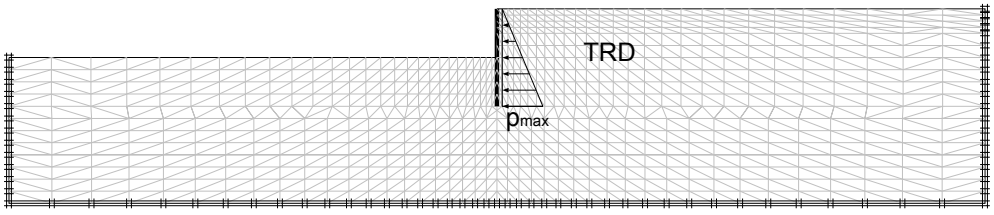

a)

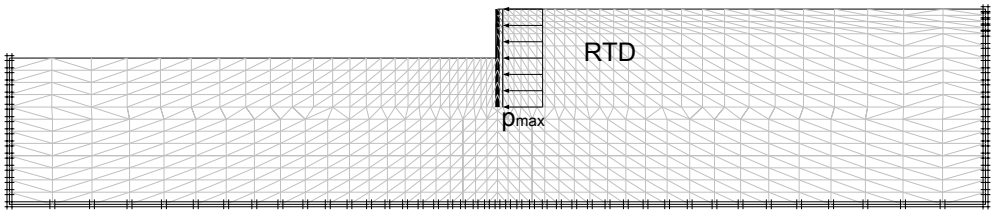

b)

Figure 6-19. *Sketch of the FE models used in the pushover analyses: a) triangular loading distribution, TRD; b) rectangular loading distribution, RTD.*

From Figure 6-20 to Figure 6-22, the seismic capacities of the diaphragms in loose and dense sand layers obtained by the three types of pushover analyses are shown, in terms of horizontal and vertical displacements and maximum bending moments. The plotted values are referred to the normalized seismic increments of the quantities with respect to the static conditions. The limit equilibrium capacities are also represented with dashed black lines.

Referring to the Figure 6-20, it is very interesting to note the perfect agreement between the capacity curves given by the HAIP and the TRD procedures for every analyzed systems. The critical seismic coefficients k_{crit} predicted by the pushover analyses are not so different from the limit equilibrium solutions, especially for the dense sand that is better modelled by the rigid-perfectly plastic hypothesis of the LE method. These values should be interpreted as threshold accelerations. Every time that the acceleration near to the ground surface exceeds the limit, the walls accumulate permanent displacements.

The rectangular distribution seems to predict more conservative seismic capacities of the retaining system. Then, in the view of the design of a new structure, to take into account the cyclic nature of the earthquake loadings, this one may be preferred to the TRD and HAIP.

Some discrepancies can be observed on the vertical displacements calculated by the different procedures. These are principally due to the low capacities of the adopted linearly elastic perfectly plastic model to account for the volumetric-distortional coupling of the soil behaviour when the shear strains increase. Then, these capacities curves should be intended with the only illustrative aim.

Another interesting aspect is the evolution of the seismic demand, in terms of the maximum bending moment, with the horizontal displacement of the wall. Initially, for low levels of seismic loading, the maximum bending moment linearly increase with the movements of the wall. When the seismic coefficient achieve the critical value, the diaphragms can move into the soil as rigid body and the bending moments can not amplify. This means that the structural design of the RC diaphragms can be performed by referring to the limit equilibrium conditions. If the formation of a plastic hinge on the wall at a certain depth from the dredge level can be retained more suitable than the generalized collapse of the soil-wall system, a hierarchical strength criterion may be applied on the dimensioning of the wall section in order to attain the flexural failure of the wall instead that the soil collapse.

In Figure 6-24 the comparisons between the seismic capacities in terms of horizontal displacements predicted by the HAIP, TRD and RTD procedures are shown. The more stiff and heavy walls have a worst seismic response for the larger inertia forces related to their masses that affect the limit equilibrium conditions, especially for the diaphragms in loose sand.

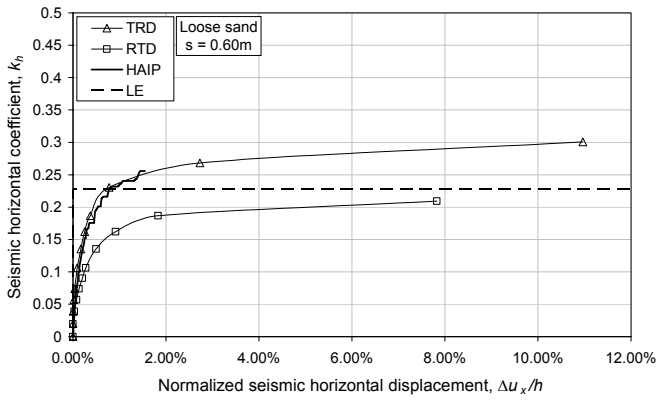

a)

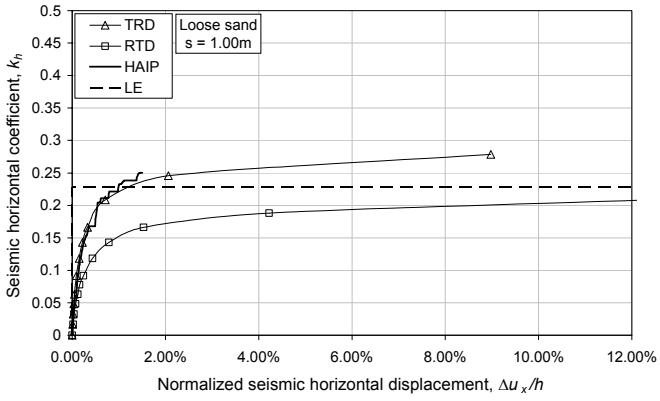

b)

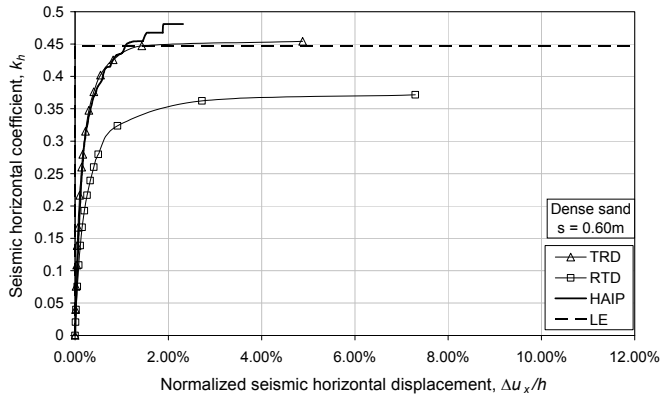

c)

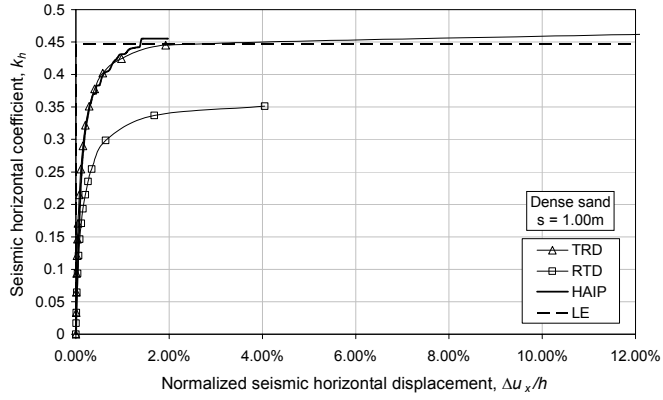

d)

Figure 6-20. *Seismic capacities of the diaphragms in terms of normalized horizontal displacements: a) loose sand, s = 0.60m; b) loose sand, s = 1.00m; c) dense sand, s = 0.60m; d) dense sand, s = 1.00m*

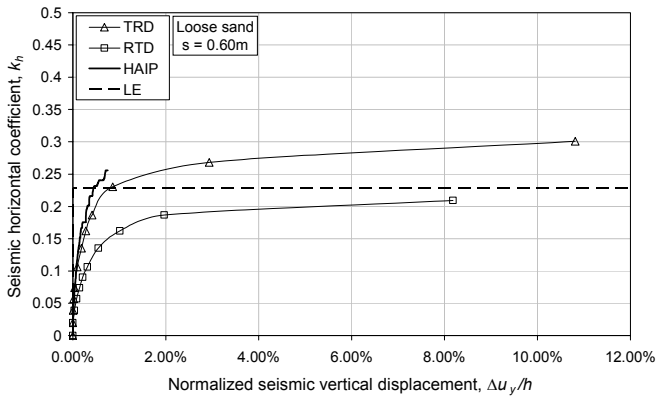

a)

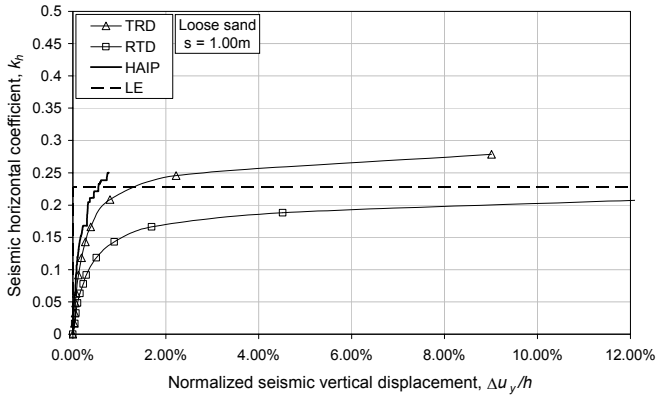

b)

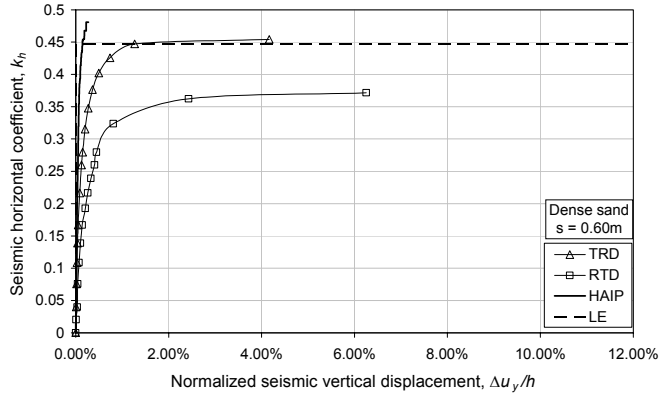

c)

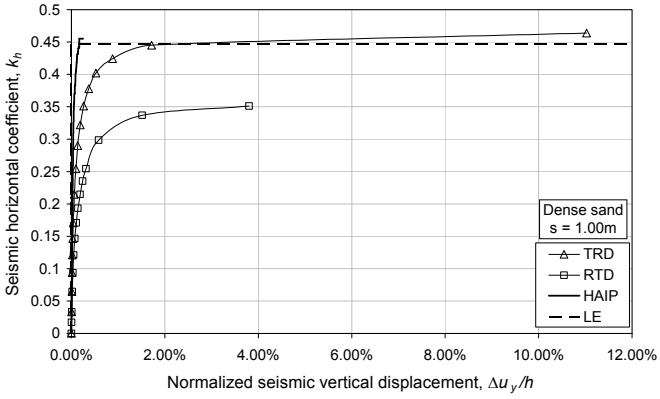

d)

Figure 6-21. *Seismic capacities of the diaphragms in terms of normalized vertical displacements: a) loose sand, s = 0.60m; b) loose sand, s = 1.00m; c) dense sand, s = 0.60m; d) dense sand, s = 1.00m*

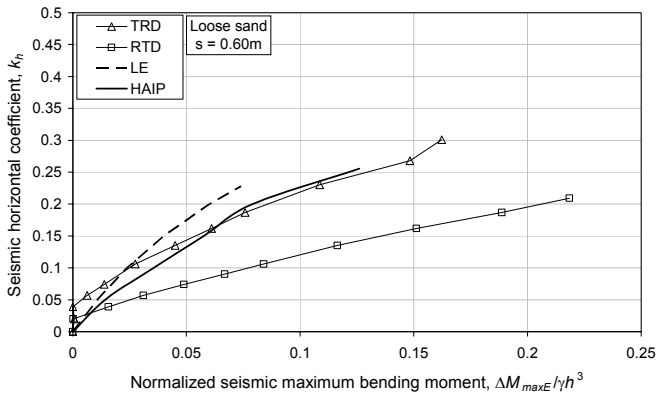

a)

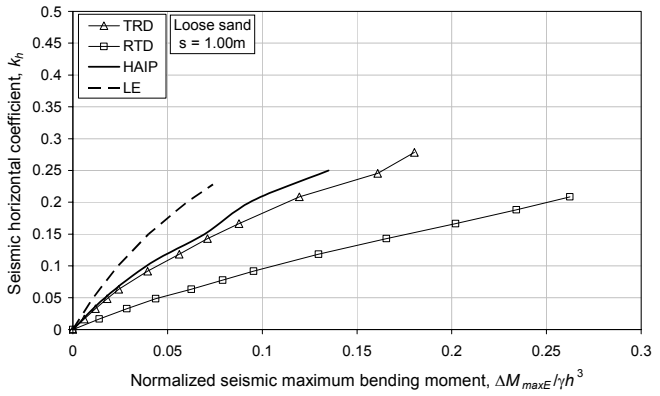

b)

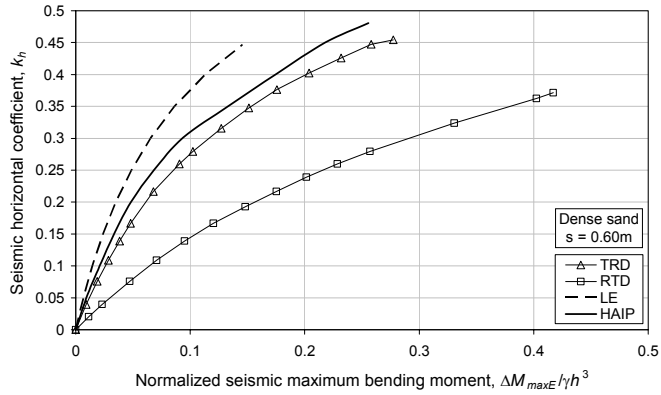

c)

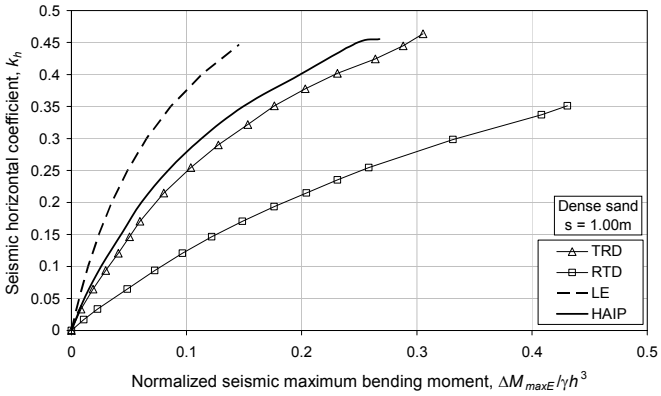

d)

Figure 6-22. *Seismic capacities of the diaphragms in terms of normalized maximum bending moment: a) loose sand, s = 0.60m; b) loose sand, s = 1.00m; c) dense sand, s = 0.60m; d) dense sand, s = 1.00m*

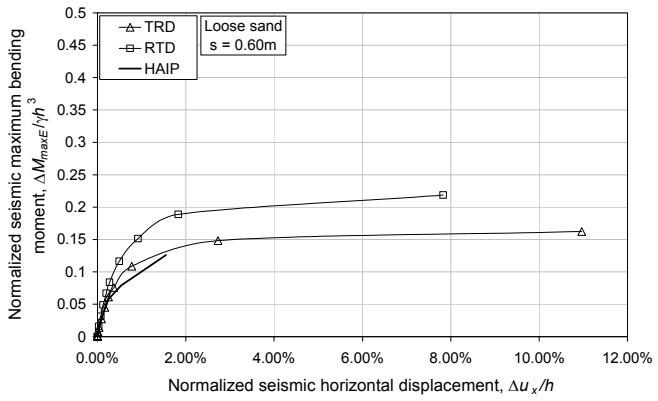

a)

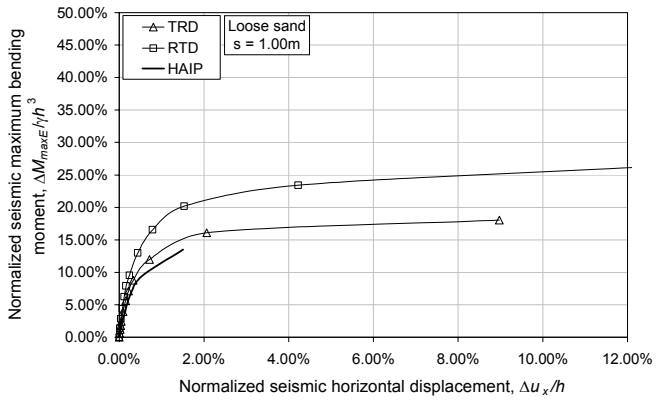

b)

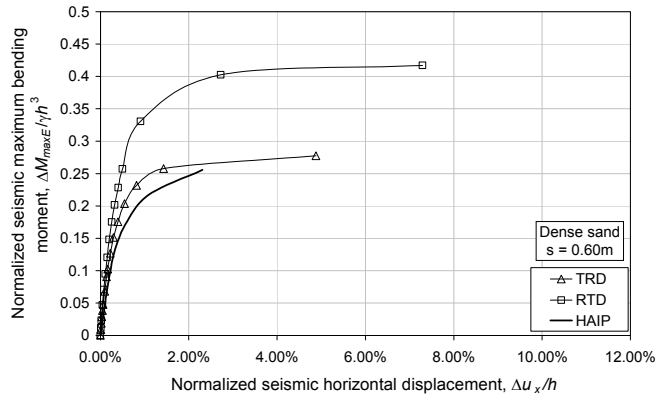

c)

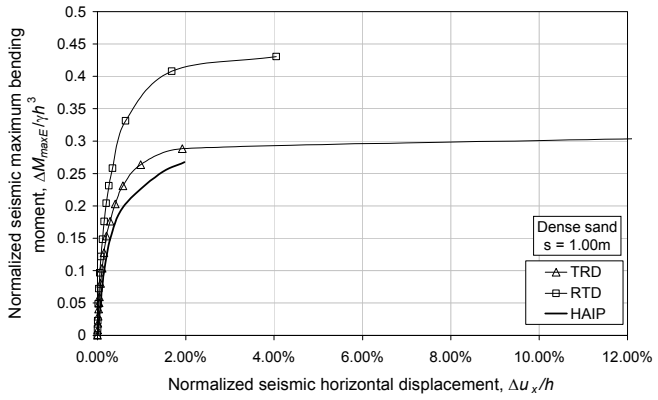

d)

Figure 6-23. *Development of the maximum bending moments with the horizontal displacements: a) loose sand, s = 0.60m; b) loose sand, s = 1.00m; c) dense sand, s = 0.60m; d) dense sand, s = 1.00m*

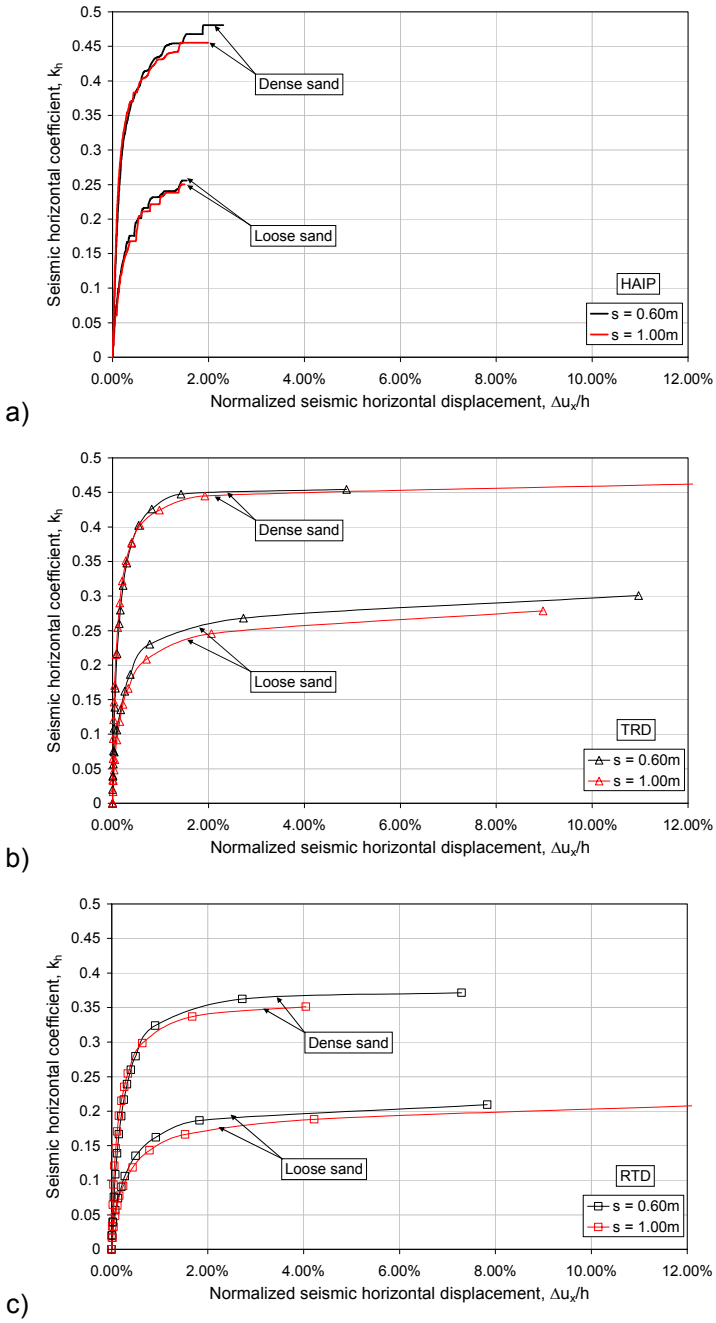

Figure 6-24. *Comparisons between the seismic behaviours of the two walls predicted by the pushover analyses: a) HAIP; b) TRD; c) RTD.*

6.5 DYNAMIC ANALYSES.

The dynamic analyses represent the more sophisticated instrument to predict the seismic response of any type of geotechnical system. This type of analysis is based on soil-structure interaction, generally using FE or FD methods. The effects of earthquake are represented by a set of time histories of seismic motion at the base of the analysis domain chosen for the soil-structure system.

The computational domain of interest adopted in the analyses is the same of the pushover analyses. To minimize the spurious effects of the reflected stress waves on the lateral boundaries, two rectangular domains were placed at the sides of the domain. A sketch of the FE models used for the

dynamic analyses is plotted in Figure 6-25. Only at the base of the central region the complete acceleration time histories were applied. Under the lateral domains the accelerograms were tapered to zero near to the lateral boundaries.

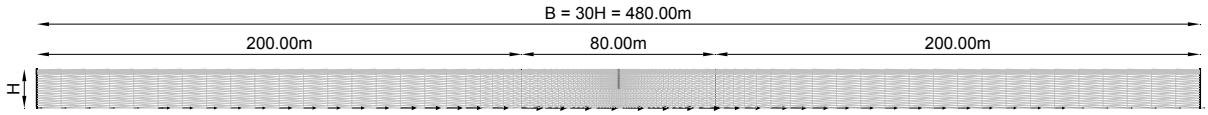

Figure 6-25. *Sketch of the FE models used in the dynamic analyses.*

The subsoil profiles in the lateral zones are the same of the central one, while the mesh is coarser to reduce the calculation time.
Material and model parameters, plate and interface elements are the same of the pushover analyses reported in the previous Table 6-10, Table 6-11 and Table 6-12. The soil behaviour was modelled as linear elastic, adopting the initial stiffness and damping parameters, and perfectly plastic, characterized by the strength parameters determined by the laboratory tests and recalled in Table 3-1, with a MC model.
The dynamic analyses of the system were performed by conducting 14 calculation phases for TMZ-270 seismic motion (6 static and 8 dynamic analyses) and 22 for STU-270 input signal (6 static and 16 dynamic analyses). In the first phase, the plate and the interface elements were activated. From phase 2 to phase 5 the excavation was executed de-activating the clusters behind the wall. Stage 7 was devoted to activate dynamic prescribed accelerations at the base of the model. In the other phases the earthquake was simulated. The input signals were divided into 8 and 16 parts, each one composed by 1000 registration points to avoid loss of information due to some limitations of the employed computer program.
Having used the same meshes in the central regions near to the walls, the configurations at the end of excavations are those discussed in the previous subsection. Then, only the numerical results of the dynamic phases are presented in the following.

6.5.1 Maximum acceleration profiles.

Figure 6-26 shows the maximum acceleration profiles computed by the dynamic analyses along the vertical of the walls (central line of the meshes), together with the free field motions presented in the previous subsection for the MC model. The presence of the excavation induces an amplification of the accelerations near to the surface, especially for stiffer walls. From 0 to 8 meters, the shape modes of the cantilever beam can be recognized.

6.5.2 Displacement time histories.

In Figure 6-27, the time histories of the seismic horizontal displacements of the top of walls relative to the bedrock and normalized with respect to the height of excavation are plotted. As it can be seen, for the cases of the loose sand, the stiffer and more weight walls have accumulated larger displacements.

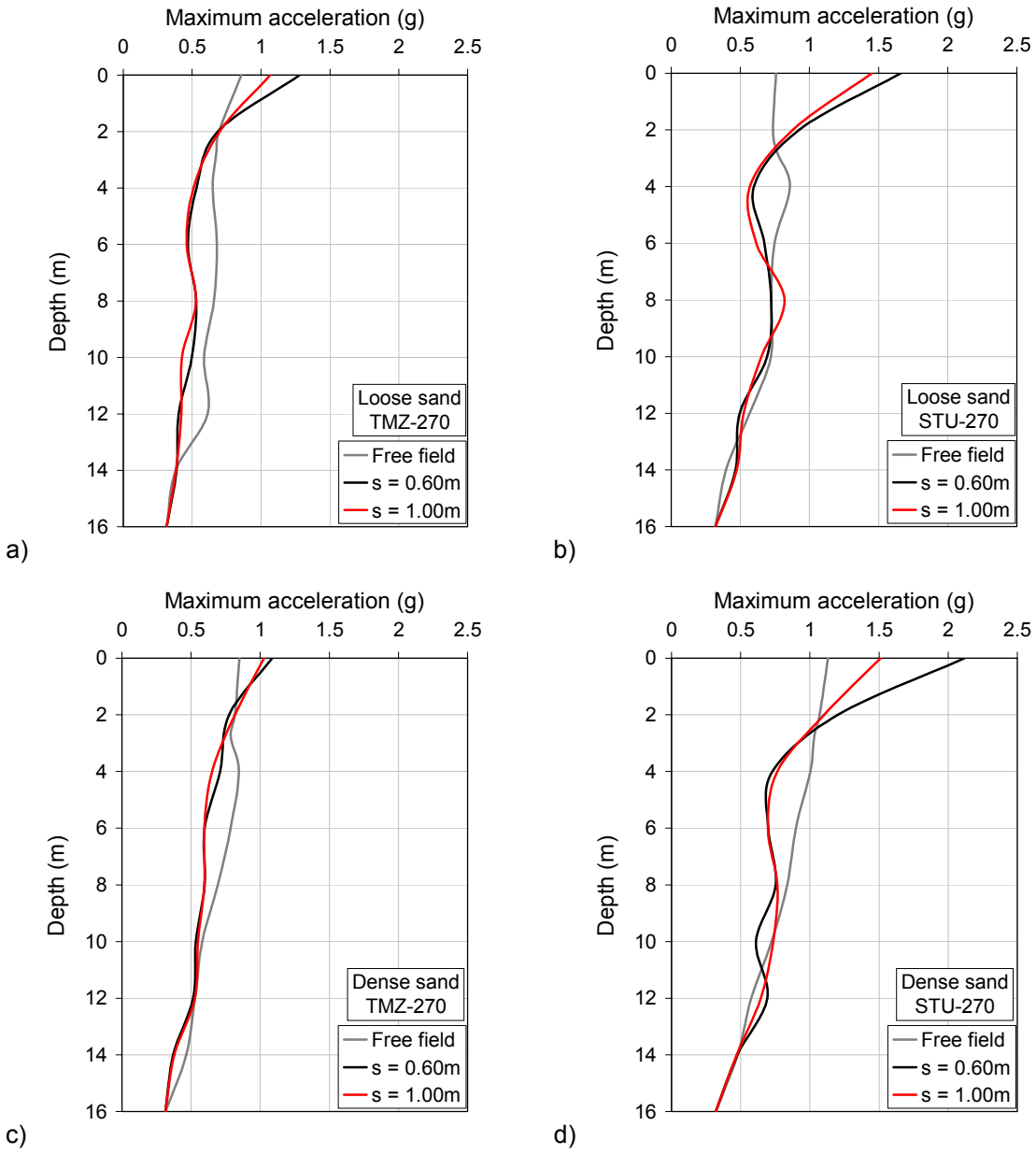

Figure 6-26. *Comparisons between the maximum acceleration profiles of the free field motions and the dynamic interactions with the walls: a) Loose sand, TMZ-270; b) Loose sand STU-270; c) Dense sand, TMZ-270; d) Dense sand, STU-270.*

This is due to the higher inertia forces associated to the greater wall masses that act on the soil passive resistance. The effect is slighter for the diaphragms in dense sand for which the differences between the wall material and soil unit weight.

The calculated time histories of the seismic horizontal displacements at the top of walls encourage the use of a Newmark sliding block approach. Figure 6-28 and Figure 6-29 show the good agreement between the results of the dynamic interactions and the Newmark analyses conducted by assuming critical accelerations that give the same u_x/h of the complete analyses and using the accelerograms computed in the complete analyses at the top of diaphragms as input motions.

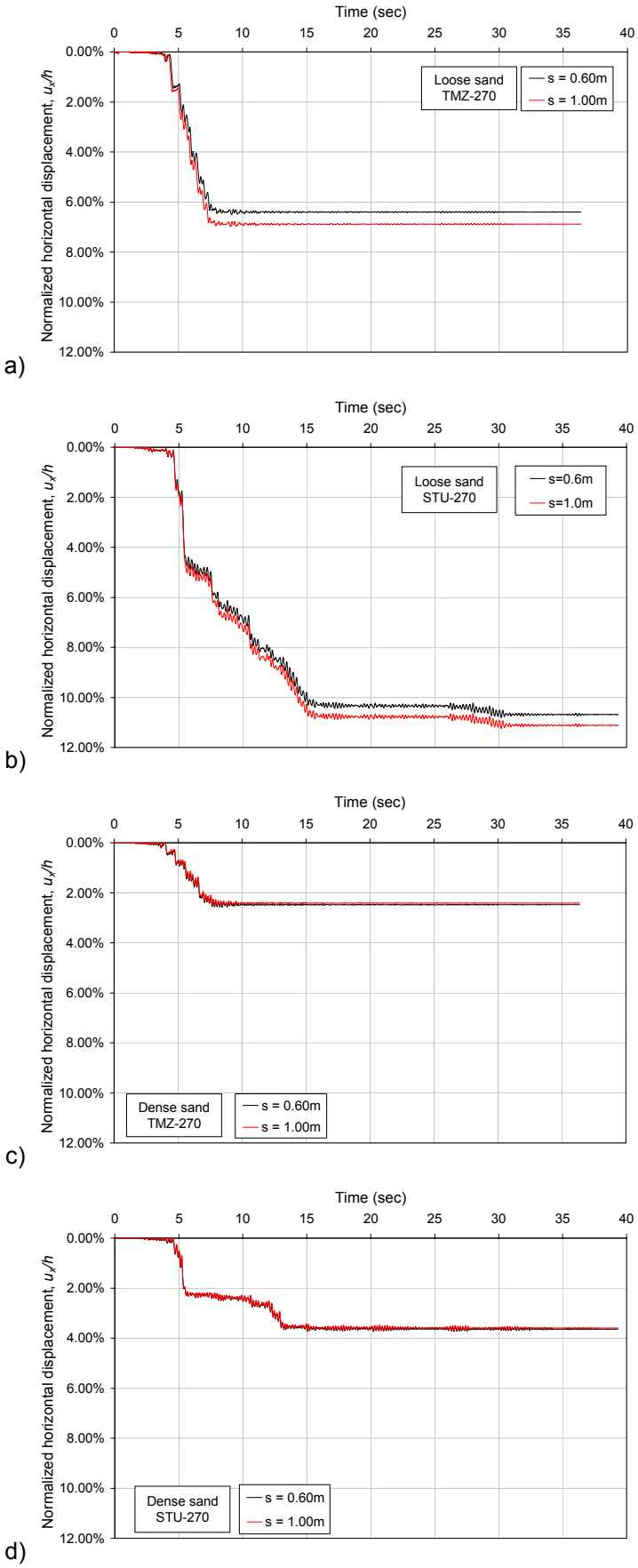

Figure 6-27. *Time histories of the normalized horizontal displacements at the top of the walls: a) Loose sand, TMZ—270; b) Loose sand, STU-270; c) Dense sand, TMZ-270; Dense sand, STU-270.*

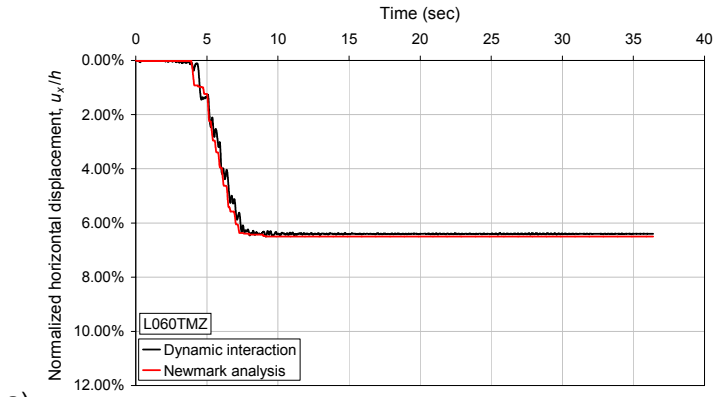

a)

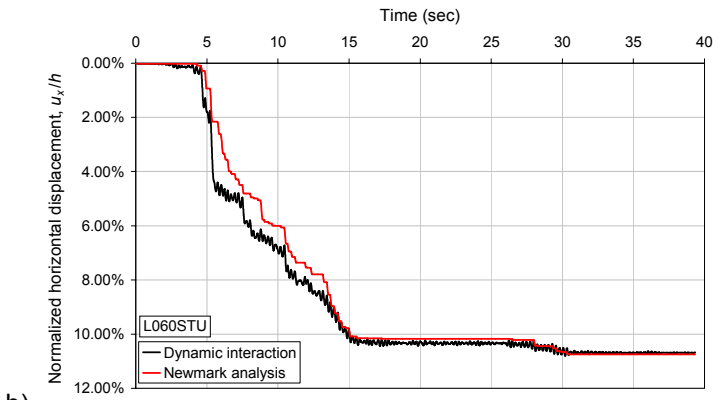

b)

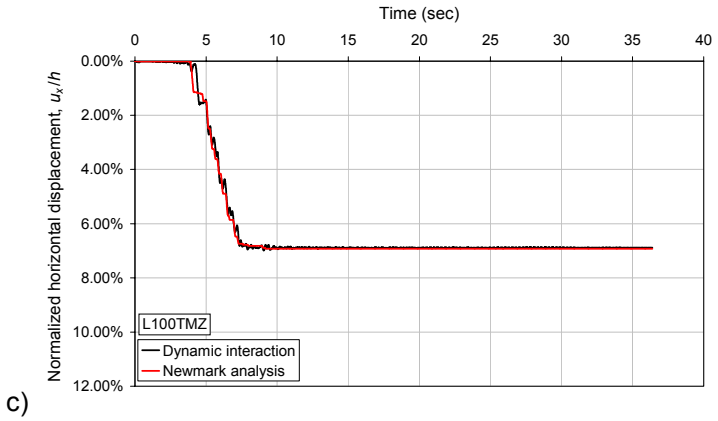

c)

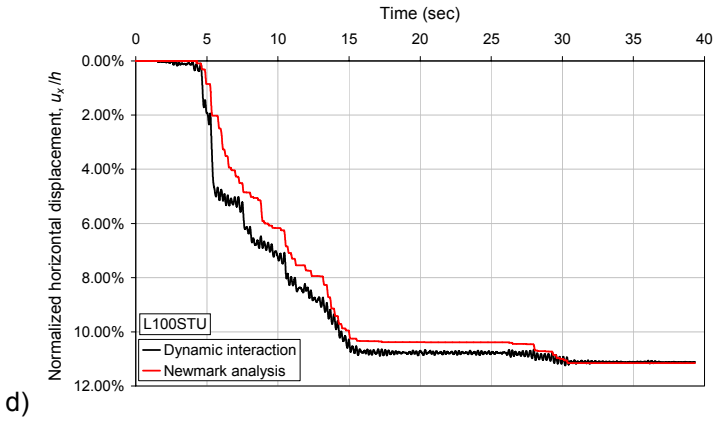

d)

Figure 6-28. *Comparisons between the normalized horizontal displacements at the top of the walls in loose sand predicted by Newmark and dynamic interaction analyses: a) L060TMZ; b) L060STU; c) L100TMZ; L100STU.*

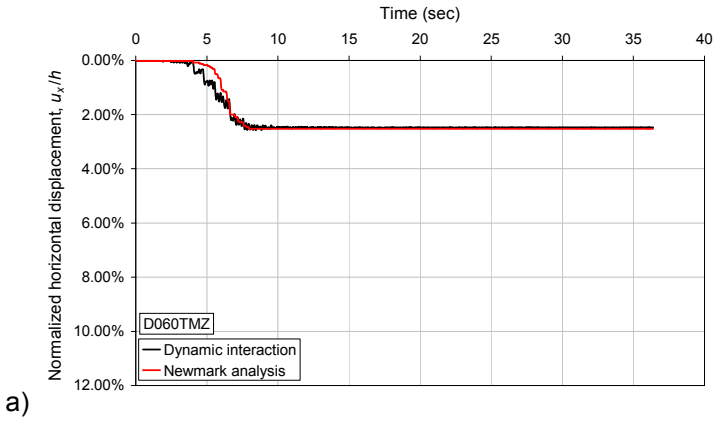

a)

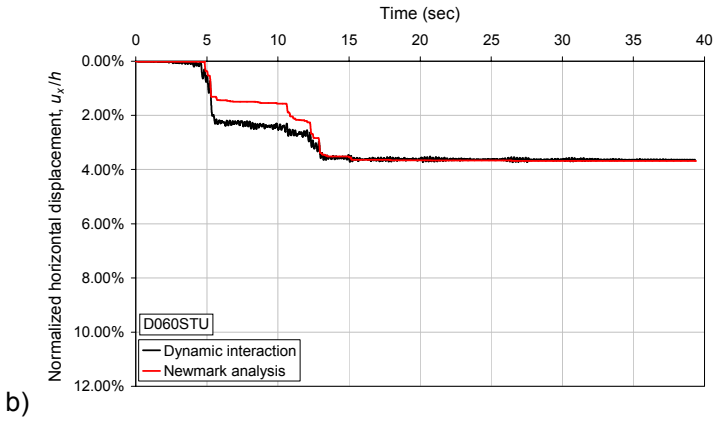

b)

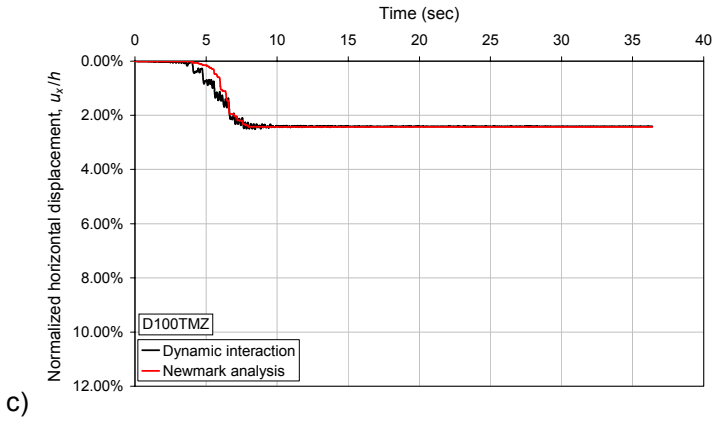

c)

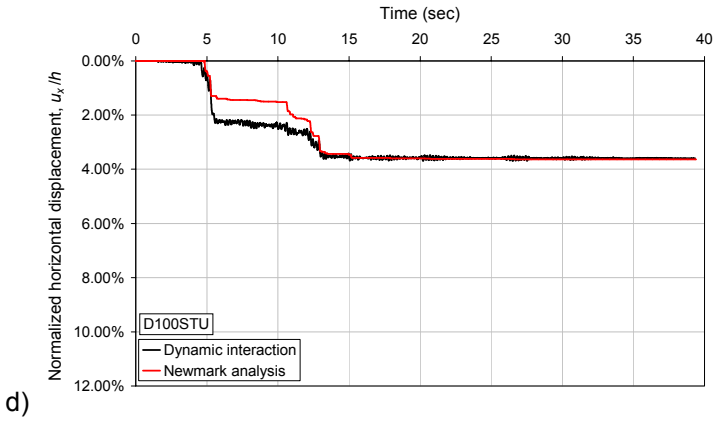

d)

Figure 6-29. *Comparisons between the normalized horizontal displacements at the top of the walls in dense sand predicted by Newmark and dynamic interaction analyses: a) D060TMZ; b) D060STU; c) D100TMZ; D100STU.*

Some differences can be noted for the STU-270 input motion, specially for dense sand. The reason is that the critical acceleration from which the wall starts to move varies during the earthquakes. In particular, the lower values of the displacements given by the Newmark simplified analyses testimony the increase of k_{crit} with the accumulated displacements of the wall.

6.5.3 Configurations at the end of the earthquakes.

At the end of the earthquakes, the walls are subjected to the normal interface stresses reported in Figure 6-30, together with those predicted by the M-O and Lancellotta (2007) methods, for active and passive limit equilibrium, respectively, and for a seismic horizontal coefficient k_h = 0.262.

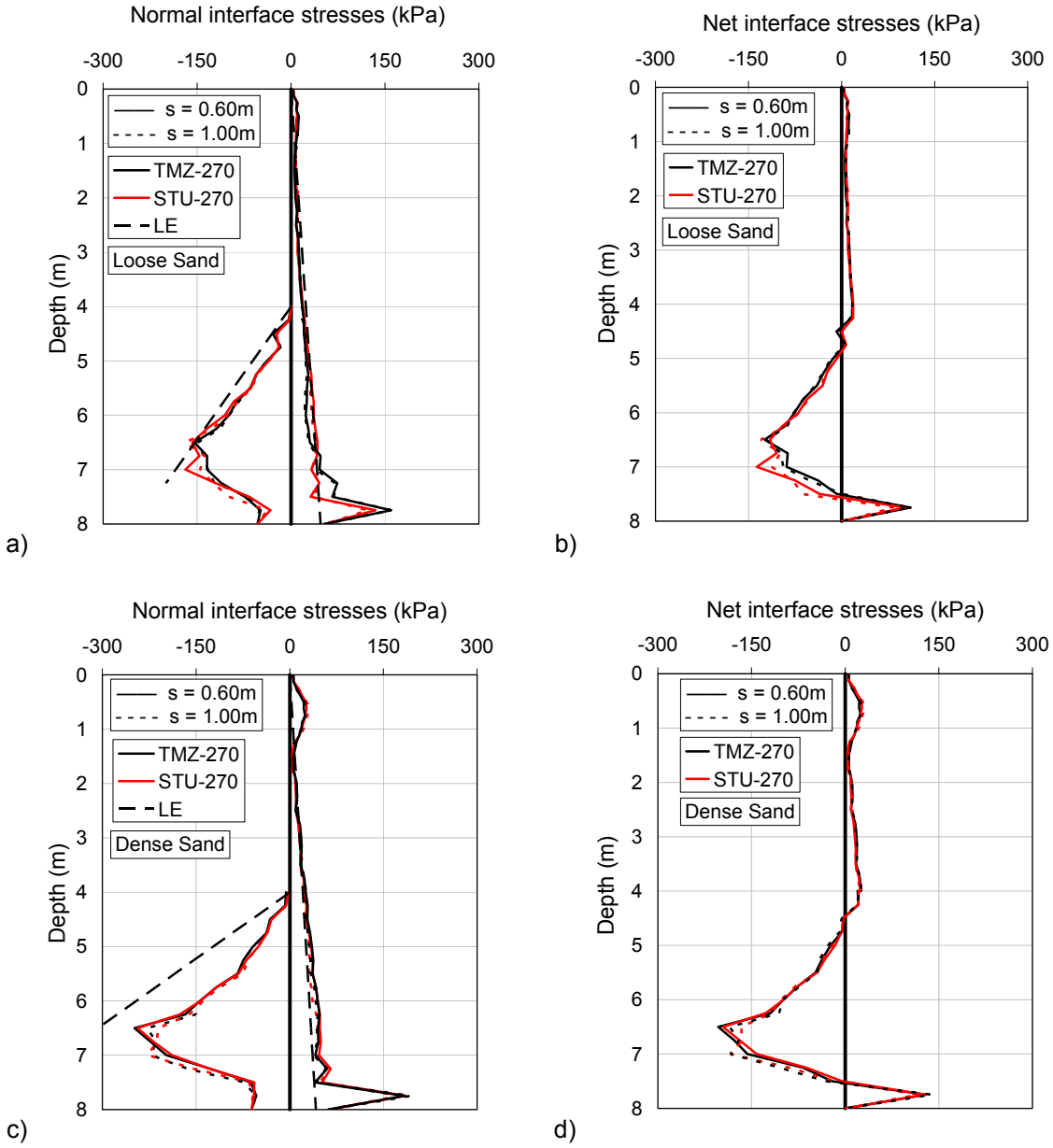

Figure 6-30. *Normal and net interface stresses acting on the walls in loose (a, b) and dense (c, d) at the end of earthquakes.*

An interesting result is the light influence of the input motion and the diaphragm thickness on soil pressure distributions, both for active and passive sides. From the net interface stresses along the wall, it can be seen the positions of the zero net pressure points near to the bottom of the walls. Independently from the soil properties, the input motions and the diaphragm stiffness, every analyses give a zero net pressure point placed at a distance z' = 0.125 d from the bottom.

The theoretical pressure distributions are quite different from those numerically determined. Figure 6-31 shows the earth pressure coefficients in front and behind the walls obtained by dividing the normal interface stresses, σ_n, for the lithostatic vertical stresses γz. The different mobilization degrees of the shear strength along the walls allow non-uniform earth pressure coefficients. At the active side near to the surface level, the coefficients are greater than the theoretical but immediately decrease till to the static value, above of which slightly increase.

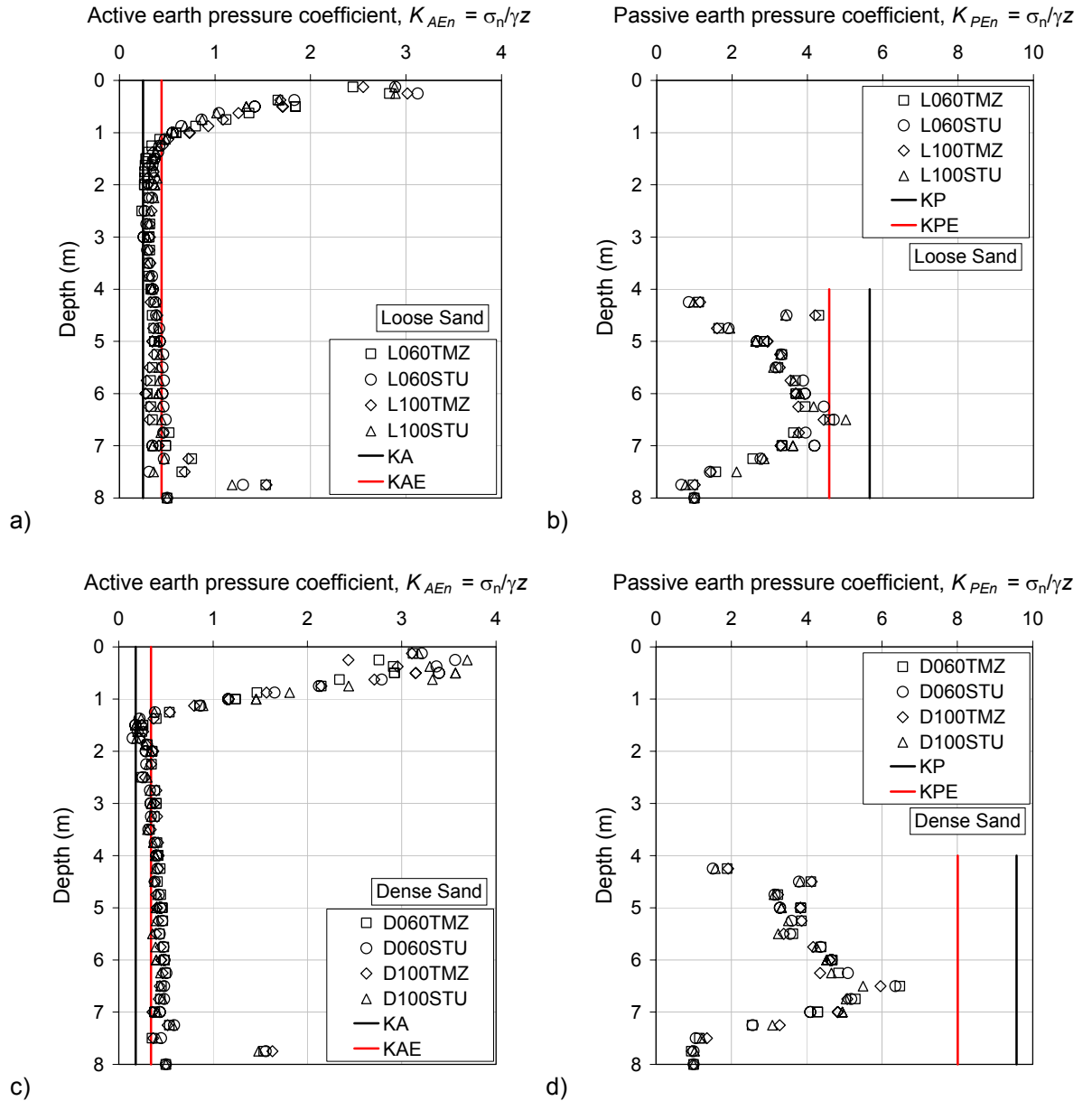

Figure 6-31. *Numerical active and passive earth pressure coefficients for walls in loose (a, b) and dense (c, d) sand at the end of earthquakes.*

The passive coefficients, instead, increase from the dredge level and reach a maximum at a depth of 0.375 d from the bottom of the diaphragms. Above this point, their values reduces.

In Figure 6-32, the shear forces and the bending moments acting on the walls at the end of the earthquakes are plotted. As the soil pressure distributions have shown, the input motions and the diaphragm thickness do not affect the results that depends only on the soil shear strength. An interesting aspect is the greater maximum bending moment of the walls embedded in the dense sand than those placed in the loose layers.

The bending moment predicted by the limit equilibrium methods for a horizontal seismic coefficient k_h = 0.262 and a soil-wall friction angle δ = 2/3 ϕ are lower than the numerical, particularly in the cases of dense sand for the high values of ϕ.

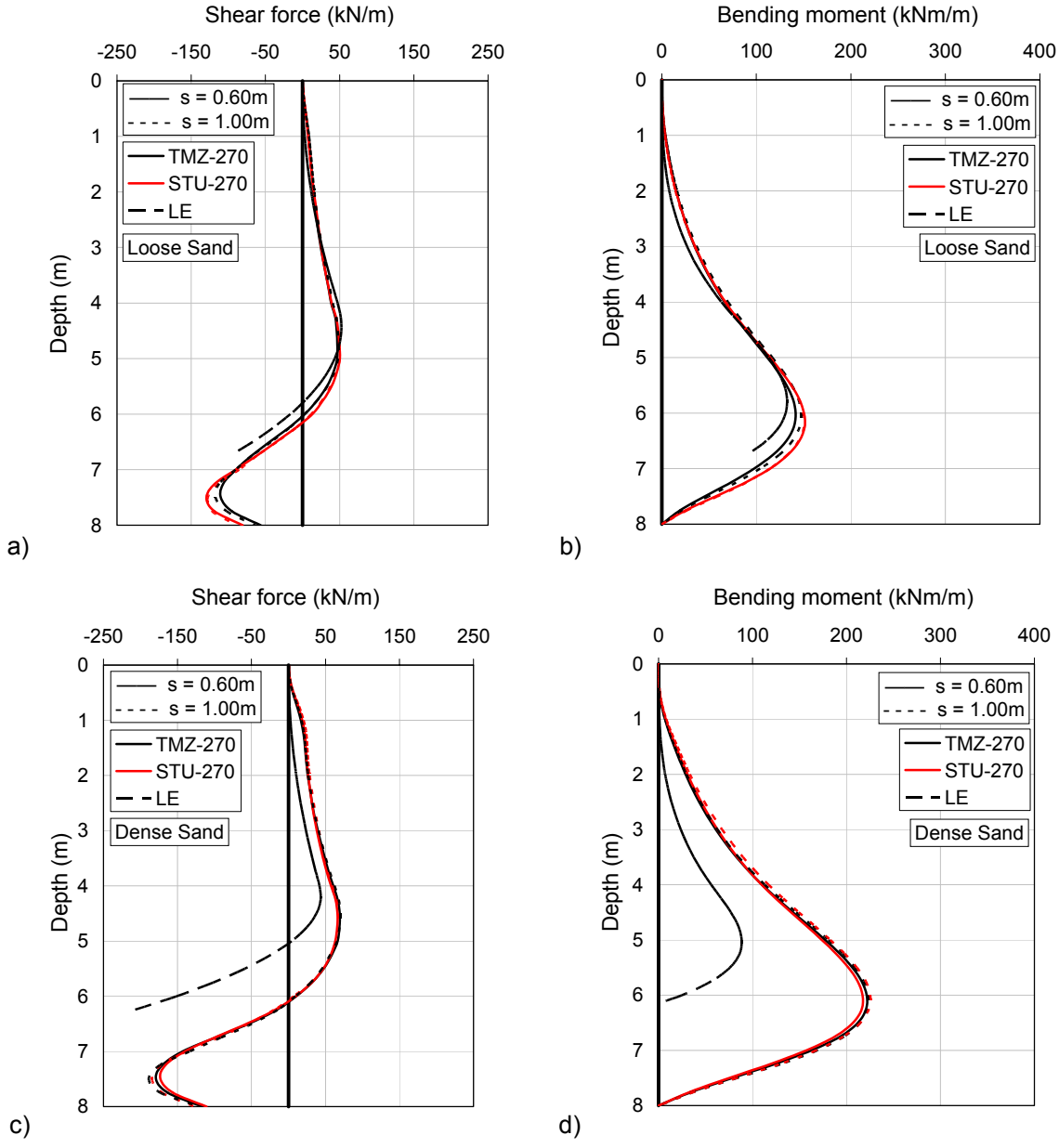

Figure 6-32. *Shear forces and bending moments acting on walls in loose (a, b) and dense (c, d) sand at the end of earthquakes.*

Instead, Figure 6-33 plots the horizontal displacements of the diaphragms at the end of the earthquakes. The small displacements related to the light curvatures of the deformed configurations respect to the total values highlight the rigid nature of the kinematical mechanism of the walls during the shaking that is essentially constituted by a rotation around a point placed at a depth of about 0.97d from the dredge level.

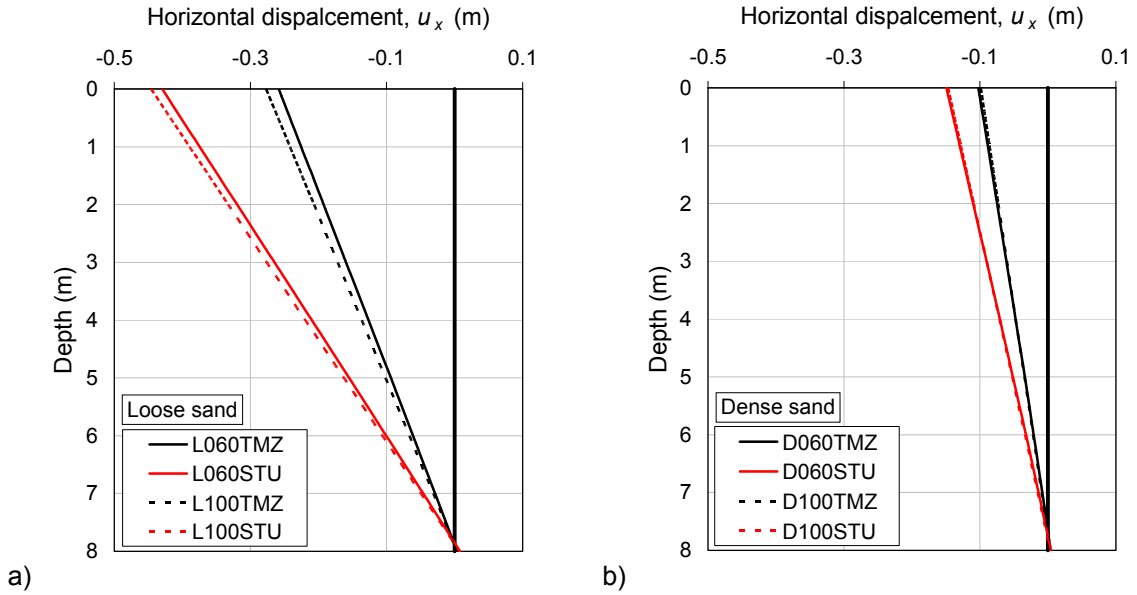

Figure 6-33. *Horizontal displacements of the walls in loose (a) and dense (b) sand at the end of earthquakes.*

Finally, in Table 6-13 the seismic performances of the walls predicted by the complete dynamic analyses are summarized in terms of seismic increments of the normalized maximum bending moment and normalized horizontal displacements. In the same table, the seismic coefficient k_h of the equivalent rigid blocks obtained by the Newmark back-analyses are also reported.

ANALYSIS CODE	k_h	u_x/h	$\Delta M_{max}/\gamma h^3$
L060TMZ	0.203	6.50%	0.242
L100TMZ	0.188	6.93%	0.256
L060STU	0.266	10.75%	0.244
L100STU	0.257	11.15%	0.264
D060TMZ	0.359	2.53%	0.311
D100TMZ	0.368	2.43%	0.316
D060STU	0.359	3.68%	0.315
D100STU	0.362	3.63%	0.351

Table 6-13. *Seismic performances of the walls predicted by the dynamic interaction analyses.*

6.5.4 Configurations at the instants of maximum bending moment.

From Figure 6-34 to Figure 6-39, the configurations of the walls at the instants of the maximum bending moment are shown. The seismic earth coefficients behind the diaphragms are greater than the theoretical active values upon the excavation level while their values are lower than the static below. The passive resistance is fully mobilized above a depth of about 0.625d and the earth coefficients reach similar values both for loose and dense sand that differ from the theoretical predictions.

The depth of the zero net pressure points have the same values of the final positions and does not depend on the seismic motion and the wall thickness. The maximum bending moment is not affected from the input motion while slightly increases with the wall thickness, as reported in Figure 6-36.

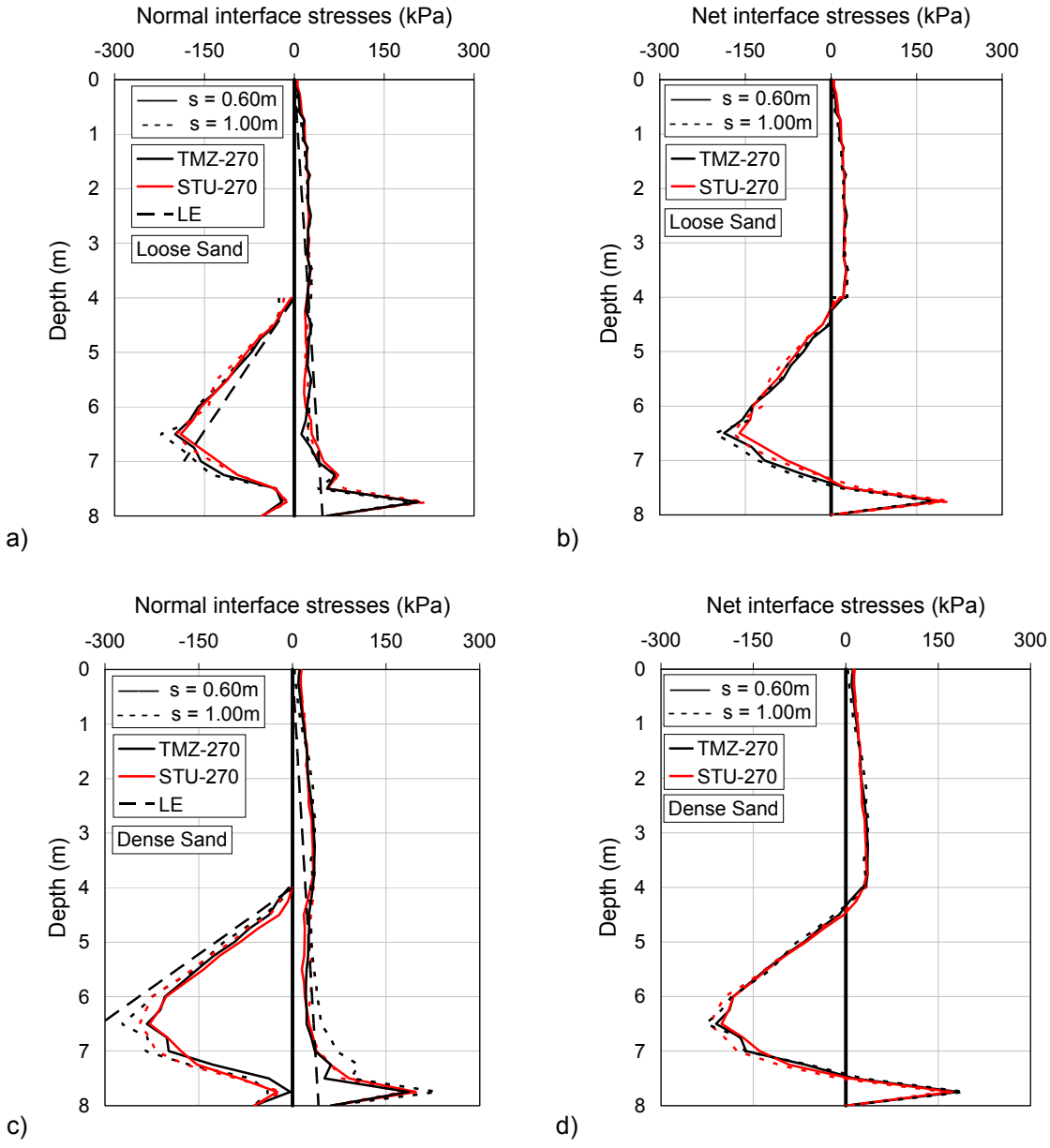

Figure 6-34. *Normal and net interface stresses acting on the walls in loose (a, b) and dense (c, d) at the instants of maximum bending moment.*

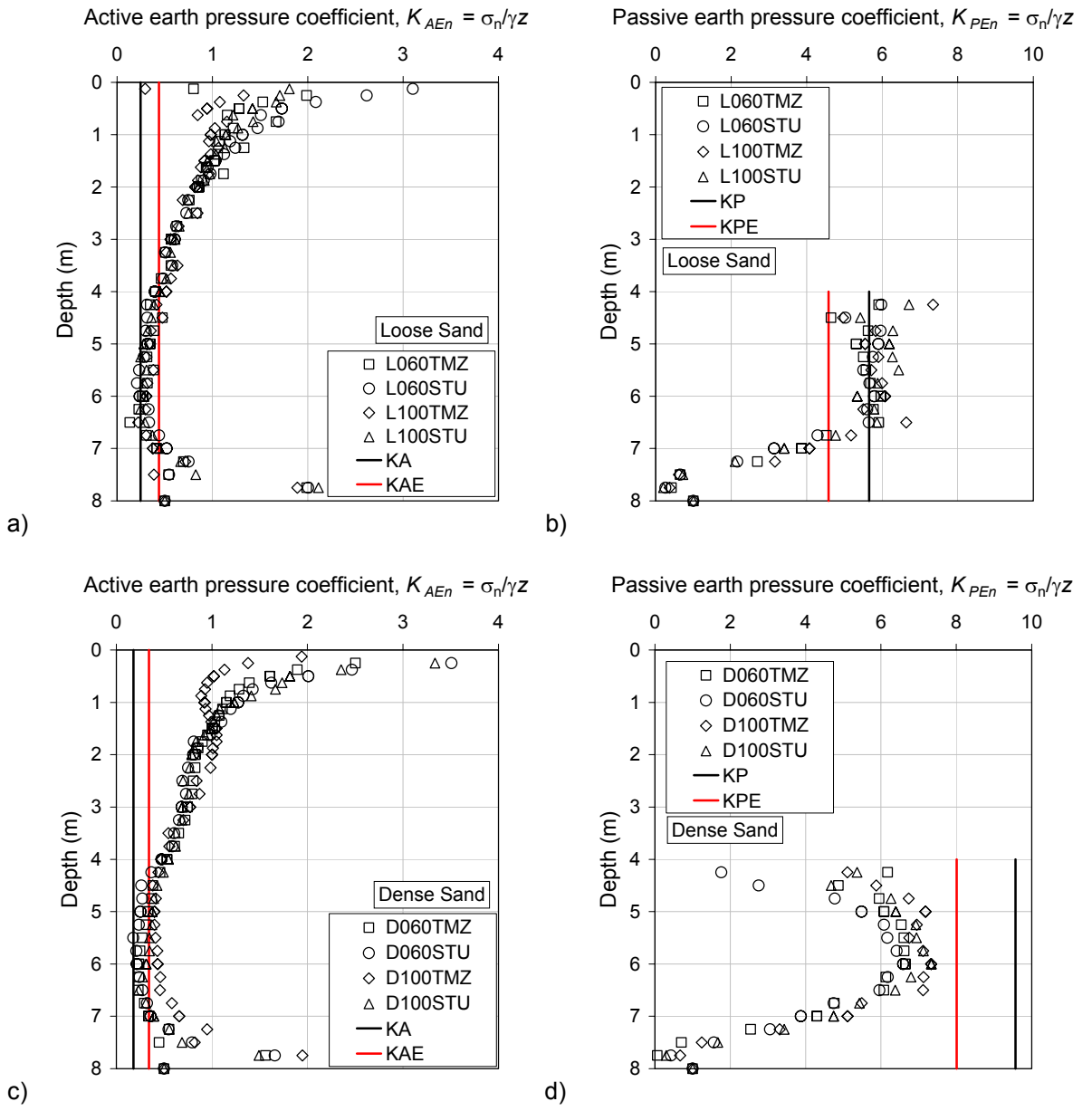

Figure 6-35. *Numerical active and passive earth pressure coefficients for walls in loose (a, b) and dense (c, d) sand at the instants of maximum bending moment.*

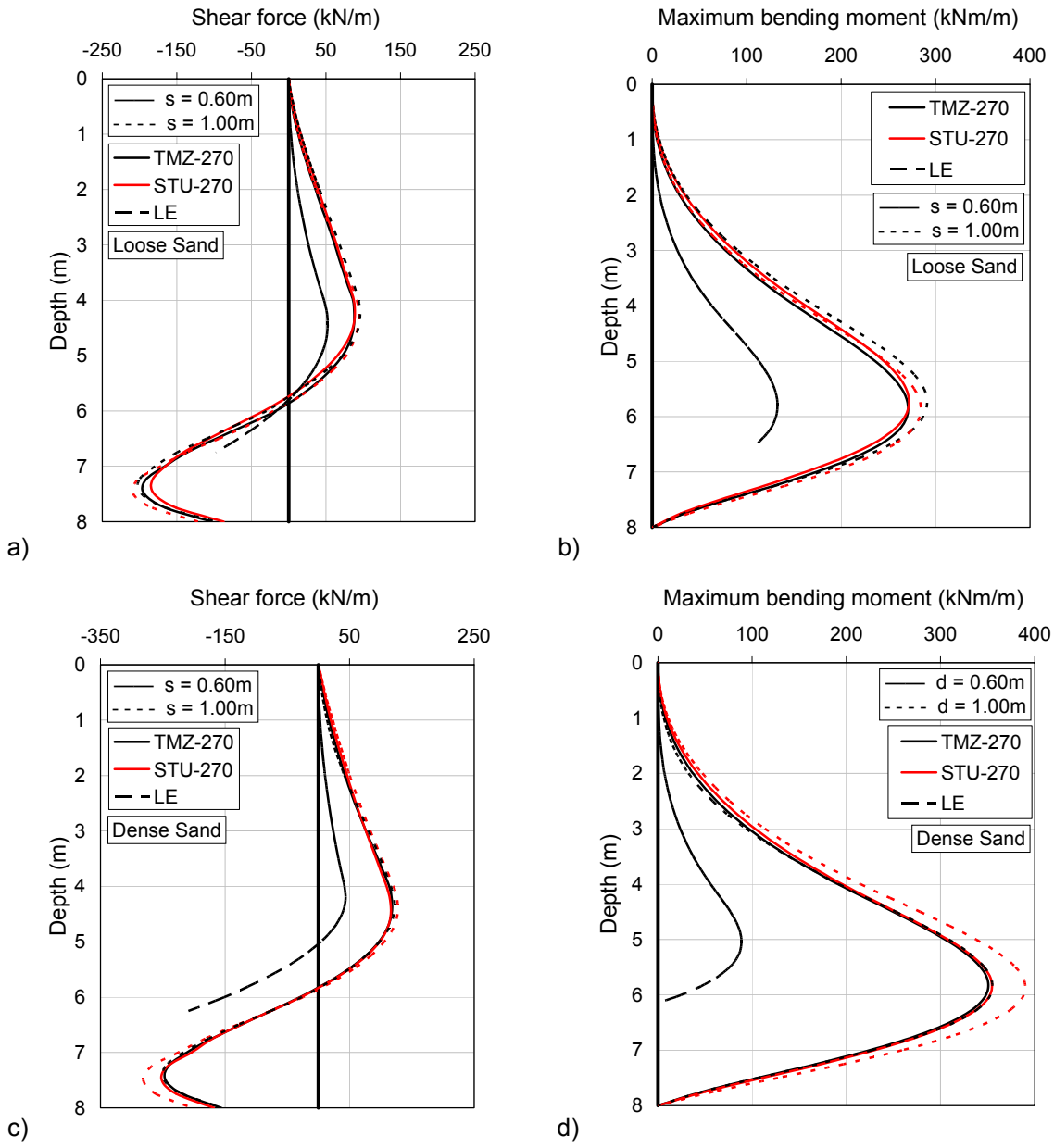

Figure 6-36. *Shear forces and bending moments acting on walls in loose (a, b) and dense (c, d) sand at the instants of maximum bending moment.*

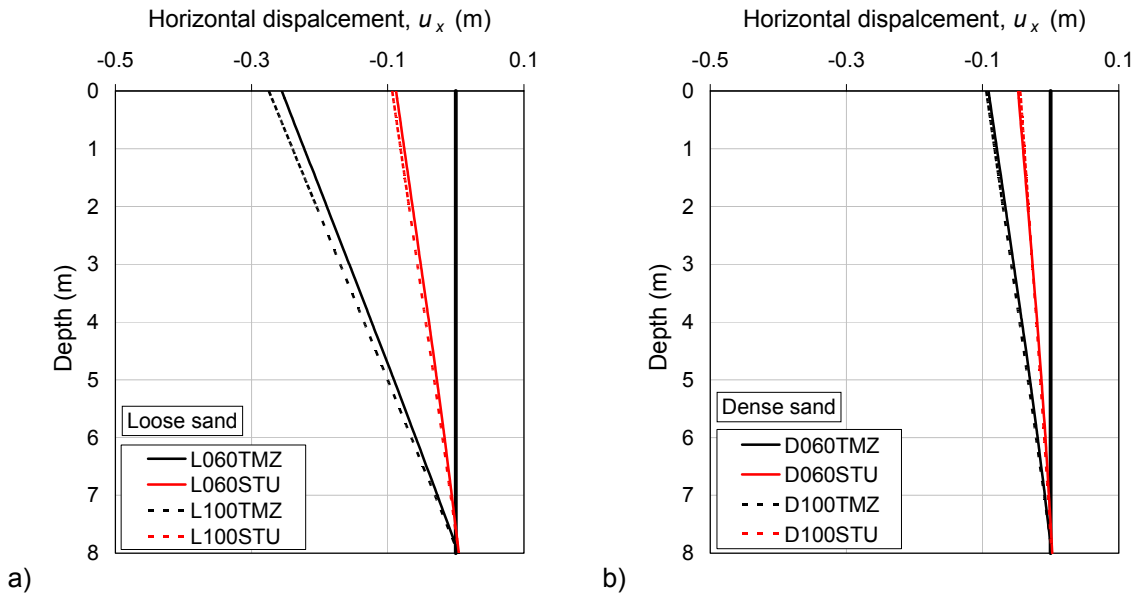

Figure 6-37. *Horizontal displacements of the walls in loose (a) and dense (b) sand at the instants of maximum bending moment.*

Figure 6-38 and Figure 6-39 show the time instants in which the maximum bending moments are achieved during the analyses in relation to the horizontal displacements of the top of the walls. It seems that when the diaphragms reach the maximum velocity, the earth pressures induce the greater bending moment.

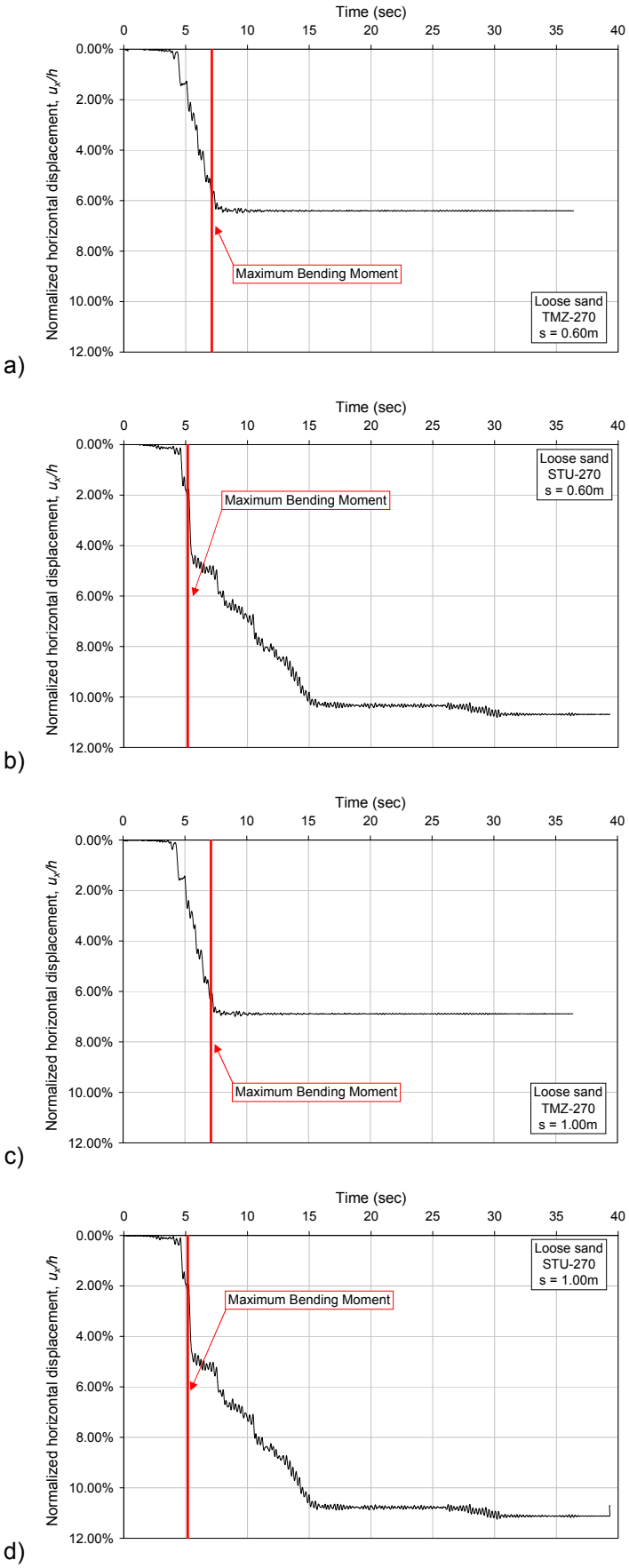

Figure 6-38. *Instants of maximum bending moment in relation to the earthquake-induced displacements of walls in loose sand: a) L060TMZ; b) L060STU; c) L100TMZ; L100STU.*

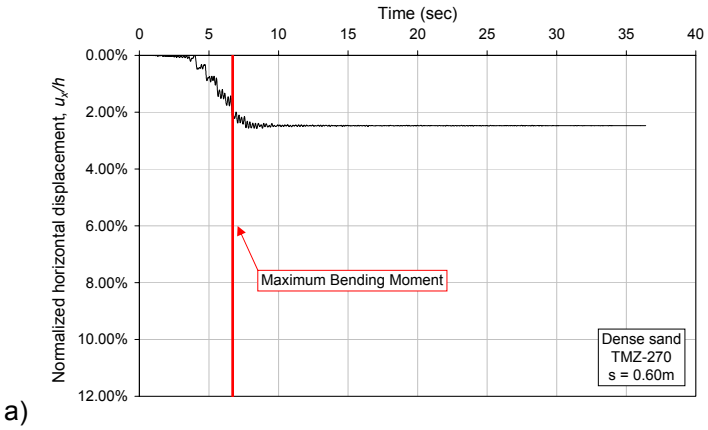

a)

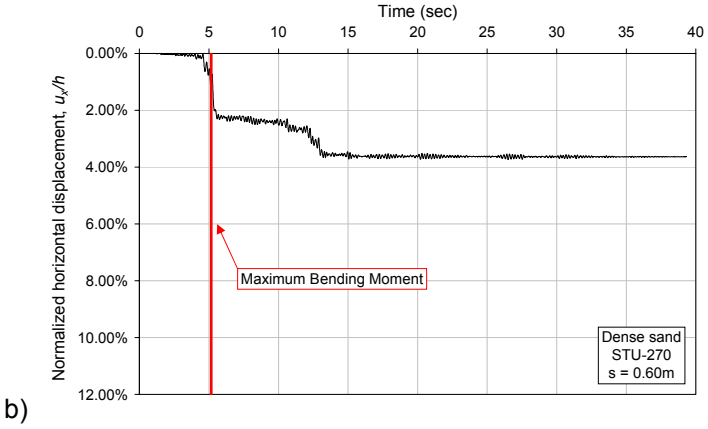

b)

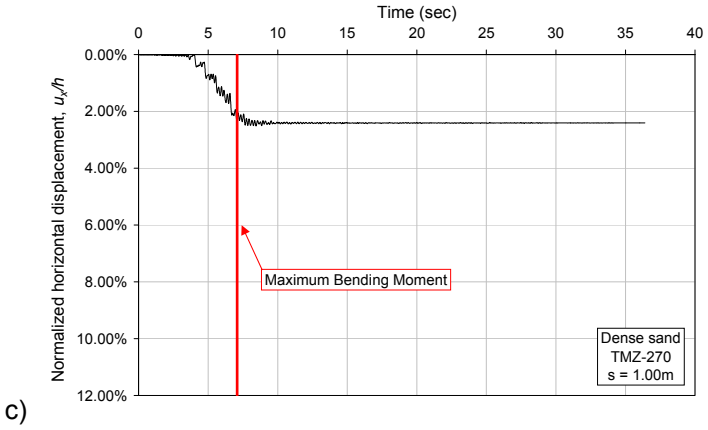

c)

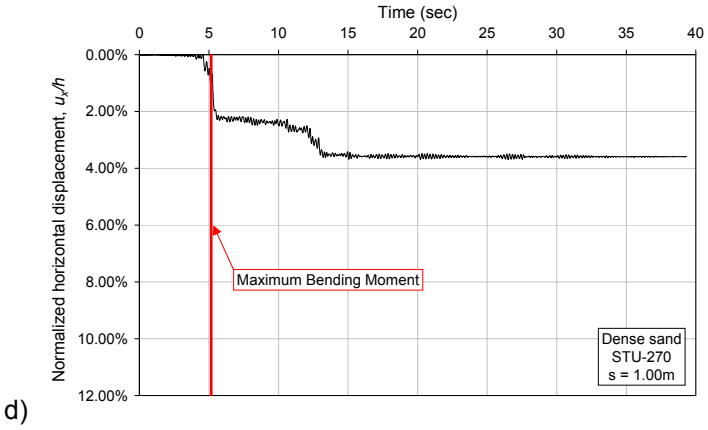

d)

Figure 6-39. *Instants of maximum bending moment in relation to the earthquake-induced displacements of walls in dense sand: a) D060TMZ; b) D060STU; c) D100TMZ; D100STU.*

6.6 COMPARISONS BETWEEN THE RESULTS OF DIFFERENT ANALYSES.

Table 6-14 summarizes the results of the various type of analyses performed on the examined schemes.

Assuming the dynamic analyses as reference solution, the first difficulty encountered in the simplified methods is the definition of the seismic horizontal coefficient associated to each earthquake. In fact, the same signal, applied to the base of the two soil columns of loose and dense sand, belonging to the same soil category, produces different seismic amplification, both for dynamic interaction and free field conditions. Furthermore, the effects on walls in terms of displacements and stresses are quite different.

The common simplified analyses of the pseudostatic limit equilibrium and the use of empirical formulas do not give very dissimilar displacements but underpredict the maximum bending moments.

Accurate displacements are furnished for diaphragms in dense sand from the simplified dynamic analyses. For loose sand, instead, the predicted values are too much large.

The pushover analyses allow completely describing the seismic performances of each wall. The difficulty consists only on the definition of the expected k_h for the seismic demand of the site and subsoil conditions of the structure. This type of analysis is also able to account for the effects of wall properties on the seismic response.

Remembering the hierarchical resistance concepts exposed in the Chapter 5, the limit equilibrium approach for the evaluation of the critical acceleration of the retaining system in the simplified analyses is a good method to control the collapse of the retaining system if the formation of a plastic hinge in the wall below the excavation level can be preferred to the failure of the structure for exceeding of the soil passive strength.

ANALYSIS CODE	k_h				u_x/h				$\Delta M_{max}/\gamma h^3$			
	SA	SDA	PA	DA	SA	SDA	PA	DA	SA	SDA	PA	DA
L060TMZ	0.260	0.260	0.260	0.203	9.55%	14.58%	-	6.50%	0.074	0.093	-	0.242
L060STU	0.264	0.264	0.264	0.266	9.70%	17.23%	-	10.75%	0.074	0.100	-	0.244
L100TMZ	0.260	0.260	0.260	0.188	9.55%	9.75%	-	6.93%	0.074	0.093	-	0.256
L100STU	0.264	0.264	0.264	0.257	9.70%	12.33%	-	11.15%	0.074	0.100	-	0.264
D060TMZ	0.260	0.260	0.260	0.359	4.68%	2.55%	0.40%	2.53%	0.146	0.159	0.228	0.311
D060STU	0.264	0.264	0.264	0.359	4.75%	3.30%	0.40%	3.68%	0.146	0.178	0.228	0.315
D100TMZ	0.260	0.260	0.260	0.368	4.68%	2.93%	0.34%	2.43%	0.146	0.159	0.258	0.316
D100STU	0.264	0.264	0.264	0.362	4.75%	4.13%	0.34%	3.63%	0.146	0.178	0.258	0.351

SA = Simplified analyses

SDA = Simplified dynamic analyses

PA = Pushover analyses (referred to RTD seismic earth pressure distributions)

DA = Dynamic analyses

Table 6-14. *Comparisons between the seismic performances of the walls predicted by the different analyses.*

7 CONCLUSIONS AND FUTURE DEVELOPMENTS.

The increasing use of the underground spaces and the last seismic events in the urban areas have driven many researchers of different countries to deepen the knowledge on the dynamic behaviour of the structure embedded in the subsoil.

Different contributes were given by the recent Italian and European building codes on these topics. The present PhD thesis has found its main role in the application of the performance based approach in the seismic design of this type of structures.

The most widespread procedure based on the extension of the limit equilibrium method to the pseudostatic conditions was analyzed and discussed. The effectiveness of the Mononobe (1929) and Okabe (1926) and Lancellotta (2007) theories for the estimation of the seismic active and passive earth pressure coefficients was shown. Some charts for the preliminary design of the depth of embedment and the maximum bending moment for walls in dry homogeneous granular materials were developed by using the Blum method. To predict the earthquake-induced displacements of the walls, the empirical relationships proposed by Uwabe (1983) for anchored bulkheads embedded in non-liquefiable sites were considered also for cantilever walls. However, their capabilities should be tested on a greater number of data deriving from advanced numerical analyses, model and full scale tests.

Another design method, consisting in a pseudostatic procedure to define the critical acceleration of the retaining system and Newmark sliding block analyses for the calculation of the seismic displacements, was highlighted. The approach can be identified such as simplified dynamic analysis but its application presents some difficulties and uncertainties for flexible walls, as recognized in the literature (Callisto, 2006).

An innovative design method to completely predict the seismic performances of a retaining system was proposed in this thesis. The procedure can be included in the framework of the "pushover analyses" and can be accomplished by conducting FE or FD pseudostatic analyses. It consists to apply the seismic loading as an increasing pressure distribution that can be expressed as a seismic horizontal coefficient by means of the normalization with respect to the weight of the active soil wedge and the wall. The performances of the system can be described by capacity curves in terms of maximum horizontal displacements, maximum settlements of the backfill, maximum bending moment, etc. The method requires more validations by means of accurate analyses with appropriate soil constitutive models, seismic in-situ monitoring of full-scale structures and dynamic centrifuge modelling. However, the good agreement between the predictions of the analyses presented in the Chapter 6 encourages deepening the application of the pushover analyses to the embedded walls that is not a consolidated procedures for the seismic design of geotechnical systems.

The most accurate tool for the estimation of the dynamic behaviour of the constructions interacting with the soil is constituted by the numerical simulations. Their use requires advanced knowledge in numerical calculations, a proper soil constitutive model, an adequate soil characterization by means of in situ and laboratory tests, a proper definition of the seismic input when dynamic analyses should be carried out. In the Annex B, the problem of the calibration of the FE model for dynamic analyses in geotechnical earthquake engineering by means of a commercial code was illustrated. The various sources of damping were recognized and the procedure to rightly estimate the damping coefficients,

both numerical and material, was presented. In order to minimize the spurious effects of the reflected stress waves on the lateral boundaries of the discrete models, an useful configuration of the boundary conditions was accomplished by testing the seismic response of the models crossed by vertical shear waves.

An example of application of the different procedures for the evaluation of the seismic performances of free cantilever walls embedded in dry loose and dense sand was shown in the Chapter 6. The predictions confirm the difficulties related to the application of the simplified methods, especially in the definition of the equivalent seismic coefficient for a given earthquake.

The material properties for the soils was chosen on the basis of the results of laboratory tests conducted on samples of Leighton Buzzard sand 100/170 (Fraction E) presented in the Annex A. The experimental data have allowed defining the mechanical behaviour of the sand under different stress paths and loading conditions. The future developments of this research line is the use of advanced constitutive models to simulate the behaviour of the sand in the controlled laboratory tests to catch its main mechanical aspects. The material was chosen in the contest of the research program ReLUIS presented in the Chapter 1 for the centrifuge model tests of retaining walls.

REFERENCES.

Ampadu S. I. K, Tatsuoka F.(1989). "The dry versus the wet Methods of setting clay specimens for triaxial testing", Proc. 28th National Conference of the Japanese Society of Soil Mechanics and Foundation Engineering, Tokyo, June

Aversa S. and Vinale F. (1985). “Improvement to a stress-path triaxial cell”, Geotechnical Testing Journal, Vol. 18, Issue 1, pp. 116-120

Bardet J.P., Ichii K. and Lin C.H. (2000). “EERA: a computer program for Equivalent-linear Earthquake site Response Analyses of layered soil deposits”, University of Southern California, Los Angeles.

Bardet J.P., Tobita T. (2001). “NERA: a computer program for Nonlinear Earthquake site Response Analyses of layered soil deposits”, University of Southern California, Los Angeles.

Berenger J.P., (1994). “A perfectly matched layer for the absorption of electromagnetic waves”, J. of Comp. Physics, vol. 114, pp. 185-200

Bica A.V.D., Clayton C.R.I. (1989). "Limit equilibrium design methods for free embedded cantilever walls", Proc. Inst. Civ. Engrs 86, 879-898.

Bica A.V.D., Clayton C.R.I. (1992). “The preliminary design of free embedded cantilever walls in granular soils”, Proc. Int. Conf. on Retaining Structures, Cambridge

Bica A.V.D., Clayton C.R.I. (1998). " An experimental study of the behaviour of embedded lengths of cantilever walls", Geotechnique, Vol. 48, no.6, pp. 731.745

Bishop A.W., Wensley L.D. (1975). "Hydraulic triaxial apparatus for controlled stress path testing", Geotechnique, Vol. 25, no. 4, pp. 657-670

Blum H. (1931).”Einspannungsverhältnisse bel Bohlwerken”,Wilh.Ernst und Sohn Berlin

Bolton M.D. (1986). "The strength and dilatancy of sands", Geotechnique, Vol. 36, no. 1, pp. 65-78

Bransby, P. L., Milligan, G. W. E. (1975). "Soil deformations near cantilever sheet pile walls", Geotechnique, Vol. 25, No. 1, 175-195

Brinkgreve R.B.J. (2002). Plaxis 2D version8. A.A. Balkema Publisher, Lisse.

Callisto L. (2006), “Pseudo-static seismic design of embedded retaining structures", Workshop of ETC12 Evaluation Committee for the Application of EC8, Athens, January 20-21

Caquot A., Kerisel F. (1948). “Tables for the calculation of passive pressure, active pressure and bearing capacity of foundations”, Gauthier-Villars, Paris

Castro G. (1969). "Liquefaction of sands", Harvard Soil Mechanics Series 87, Harvard University, Cambridge, Massachusetts

Chang M.F. (1981). “Static and seismic lateral earth pressures on rigid retaining structures”, PhD Thesis, School of Civil Engineering, Purdue University, West Lafayette, IN, 465 pp.

Chang M.F., Chen W.F. (1982). “Lateral earth pressures on rigid retaining walls subjected to earthquake forces”, Solid mechanics archives, Vol. 7, Martinus Nijoff Publishers, The Hague, The Netherlands, pp. 315-362

Chen W.F., Rosenfarb J.L. (1973). “Limit analysis solutions of earth pressure problems”, Soils and Foundations, Vol. 13, No. 4, pp. 45-60

Chen W.F. (1975). “Limit analysis and soil plasticity”, Elsevier, Amsterdam, 638 pp.

References

Chen W.F., Chang M.F. (1981). “Limit analysis in soil mechanics and its applications to lateral earth pressure problems”, Solid mechanics archives, Vol. 6, No. 3, Sijthoff & Noordhoff International Publishers, Alphen aan den Rijn, The Netherlands, pp. 331-399

Chen W.F. (1982). “Constitutive equations for engineering materials, Vol. 1: Elasticity and modelling”, Wiley Interscience, New York, NY, 580 pp.

Chen W.F. (1990). “Limit analysis in soil mechanics”, Elsevier, Amsterdam, 477 pp.

Clayton C.R.I., Milititsky J. Woods R.I. (1993). “Earth pressure and earth retaining structures”, Chapman & Hall

Coulomb C.A. (1776). “Essai sur une application des regles des maximis et minimis a quelques problemes de statique relatifs a l’architecture”, Memoires de l’Academie Royale pres Divers Savants, Vol. 7

Cundall, P., Hansteen, E., Lacasse, S., and Selnes, P. B., (1980). “NESSI, soil structure interaction program for dynamic and static problems”, Norges Geotekniske Institute, Norway

Day R.A.(1999). " Net pressure analysis of cantilever sheet pile walls", Geotechnique, Vol. 49, no.2, pp. 231-245

Dennehy K.T. (1985). "Seismic vulnerability, analysis and design of anchored bulkheads", PhD. Dissertation, Renssalaer Polytechnic Institute, Troy, New York

D'Onofrio A. (1996). "Comportamento meccanico dell'argilla di Vallericca in condizioni lontane dalla rottura", PhD. Thesis, Università degli Studi di Napoli Federico II, Napoli, Italy (in Italian)

Ebeling R.M., Morrison E.E.(1993). "The seismic design of waterfront retaining structures", NCEL Report R-939, Naval Civil Engineering Laboratory, Port Hueneme, California, 256 pp.

EN 1997-1 (October 2001). Eurocode 7: Geotechnical design – Part 1: General rules. CEN European Committee for Standardization, Bruxelles, Belgium.

EN 1998-5 (December 2003). Eurocode 8: Design of structures for earthquake resistance – Part 5: Foundations, retaining structures and geotechnical aspects. CEN European Committee for Standardization, Bruxelles, Belgium

EPRI, Electric Power Research Institute (1991): “Soil response to earthquake ground motion”, NP-5747, pp. 293

Fourie A.B., Potts D.M. (1989). “Comparisons of finite element and limiting equilibrium analyses for an embedded cantilever retaining wall”, Geotechique, Vol. 39, pp. 175-188

Franklin A.G., Chang F.K. (1977). "Permanent displacements of earth embankments by Newmark sliding block analysis", Report 5, Miscellaneous Paper S-71-17, U.S. Army Corps of Engineers Waterways Experiment Station, Vicksburg, Mississipi.

Franzius O. (1924): "Versuche mit passiven Druck", Bauingegnieur, Berlin, 314-320

Gazetas G., Dakoulas P., Dennehy K. (1990). "Empirical seismic design method for waterfront anchored sheet pile walls", Proc. ASCE, Specialty Conf. On Design and Performance of Earth Retaining Structures, Geotechnical Specialty Publication 25, pp. 232-250

Habibagahi K., Ghahramani A. (1977). “Zero extension theory of earth pressure”, Journal of Geotechnical Division, ASCE, Vol. 105 (GT7), pp. 881-896

References

Hardin B.O., Drnevich V.P. (1972). "Shear modulus and damping in soils: Measurement and parameter effects", Journal of Soil Mechanics and Foundations Division, ASCE, Vol. 98, no. SM6, pp. 603-624

Hettiaratchi R.P., Reece A.R. (1975). “Boundary wedges in two-dimensional passive soil failure”. Geotechnique, Vol. 25, No. 2, pp. 197-220

Iai S., Ichii K. (1998). “Performance Based design of port structures", U.S./Japan Natural Resources Development Program (UJNR). Wind and Seismic Effects. Joint Meeting of the U.S./Japan Cooperative Program in Natural Resources Panel on Wind and Seismic Effects, 30th. May 12-15, 1998, Gaithersburg, MD, Raufaste, N. J., Jr., Editor(s), 84-96 pp, 1998

Iai, S., Ichii, K., Liu, H., Morita, T. (1998). "Effective stress analyses of port structures", Soils and Foundations, Special Issue on Geotechnical Aspects of the January 17 1995 Hyogoken-Nambu Earthquake, No.2, pp. 97-114

Iwan W.D. (1967). “On a class of models for the yielding behaviour of continuous and composite systems”, ASME, Journal of Applied Mechanics, Vol. 34, pp.612-617

Ishihara K. (1993). " Liquefaction and flow failure during earthquakes", geotechnique, Vol. 43, no. 3, pp. 351-415

James R.G., Bransby P.L. (1970). “Experimental and theoretical investigations of a passive earth pressure problem”, Geotechnique, Vol. 20, No. 1, pp. 17-37

Jamiolkowski M. et al. (1985). "Laboratory validation of in situ tests", in Geotechnical Engineering in Italy, ISSMFE, Golden Jubilee Volume, AGI 251-270

Jeyatharan K. (1991). " Partial liquefaction of sand fill in a mobile arctic caisson under dynamic ice-loading", PhD. Thesis, Cambridge University, Cambridge, U.K.

King G. J. W., McLoughlin J. P. (1992). "Centrifuge model studies of a cantilever retaining wall in sand", Proceedings of an international conference on Retaining Structures, Cambridge, pp. 711-720.

King G. J. W. (1995). "Analysis of cantilever sheet-pile walls in cohesionless soil", J. Geotech. Engng Div., ASCE, Vol. 121, No. 9, 629-635

Kramer, S.L. (1996). “Geotechnical Earthquake Engineering”, Prentice Hall, Inc., Upper Saddle River, New Jersey, 653 pp.

Kuhlmeyer R.L, Lysmer J. (1973). “Finite Element Method Accuracy for Wave Propagation Problems”, J. of the Soil Mechanics and Foundation Division, vol.99 n.5, pp. 421-427

Kunar R. R., Beresford P. J., Cundall P. A. (1977). “A Tested Soil-Structure Model for Surface Structures,” in Proceedings of the Symposium on Soil-Structure Interaction (Roorkee University, India, January, 1977), Vol. 1, pp. 137-144. Meerut, India: Sarita Prakashan

Lancellotta R. (2002). “Analytical solution of passive earth pressure”, Geotechnique, Vol. 52, No. 8, pp. 617-619

Lancellotta R. (2007). “Lower-Bound approach for seismic passive earth resistance”. Geotechnique, Vol. 57, No. 3, pp. 319-321

Lanzo G., Vucetic M. (1999). "Effect of Soil Plasticity on Damping Ratio at Small Cyclic Strains", Soils and Foundations, Vol. 39, No. 4, pp. 131-141

References

Lanzo G., Pagliaroli A., D'Elia B. (2004). "L'influenza della modellazione di Rayleigh dello smorzamento viscoso nelle analisi di risposta sismica locale", ANIDIS, XI Congresso Nazionale "L'Ingegneria Sismica in Italia", Genova 25-29 Gennaio 2004 (in Italian)

Lanzo G. (2005): "Risposta sismica locale", Aspetti geotecnici della progettazione in zone sismiche, Linee Guida AGI (in Italian)

Leiper Q.J. (1984). "Instrumentation of diaphragm walls", M. Sc. Dissertation, University of Surrey

LUSAS (2000). Theory Manual, FEA Ltd., United Kingdom

Lyndon A., Pearson R. A. (1984). "Pressure distribution on a rigid retaining wall in cohesionless material", Proceedings of a symposium on the application of centrifuge modelling to geotechnical design, Manchester, pp. 271-280

Lysmer J., Kuhlmeyer R.L. (1969). "Finite Dynamic Model for Infinite Media", ASCE, Journal of Engineering and Mechanical Division, pp. 859-877

Lysmer, J., and G.Waas. (1972). "Shear Waves in Plane Infinite Structures", ASCE J. Eng. Mech., Vol. 98, no. EM1, pp. 85-105

Lysmer J. (1978): "Analytical procedures in soil dynamics", Report no. UCB EERC-78/29, University of California, Berkeley

Madabhushi, S.P.G., Schofield, A.N., Lesley, S. (1998). "A new stored angular momentum (SAM) based earthquake actuator", In Kimura, Kusakabe & Takemura (eds.), Proc. Int. conf. Centrifuge '98, Tokyo, 23-25 September 1998, Rotterdam, Balkema

Mak K.W. (1984). "Modelling the effects of a strip load behind rigid retaining walls", PhD. Thesis, Cambridge University, Cambridge, U.K.

Masing G. (1926). "Eigenspannungen und Verfertigung beim Messing", Proc., 2nd International Congress on Applied Mechanics, Zurich

Ministry of Transport, Japan, (1999). "Design Standard for Port and Harbour Facilities and Commentaries", Japan Port and Harbour Association, 1181 pp. (in Japanese)

Mononobe N., Matsuo H. (1929)."On the determination of earth pressures during earthquakes", Proc. World Engineering Conference, Vol. 9, pp. 176

Mroz Z. (1967). "On the description of anisotropic work hardening", Journal of Mechanics and Physics of Solids, 15, pp. 163-175

Mulilis J.P., Seed H.B., Chan C.K., Mitchell J.K. (1977). "The effects of method of sample preparation on the cyclic stress-strain behaviour of sands", Report no. EERC 75-18, Earthquake Engineering Research Center, University of California, Berkeley

Nadim F. (1980). "Tilting and sliding of gravity retaining walls", S.M. Thesis, Department of Civil Engineering, Massachusetts Institute of Technology, Cambridge, Massachusetts

Nadim F. (1982). "A numerical model for evaluation of seismic behaviour of gravity retaining walls", Sc. D. thesis, Research Report R82-33, Department of Civil Engineering, Massachusetts Institute of Technology, Cambridge, Massachusetts

Newmark, N. M. (1959). "A Method of Computation for Structural Dynamics", ASCE, Journal of the Engineering Mechanics Division, Vol. 85 No. EM3

Newmark N. (1965). "Effects of earthquakes on dams and embankments", Geotechnique, Vol. 15, no. 2, pp. 139-160

References

NTC 2008. Approvazione delle nuove norme tecniche per le costruzioni. Gazzetta Ufficiale della Repubblica Italiana, n. 29 del 4 febbraio 2008 - Suppl. Ordinario n. 30, http://www.cslp.it/cslp/index.php?option=com_docman&task=doc_download&gid=3269&Itemid=10 (in Italian).

Okabe S. (1926). “General theory of earth pressure”, Journal of Japanese Society of Civil Engineering, Vol. 12, No. 1

Okamoto S. (1956). “Bearing capacity of sandy soil and lateral earth pressure during earthquakes”, Proc. 1st World Conf. on Earthquake Engineering, Tokyo, pp. 231-247

Padfield C.J., Mair R.J. (1984). “Design of retaining walls embedded in stiff clays”, CIRIA, Report no 104, Construction Industry Research and Information Association, London

Pal O. (1998). "Modélisation du comportement dynamique des ouvrages grace à des elements finis de haute precision”, Thesis, L’université Joseph Fourier – Grenoble I

Pane V., Tamagnini C. (2004). “Analisi di paratie pluriancorate”, Hevelius, Benevento (in Italian)

Park D., Hashash Y.M.A. (2004). "Soil Damping Formulation in Nonlinear Time Domain Site Response Analysis”, Journal of Earthquake Engineering, Vol.8, no. 2, pp. 249-274

PHRI (1997). “Handbook on liquefaction remediation of reclaimed land", Port and Harbour Research Institute, A.A. Balkema, Rotterdam, Brookfield

PIANC (2001). “Seismic Design Guidelines for Port Structures”, Working Group n.34 of the Maritime Navigation Commission, International Navigation Association, Balkema, Lisse, 474 pp.

Rankine W. (1857). “On the stability of loose earth”, Philosophical Transactions of the Royal Society of London, Vol. 147

Pyke, (1979). "Nonlinear soil models for irregular cyclic loading", Journal of the Geotechnical Engineering Division, Vol. 105, pp. 715 - 726

Richards R., Elms D. (1979). "Seismic behaviour of gravity retaining walls", Journal of geotechnical Engineering Division, ASCE, Vol. 105, no. GT4, pp. 449-464

Roesset, J.M. (1970): “Fundamentals of Soil Amplification”, in Seismic Design for Nuclear Power Plants, ed. R.J. Hansen, The MIT Press, Cambridge, MA, pp. 183-244

Roesset, J. M., Ettouney M. M. (1977). “Transmitting Boundaries: A Comparison”, Int. J. Num. & Analy. Methods Geomech., Vol. 1, pp. 151-176.

Ross M., (2004). "Modeling Methods for Silent Boundaries in Infinite Media", ASEN 5519-006: Fluid-Structure Interaction, University of Colorado at Boulder

Rowe P.W. (1951). “Cantilever sheet piling in cohesionless soil", Engineering September 7, pp. 316-319

Rowe P.W. (1952). “Anchored sheet pile walls”, Proc. ICE, Vol. 1, no.1, pp. 27-70

Rowe P.W. (1957). “Sheet pile walls in clay”, Proc. ICE, Vol. 7, pp. 629-654

Santucci de Magistris F. (1992). "Una cella triassiale a stress path controllato: messa a punto e primi risultati sperimentali", Sc.M. Thesis, Università degli studi di Napoli Federico II (In Italian)

Santucci de Magistris F., Koseki J., Amaya M., Hamaya S., Sato T., Tatsuoka, F (1999). "Triaxial testing system to evaluate stress-strain behaviour of soils for wide range of strain and strain rate", ASTM Geotechnical Testing Journal, Vol. 22, no. 1, pp. 44-60

References

Schnabel, P. B., Lysmer, J., Seed, H. B. (1972): “SHAKE: a computer program for earthquake response analysis of horizontally layered sites”, Report n° EERC72-12, University of California at Berkeley

Scott R.F. (1963). “Principle of soil mechanics”, Addison-Wesley, Reading, MA, 523 pp.

SEAOC (1995). “Vision 2000 - A Framework for Performance Based Earthquake Engineering", Vol. 1, January

Seed H.B., Idriss I.M. (1970): “Soil moduli and damping factors for dynamic response analyses”, Report ERC 70-10, Earthquake Engineering Research Center, University of California, Berkeley

Seed H.B., Whitman R.V. (1970). “Design of earth retaining structures for dynamic loads”, Proc. ASCE Specialty Conference on lateral stresses in the ground and design of earth retaining structures, pp. 103-147

Siddharthan R., Ara S., Norris G.M. (1992). "Simple rigid plastic model for seismic tilting of rigid walls", Journal of Structural Engineering, ASCE, Vol. 118, no. 2, pp. 469-487

Skempton A.V. (1953). “Earth pressure, retaining walls, tunnels and strutted excavation”, Proc. of 3rd Int. Conf. Soil Mech. Found. Engin.

Smith, I.M., Griffith, D.V. (1982): “Programming the Finite Element Method”, Second Edition. John Wiley & Sons, Chisester, U.K.

Sokolovskii V.V. (1965). “Static of granular media”, Pergamon Press, New York, NY, 232 pp.

Steedman R.S., Zeng X. 1990. “The seismic response of waterfront retaining walls”, Proc. ASCE Specialty Conference on Design and Performance of Earth Retaining Structures, Special Technical Publication 25, Cornell University, Ithaca, New York, pp.872-886

Steedman R.S. (1998). “Seismic design of retaining walls", Proc. Instn Civ. Engng, Vol. 131, pp. 12-22

Tan F.S.C. (1990). "Centrifuge and theoretical modelling of conical footings on sand", PhD. Thesis, Cambridge University, Cambridge, U.K.

Tatsuoka F., Iwasaki T., Takagi Y. (1978). “Hysteretic damping of sands and its relation to shear modulus”, Soils and Foundations, Vol. 18, no. 2, pp. 25-40

Tatsuoka F., Ochi K., Fujii S., Okamoto M. (1986). “Cyclic undrained triaxial and torsional shear strength of sands for different sample preparation methods”, Soils and Foundations, Vol. 26, no. 3, pp. 11-16

Tatsuoka F., Sato T., Park C.S., Kim Y.S., Mukabi J.N., Kohata Y. (1994). "Measurements of elastic properties of geomaterials in laboratory compression tests", ASTM Geotechnical Testing Journal, Vol. 17, no. 1, pp. 80-94

Taylor D.W. (1948). “Fundamentals of Soil Mechanics”, Wiley, New York, 700 pp.

Teng W.C. (1962). “Foundation design”, Prentice-Hall, New Jersey

Terzaghi K. (1943). “ Theoretical Soil Mechanics”, Wiley, Inc., New York

Terzaghi K. (1954). “Anchored bulkheads”, Trans. ASCE, Vol. 119, pp. 1243-1280

Towhata I., Islam S. (1987). “Prediction of lateral movement of anchored bulkheads induced by seismic liquefaction”, Soils and Foundations, Vol. 27, No. 4, pp. 137-147

Trifunac M.D., Brady A.G. (1975): “A study of the duration of strong earthquake ground motion”, Bulletin of the Seismological Society of America, 65, 581-626

Tschebotarioff G.P. (1973). “Foundations, retaining and earth structures”, MGraw-Hill, New York

Uwabe T. (1983). "Earthquake response and seismic design of composite type breakwater in deep sea", Proc. Of 1983 Annual Research Presentations of Port and Harbour Research Institute, pp. 103-165 (in Japanese)

Visone C., Santucci de Magistris F. (2007). “Some aspects of seismic design methods for flexible earth retaining structures”, ISSMGE – ERTC 12 Workshop – XIV European Conference on Soil Mechanics and Geotechnical Engineering, 25th September 2007, Madrid

Vucetic M., Dobry R. (1986). "Pore Pressure Build Up and Liquefaction at Level Sandy Sites During Earthquakes”, Research Report, Department of Civil Engineering, Rensselaer Polytechnic Institute, Troy

Vucetic M. (1990). "Normalized behaviour of clay under irregular cyclic loading", Canadian Geotechnical Journal, Vol. 27, no. 1, pp. 29-46

Wang Z.L., Qing-Yu H., Gen-Shou Z. (1980). “Wave Propagation Method of Site Seismic Response by a Visco-Elastoplastic Model”, Proceedings: Seventh World Conference on Earthquake Engineering, Vol. 2, p. 279-386

Werner (1998). “Seismic Guidelines for Ports", Technical Council on Lifeline Earthquake Engineering, Monograph n.12, ASCE

White W., Valliappan S., Lee I. K. (1977). “Unified Boundary for Finite Dynamic Models”, J. Eng. Mech., Vol. 103, pp. 949-964

Whitman R., Liao S. (1984). "Seismic Design of Gravity Retaining Walls", Proc., 8th World Conference on Earthquake Engineering, San Francisco, California, Vol. 3

Whitman R., Liao S. (1984). "Seismic Design of Gravity Retaining Walls", Miscellaneous Paper GL-85-1, U.S. Army Engineer Waterways Experiment Station, Vicksburg, Mississipi

Wilson E. L. (1962). “Dynamic Response by Step-By-Step Matrix Analysis”, Proceedings, Symposium On The Use of Computers in Civil Engineering, Laboratorio Nacional de Engenharia Civil, Lisbon, Portugal, October 1-5

Wilson E. L., Farhoomand I., Bathe K. J. (1973). “Nonlinear Dynamic Analysis of Complex Structures”, Earthquake Engineering and Structural Dynamics, Vol. 1, 241-252

Wolf J.P. (1985). "Dynamic soil-structure interaction", Prentice Hall, New Jersey, 466 pp.

Wong C.P. (1982). "Seismic analysis and an improved design procedure for gravity retaining walls", S.M. Thesis, Department of Civil Engineering, Massachusetts Institute of Technology, Cambridge, Massachusetts

Yoshimine M., Ishihara K., Vargas W. (1998). "Effects of principal stress direction and intermediate principal stress on undrained shear behavior of sand", Soils and Foundations, Vol. 38, No. 3, pp. 179-188

Zarrabi-Kashani K. (1979). "Sliding of gravity retaining wall during earthquakes considering vertical accelerations and changing inclinations of failure surface”, S.M. Thesis, Department of Civil Engineering, Massachusetts Institute of Technology, Cambridge, Massachusetts

Zienkiewicz O.C., Taylor R.L. (1991). "The finite element method", 4th edition, Vol. 2, Solid and Fluid mechanics, Dynamics and Non-Linearity, Mc Graw-Hill, U.K.

ANNEX A MECHANICAL BEHAVIOUR OF LEIGHTON BUZZARD SAND 100/170 BY MEANS OF LABORATORY TESTS.

The interpretation of the centrifuge data registered during the seismic excitations on embedded wall models requires an advanced characterization of the sand behaviour. In this section, the results of a series of triaxial and torsional shear tests on dry and saturated sand specimens prepared by means of different techniques are described. The experimental study was conducted at the Laboratory of Soil Dynamics (DYNALAB) of the Hydraulic, Geotechnical and Environmental Engineering Department (D.I.G.A. – Dipartimento di Ingegneria Idraulica, Geotecnica ed Ambientale) at University of Napoli Federico II.

A.1 PHYSICAL PROPERTIES OF SAND.

The Leighton Buzzard sand (denoted as LBS in the following) used in the centrifuge modelling is a commercial sand, and according to the British Standard, the 100/170 sand passes through the No. 100 British Standard sieve (0.15mm) and is retained on the No. 170 sieve (0.09mm), being in the category of fine sands. Thus, the nominal grain size of the sand can be taken as 0.12mm, which is simply the average of the maximum and minimum grain sizes. However, these values are merely estimate and particle size distribution tests are often done in order to establish the distribution of sizes under more controlled conditions.

The particle size distribution for this sand has been determined using the dry sieve method and is shown in Figure A-1. The grain size of D_{50} is 0.14mm, where D_{50} is the grain size diameter at which 50% of the soil weight is finer. The uniformity of a soil is often expressed by a uniformity coefficient U_c, which is defined as the ratio of D_{60} and D_{10}. For LBS, these values are 0.15mm and 0.095mm, respectively, giving $U_c = D_{60} / D_{10} = 1.58$, thus classifying the sand as a uniform sand.

LBS is a quartz based sand and should therefore have a specific gravity G_s similar to that of a silica sand, which is known to be 2.65. Mak (1984) also conducted specific gravity tests according to the British Standard and obtained the same results, thereby confirming the value of $G_s = 2.65$ for the specific gravity of LBS.

The minimum void ratio e_{min} was obtained by filling a 4-inches diameter compaction cylinder (Proctor's type) with dry sand and vibrating it in 3 layers on a vibrating table, at an amplitude of 0.95mm, a frequency of 50Hz and for a duration of 15 minutes. The density and the voids ratio of the specimen were then determined from the overall mass and volume resulting in an e_{min} value of 0.613 Tan (1990).

The maximum void ratio e_{max} was obtained using the quick tilt test in which 1 kg of sand was placed in a 2 litres measuring cylinder with a rubber stopper, shaken several times, turned upside down and then very quickly over again. The volume was then read and the density and void ratio calculated giving $e_{max} = 1.014$ (Tan, 1990).

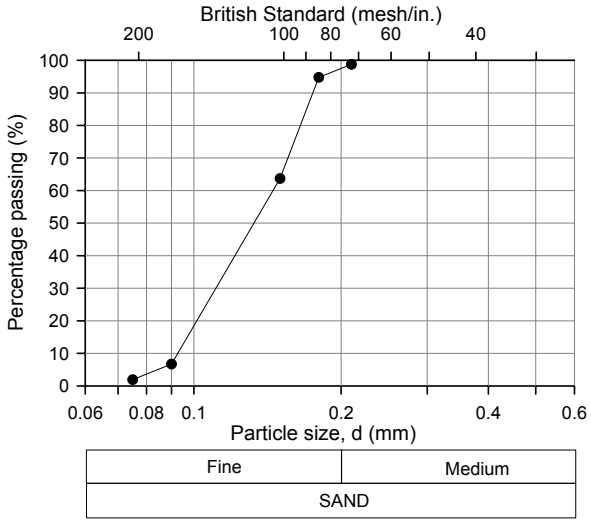

Figure A-1. *Particle size distribution for Leighton Buzzard sand 100/170 (modified from Tan, 1990).*

Permeability tests have been carried out (Jeyatharan, 1991) using the constant head permeameter and the average permeability of specimens at void ratios of approximately 0.72 to de-aired water was found to be 0.98×10^{-4} m/s.

Figure A-2 shows the gravimetric properties of the sand for different densities.

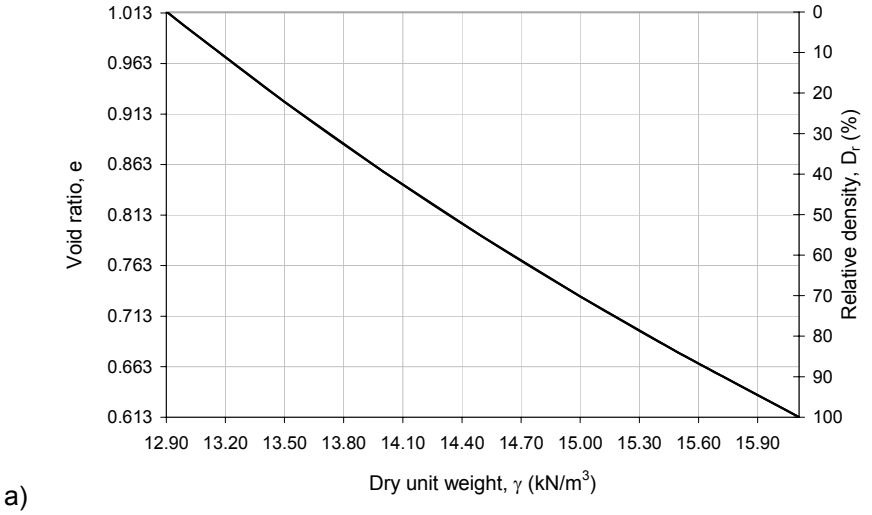

a)

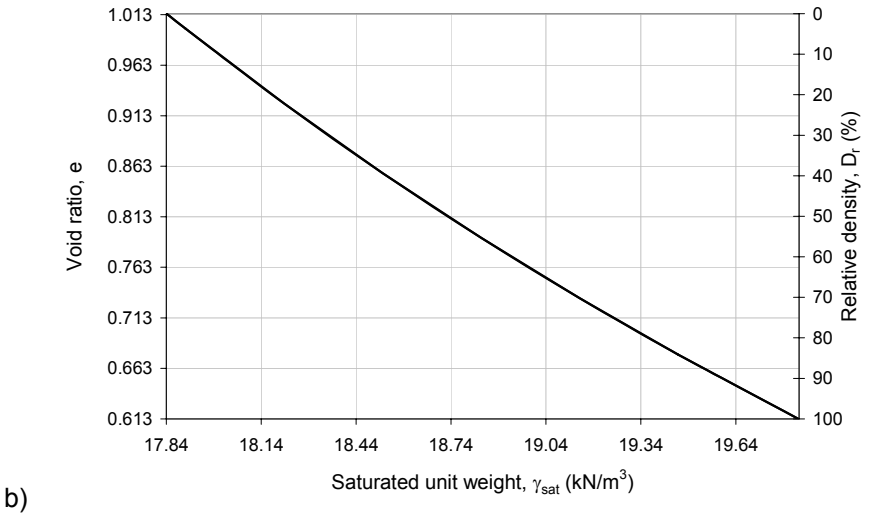

b)

Figure A-2. *Unit weight of LBS for different densities: a) dry conditions; b) saturated conditions.*

The relationships between the void ratio e, the relative density D_r, the specific weight of the grains $\gamma_s = G_s \cdot g$ (g is gravity acceleration = 9.80665 m/s^2), the dry γ and the saturated γ_{sat} unit weight used in the diagrams are the following:

$$D_r = \frac{e_{max} - e}{e_{max} - e_{min}} \qquad (A\text{-}1)$$

$$\gamma = \frac{\gamma_S}{1+e} \qquad (A\text{-}2)$$

$$\gamma_{sat} = \frac{\gamma_S}{1+e} + \frac{e}{1+e}\gamma_w \qquad (A\text{-}3)$$

A.2 EXPERIMENTAL PROGRAM.

In order to adequately characterize the sand behaviour both in terms of stiffness and strength for various relative densities and different loading paths, a series of triaxial and torsional shear tests were programmed. Table A-1 shows a summary of the experimental program.

Four undrained triaxial compressions and extensions were conducted on relatively loose air-pluviated specimens by using the TX apparatus to clearly highlight the undrained behaviour of the material (i.e. volumetric instability, phase transformation, ultimate state conditions).

Moreover, to evaluate the strength characteristics at peak conditions, drained triaxial tests were performed on medium to dense sand specimens in the B&W cell. The samples are prepared by the freezing procedure described in the next section.

Finally, resonant column and cyclic torsional shear tests were carried out on dry air-pluviated specimens, which were prepared with different relative densities. The stiffness and the damping parameters for low and medium strain levels are measured. The last test (RCTS400b) was realized with the aim to show the loading rate effects on initial values of the shear modulus, G_0, and damping ratio, D_0.

TEST CODE	APPARATUS	PREPARATION METHOD	Initial Relative Density D_r	Pore Fluid	COMPRESSION	SHEAR
UTC200	TX	AP	29.0%	Water	30 to 200 kPa	UTC
UTC400	TX	AP	31.4%	Water	30 to 400 kPa	UTC
UTE200	TX	AP	28.1%	Water	30 to 200 kPa	UTE
UTE400	TX	AP	29.5%	Water	30 to 400 kPa	UTE
DTC100	B&W	FR	80.7%	Water	30 to 100 kPa	DTC
DTC200	B&W	FR	70.2%	Water	30 to 200 kPa	DTC
DTE100	B&W	FR	53.9%	Water	30 to 100 kPa	DTE
DTE200	B&W	FR	52.7%	Water	30 to 200 kPa	DTE
DTCp'100	B&W	FR	76.0%	Water	30 to 100 kPa	DTCp'
DTCp'200	B&W	FR	77.1%	Water	30 to 200 kPa	DTCp'
DTEp'100	B&W	FR	79.2%	Water	30 to 100 kPa	DTEp'
DTEp'200	B&W	FR	63.3%	Water	30 to 200 kPa	DTEp'
RCTS100	THOR	AP	47.1%	Air	30 to 100 kPa	RCTS
RCTS200	THOR	AP	52.4%	Air	30 to 200 kPa	RCTS
RCTS400	THOR	AP	71.3%	Air	30 to 400 kPa	RCTS
RCTS400b	THOR	AP	57.8%	Air	30 to 400 kPa	RCTS

Table A-1. *Experimental program.*

APPARATUSES.

TX = Triaxial apparatus developed at University of Tokyo (Tatsuoka et al., 1994; Santucci de Magistris et al., 1999).

B&W = Bishop & Wesley-type stress path triaxial cell (Bishop & Wesley, 1975; Santucci de Magistris, 1992; Aversa & Vinale, 1995)

THOR = Torsional High Output Rig – Resonant Column (RC) and Torsional Shear (TS) Apparatus (D'Onofrio, 1996)

PREPARATION METHODS.

AP = Air Pluviation

FR = Freezing

COMPRESSION.

All compression tests are isotropic.

SHEAR PHASES.

UTC = Undrained Triaxial Compression

UTE = Undrained Triaxial Extension

DTC = Drained Triaxial Compression

DTE = Drained Triaxial Extension

DTCp' = Drained Triaxial Compression with constant effective mean stress

DTEp' = Drained Triaxial Extension with constant effective mean stress

RCTS = alternated series of Resonant Column and cyclic Torsional Shear tests with increasing loading magnitude

A.3 SAMPLES PREPARATION AND TESTING PROCEDURES.

Different kinds of procedure are used for the preparation of samples of sand for laboratory testing. The basic requirements for all the methods are firstly to obtain homogeneous samples with uniform distribution of void ratio, and secondly to be able to prepare samples of the lowest possible density, to cover a wide range of density in samples reconstituted by an identical method. Different methods of sample reconstitution have been known to create different fabrics, thereby yielding different responses to load application.

In this experimental campaign, two procedures were used: Air-Pluviation (AP) method (Mulilis et al., 1977; Tatsuoka et al., 1986), for loose to medium dense specimens, and Freezing (FR) method, to prepare dense samples.

In the first method, the dry sand is discharged vertically in air from a nozzle with standard dimensions (a nozzle with 15x2mm rectangular cross-section was used in this experimentation) into the forming mould by rotating the apparatus with a constant rate. The AP method is known to produce dilative samples (Ishihara, 1993). However, their behaviour depends on the height of fall during the preparation and on the followed stress-path (Yoshimine et al., 1998).

Figure A-3 shows the densities obtained by fall tests on LB sand for two specimen dimensions.

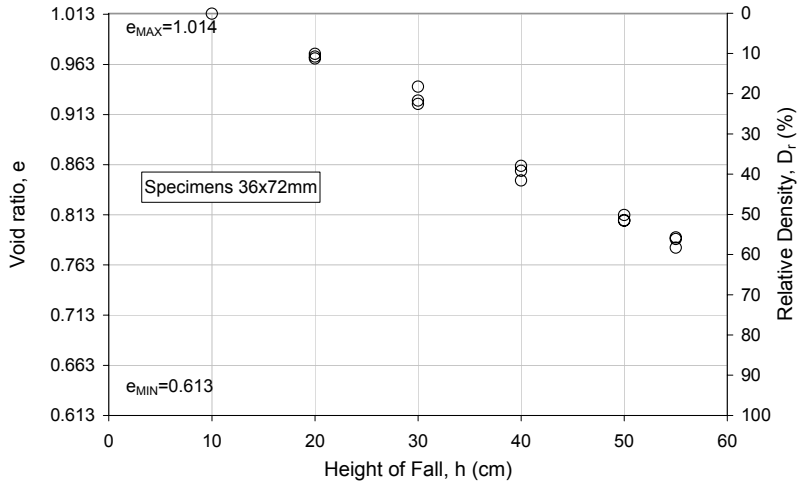

a)

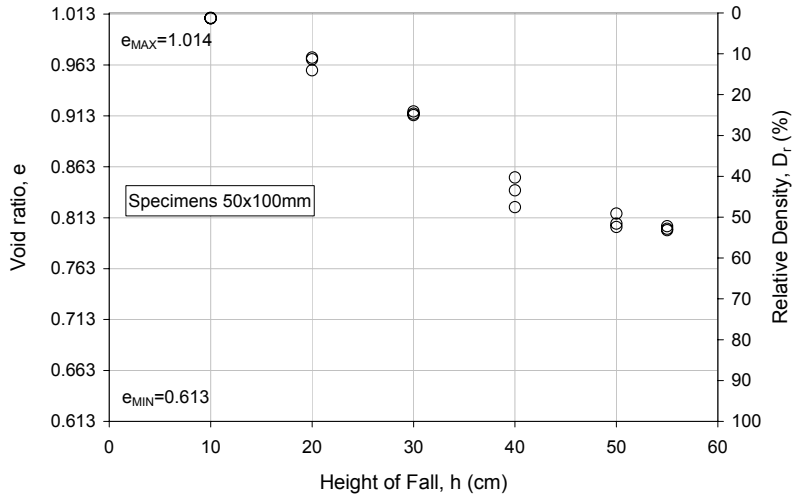

b)

Figure A-3. *Experimental densities of dry LB sand specimens for different heights of fall: a) samples 36x72mm for RCTS tests; b) samples 50x100mm for UT tests.*

It can be seen that the dimensions of the mould do not affect the reached density of the specimen, while it increase with the height of fall.

The second is the Freezing (FR) method, which is largely used for the in-situ sampling in granular material subsoils. In the laboratory application of this procedure, the dry sand was putted in a mould filled with distilled water. The mould was simply made with an overhead transparent folded to make a cylinder having an inner diameter equal to 38mm and an height of around 100mm. The lower base of the mould was closed with a cap and then the soil was gently poured with a teaspoon. Then the mould with the saturated soil was frozen at -30°C. Before starting the mechanical test, the two bases were trimmed to have a 76mm high specimen that was placed in the triaxial cell, after removing the folded overhead. Finally, the unfreezing of specimen was waited, a backpressure of 250 kPa was applied and, then, the isotropic compression was initialized.

During the unfreezing process, the void ratio *e* of the specimen changes slightly its value, as shown by the axial and volumetric strain measures. The volume changes ΔV_w of the pore water due to the temperature variations can be estimated by means of the relationship

$$\Delta V_w = \left(\frac{\rho_{ice}}{\rho_w} - 1 \right) \frac{e}{1+e} V \qquad \text{(A-4)}$$

where ρ_{ice} and ρ_w are the mass density of the ice and water, and V is the total volume of the specimen. The assumed values for ρ_{ice} and ρ_w are 0.917 and 1.000 g/cm^3, respectively. The volume changes ΔV_m measured by the double bellofram volume gauge are not equal to ΔV_w. The difference between the two value is the volume change ΔV_{un} (= ΔV_m – ΔV_w) of the specimen due to a rearrangement of the sand particles during the unfreezing process. Assuming that this volumetric deformation is isotropic, the measured axial strain ε_a is the third part of ΔV_{un} . Then, the void ratio values of the specimens tested into the B&W cell at the start of the isotropic compression are corrected by considering this volumetric deformation.

The testing procedure adopted in the undrained triaxial tests with air-pluviated specimens can be summarized as follows:

- Prepare two filter paper disks with the specimen diameter, to avoid the entering of the fine components of the sand into the pore hydraulic system, and place one on the pedestal and securing it with adhesive tape
- Putting the membrane on the pedestal and securing it by lattice lace
- Assembling the split mould on the pedestal and stretch the membrane against the mould by vacuum
- Fall the sand from the nozzle into the forming mould and level carefully the top of the specimen
- Put the second disk of filter paper on the top of the specimen
- Connect carefully the cap and the specimen by reading the load cell signal to guarantee the good link
- Sealing the top cap with the membrane and the lattice lace
- Apply a pore vacuum of 20 kPa to supply an initial effective stress sufficient to support the assembly

- Remove the mould
- Measure the sample dimensions
- Assemble and fill the cell with water
- Adjust the axial strain transducers (Gap sensor and LVDT)
- Apply a cell pressure of 20 kPa reducing in the same time the pore vacuum to have a constant effective mean stress acting on the specimen
- Start with the flushing procedure to saturate the specimen.

The saturation procedure used in these experiments is constituted by a combination of vacuuming, flushing with distilled water, time lag and back pressurization (250 kPa) in a procedure called "Dry Setting Method" (Ampadu and Tatsuoka, 1989).
For dry specimens tested with the THOR apparatus, the preparation technique is the same of that previously exposed for undrained tests till to the saturation process.

A.4 STIFFNESS OF SAND.

During the RCTS and UT tests, the stiffness properties of sand were investigated. In this section the results are shown.
It should be underlined that the configuration of the THOR apparatus for tests on dry sand does not permit the measurement of the volume changes of specimen. To provide these information, the volumetric strains during the isotropic compressions were assumed isotropic. The radial strain εr was taken equal to the axial strain εa measured by means of LVDT. During the torsional shear phases, the radial strain was fixed to be zero and, then, the volumetric strains are equal to the axial strains.
Another aspect should be highlighted on the elaboration of the experimental measurements deriving from cyclic torsional shear tests. The measured stress-strain loops at low strain levels ($\gamma < 10^{-3}\%$) were reconstructed by interpolating the stress $\tau(t)$ and strain $\gamma(t)$ time histories by means of sinusoidal laws and taking the data calculated from the elaboration. This allows avoiding the data scattering due to the electrical noises of the acquired signals. The stiffness parameters at intermediate strain levels ($10^{-3}\% < \gamma < 10^{-2}\%$) were defined as the mean values registered during the loading cycles and, finally, at high strain levels ($\gamma > 10^{-2}\%$), the data were referred to the first cycle.

A.4.1 Evolution of elastic properties with mean effective stress.

During the isotropic compressions of the RCTS specimens, resonant column tests at low strains were performed to describe the evolution of the elastic stiffness, both in terms of initial shear modulus G_0 and the shear wave velocity V_S, and damping properties of sand with the mean effective stress p'. The measured values are plotted in Figure A-4. The damping ratios were evaluated by the resonance factor method. It can be seen the larger dispersion of the shear modulus data than the shear wave velocity. This is due to the effect of the different relative densities of the specimens on G_0 and V_S. Remembering the following relationship for an elastic medium:

$$V_S = \sqrt{\frac{G_0}{\rho}} \qquad \text{(A-5)}$$

where ρ is the mass density of the material, it can be explained the fact that different relative densities have lower effects on V_S-values than on G_0-values.

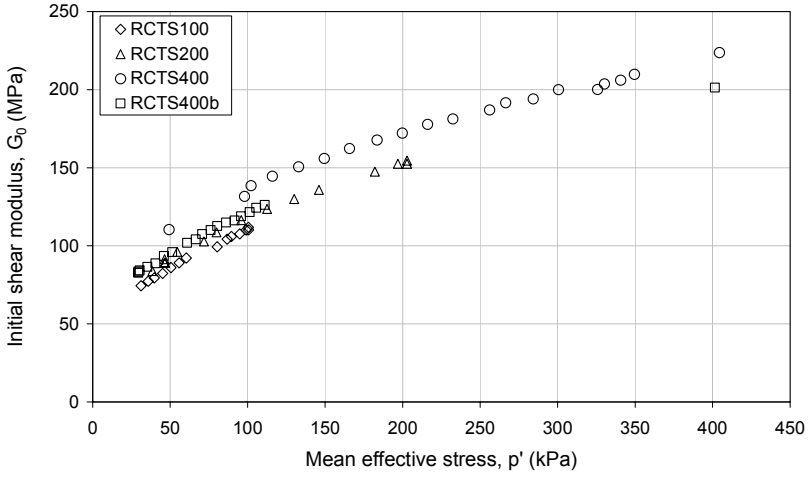

a)

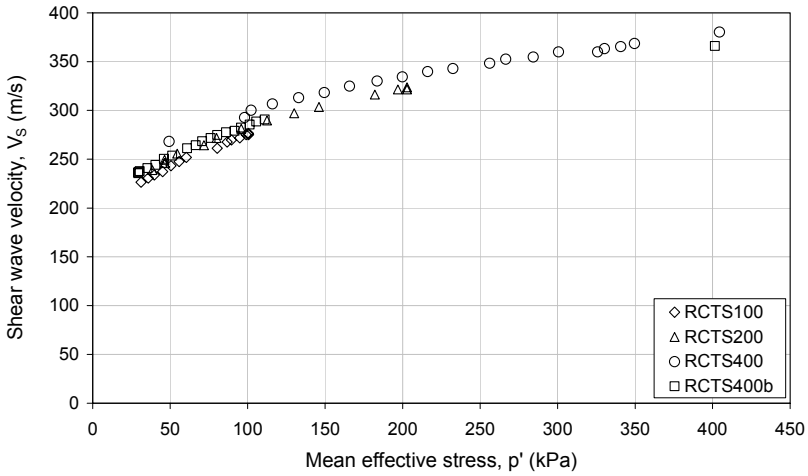

b)

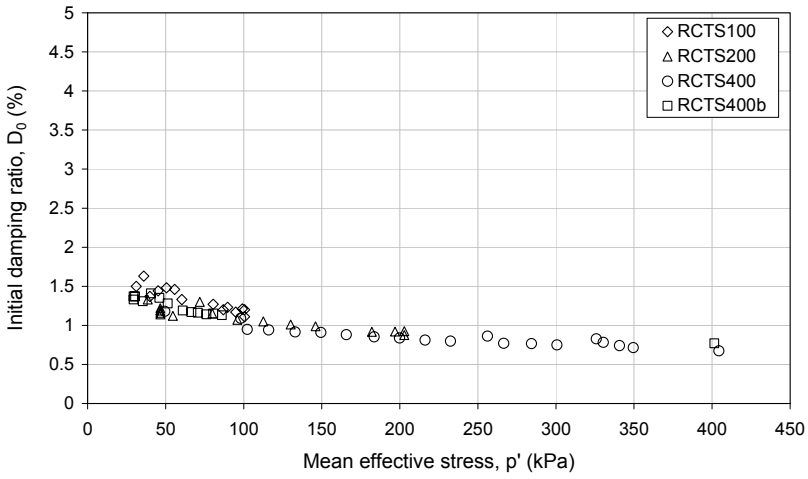

c)

Figure A-4. *Evolution of elastic properties of LB sand during isotropic compressions: a) initial shear modulus; b) shear wave velocity; c) initial damping ratio.*

Analytical relationships proposed in the literature to describe the evolution of the initial shear modulus G_0 with mean effective stress p' taking into account the current state of density through the void ratio e, have the following form:

$$G_0 = S\left(\frac{p'}{p_a}\right)^n F(e) \qquad (A\text{-}6)$$

where p_a is the atmospheric pressure, $F(e)$ is a void ratio function, S and n are two coefficients that depends on the material. Several expressions were also proposed for $F(e)$. For clean sands (Iwasaki et al., 1977)

$$F(e) = \frac{(2.17 - e)^2}{1 + e} \qquad (A\text{-}7)$$

Figure A-5 shows the evolution of the normalized initial shear modulus $G_0/F(e)$ with the mean effective stress.

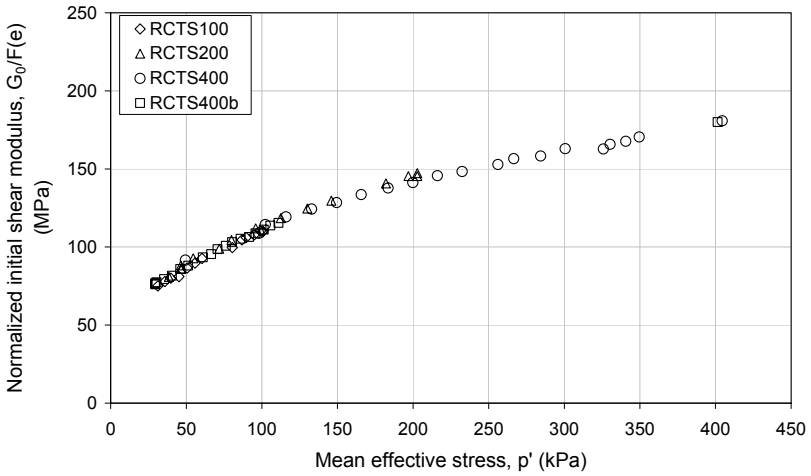

Figure A-5. *Evolution of the normalized initial shear modulus with mean effective stress.*

To establish a direct relation between the shear wave velocity and the relative density of the sand, the V_S-values at p' = 100 kPa measured during the tests were correlated to the initial relative density of specimens. In Figure A-6 the experimental points and a simple linear interpolation to estimate the reference value V_{Sref} at p' = 100 kPa for a given initial relative density are reported.
The proposed V_{Sref} (D_{r0}) law is

$$V_{Sref}(m/s) = 229.4 + 98.7 \cdot D_{r0} \qquad (A\text{-}8)$$

The shear wave velocity laboratory measurements during isotropic compressions are well-described by the following type of relationship:

$$V_S = V_{Sref}\left[1 + a(p' - p'_{ref})\right]^{0.5} \qquad (A\text{-}9)$$

in which V_{Sref} is the V_S value at $p' = p'_{ref}$ = 100 kPa and a is an empirical coefficient that takes into account the effect of the initial relative density on the evolution of the stiffness with mean effective stress. The experimental values of a obtained by the tests are plotted in Figure A-7 for the various values of the initial relative density. The small number of points and the scattering of data do not allow to provide quantitative information.

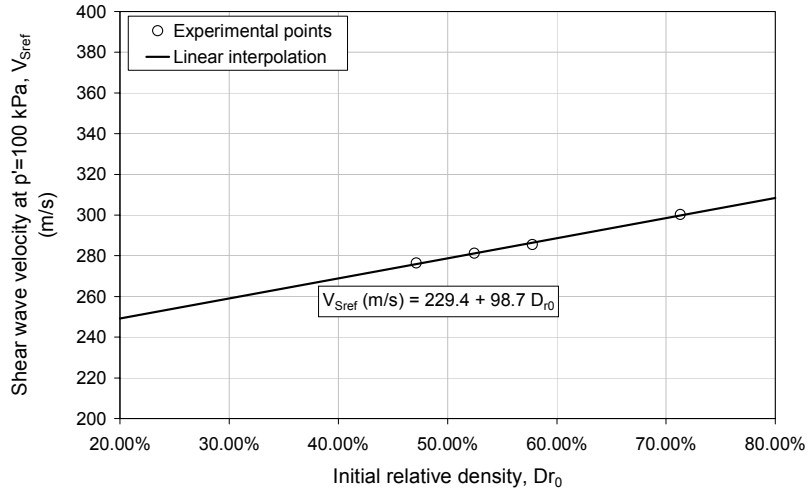

Figure A-6. *Effects of initial relative density on shear wave velocity.*

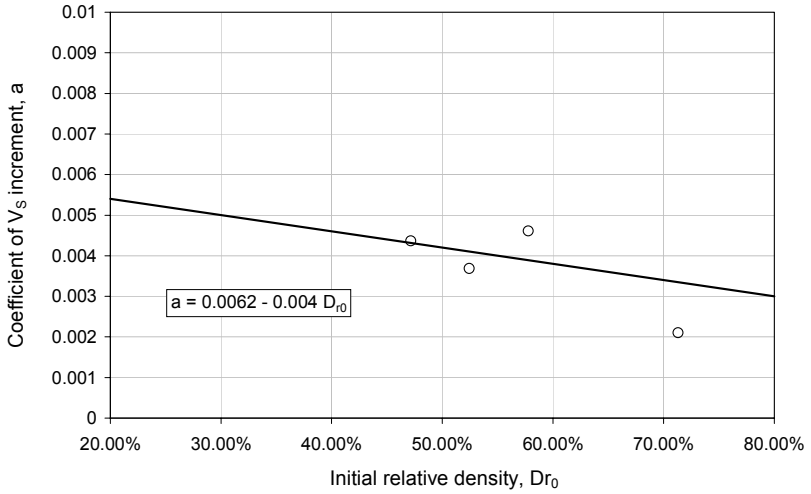

Figure A-7. *Effects of initial relative density on the evolution of V_S with p'.*

Qualitatively, the data confirm the smaller effect on the V_S increment of the higher values of initial relative density.

In order to quantify this effect, the following linear relationship can be adopted:

$$a = 0.0062 - 0.004\, D_{r0} \qquad \text{(A-10)}$$

Then, for a given LB sand layer with a constant relative density, the shear wave velocity evolution with p' can be easily estimated by means of the equations (A-8) to (A-10).

It should be noted that the data previously presented are referred to an isotropic stress state. To traduce these $V_S(p')$ laws in shear wave velocity profiles $V_S(z)$, the anisotropy effects on the soil stiffness should be neglected. Accepting this assumption, the following analytical relationships can be used to define the soil stiffness profiles of homogeneous LB sandy layer for different initial relative density.

$$V_S = V_{Sref}\left[1 + a\frac{1+2k_0}{3}\gamma\left(z - z_{ref}\right)\right]^{0.5} \qquad \text{(A-11)}$$

where k_0 is the earth pressure coefficient at rest, γ is the unit weight of sand, V_{Sref} and a can be estimated by means of equations (A-8) and (A-10), and

$$z_{ref} = \frac{p'_{ref}}{\gamma}\frac{3}{1+2k_0} \qquad (A\text{-}12)$$

The dependence of k_0 on relative density of sands is not so clear as for the cohesive materials. Jamiolkowski et al. (1985) report the k_0-values of different sand specimens measured in calibration camera at the end of the consolidation phase. The results are enough scattered but show a slight reduction of k_0 when D_r increases. However, for relative densities comprises between the range 20÷80%, k_0 can be assumed equal to 0.5.

The empirical relationships proposed in the literature to describe the evolution of the initial damping ratio D_0 with the mean effective stress p' have the following form:

$$D_0 = D_{0ref} \cdot p'^{-n} \qquad (A\text{-}13)$$

where D_{0ref} and n are two coefficients that should be determined with advanced laboratory tests (e.g., resonant column tests). This analytical forms conduct to high values of initial damping ratio for low values of p'. In the view to define initial damping ratio profiles $D_0(z)$, the laboratory data obtained on the LB sand, were interpolated with the following expressions:

$$D_0 = D_{0ref}\left(1+e^{-n\frac{p'}{p'_{ref}}}\right) = D_{0ref}\left(1+e^{-n\frac{z}{z_{ref}}}\right) \qquad (A\text{-}14)$$

D_{0ref} represents the half-value of the initial damping ratio near to the surface, n expresses the heterogeneity of the layer and p'_{ref} = 100 kPa is the reference pressure. This type of relationship allows predicting more reasonable D_0-values for the shallow depths of LB sandy deposits.

The experimental data interpolation and the coefficients D_{0ref} and n are shown Figure A-8

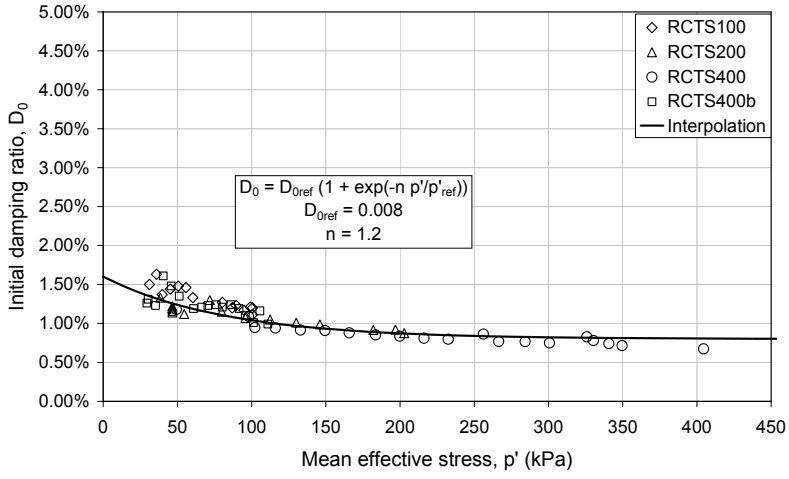

Figure A-8. *Analytical interpolation of the evolution of initial damping ratio with mean effective stress.*

The initial damping ratio profiles of sandy layer characterized by a uniform relative density can be then described by means of (A-14) assuming D_{0ref} = 0.008 and n = 1.2.

A.4.2 Effects of loading rate on elastic shear modulus and damping ratio.

The test RCTS400b was devoted to investigate the effect of the frequency of the applied loads on the elastic properties of LB sand. Twelve cyclic torsional shear tests with six different frequencies and two fixed amplitudes were performed on the sand specimen. The results are reported in Figure A-9.

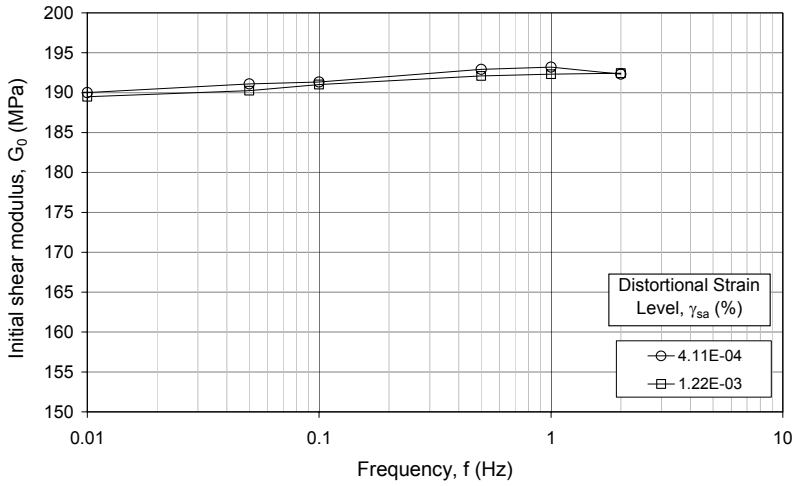

a)

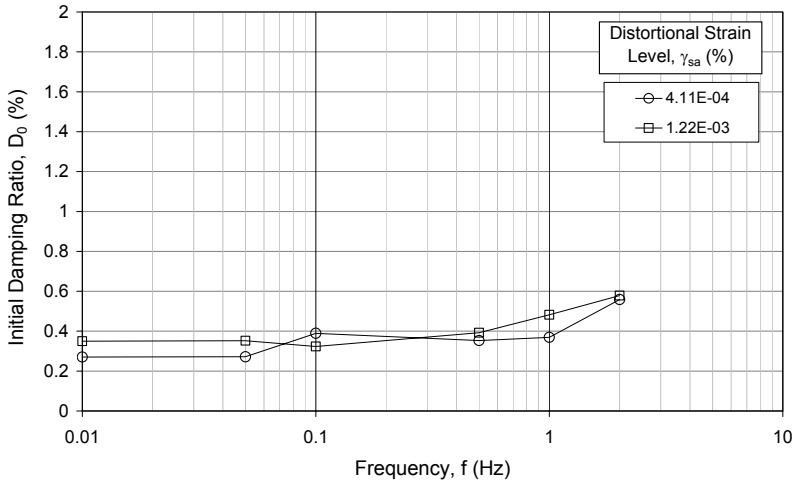

b)

Figure A-9. *Effects of loading frequency on elastic properties of LB sand: a) initial shear modulus; b) initial damping ratio.*

The data were assembled according to the average distortional strain levels induced by the constant loading amplitudes. As expected, the shear modulus slightly increases with the frequency while less clear is the influence of the loading rate on the damping ratio.

A.4.3 Decay curves of shear modulus and damping ratio.

After the isotropic compressions, the tests RCTS100, RCTS200 and RCTS400 were conducted by alternating series of RC and TS tests with loading magnitudes increased until to reach the maximum distortional strain allowed from the THOR apparatus The TS tests were performed assuming a loading frequency of 0.5Hz. The loading amplitudes of RC and TS tests were calibrated to induce comparable distortional strain levels.

The results of the tests are plotted in Figure A-10

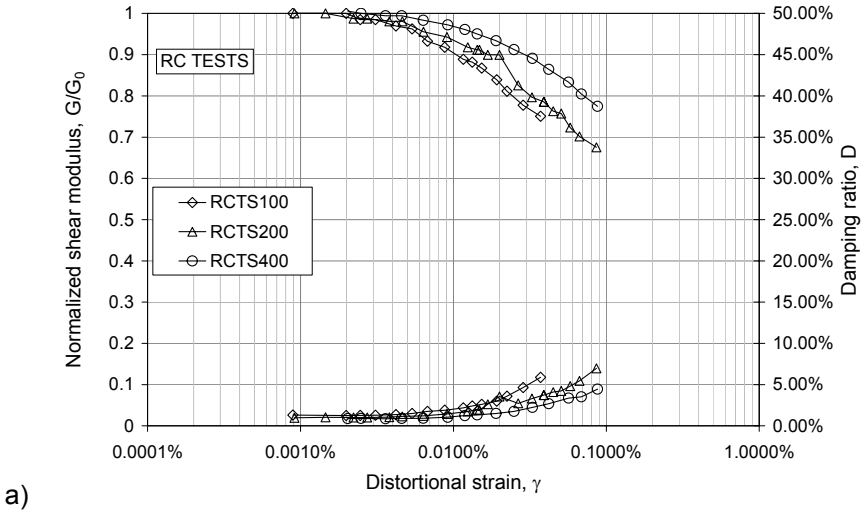

a)

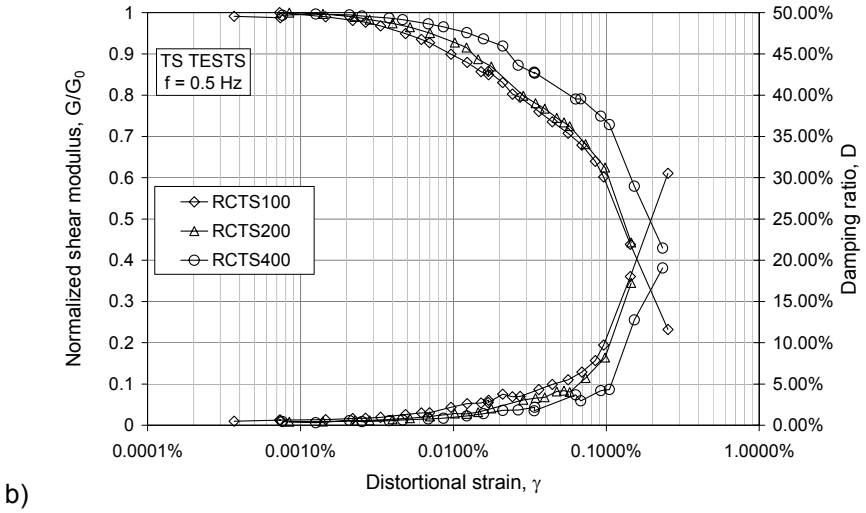

b)

Figure A-10. *Decay curves of shear modulus and damping ratio with distortional strain level: a) RC Tests; b) TS Tests.*

For distortional strain level larger than 0.1%, the RC tests were not considered suitable to define the soil properties. Up to these levels, only the cyclic torsional shear tests were carried out.

It can be noted the effects of the mean effective stress on the decay curves that are moved on the left of the diagram. As expected, the linear ($\gamma_{lin} \approx 3x10^{-3}\%$) and the volumetric ($\gamma_{vol} \approx 1x10^{-1}\%$) thresholds of the sand increase when p' assumes higher values.

A.5 STRENGTH OF SAND.

The strength of the sand was also investigated by means of several triaxial tests with two apparatuses. The tests, both in drained and undrained conditions, were performed following various stress-paths and starting from different mean effective stress. In this section, the experimental results are presented.

A.5.1 Undrained triaxial tests (UTC and UTE).

Four triaxial tests, two in compression and two in extension, were carried out on relatively loose air-pluviated specimens. Before to conduct the undrained shear phases, the samples were isotropically compressed till to 200 and 400 kPa. During these phases, the volumetric strains can not be measured. The current states of the specimens are defined by assuming an isotropic deformation ($\varepsilon_r = \varepsilon_a$).

The tests results are plotted in Figure A-11. By conducting this type of test on loose specimens, it has been possible to clearly recognize the phase transformation of the sand, in which the behaviour from contractive becomes dilative (maximum excess pore pressures condition). Greater difficulties have been encountered for the definition of the critical state conditions (stabilization of the excess of pore pressures). In fact, for reached distortional strain $\varepsilon_q = \varepsilon_a$ (≈ 15÷20%), the steady state conditions are not observed in the tests. Up to these levels of strains the specimens are not cylindrical and uncertainties arise on stress and strain evaluations.

An interesting aspects shown by the data is the more contractive behaviour registered during the triaxial extensions respect to the compressions. In correspondence of the maximum ratio q/p' before the phase transformation, it can be read the volumetric instability condition (Castro, 1969). These results agree with those obtained by Yoshimine et al. (1998) that attribute these effects to the direction of the principal stress relative to the layered structure of soil and to the magnitude of the intermediate principal stress.

A.5.2 Drained triaxial tests (DTC and UTE, DTCp' and DTEp').

To investigate the peak strength of the sand, eight drained triaxial tests were performed by using the B&W apparatus. The dense samples were prepared with the freezing technique, as previously described. After the isotropic compressions, the drained shear phases, both in compression and in extension, were conducted by increasing and decreasing the axial stress, respectively.

Figure A-12 reports the results of all drained tests. As observed in undrained conditions, for similar values of the relative density, the sand behaviour is more dilative in triaxial compressions than in extensions.

In these tests, the phase transformation can be identified to the condition at which the dilatancy is zero. The variations of volumetric strains change the sign becoming negative.

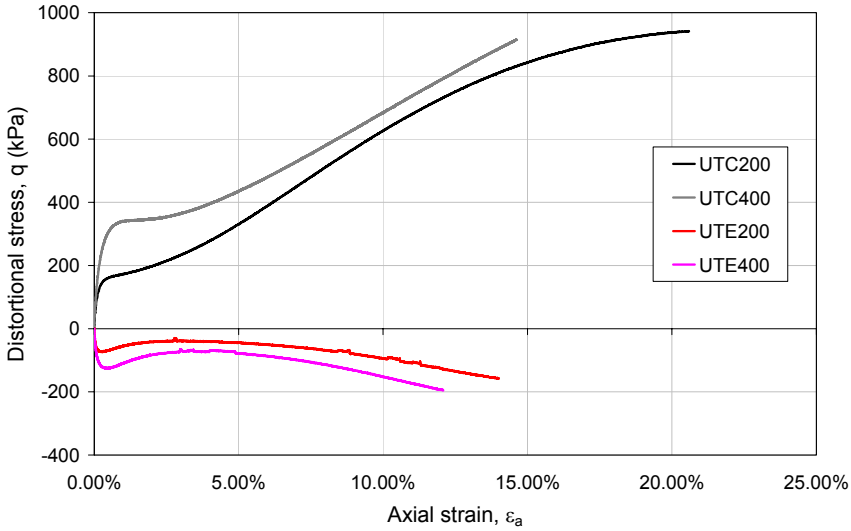

a)

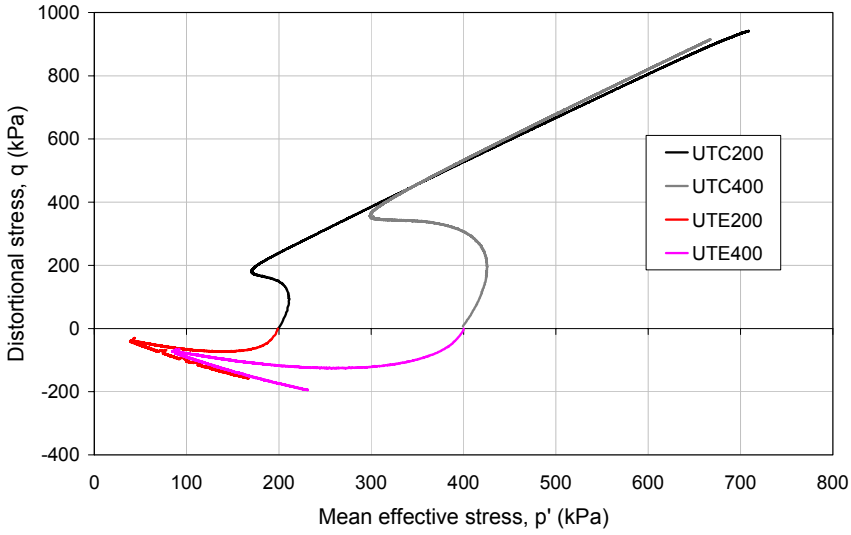

b)

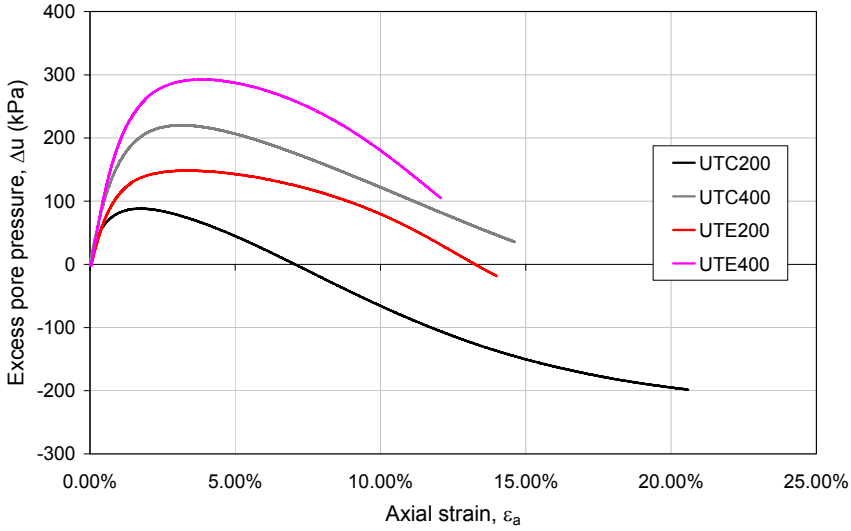

c)

Figure A-11. *Mechanical behaviour of LB sand measured during UT tests: a) stress-strain response; b) stress-paths; c) development of excess of pore pressure.*

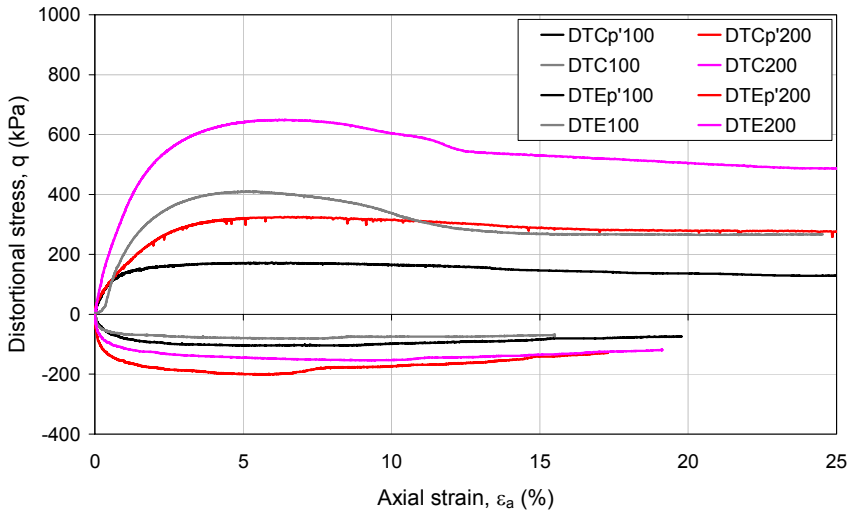

a)

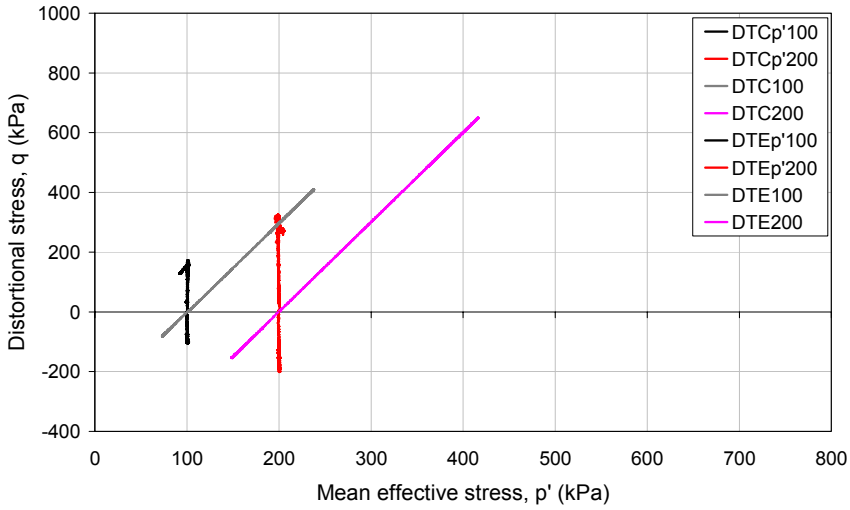

b)

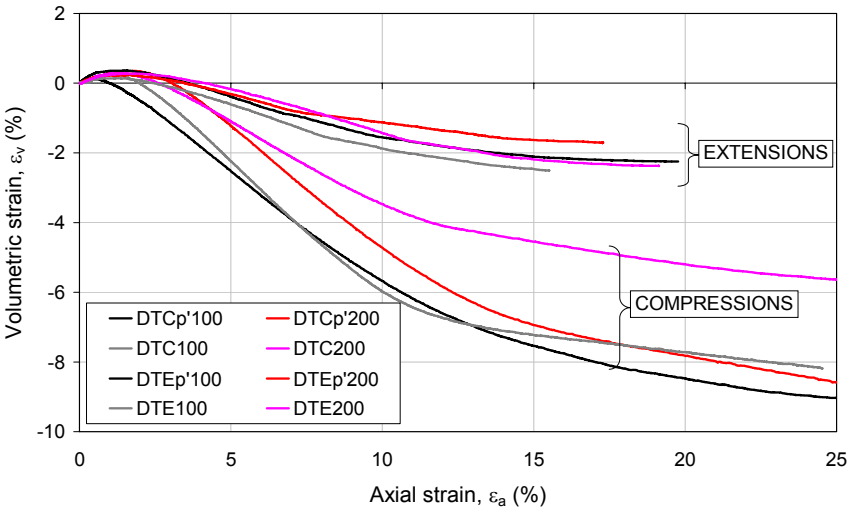

c)

Figure A-12. *Mechanical behaviour of LB sand measured during DT tests: a) stress-strain response; b) stress-paths; c) development of volumetric strains.*

A.5.3 Phase transformation, peak strength and critical state conditions.

The results of the various triaxial tests can be then utilized to identify the strength of the LB sand. Isolating the data of undrained tests corresponding to the maximum excess of pore pressure and those of drained tests at which the derivative of volumetric strains respect to the axial strains (dilatancy) from positive becomes negative, the phase transformation line (PTL) can be defined into the <q, p', e> space. The experimental points and the interpolation laws are plotted in Figure A-13.

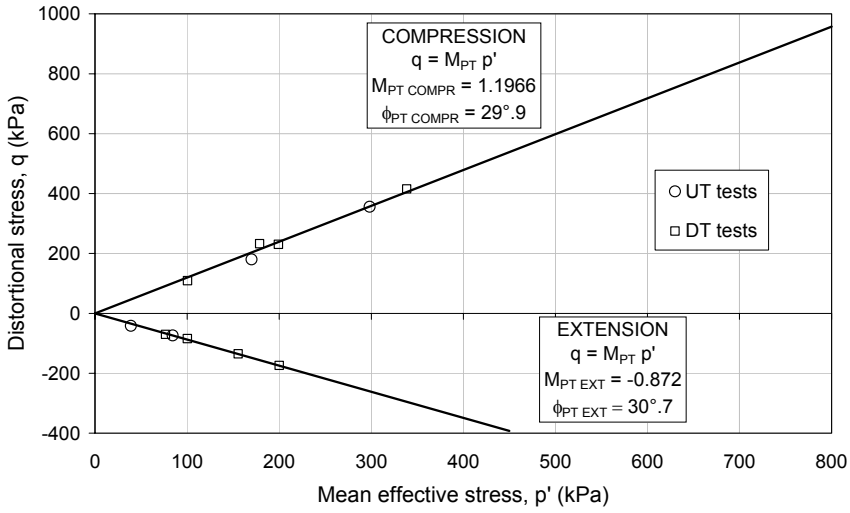

a)

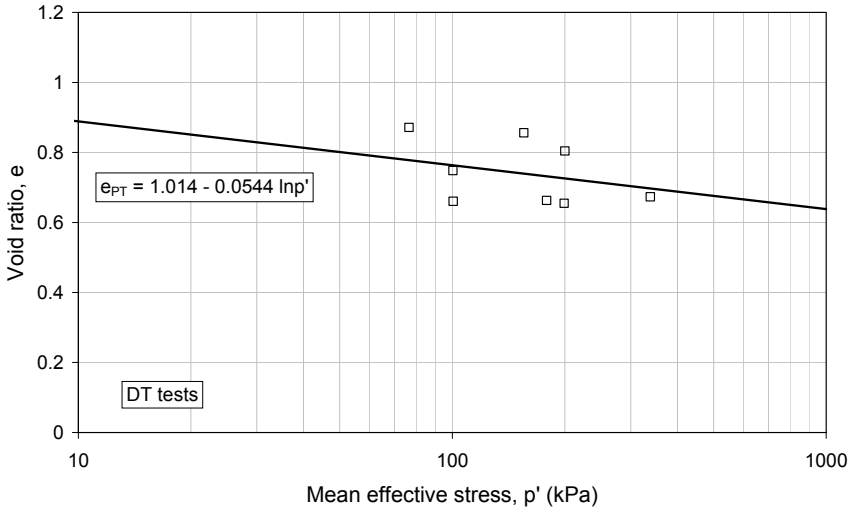

b)

Figure A-13. *Phase transformation of LB sand from UT and DT tests: a) <q, p'> plane; b) <e, p'> plane.*

In the <q, p'> plane the data were well-interpolated by a linear regression. The slopes M_{PT} of the PTL, both in compression and in extension, can be converted in a friction angle value ϕ_{PT} by means of the following relationships:

$$\phi_{PT} = arcsen\left(\frac{3M_{PT}}{6 + M_{PT}}\right) \quad \text{for Triaxial compression} \qquad (A\text{-}15)$$

$$\phi_{PT} = arcsen\left(\frac{3M_{PT}}{6 - M_{PT}}\right) \quad \text{for Triaxial extension} \qquad (A\text{-}16)$$

The values of ϕ_{PT} and M_{PT} for triaxial compression and extension conditions obtained by the linear regression are given in Figure A-13a.

The data shown in the <e, p'> plane, referred only to the drained tests, are very scattered. This is due to the difficulties to rightly estimate the void ratio evolution during the tests for the low capacities of the measurement systems adopted for the volume changes evaluation. However, a logarithmic regression of data was reported in Figure A-13b. The interpolation was done by fixing the constant value as the maximum void ratio (e_{max} = 1.014) of LB sand. The slope of the PTL is λ_{PT} = 0.0469.

The drained triaxial tests performed on the dense samples of the LB sand have allowed defining the strength at peak for relative densities varying in the range of 60÷80%.

Figure A-14 shows the experimental data and the interpolations.

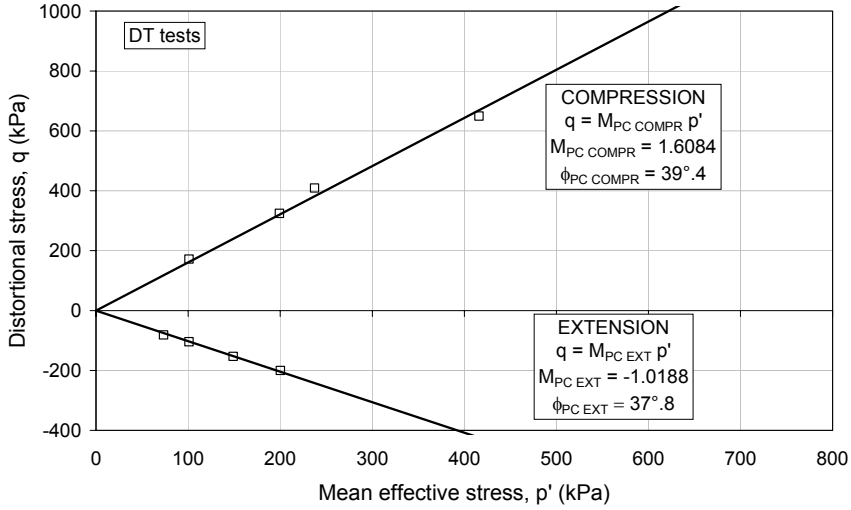

a)

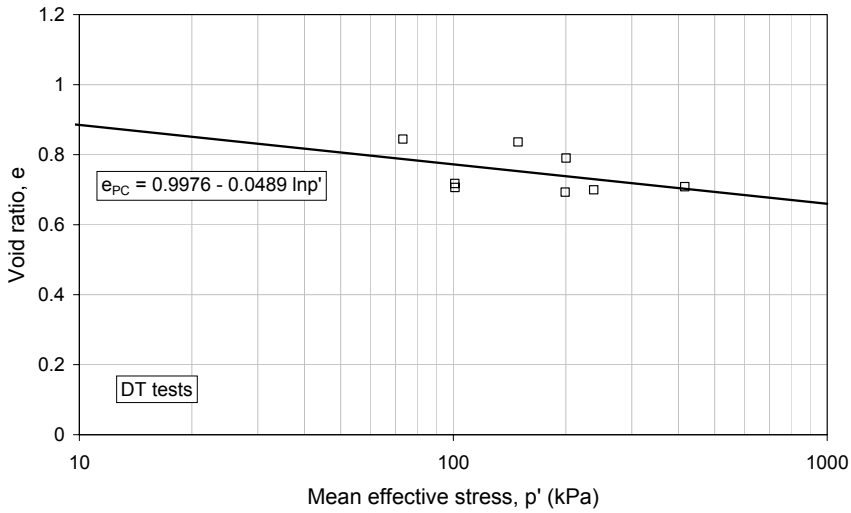

b)

Figure A-14. *Peak strength of LB sand measured in DT tests on dense samples (Dr = 60÷80%): a) <q, p'> plane; b) <e, p'> plane.*

As it can be seen in Table A-1, the triaxial extensions were carried out on less dense specimens than the compressions. This fact contributes to the lower value of the friction angle ϕ_{PC} measured in extension with respect to the corresponding of compression conditions.

The steady state, defined as the state of deformation of soil without effective stress increment or decrement and with no migration of pore water, was not individuated in the tests. For this reason, a conventional definition of the critical state parameters of the LB sand was given. In particular, the ultimate strength conditions were assumed to be the last states of all tests. In Figure A-15 are summarized the experimental points and the CSL line in the <q, p'> and <e, p'> planes.

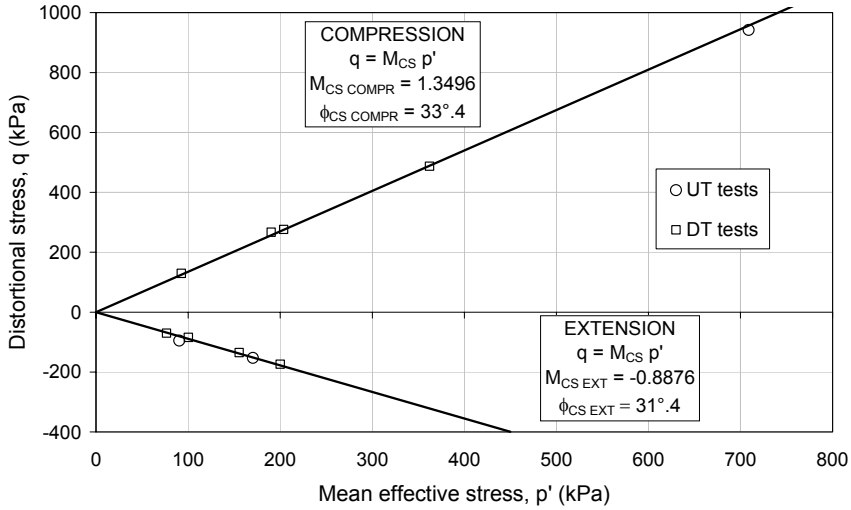

a)

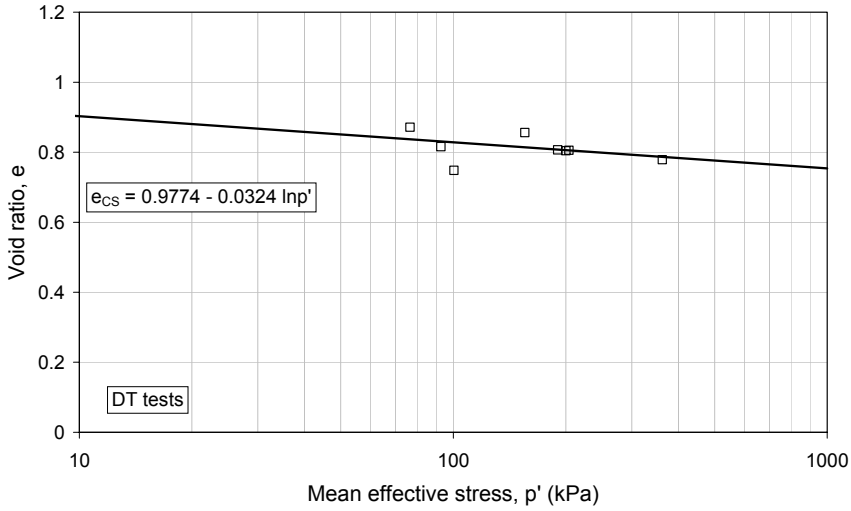

b)

Figure A-15. *Critical state of LB sand measured in UT and DT tests: a) <q, p'> plane; b) <e, p'> plane.*

The lower value of the friction angle ϕ_{CS} measured in triaxial extension respect to the corresponding of compression conditions can be explained by remarking the lower values of the maximum axial strains reached in the extension tests assumed for the conventional definition of the CS conditions. It is useful to remember that the initial relative density of the specimen does not affect the ultimate strength of sand. Then, the smaller of ϕ_{CS} should not be attributed to the lower densities of the samples used in triaxial extensions.

Having identified the critical state (ϕ_{CS}) and the peak strength (ϕ_{PC}) corresponding to relative densities of about 75% and assuming a linear dependence of the peak friction angle from D_r, the following relationships can be used to determine the strength parameters of the LB sand in relation to the relative density.

$$\phi_{PC} = \phi_{CS} + 10 \cdot D_r \qquad \text{(A-17)}$$

$$\psi_{PC} = \frac{\phi_{PC} - \phi_{CS}}{0.8} \qquad \text{(A-18)}$$

The (A-18) represents the inverse form of the empirical relationship between the maximum friction angle (ϕ_{MAX}) exhibited by the soil, the critical friction angle (ϕ_{CS}) and the dilatancy angle ψ proposed by Bolton (1986).

A conservative value of the critical friction angle is ϕ_{CS} = 32° that agrees with the estimation of Tan (1990).

In Table A-2 the strength parameters of the LB sand estimated by the triaxial tests for different states are summarized.

STATE	TRIAXIAL STRESS-PATH	PLANE					MOHR-COULOMB Failure parameters	
		<q, p'>		<e, p'>				
		Failure envelope	Failure parameters	Failure envelope	Failure parameters			
			M		e_0	λ	c	ϕ
PHASE TRANSFORMATION	COMPRESSION	$q = Mp'$	1.1966	$e = e_0 - \lambda \ln p'$	1.014	0.0544	0	29°.9
	EXTENSION		-0.872				0	30°.7
PEAK CONDITIONS (At a relative density of about 80%)	COMPRESSION		1.6084		0.9976	0.0489	0	39°.4
	EXTENSION		-1.0188				0	37°.8
CRITICAL STATE	COMPRESSION		1.3496		0.9774	0.0324	0	33°.4
	EXTENSION		-0.8876				0	31°.4

Table A-2. *Summary of strength parameters of LB sand.*

ANNEX B CALIBRATION OF FE MODELS FOR DYNAMIC ANALYSES IN GEOTECHNICAL EARTHQUAKE ENGINEERING.

Dynamic interaction problems involve the determination of the response of a structure placed in a seismic environment created by an earthquake or some other source such as vibrating machine foundation. Such an environment is defined in terms of free field motion prior to placement of the structure. The spatial and the temporal variation of the free field motion used as input must be such that they satisfy the equations of motions for the free field. They may be obtained from a site response analysis. Thus, a free field solution must be available before a true interaction problem can be solved (Lysmer, 1978).

Numerical methods is often adopted to predict the behaviour of the geotechnical systems (e.g. retaining walls, pile foundations, embankments, dams) under seismic loadings, both for scientific and practical applications.

Dynamic finite element analyses can be considered one of the most complete available tools in geotechnical earthquake engineering for their capabilities to provide indications on the soil stress distribution and deformation/displacements and on the forces acting on the structural elements that interact with the ground (PIANC, 2001). However, they require at least a proper soil constitutive model, an adequate soil characterization by means of in situ and laboratory tests and a proper definition of the seismic input. The response of a finite element model is also conditioned by the setting of several parameters influencing the sources of energy dissipation in time-domain analyses. The amount of damping shown by a discrete numerical system is determined by the choice of the constitutive model (material damping), the integration scheme of the equations (numerical damping), and the boundary conditions. Material damping models the effects of viscous and hysteretic energy dissipations in the soils; numerical damping appears as a consequence of the numerical algorithm of solution of the dynamic equilibrium in the time domain; boundary conditions affect the way in which the numerical model transmits the specific energy of the stress waves outside the domain.

Lists of widespread computer codes used to perform 1-D seismic site response analyses are reported by several authors (EPRI, 1991; Kramer, 1996; Lanzo, 2005).

The influence of the sources of damping on the seismic response of a soil layer has been investigated in this chapter.

A series of dynamic analyses of the vertical propagation of S-waves in a homogeneous elastic layer was carried out. This scheme was chosen because a well-known theoretical solution of the problem is available in literature and some comparisons can be easily done.

The FE code Plaxis 2D v.8.2 (Brinkgreve, 2002), that allows time domain dynamic analyses, was used in this research as it is largely adopted both from practitioners and academics.

The reference solution in the frequency domain was calculated by means of the well-known EERA code (Bardet et al., 2000).

A simple calibration procedure of the damping parameters and some suggestions on how to reduce the spurious lateral boundaries effects on the wave propagation are presented.

B.1 REFERENCE SOLUTION: 1-D VERTICAL PROPAGATION OF S-WAVES IN A HOMOGENEOUS VISCO-ELASTIC LAYER.

Vertical one-dimensional propagation of shear waves in a visco-elastic homogeneous layer that lies on rigid bedrock can be described, in the frequency domain, by its amplification function. The latter is defined as the modulus of the transfer function, which is the ratio of the Fourier spectrum of amplitude at the free surface motion to the corresponding spectrum of the bedrock motion. For a given linear visco-elastic stratum and a given seismic motion acting at the rigid bedrock, the motion at the free surface can be easily obtained from the amplification function. First, the Fourier spectrum of the input signal is computed. Then, this function is multiplied by the amplification function and finally the motion is given by the inverse Fourier transform of the previous product.

If the properties of the visco-elastic medium (density, ρ or total unit weight of soil, γ; shear wave velocity, V_S; damping ratio, D) and its geometry (layer thickness, H) are known, the amplification function is univocally defined.

For a soil layer on rigid bedrock, the amplification function (Roesset, 1970) is:

$$A(f) = \frac{1}{\sqrt{\cos^2 F + (DF)^2}} = \frac{1}{\sqrt{\cos^2\left(2\pi \frac{H}{V_S} f\right) + \left(2\pi \frac{HD}{V_S} f\right)^2}} \qquad \text{(B-1)}$$

where F is the frequency factor, defined as $F = \omega H/V_S = 2\pi f H/V_S$.

Figure B-1 shows its graphical representation in the amplification ratio-frequency plane, assuming that the soil layer has the following parameters:

H =16 m; γ = 14.1 kN/m^3; ρ = 1440 kg/m^3; V_S = 361.5 m/s; D = 2 %.

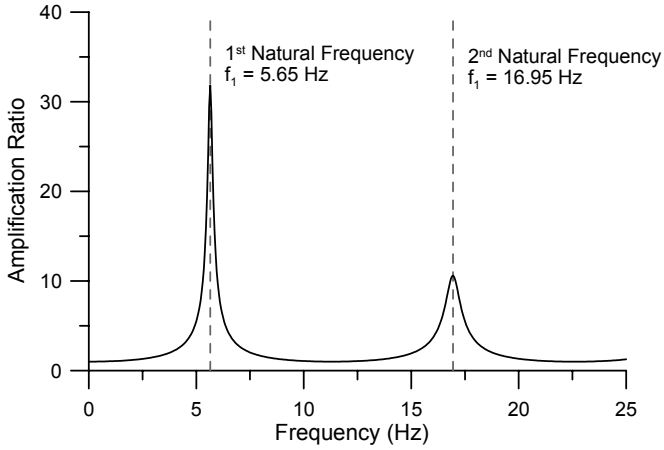

Figure B-1. *Amplification function of a linear visco-elastic layer over rigid bedrock.*

The two vertical dashed grey lines remark the first and the second natural frequencies of the system. In the previously listed hypotheses, the n-th natural frequency f_n and maximum amplification ratio $A_{max,n}$ of the layer can be deduced by means of the following approximated relationships, respectively:

$$f_n = \frac{\omega_n}{2\pi} \cong \frac{V_S}{4H}(2n-1) \qquad \text{(B-2)}$$

$$A_{\max,n} \cong \frac{2}{(2n-1)\pi D} = \frac{V_S}{HD\omega_n} \qquad \text{(B-3)}$$

B.2 NUMERICAL MODELING OF THE REFERENCE PROBLEM.

The finite element modelling of the one-dimensional vertical propagation of shear waves into a visco-elastic layer based on a rigid bedrock can be performed by following the next steps:

1. define the FE model (damping parameters; numerical parameters; boundary conditions)
2. define input motion (in terms of accelerations, velocities, displacements, forces time-histories and Fourier spectra)
3. conduct the dynamic analysis for the specified seismic motion
4. check the goodness of the model response both in the frequency and in the time domains (e.g., in terms of maximum acceleration profiles, amplification function, etc.)

B.2.1 Finite element models.

The discretization of a continuum through the use of finite elements or finite differences requires the existence of a finite domain with well defined boundaries, where conditions are specified for forces and displacements. If these boundaries do not exist naturally but are created artificially, it is necessary to determine appropriate boundary conditions that will simulate the physical behaviour of the actual problem.

For a horizontally stratified soil deposit with shear waves propagating vertically, the existence of an underlying half-space could be reproduced in a discrete model by placing at the bottom different static and kinematic conditions depending on the bedrock properties. If the last is rigid, its motion is not affected by the presence of the overlying soil. It acts as a fixed end boundary. Any downward-travelling waves in the soil is completely reflected back toward the ground surface by the rigid layer, thereby trapping all of the elastic wave energy within the soil layer. In a time domain analysis, the rigid bedrock is simply modelled imposing an acceleration (or velocity or displacement) time-history at the base of the numerical model. When the rock is elastic, however, downward-travelling stress waves that reach the soil-rock boundary are reflected only partially; part of their energy is transmitted through the boundary to continue travelling downward through the rock. If the rock extends to great depth, the elastic energy of these waves is effectively removed from the soil layer. This is a form of radiation damping and it causes the free surface motion amplitudes to be smaller than those for the case of rigid bedrock. In a time domain analysis, the presence of an elastic bedrock can be modelled by imposing a force time history rather than a base motion at the bottom of the soil layer. The continuity of the stresses along the rock-soil boundary requires that the shear stress in the rock side is equal to the shear stress in the soil side. For this reason, the motion of an elastic bedrock is usually specified by adopting a shear stress time history $\tau(t)$. It can be simply obtained by the motion expected at the outcropping rock in terms of velocity time-history $\dot{u}(t)$ by means of the relationship (Tsai, 1969):

$$\tau(t) = \rho_R V_{SR} \dot{u}(t) \qquad \text{(B-4)}$$

where ρ_R and V_{SR} are the mass density and the shear wave velocity of the elastic bedrock.

Another way to specify the motion of an elastic bedrock at the bottom of a FE model is to run a frequency domain analysis by applying the seismic signal at the outcropping rock and then computing the time-history of acceleration at the interface between the soil layer and the rock (called “inside” in the EERA code). Such time history accounts for the shear stress transmission between the bedrock and the layer and can be directly applied to the lower boundary of the FE mesh.

For the simple cases of SH, SV or P waves travelling into the subsoil at a specified angle, when the geometry is one-dimensional and only one train of plane waves is considered, appropriate conditions for the lateral boundaries can also be obtained easily. For example,

- For SH waves with normal incidence the lateral boundary nodes should be left free
- For SV waves with normal incidence, the nodes on the lateral boundary should have free displacements in the horizontal direction and completely restrained displacements in the vertical direction
- For P waves with normal incidence, the nodes on the lateral boundary should have free displacements in the vertical direction and completely restrained displacements in the horizontal direction
- For SH, SV, or P waves with a specified nonzero angle of incidence, the nodes on the lateral boundary should have lumped dashpots or consistent damping matrices with properties that are functions of the angle.

In the case of interest, simple vertical fixities allowing horizontal displacements of nodes placed on the lateral boundaries are the best solution to reproduce the vertical propagation of S-waves polarized in the horizontal plane of layered subsoils. In order to equilibrate the horizontal lithostatic stresses acting on lateral boundaries, it is suitable to introduce load distributions at the left-hand and right-hand vertical boundaries, as sketched in Figure B-2. In such conditions, the width of the FE model does not affect its response. The influence of the various sources of dissipation in time domain analyses can be examined by adopting a simple soil column (for example B = 1m) reducing the required calculation time.

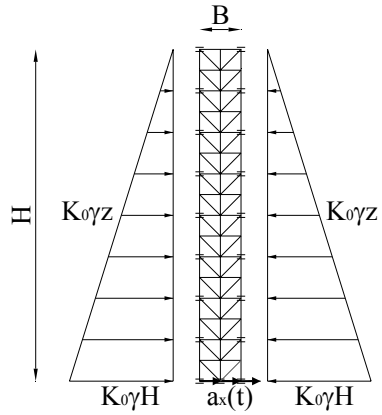

Figure B-2. *FE model for 1-D dynamic analysis of visco-elastic layers.*

The FE model of Figure B-2 is only reasonable for non-plastic material and if local site response is the aim of the study. When a more complex constitutive law, such as elastic-plastic models, or geometry configuration should be analyzed, the soil column is not suitable for the calculation. In these cases, a FE configuration for the dynamic analyses could be that sketched in Figure B-3. The region of interest is constituted only by the central domain. The two lateral domains, characterized by a coarse mesh, to reduce the computational costs, and a tapered input motion, have the aim to minimize the spurious effects of reflection on the boundaries. In spite of higher calculation time respect to other silent boundary conditions (Ross, 2004), such a solution allows minimizing the boundaries effects. Its effectiveness is shown in the next sections.

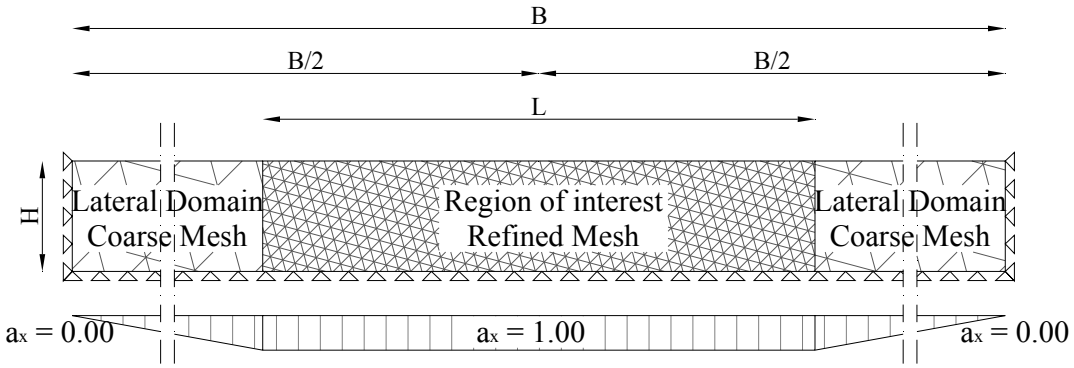

Figure B-3. *FE model for 2-D dynamic analysis.*

B.2.2 Seismic input motions.

In numerical computation, the earthquake loading is often imposed as an acceleration time-history at the base of the model.

The amplification function of a visco-elastic layer is independent from the input motion. However, to confirm the effectiveness of the calibration procedure proposed in this chapter, two earthquake signals were considered.

The first is the WE component of the accelerometer registration at Tolmezzo Station for the main shock of the earthquake of Friuli (Italy) on May 6th, 1976, denoted as TMZ-270. The data were sampled at 200 Hz for a total number of 7279 registration points. The horizontal peak acceleration, equal to 0.315 g, was reached at the time t=3.935 s. Most of the energy is included into a frequency range between 0.8 and 5 Hz, with a predominant frequency of 1.5 Hz. The Arias intensity is 1.20 m/s and the significant duration (Trifunac and Brady, 1975) is 4.92 s. The time-history of accelerations and the Fourier spectrum of amplitude are reported in Figure B-4.

The second is the WE component of the accelerometer registration at Sturno Station for the main shock of the earthquake of Irpinia (Italy) on November 23rd, 1980, denoted as STU-270. The sampling frequency is 400 Hz for a total number of 15737 registration points. The horizontal peak acceleration, equal to 0.321g, was reached at the time t = 5.2375 s. The predominant frequency is 0.44 Hz. The Arias intensity and the significant duration are 1.39 m/s and 15.2 s, respectively. The acceleration time-history and the Fourier spectrum of amplitude are plotted in Figure B-5.

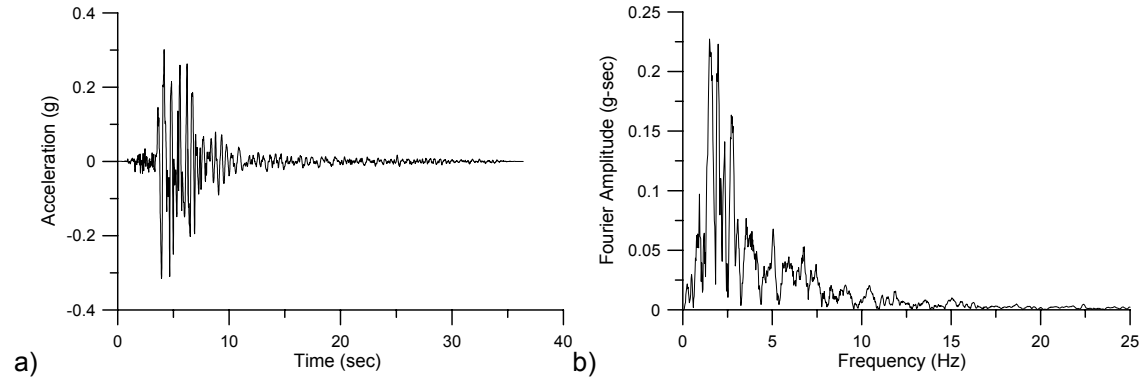

Figure B-4. *Seismic input TMZ-270: a) acceleration time-history; b) Fourier spectrum.*

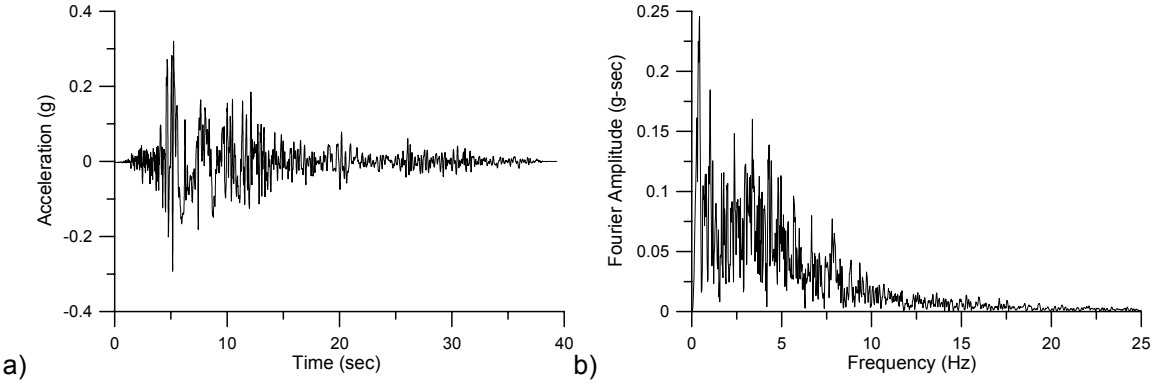

Figure B-5. *Seismic input STU-270: a) acceleration time-history; b) Fourier spectrum.*

B.3 ANALYSIS OF THE SOURCES OF ENERGY DISSIPATION IN TIME DOMAIN ANALYSES.

In time domain seismic analyses different sources of energy dissipation exist: material damping, which includes viscous and hysteretic soil damping, numerical damping, arising from the adopted time integration scheme, and energy dissipation at the lateral boundaries. In this section, the various causes of the motion attenuation are analyzed.

B.3.1 Material damping.

The dissipation of elastic energy due to the intrinsic characteristics of the material can be modelled by viscous damping, according to the Rayleigh formulation. Figure B-6 shows the different amplification functions for three values of the Rayleigh damping coefficients α_R and β_R, respectively. Both sets of curves were obtained by fixing the numerical damping to zero, as described in the next § B.3.2, and assuming $\beta_R = 0$, for the first set (Figure B-6a), and $\alpha_R = 0$, for the second set (Figure B-6b).

The observed effects on the seismic response of the layer can be explained with the theory of a viscous damped single-degree-of-freedom (SDOF) system subjected to forced vibrations (Kramer, 1996). First, it seems helpful to remind of the distinction between the damping ratio D and the critical damping ratio ξ: the former is defined as the ratio between the energy dissipated in one cycle of oscillation of a hysteresis loop and the strain energy stored in the system, the latter is equal to the

ratio between the damping coefficient and the critical damping coefficient in the equation which expresses the dynamic equilibrium.

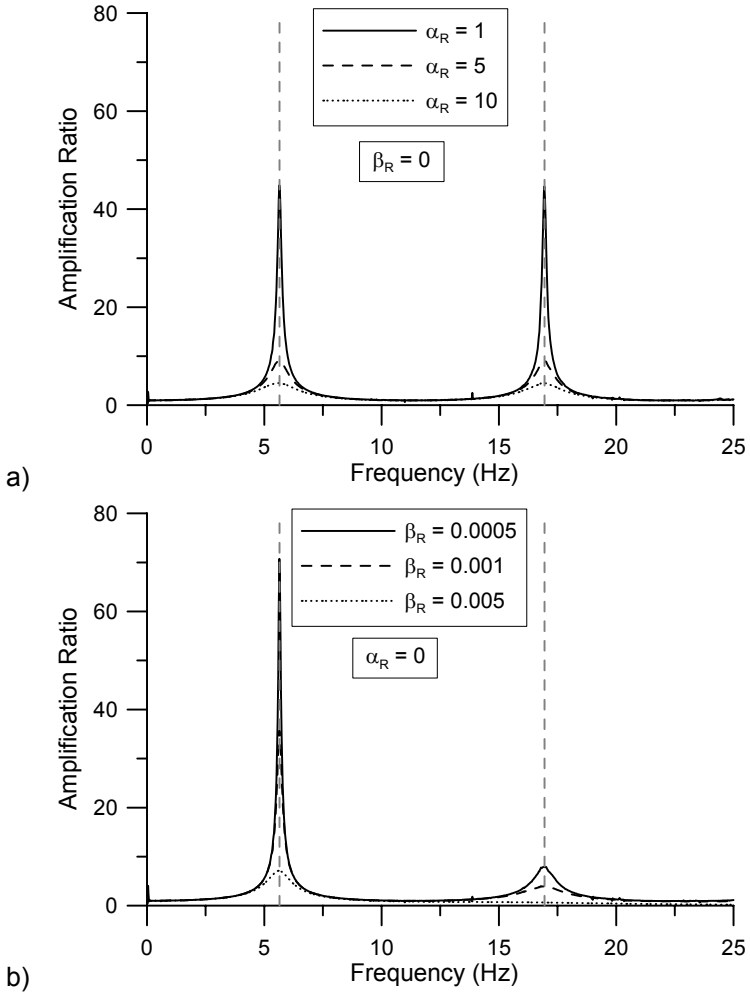

Figure B-6. *Influence of Rayleigh damping coefficients on the amplification function of the soil column: a) influence of α_R; b) influence of β_R.*

For a SDOF system , the relationship between the two quantities, is:

$$D = \xi \frac{\omega}{\omega_n} \qquad \text{(B-5)}$$

in which ω is the circular frequency of the harmonic loading and ω_n is the natural circular frequency of the SDOF system.

In the Rayleigh formulation, the modal damping $\xi_n = \xi(\omega_n)$ depends on the circular natural frequency ω_n of the system, according to the following law:

$$\xi_n = \frac{1}{2}\left(\frac{\alpha_R}{\omega_n} + \beta_R \omega_n\right) \qquad \text{(B-6)}$$

If $\omega = \omega_n$, than

$$D_n = \xi_n = \frac{1}{2}\left(\frac{\alpha_R}{\omega_n} + \beta_R \omega_n\right) \qquad \text{(B-7)}$$

Therefore, according to the Rayleigh formulation, the modal damping ratio D_n is affected from the natural frequency of the examined SDOF system.

A soil layer resting on rigid bedrock is theoretically characterized by an infinite number of natural frequencies. The amplification factor corresponding to the *n*-th natural circular frequency ω_n of the system can be expressed as follows, by introducing the equation (B-7) into the (B-3):

$$A_{\max,n} = \frac{V_S}{HD_n\omega_n} = \frac{2V_S}{H}\left(\frac{1}{\alpha_R + \beta_R\omega_n^{\,2}}\right) \qquad \text{(B-8)}$$

The maximum amplification ratio calculated according to equation (B-8) is consistent with the amplification functions computed from the results of the analyses and represented in Figure B-6.

For $\beta_R = 0$ (as in Figure B-6a), A_{max} does not change with the modal number *n* while it decreases hyperbolically with α_R . On the contrary, by setting $\alpha_R = 0$ (as in Figure B-6b), the maximum amplification ratio decreases with the square of the natural frequency, for any given β_R.

If no numerical dissipation is introduced in the time integration scheme, the damping of the system can be modelled by using the Rayleigh parameters only. For a soil layer with a constant value of the damping ratio D*, the linear system of equations that provides α_R and β_R is:

$$\alpha_R + \beta_R\omega_{ni}^{\,2} = 2\omega_{ni}D^* \qquad \text{(B-9)}$$

in which ω_{ni} are two circular natural frequencies of the layer.

Assuming ω_{ni} as the first and the second natural frequencies (ω_{n1} = 35.5 rad/s; ω_{n2} = 106.5 rad/s), the numerical calculation gives the results plotted in Figure B-7, in which the comparisons with the frequency domain analysis solutions were done for TMZ-270 and STU-270 input motions. The reference maximum acceleration profile was computed with the EERA code. The two types of analyses agree both in terms of amplification functions and maximum acceleration profile. The numerical parameters (α and dt) was fixed to have zero numerical dissipation and to respect the accuracy condition (5–60) for a stable solution.

B.3.2 Numerical damping.

The Newmark scheme, which is used in many FE codes for time integration, can be varied adopting different values of the parameter α, according to the HHT method (LUSAS, 2000). If no damping is introduced in a dynamic analysis, either material or numerical, the model reaches the resonant conditions at the natural frequencies of the system with a corresponding theoretically infinite amplification ratio. Figure B-8 shows the response at a control point on the free-surface obtained for an undamped analysis ($\alpha = 0$; $\alpha_N = 0.25$; $\beta_N = 0.5$; $\alpha_R = \beta_R = 0$) both in terms of the acceleration time-history and the Fourier spectrum. The estimated natural frequencies of the layer are very close to the expected theoretical values. The analysis was performed by applying at the base of the model the TMZ-270 acceleration time history.

The standard setting of the Plaxis code is the damped Newmark scheme with $\alpha_N = 0.3025$ and $\beta_N = 0.6$, that corresponds to $\alpha = 0.1$, according to equations (5-56). This assumption introduces a numerical energy dissipation which should be considered when calibrating the model damping against the true soil damping.

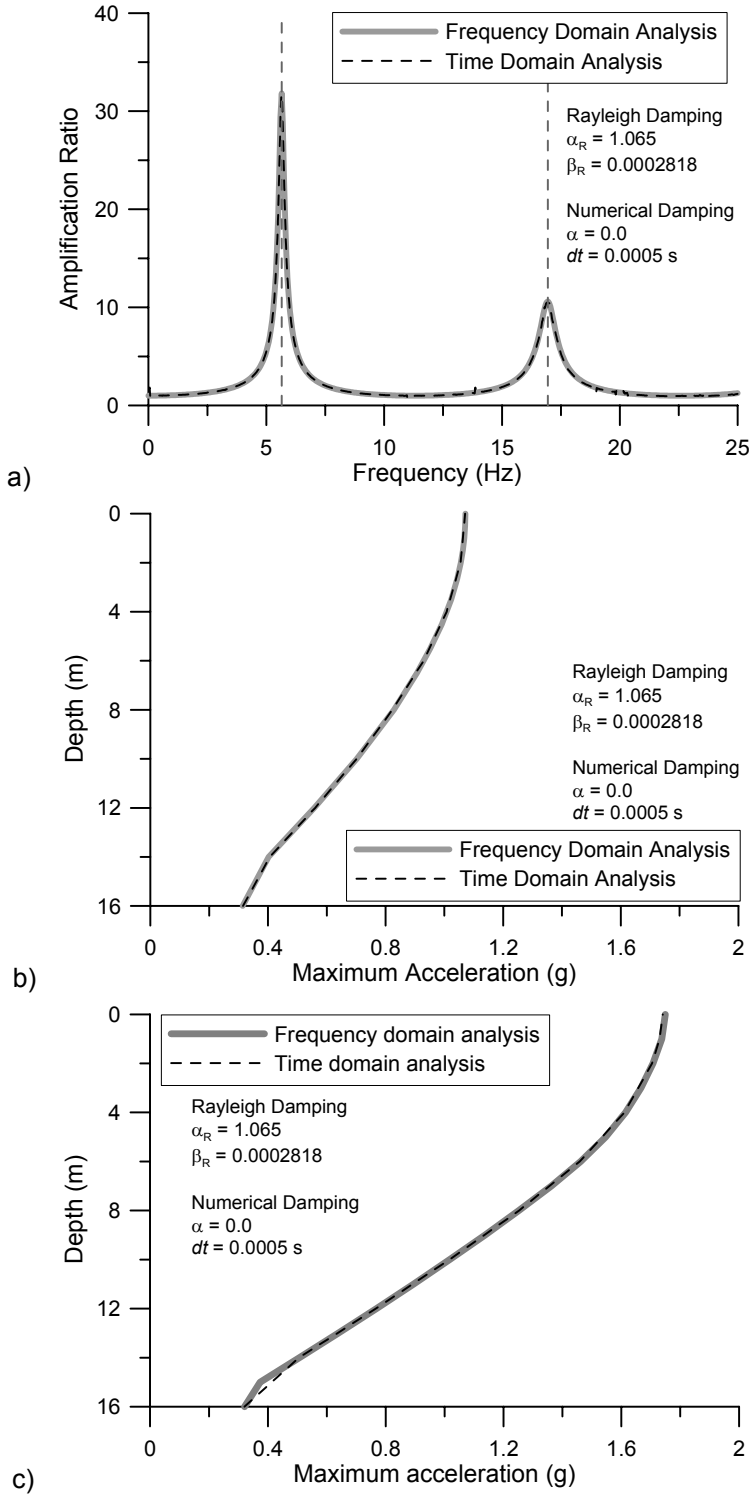

Figure B-7. *Comparisons between numerical and reference solutions: a) amplification functions; b) maximum acceleration profiles for TMZ-270 input motion; c) maximum acceleration profiles for STU-270 input motion.*

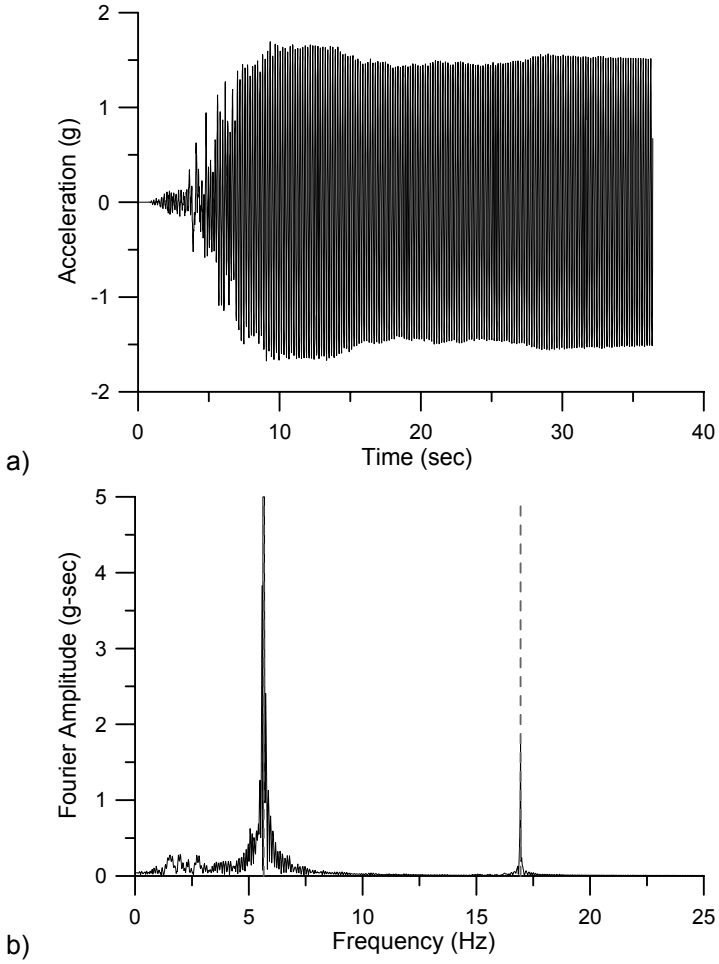

Figure B-8. *Seismic response of the soil column for an undamped analysis (TMZ-270 input motion): a) acceleration time history; b) Fourier spectrum.*

Figure B-9 shows the results of numerical analyses for three different values of α. The Rayleigh coefficients were set equal to the values given by the system of equations (B-9), for the first and the second natural frequencies of the layer. When α increases, the values of the amplification ratio around the second natural frequency of the layer decrease. This means that the computed motion is excessively under-amplified at the natural frequencies when using the damped Newmark integration scheme and evaluating the Rayleigh parameters according to the (B-9).

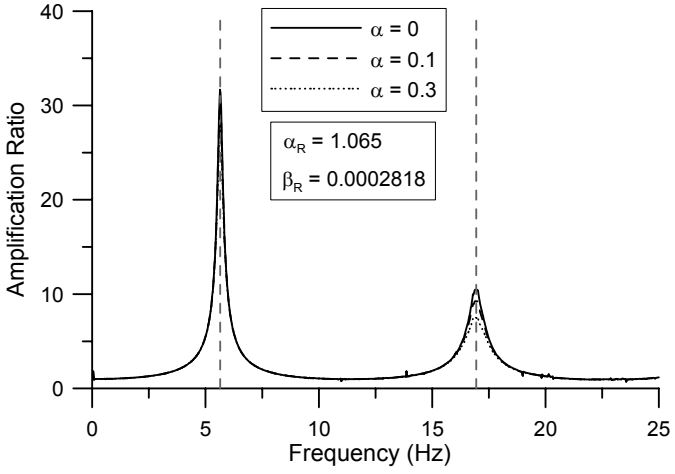

Figure B-9. *Influence of the numerical damping coefficient on the amplification function of the model.*

The amplification functions plotted in Figure B-9 were calculated for a time-step *dt* equal to 0.5 ms. This value was established in order to respect the stability rule (5-60) on the critical time step dt_{crit} in a dynamic calculation for a single mesh element (Pal, 1998 as quoted by Brinkgreve, 2002).
In a finite element model the critical time step is equal to the minimum value of dt_{crit} according to (5-60) all over the elements. The setting of higher time-steps *dt* to reduce the computational time needs an accurate check to control the accuracy of the results.
The comparison of the system response to the same signal with three different time steps *dt* is represented in Figure B-10. The curves were obtained by assuming the previous Rayleigh damping coefficients and using constant average acceleration scheme (α = 0). It can be noted the underestimation of the second natural frequency when the time-step was increased . This loss of accuracy cannot be eliminated by adopting others integration methods (i.e., α > 0).

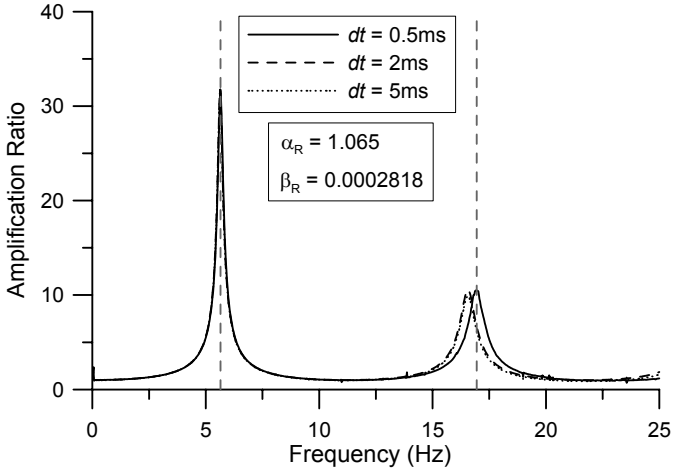

Figure B-10. *Influence of the time step dt on the amplification function of the model.*

From Figure B-9 and Figure B-10, it results that the choice of the parameters α and *dt* affects the value of the maximum amplification ratios $A_{max,n}$ and introduces a numerical source of damping.
In order to quantify the effects of such numerical damping on the seismic response of the soil column, the damping ratios D_n of the first and the second vibration mode of the layer were calculated from $A_{max,n}$ by using the inverse form of equation (B-3). The calculated values for the TMZ-270 seismic motion are reported in Table B-1. When α ≠ 0, the damping ratio D increases with both α and *dt*, whereas for α = 0 (constant average acceleration scheme) any changes in *dt* do not influence the value of D.
The increase of D due to numerical damping is larger at the higher vibration modes of the system. Therefore, the increases of the damping ratios, ΔD_n, have been normalized with respect to the corresponding circular natural frequencies, ω_n, and plotted as function of both α and *dt* in Figure B-11. The solid and the hollow points, referred to the 1*st* and the 2*nd* mode of vibration respectively, are aligned on straight lines with the following equation:

$$\frac{\Delta D_n}{\omega_n} = \frac{1}{2}\,\mathrm{dt}\,\alpha \qquad \text{(B-10)}$$

1st Vibration Mode				2nd Vibration Mode			
α	*dt* (ms)			α	*dt* (ms)		
	0.25	0.5	1		0.25	0.5	1
0.0	2.00%	2.00%	2.00%	0.0	2.00%	2.00%	2.00%
0.1	2.05%	2.10%	2.19%	0.1	2.16%	2.29%	2.56%
0.2	2.10%	2.19%	2.36%	0.2	2.29%	2.56%	3.09%
0.3	2.14%	2.27%	2.54%	0.3	2.42%	2.82%	3.63%

Table B-1. *Effects of numerical dissipation (α and dt) on the modal damping ratio D_n of the soil column.*

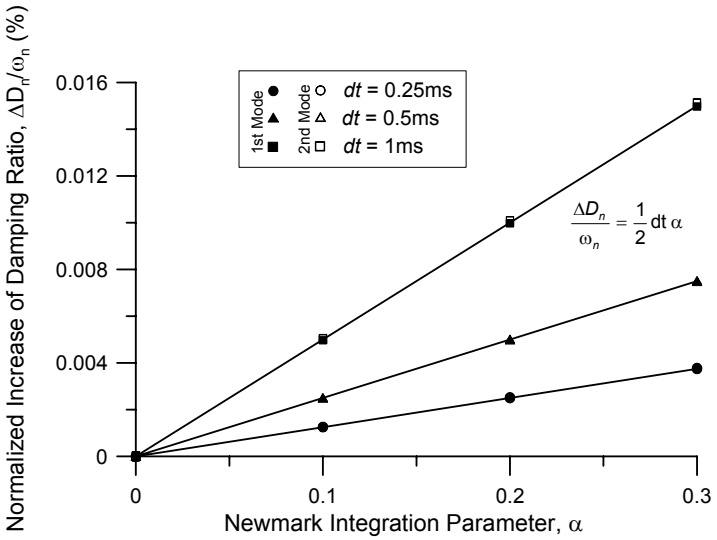

Figure B-11. *Normalized increase of modal damping ratio induced by the Newmark damped integration schemes.*

For the time step *dt* = 1ms, larger than the limit value given by the accuracy condition (5-60), a small scattering of data can be noticed.

The relationship (B-10) was validated on other homogeneous layers with various values of thickness, damping ratio and shear wave velocity.

On the basis of these outcomes, it can be concluded that, if the modified Newmark integration scheme is used, the entire modal damping ratio, both numerical and material, in a time domain analysis of a homogenous layer crossed by vertical propagating S-waves is equal to:

$$D_n = \xi_n = \frac{1}{2}\left[\frac{\alpha_R}{\omega_n} + (\beta_R + \gamma\,\mathrm{dt})\omega_n\right] \qquad (\text{B-11})$$

In other words, the adoption of a damped Newmark integration scheme (α > 0) according to the HHT method is equivalent to the use of a stiffness proportional damping.

The amplification function and the maximum acceleration profile of the reference layer computed for the TMZ-270 earthquake by assuming *dt* = 0.5ms and α = 0.2 are plotted in Figure B-12. The Rayleigh coefficients were chosen assuming the first and the second natural frequencies of the layer and reducing β_R of the quantity α·dt. Comparing the Figure B-7 and Figure B-12, it appears that the

dynamic analyses performed by using the two sets of parameters, which respect the equation (B-11), give the same results.

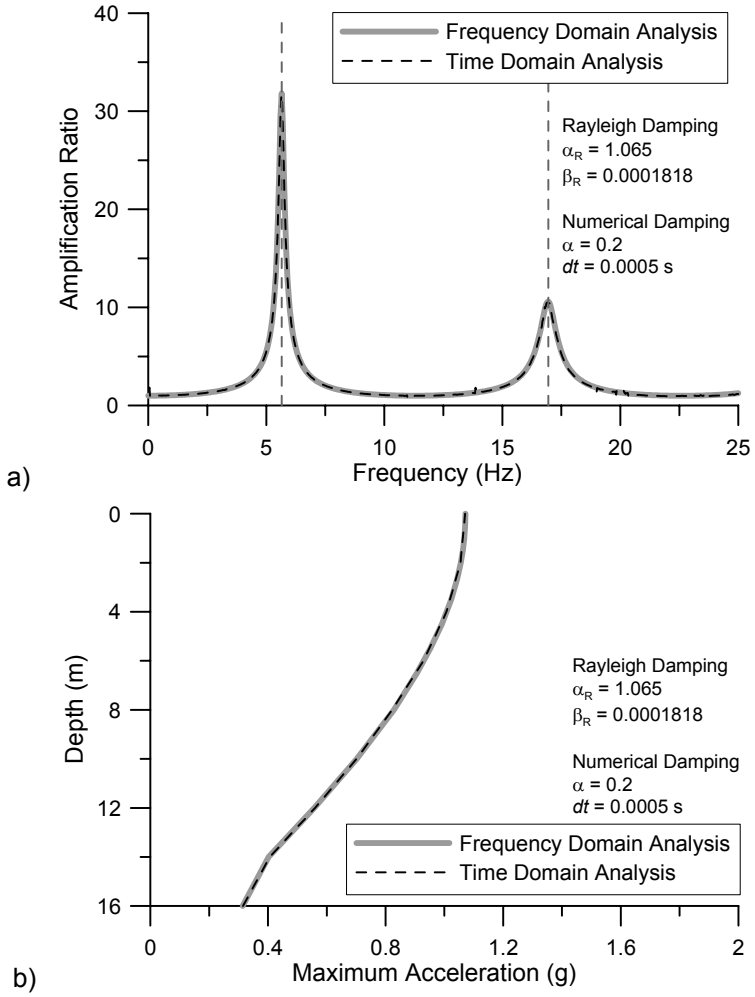

Figure B-12. *Comparisons between the reference and the numerical solutions obtained by adopting a damped Newmark integration scheme for the TMZ-270 input motion: a) amplification functions; b) maximum acceleration profiles.*

B.3.3 Boundary conditions.

The solution obtained by assuming free horizontal displacements on lateral boundaries is only reasonable for non-plastic material and when local site response is the aim of the study. In many other cases, horizontal fixities on the sides of the model should be applied. As underlined in the previous Chapter 5, viscous dampers are often used to simulate infinite media (Lysmer & Kuhlemeyer, 1969), but there is a lack of well-established criteria in the literature for the choice of the parameters c_1 and c_2; following common suggestions, the values of c_1 and c_2 have been set in the analyses to 1.0 and 0.25, respectively. However, if the lateral boundaries are sufficiently far from the central zone, their effects due to the reflection of waves on the boundaries should decrease. In Figure B-13 the results of analyses performed with two values of the ratio between the half-width, B/2, and the height, H of the mesh, in terms of amplification functions and maximum acceleration profile, are plotted together with the frequency domain solution of 1D ground motion. The two computed amplification curves differ from the theoretical solution for the presence of the lateral boundaries. In general, the viscous dampers

affect the values of maximum amplification ratio, which change with the width of the FE model. By varying the mesh dimension ratio B/2H, the peaks of amplification can exceed the desired values, as it is obtained for B/2H=15. Instead, the maximum accelerations at different depths for the smaller model (B/2H=5) are larger than for the wider. This is likely due to the spurious waves reflected on the lateral boundaries. In fact, the computed time histories of acceleration show singular peaks at single time instants, whereas the energy contents of the signals are very close to the theoretical reference solution. Furthermore, by using silent boundaries the surface points have not the same amplification. Figure B-14 shows the amplification functions computed in two different points, one located in the middle of the model, point I, and the other 40 m away from the first, point J. By increasing the width of the mesh, the motion differences at surface can be reduced but the abovementioned effects of the lateral boundaries on the amplification function cannot be completely eliminated. Furthermore, it appears that there is not a threshold for the ratio B/2H making the response of the central domain independent of the boundaries position.

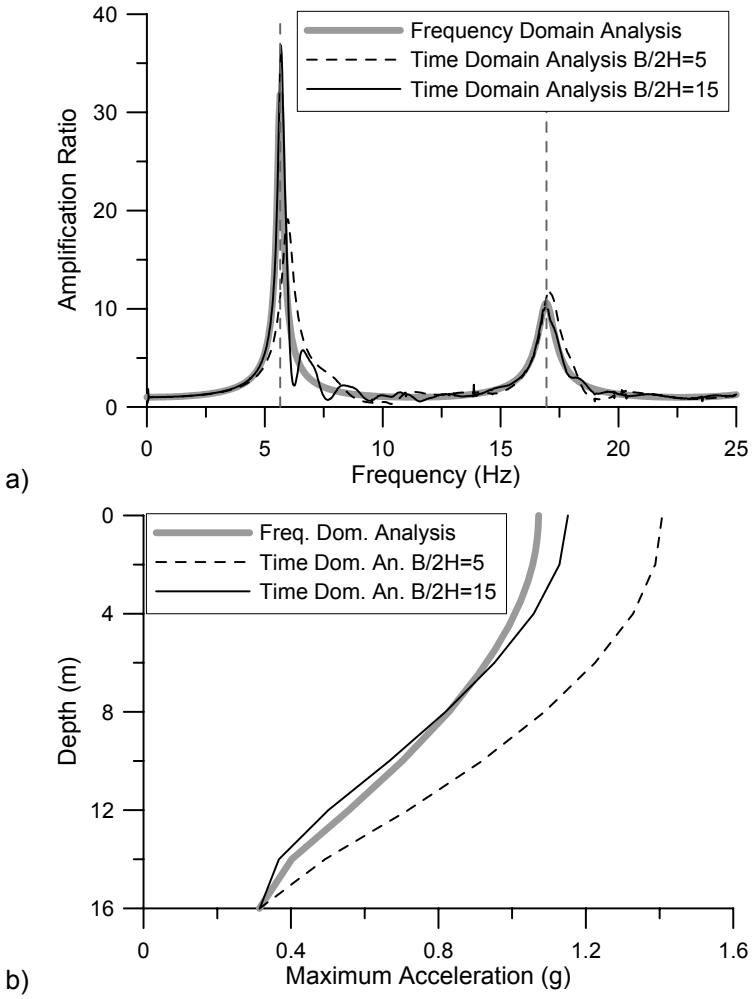

Figure B-13. *Influence of the lateral adsorbent boundaries position on dynamic response of the FE model: a) amplification functions; b) maximum acceleration profile.*

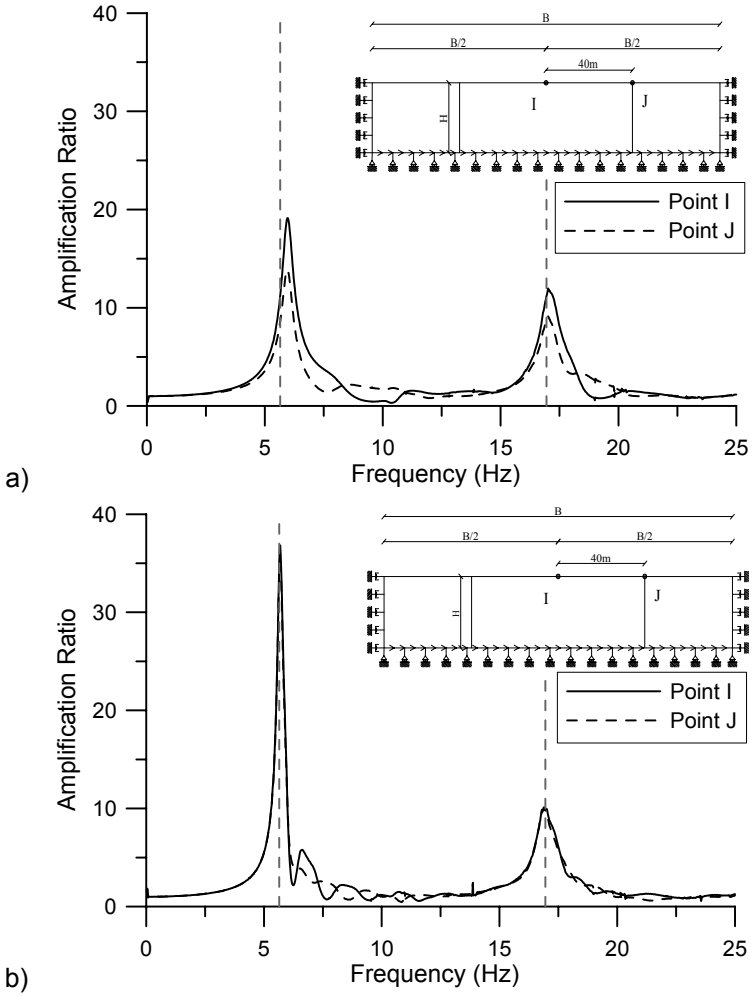

Figure B-14. *Amplification functions at different surface points by using adsorbent boundaries: a) B/2H = 5; b) B/2H = 15.*

Further numerical analyses have been performed by using the Plaxis code on the FE models presented in the previously Figure B-3 in which the peak acceleration of the input signal at the base is decreased linearly from the central part to the vertical boundaries until zero. As in the previous cases, horizontal fixities have been used on the lateral boundaries, with or without the viscous dashpots. The adopted damping parameters, material and numerical, are equal to those established in the previous section for the examined layer (α_R = 1.065; β_R = 2.818x10^{-4}; α = 0; *dt* = 0.0005s).

These models have shown that in such a way the boundary influence decreases and the computation time can be minimized with an increment of the element sizes in the lateral regions, where a rough approximation of the solution can be accepted. In Figure B-15 the obtained results for two values of B/2H are plotted and compared with the solution of the analysis performed in the frequency domain, both in terms of amplification functions and maximum acceleration profiles. For B/2H = 15, the results given by the time and the frequency domain analyses are very similar.

Considering that, for a point source, the body and surface wave amplitudes decrease at a rate of 1/r and , where r is the distance from the source, more suitable lateral attenuation laws of the prescribed accelerations at the base of the model can be used.

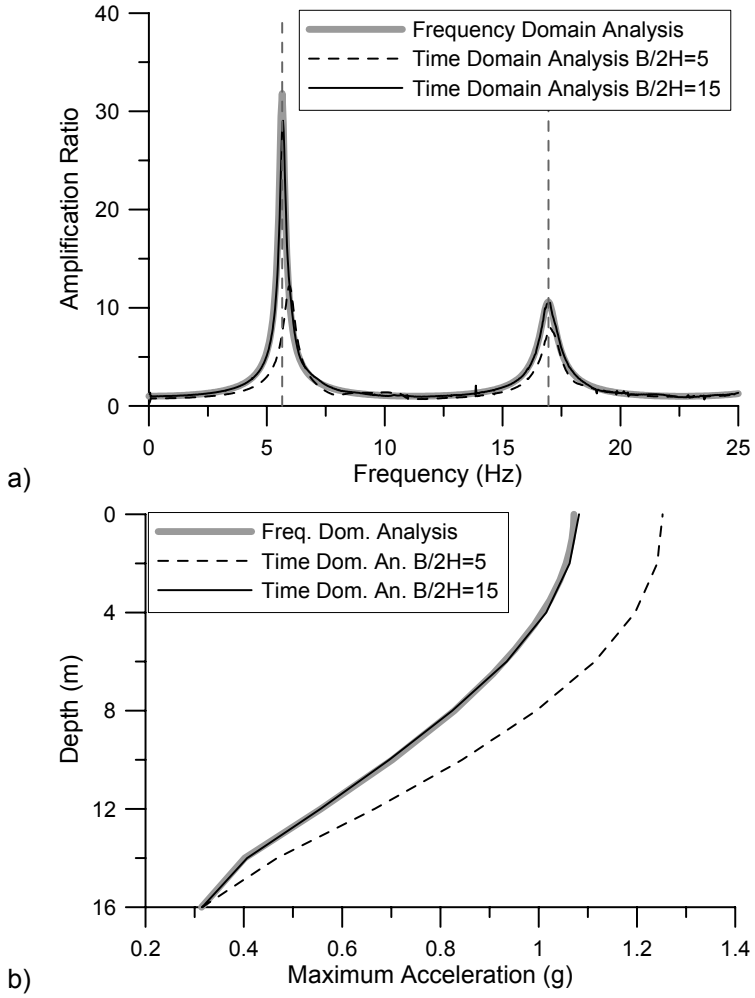

Figure B-15. *Influence of the lateral adsorbent boundaries position on dynamic response of the FE model sketched in Figure B-3: a) amplification functions; b) maximum acceleration profiles (TMZ-270).*

However, even the linear attenuation law adopted in the analyses together with the use of coarser mesh at the sides enables good radiation damping from the central part of the mesh, minimizing the boundaries effects, as it can be deduced from Figure B-16. In this figure, the amplification functions at the two surface points I and J for B/2H=15 are shown, as obtained with and without using lateral adsorbent boundaries.

Even though other techniques might be adopted to model the energy exchanges at the boundaries of the computation domain (e.g., Ross, 2004), the proposed procedure seems to be a simple and pragmatic solution of the problem, requiring only a slightly higher calculation cost.

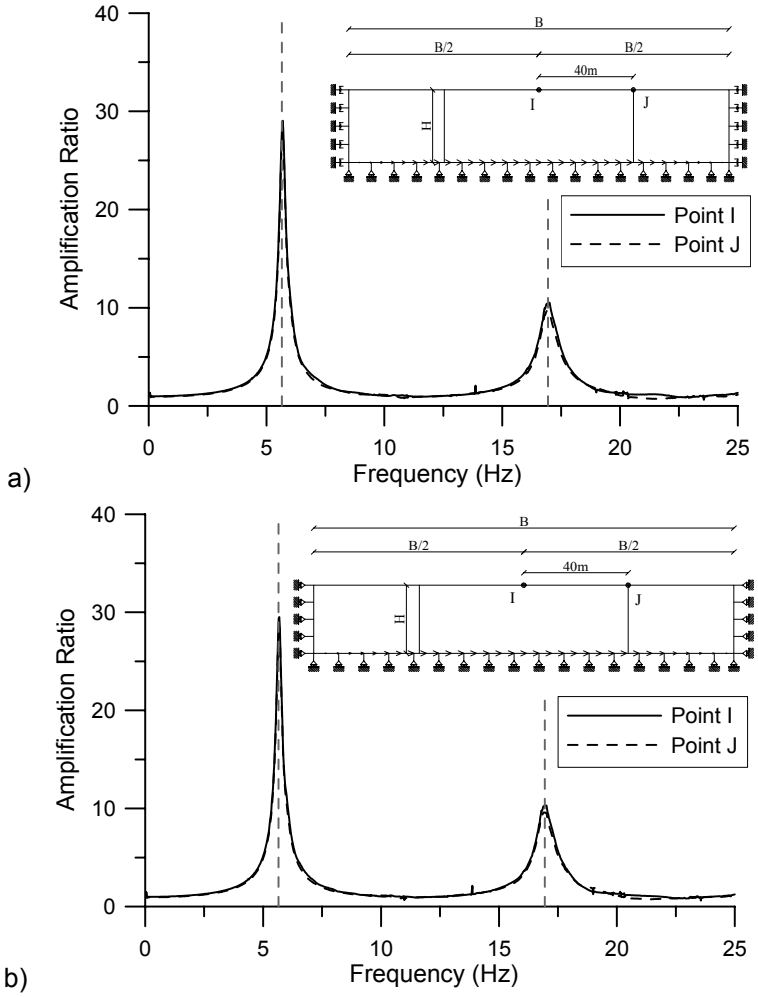

Figure B-16. *Amplification functions at different surface points for B/2H = 15 using the FE model of Figure B-3: a) with lateral adsorbent boundaries; b) without lateral adsorbent boundaries.*

B.4 OUTLINE OF 1-D CALIBRATION PROCEDURE FOR FE MODELS.

On the basis of the previously described results of the dynamic finite element analyses performed in this research, the following steps for the calibration of the seismic response of FE models can be recognized.

To model the material damping by using the Rayleigh formulation:

1. consider a FE soil column (Figure B-2) of a layered deposit (at this stage, the width of the model does not affect the results), constrained by total fixities at the bottom and vertical fixities at the sides;
2. if a constant average acceleration scheme ($\alpha = 0$) is used for the time integration, choose the Rayleigh damping coefficients assuming as target the match of the damping ratio D at two natural frequencies of the subsoil; for a damped Newmark integration scheme ($\alpha > 0$), instead, the β_R Rayleigh parameter should be reduced of the quantity $\alpha \cdot dt$
3. compare the numerical results in terms of both amplification functions and maximum acceleration profiles with those obtained by theoretical solutions or frequency domain

analyses, in order to check the accuracy of the mesh discretization and the time step *dt*.

To reduce the effect of the lateral boundaries (needed for boundary value problems):

4. add two rectangular domains with a coarse mesh at the sides of the region of interest; the acceleration time-history at the base of the FE model under the region of interest has full amplitude whereas it is linearly tapered down to zero under the lateral domains. The zero value is set in correspondence of the lateral boundaries;
5. increase the width of the model (the lateral regions only should be changed at this stage) and choose the more suitable mesh dimension ratio B/2H to attain a good agreement with the 1D reference solution both in the frequency domain (amplification function) and in the time domain (maximum acceleration profile).